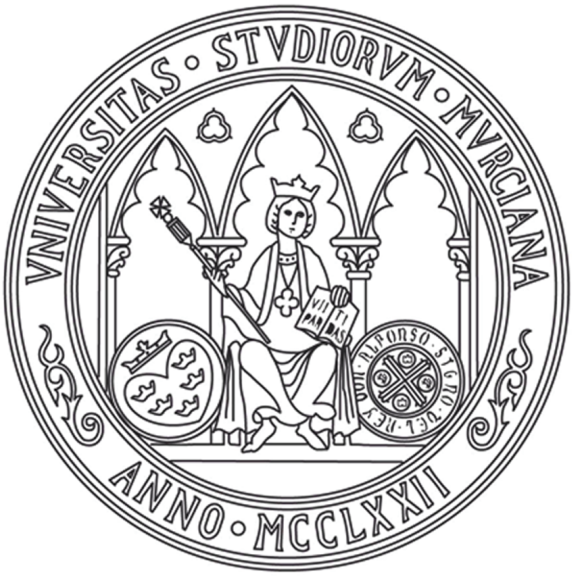

UNIVERSIDAD DE MURCIA

FACULTAD DE MEDICINA

Design of an Open-View Binocular Sensor
for the Study of Accommodation

Desarrollo de un Sensor Binocular en Visión
Abierta para el Estudio de la Acomodación

D. Emmanuel Chirre

2017

Universidad de Murcia

Departamento de Física
Laboratorio de Óptica

DESIGN OF AN OPEN-VIEW BINOCULAR SENSOR FOR THE STUDY OF ACCOMMODATION

DESARROLLO DE UN SENSOR BINOCULAR EN VISIÓN ABIERTA PARA EL ESTUDIO DE LA ACOMODACIÓN

Thesis presented at the Faculty of Medicine
of the University of Murcia by:

Emmanuel Chirre

To attain the degree of PhD from the University of Murcia.

Laboratorio de Óptica. Departamento de Física. Universidad de Murcia.

Abril de 2017

Don Pablo Artal, Catedrático de Universidad del Área de Óptica en el Departamento de Física, y Don Pedro María Prieto Corrales, Profesor Titular de Universidad del Área de Óptica AUTORIZAMOS:

La presentación de la tesis doctoral titulada "DESARROLLO DE UN SENSOR BINOCULAR EN VISIÓN ABIERTA PARA EL ESTUDIO DE LA ACOMODACIÓN", realizada por D. Emmanuel Chirre bajo nuestra inmediata dirección y supervisión en el Departamento de Física, y que presenta para la obtención del grado de Doctor por la Universidad de Murcia.

Murcia, 24 de Abril 2017

Resumen

El objetivo de esta tesis es el diseño y desarrollo de un sensor de frente de onda Hartmann-Shack (H-S) binocular en visión abierta y su utilización para estudiar el comportamiento de distintos aspectos del mecanismo de acomodación y fenómenos relacionados, como la convergencia o la miosis acomodativa, en condiciones más realistas que los experimentos realizados hasta la fecha. El concepto de "visión abierta" (open-view) se refiere a que las medidas de acomodación y de aberraciones se realizan de manera desapercibida para el sujeto mientras observa de forma prácticamente "natural" el mundo situado ante sus ojos. Un instrumento de estas características ofrece una gran versatilidad ya que será posible realizar medidas aberrométricas y de acomodación mientras el sujeto realiza cualquier tipo de test visual que situemos frente a él.

Objetivos

Los principales objetivos de esta tesis han sido:

- Desarrollo, calibración y utilización de un sensor binocular de Hartmann-Shack (H-S) empleando radiación infrarroja invisible que permita realizar medidas desapercibidas del frente de onda ocular en visión abierta, combinado con un algoritmo de seguimiento de pupila en tiempo real (25 Hz).
- Validación del instrumento en condiciones experimentales con sujetos jóvenes: Medición simultánea y continua de la acomodación, convergencia, del tamaño pupilar y de las aberraciones monocromáticas en ambos ojos para diferentes vergencias.
- Estudio de la dinámica de la respuesta acomodativa (acomodación, vergencia y tamaño pupilar) para una tarea de acomodación de lejos a cerca en visión binocular y monocular.
- Estudio de la acomodación y refracción en baja luminancia y el posible origen acomodativo de la miopía nocturna.
- Estudio de la respuesta de acomodación en luz policromática.

Instrumento

El sensor de H-S binocular en visión abierta desarrollado en esta tesis permite la caracterización de las aberraciones oculares de ambos ojos simultáneamente en tiempo real mientras el sujeto realiza cualquier tarea visual en condiciones realistas. Las medidas se realizan en iluminación infrarroja (1050 nm) utilizando intensidades del orden de decenas de μw lo que, además de ser totalmente seguro, resulta invisible para los sujetos. Un ancho espejo dicroico, transparente para el visible y situado a 45º de la horizontal, preserva una visión natural del mundo mientras que refleja la luz infrarroja permitiendo que tanto la iluminación como el propio sensor se sitúen en un plano por debajo de la línea de mirada del sujeto. Adicionalmente, se ha incorporado un brazo

de calibración que emplea iluminación visible (633 nm) para caracterizar la distancia focal efectiva del H-S, la precisión, el rango dinámico y comprobaciones iniciales de calibración.

Validación de Instrumento

Se ha comprobado que el sistema proporciona medidas precisas de refracción para ángulos de rotación del ojo por debajo de 12.5º, por lo que el uso experimental del instrumento se restringió a valores de vergencia que requieran rotaciones inferiores a dicho valor. En un grupo de sujetos jóvenes normales se comprobó que la refracción objetiva obtenida a partir de los coeficientes de Zernike de 2º orden, mostró una evolución lineal con el incremento de la demanda dióptrica, acompañado de un lag acomodativo a niveles dióptricos altos. Se observaron comportamientos lineales de la convergencia (disminución de la distancia entre pupilas) y del tamaño de pupila en ambos ojos. Se encontró una buena correlación entre los cambios relativos de acomodación y de convergencia. La aberración esférica presentó un desplazamiento negativo estadísticamente significativo, también lineal con el aumento de la respuesta acomodativa. No se observó tendencia clara para la aberración de astigmatismo. Para aberraciones de altos órdenes los valores observados fueron en promedio consistentes con la literatura.

Dinámica de la respuesta acomodativa (acomodación, convergencia y tamaño pupilar)

En visión binocular las respuestas de acomodación, convergencia y tamaño pupilar fueron más rápidas que en visión monocular. Se observó que binocularmente la convergencia se realiza de manera muy rápida y eficaz y la rotación de los ojos se desencadena de forma simultánea y sincronizada. En visión monocular, la acomodación y la convergencia fueron más lentas y presentaron una mayor variabilidad entre sujetos. En estas condiciones se observó que al pasar de un estímulo lejano a cercano, el ojo ocluido realiza un primer movimiento en dirección temporal lo que correspondería a un movimiento sacádico entre objetos en el mismo plano, para posteriormente converger de forma relativamente lenta y, sincronizada con la acomodación. El desenfoque monocular produce acomodación, lo que a su vez estimula la interacción acomodación-convergencia, induciendo la rotación del ojo sin estímulo. La dinámica temporal de los reflejos de acomodación (acomodación, convergencia y tamaño de pupila) ha mostrado una gran similitud entre ojos en visión binocular como monocular, excepto para el movimiento de los ojos cuando no existe disparidad. Estos resultados ponen de manifiesto la importancia de la binocularidad en la respuesta dinámica de la acomodación a un estímulo cercano. Como ejemplo, se realizaron medidas en un único sujeto con la acomodación paralizada en uno o ambos ojos. Se observó que incluso en ausencia de desenfoque monocular, la convergencia ante un estímulo cercano se produce en visión binocular. No obstante en ausencia de disparidad y desenfoque monocular, la convergencia no se realiza de forma eficaz, lo que pone de manifiesto la complejidad de la repuesta acomodativa.

Mecanismo de acomodación en bajas luminancias.

Se observó en promedio un desplazamiento miópico del equivalente esférico en visión binocular y monocular en baja luminancia, un fenómeno denominado miopía nocturna, si bien se encontró una gran variabilidad entre sujetos, incluyendo algunos casos con gran cambio miópico, otros estables y con desplazamiento hipermetrópico. El cambio en el desenfoque se acompañó de valores de convergencia espuria. Este comportamiento se observó con menor amplitud en visión binocular. Se calculó que la aberración esférica solo puede tener un leve impacto en este comportamiento. La reducción de la ametropía aparente en condiciones binoculares puede deberse principalmente a que la disparidad retiniana actúa como pista acomodativa que previene la sobre acomodación y a que la sumación binocular reduce el umbral de detección. Se encontró que el cambio acomodativo en baja luminancia está altamente relacionado con la posición tónica de acomodación o foco a oscuras, y que es altamente correlacionado en ambos ojos, lo que explicaría la semejanza del fenómeno entre ojos y apoya la hipótesis que la miopía nocturna puede tener un origen acomodativo. Sin embargo, el estado de reposo de la convergencia o convergencia a oscuras está sólo moderadamente correlacionado con el foco a oscuras, lo que hace intuir una disociación de los procesos en la oscuridad. Este trabajo demuestra la hipótesis que la miopía nocturna tiene una génesis acomodativa, desplazando el foco hacia el estado de reposo del alojamiento en la oscuridad total.

Acomodación en luz policromática.

La refracción estimada a partir de los coeficientes de Zernike de 4º orden incluyendo la aberración esférica presentó un comportamiento consistente con la acomodación en función de la longitud de onda del estímulo. El cambio de foco cromático para vergencia cercana compensa de manera efectiva el efecto de la aberración cromática longitudinal del ojo. No obstante, se observaron algunas discrepancias para el azul. Para estímulos verdes y blancos, se observó un comportamiento muy similar tanto para lejos como para cerca, en torno a la vergencia teórica. Se observó un aumento estadísticamente significativo de los tiempos de acomodación con el aumento del gap de refracción. Al contrario, no se observó una tendencia clara para la velocidad media y máxima de acomodación y con grandes variaciones entre sujetos. La amplitud de miosis era estable sin cambios significativos con la longitud de onda. Tampoco se midieron cambios de convergencia correlacionados con el gap de refracción en visión binocular. La disparidad retiniana y el emborronamiento monocular proporcionan información contradictoria al sistema visual: mientras que la disparidad ayuda a mantener la convergencia a la vergencia adecuada, el emborronamiento monocular produce cambios de acomodación para contrarrestar la aberración cromática del ojo.

Resumen

Conclusiones de la tesis

1. Se desarrolló un sensor de frente de onda de Hartmann-Shack infrarrojo para medir la repuesta acomodativa y las aberraciones de ambos ojos simultáneamente. El instrumento permitió medidas desapercibidas a 1050 nm y hasta 25Hz. El diseño en doble nivel del sensor permite una configuración de visión abierta y un campo de vista realista.

2. El instrumento H-S demostró buenas capacidades permitiendo medir simultáneamente la refracción, el tamaño de pupila y las aberraciones monocromáticas en ambos ojos, así como la convergencia en estado estable de acomodación.

3. El rango dinámico del instrumento está limitado a rotación del ojo alrededor de 12.5º, lo que corresponde a vergencia de 3.5 D para convergencia monocular, o 7D si la convergencia se divide uniformemente entre los ojos.

4. La dinámica temporal de los reflejos de acomodación (acomodación, convergencia y tamaño de pupila) ha mostrado una gran similitud entre los ojos en visión binocular y monocular, excepto para el movimiento ocular en monocular. Los tres reflejos han mostrado una respuesta temporal más rápida en visión binocular.

5. En visión monocular, se produce inicialmente un movimiento rápido de tipo sacádico del ojo seguidor en dirección temporal. Luego el desenfoque monocular proporciona una señal de acomodación activando el enlace de acomodación-convergencia seguido de un movimiento del ojo ocluido en dirección nasal de forma sincronizada con la acomodación.

6. Se observó un desplazamiento miópico de la acomodación en promedio con la disminución de la luminancia y con alta variabilidad entre sujetos. Algunos sujetos no presentan cambios de acomodación significativos cuando otros si un ligero cambio hipermetrópico.

7. El error acomodativo promedio fue menor en visión binocular que en monocular para cada nivel de luminancia, probablemente debido a sumación binocular.

8. En cada caso, el desplazamiento de acomodación en visión monocular ($R^2 = 0{,}77$) y binocular ($R^2 = 0{,}92$) a baja luminancia está altamente correlacionado con la acomodación tónica, también correlacionado entre ambos ojos ($R^2 = 0.90$). Esto explicaría la similitud del fenómeno de miopía nocturna entre ojos y sugiere que tiene una génesis acomodativa.

9. La convergencia a oscuras está moderadamente correlacionada con la acomodación a oscuras ($R^2 = 0{,}43$) sospechando una disociación de dichos procesos en oscuridad total.

10. La refracción medida en el espectro visible ha mostrado cambios consistentes con la acomodación para contrarrestar el efecto de la aberración cromática longitudinal, aunque con algunas discrepancias en el azul.

11. Los tiempos de acomodación han mostrado un aumento lineal con el aumento del gap de refracción lo que sugiere una relación con la longitud de onda de los estímulos. No obstante, no se observó tendencia clara para la velocidad media y pico de acomodación y con alta variabilidad entre sujetos.

12. No se observaron cambios significativos de convergencia con el gap de refracción. La disparidad retiniana y el desenfoque monocular proporcionan información contradictoria al sistema visual: la primera ayuda a mantener la convergencia en visión binocular, cuando la última genera cambios de acomodación para contrarrestar la aberración cromática longitudinal del ojo.

Índice

Experimentos

Conclusiones

Summary

The main goal of this thesis is the design and development of an innovative binocular Hartmann-Shack (H-S) wavefront sensor in open-view configuration and its use to study the behavior of various aspects of the mechanism of accommodation and related phenomena, such as convergence or accommodative miosis, under more realistic conditions than in the experiments conducted to date. The concept of open-view refers to unobtrusive measurements of accommodation and ocular aberrations while the subject has a field of view dissociated from the actual instrument. An apparatus with such features offers great versatility allowing real time measurements when subjects perform any visual tasks that we set in front of them.

Goals

The general goals of this thesis were:

- Design, assembly, and calibration of a binocular Hartmann-Shack sensor using invisible IR light that allows unobtrusive ocular wavefront measurements in an open-view field, combined with a real time binocular pupil tracker (25 Hz).
- Instrument validation under experimental conditions in young subjects with normal vision: Simultaneous, continuous measurement of steady accommodation, convergence, pupil size, and aberrations for different target vergences.
- Study of the dynamics of the accommodative response (accommodation, convergence and pupil size) in binocular and monocular vision for a far-to-near visual task.
- Study of accommodation and refraction at low luminance and the accommodative genesis of night myopia.
- Study of accommodation in polychromatic light.

Instrument

The open-view Hartmann-Shack sensor developed in this thesis allows the characterization of ocular imperfections of both eyes simultaneously in real time while the subject performs any visual task set in front of them under realistic conditions. The apparatus uses tens of microwatts of infrared light in the micron range (1050 nm), which is completely safe and invisible for the subject. A large 45º horizontally-titled dichroic mirror located in front of the subject's eyes preserves a natural field of view, since visible light is transmitted, but allows transfer by reflection of IR beams to and from a level below the subject's line of sight, where both the illumination source and the wavefront sensor are located. Additionally, a calibration arm using red (633 nm) light has been incorporated for characterization of the effective focal length of the H-S, precision and dynamic range, and other initial calibration tasks.

Instrument Validation

We found that the instrument provides accurate measurements of refraction for eye rotation angles below 12.5º. Consequently, the experimental use of the instrument was limited to vergence values requiring rotation angles above this value. In a group of normal subjects, we found that ocular refraction, obtained from the 2nd order Zernike coefficients, showed a linear behavior with increasing dioptric demand, although accompanied by an accommodative lag at high dioptric levels. Convergence (decrease in interpupillary distance) and pupil size in both eyes also showed a linear dependence on dioptric demand. The relative changes of convergence and accommodation were well correlated. Spherical aberration also presented a linear negative shift ($p<0.05$) with increasing accommodation and no clear trend was observed for astigmatism. The behavior for high-order aberrations was consistent on average with literature.

Dynamic of accommodation responses (accommodation, convergence and pupil size)

In binocular vision, accommodation, convergence, and pupil size responses were faster than in monocular conditions. We found that convergence is performed fast and efficiently and rotation of the eyes are triggered simultaneously and synchronized in binocular vision. In monocular conditions, accommodation and convergence were slower and showed greater variability among subjects. Under these conditions, when the unoccluded eye switches fixation from far to near, its fellow eye (occluded) first shifts in temporal direction in a saccadic-like movement and then more slowly converges to the (occluded) object, synchronous with accommodation. Monocular blur is known to activate accommodation, which in turn stimulates the cross-link accommodation-convergence inducing rotation of the occluded eye. These results stress the important role of binocularity on the accurate dynamic response to near targets. As an example, measurements were repeated in one subject with the accommodation paralyzed in one or both eyes. We observed that even in the absence of monocular blur, convergence occurred to a near stimulus in binocular vision. In the absence of retinal disparity and monocular blur, convergence was very slow and inefficient showing the complexity of accommodative response.

Accommodation and refraction at low luminance.

A myopic shift on average was observed in monocular and binocular vision with decreasing luminance, producing night myopia. Individually, there was a wide range of behaviors, with some subjects showing large myopic shifts and others remaining stable or even having a slight hyperopic shift. Under binocular vision, the accommodative error was smaller. Possible causes of the binocular reduction were the convergence cue produced by retinal disparity and binocular summation. We observed that spherical aberration did not play a major role in night myopia. In all cases, the accommodative shift was highly correlated to the tonic accommodation or dark focus, which was also highly correlated between eyes. This may explain the similarity of the

phenomenon of night myopia between eyes. Dark convergence, on the other hand, was only moderately correlated with dark focus, but the change in defocus (when occurring) with decreasing luminance came associated with vergence. Our results strongly support the idea suggesting that night myopia has an accommodative genesis, shifting defocus towards the resting state of accommodation in total darkness.

Accommodation response in polychromatic light

Refraction, estimated from the fourth-order Zernike terms including spherical aberration, showed a consistent behavior of accommodation as a function of stimulus wavelength. For near accommodation, experimental data closely followed the theoretical refraction. However, for far accommodation refraction presented some discrepancies for short wavelength (blue). A linear increase of accommodation time with increasing refraction step was observed. Nonetheless, mean accommodation velocity did not show any tendency with wavelength nor peak velocity of accommodation. Specially, the latter varied widely across subjects. The amplitude of miosis was relatively stable on average with refraction and no statistical changes of convergence were observed as a function of stimulus wavelength. Retinal disparity and monocular blur seem to provide conflicting information, the former helping to maintain vergence at the stimulus vergence by binocular fusion and the latter driving accommodation changes to counterbalance the eye's longitudinal chromatic aberration.

Conclusions of the Thesis

1. An infrared Hartmann-Shack (H-S) wavefront sensor was developed for measuring the accommodation response and monochromatic aberrations in both eyes simultaneously. The instrument allowed unobtrusive measurements at 1050 nm up to 25 Hz. A two levels-design provided an "open-view" configuration where the field of view was realistic.

2. The H-S instrument demonstrated good capacities, allowing simultaneous measurement of refraction, pupil size and monochromatic aberrations in both eyes as well as convergence from the interpupillary distance under steady states accommodation.

3. The instrument operating range was limited to a maximum rotation of eye about 12.5º for monocular convergence for monocular convergence. If convergence is split evenly between eyes, this allows measurements of target vergence up to 7 D.

4. Temporal dynamics of the accommodation responses (accommodation, pupil miosis and convergence) have shown strong similarity between eyes in binocular and monocular

vision, except for eye motion in monocular. All three processes have shown a faster temporal response in binocular.

5. In monocular vision, an initial fast saccadic-like eye movement in temporal direction of the fellow eye occurred at the onset of accommodation. Then, monocular blur provided a cue to accommodate and the cross-link accommodation-convergence triggered convergence of the fellow eye in nasal direction, synchronized with accommodation.

6. An increasing myopic shift of accommodation was observed on average with decreasing luminance with high intersubject variability. Some subjects presented no changes or slight hyperopic shifts of accommodation.

7. The shift of accommodation at low luminance in binocular had the same tendency as in monocular vision for all subjects but with a reduced magnitude, probably caused by binocular summation.

8. The dark focus or tonic accommodation was highly correlated between eyes ($R^2 = 0.90$), and to the magnitude of defocus shift in both monocular (R^2=0.77) and binocular (R^2=0.92) conditions. This is explained the similarity of night myopia phenomenon between eyes and it suggests that the shift of accommodation at low luminance has an accommodative genesis.

9. Dark convergence was moderately correlated ($R^2 = 0.43$) with dark focus suspecting a dissociation of vergence and accommodation in total darkness.

10. Refraction measured though the visible spectrum showed consistent changes of accommodation to counterbalance the effect of longitudinal chromatic aberration, although with some discrepancies at short wavelength.

11. A linear increase of accommodation time following an increase of the refraction step suggested a correlation with stimulus wavelength, while mean and peak velocity of accommodation did not seem to be influenced.

12. No significant changes of convergence were observed with refraction step. Retinal disparity and monocular blur provided conflicting information: the first helping to maintain convergence at the stimulus vergence, the latter driving accommodation changes to counterbalance the eye's longitudinal chromatic aberration

Table of Contents

Experiments

Conclusions

List of abbreviations

AC	Accommodation-Convergence
AE	Artificial Eyes
BS	Beam Splitter
CA	Convergence-Accommodation
CCD	Charge-coupled device
CDF	Chromatic Difference of Focus
DE	Dominant Eye
DM	Deformable Mirrors
H-OA	High-Order Aberrations
H-S	Hartman-Shack
HSWS	Hartmann-Shack Wavefront Sensor
NIR	Near Infrared
IPD	Interpupillary Distance
LASER	Light Amplification by Stimulated Emission of Radiation
LCA	Longitudinal Chromatic Aberration
LCoS-SLM	Liquid Crystal on Silicon Spatial Light Modulator
LED	Light Emitting Diode
L-OA	Low-Order Aberrations
NDE	Non-Dominant Eye
OD	Oculus Dexter, right eye
OLED	Organic Light Emitting Diode
OS	Oculus Sinister, Left eye
PSF	Point Spread Function
TCA	Transverse Chromatic Aberration
RMS	Root Mean Square

Introduction

1 Introduction

This chapter provides a general overview of the different topics studied in this thesis with a detailed review of the corresponding literature. The last section of this chapter presents the purpose and outlines the thesis.

1.1 The eye

The eye is the sense organ of vision of the human being. It allows a 120º large field of view for a broad spectrum from 390 nm to 700 nm called the visible spectrum. The eye consists of the cornea, the aqueous humor, the crystalline lens, and the vitreous humor, all of them mostly transparent in the visible spectrum, and other non-transparent tissues such as the sclera, the iris, the choroid, and the retina. The pupil is the aperture delimited by the iris, where light enters into the eye. The rays of light, coming from objects located in the visual field, go through the transparent media of the eye towards a photosensitive layer: "the retina". When light strikes the retina, the photoreceptors absorb the photons and chemically trigger a signal that is transmitted to the optic nerve. The latter connects the retina to the brain, where a complex neurological process accomplishes vision. Figure 1.1 shows an anatomical section of the human eye.

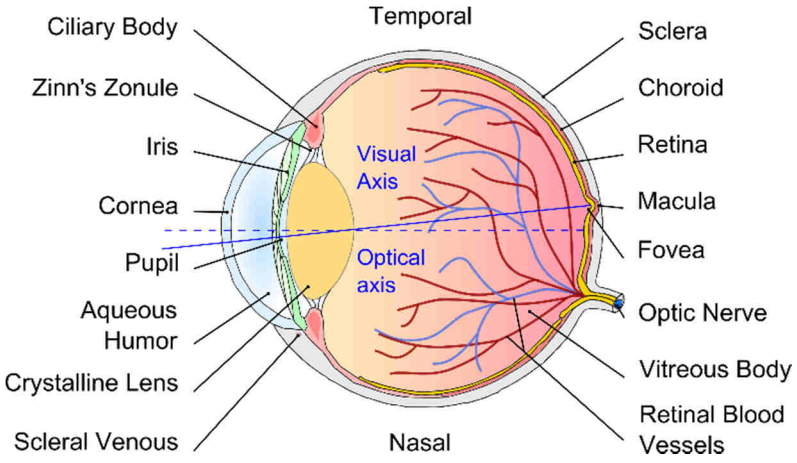

Figure 1.1: Anatomy of the human eye.

The retina contains two types of photoreceptor called cones and rods. Cones are massively concentrated on the fovea where rods are lacking. Three types of cones exist in normal eyes: L, M, and S cones (standing for Long-, Medium-, and Short-wavelength sensitive). The central area of the retina containing cones, the fovea, provides high visual acuity allowing sharp vision of small objects such as for reading. In peripheral retina, rods are more numerous. They are more sensitive than cones but do not provide color information, and they are essentially involved in movement detection in peripheral vision.

The visual and optical axes are marked in Figure 1.1 in solid and dashed blue lines respectively. The optical axis coincides with the center of each optical component of the eye (cornea, pupil and crystalline lens) while the visual axis is centered on the fovea slightly off-axis in temporal direction. The cornea and the crystalline lens are the two optical elements of the eye. The cornea acts as a protective layer and provides the main refractive power of the eye: ~43 D (Atchison & Smith, 2000). The crystalline lens is a biconvex lens located behind the cornea and the iris. In young subjects, it possesses elastic properties and can change its refractive power to focus the image of a near object onto the retina. The emmetropic eye is defined as being 22.6 mm in length and has a total refractive power of 59.98 D.

The iris plays a role on light regulation through pupil constriction or dilation. High luminance levels induce pupil shrinking while low light levels cause pupil widening. Independently of light intensity, accommodation and disaccommodation also stimulate changes in pupil size called miosis (constriction) and mydriasis (dilation) respectively.

The choroid is the vascular layer of the eye and contains the blood vessels and connective tissue of the retina. It is located between the retina layer and the sclera providing oxygen and nutrients. The vitreous humor is a transparent media that is around 99 % water with a gelatinous consistency, which fills the eye and keeps the retina connected to the choroid by pressure. The production and drainage equilibrium of the aqueous humor in the anterior and posterior chambers of the eye regulates the intraocular pressure.

1.2 History

The Greek philosopher Empedocles (490-430 BC) postulated the hypothesis of the active eye to explain sight. Empedocles' theory, also known as emission theory and supported by Plato (424-348 BC), evoked the interaction of two fires, one emitted by the eyes illuminating the world and another emitted from the world to the eyes. The union of these fires allowed visual perception of the world. Euclid (III century BC) proposed a geometrical method to explain the straight-line propagation of light going out of the eye. Aristotle (384–322 BC), on the other hand, did not support Empedocles' theory and proposed the intromission theory, where eye received rays of light rather than sending them outwards.

In the tenth century, the Persian scientist Ibn Al Haytham (or Al Hazen 965-1039 AD) also contradicted the idea of active eye. Al Hazen suggested that rays of light coming from the sun were scattered by objects in all directions and some of them reached the eyes. According to his theory, the pupils were photosensitive while the role of retina was still unknown. The translations from Arabic to Latin of Al Hazen's works brought about the invention of the spectacles in the thirteen-century, attributed to Roger Bacon.

At the beginning of the XVI century, several scientists pointed out the accommodative process of the human eye. The astronomer Johannes Kepler (1571-1630) mentioned the role of

the cornea and crystalline lens as a refractive element of the human eye. Kepler defined also the function of the retina as a vision receptor and showed a movement of the crystalline lens in the near accommodation response. Some decades later, René Descartes (1596-1650) noticed the change in shape of the crystalline lens (diameter and curvature of the posterior and anterior surfaces) with accommodation. He formulated the well-known law of light refraction between two transparent media of different refractive index (The Snell-Descartes law). In Parallel, Scheiner corroborated Kepler's hypothesis by a demonstration of the image projection onto the retina. Later, Thomas Young (1773-1829) established the relationship between the change in curvature of the crystalline lens and accommodation (Atchison & Charman, 2010).

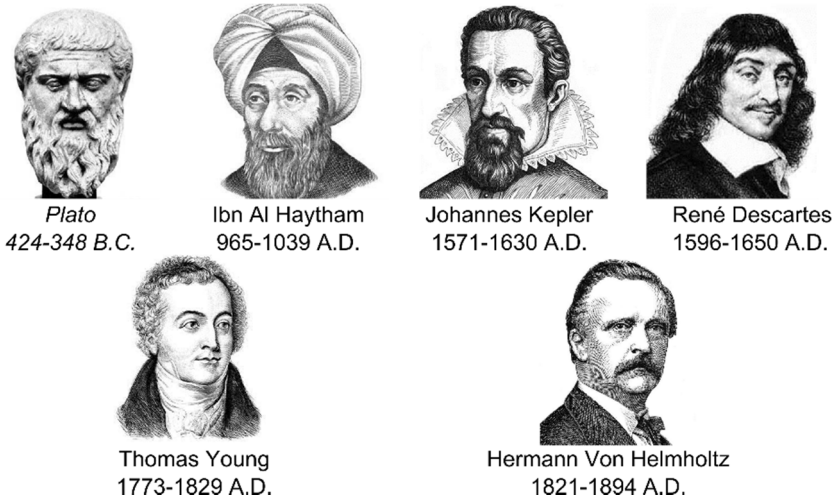

Figure 1.2: Some classical contributors to our understanding of the visual function of the human eye.

Two centuries after Kepler and Descartes, Hermann Von Helmholtz (1821-1894), today recognized as one of the pioneers in vision science, extensively investigated the structure and functioning of the human eye, including the eye's aberrations. He looked at a living retina in 1850 and he published the theory of accommodation in 1855 (Helmholtz, 1855). Figure 1.2 shows pictures of these scientists in chronological order.

1.3 Helmholtz's Theory of accommodation

Helmholtz formulated a theory about the mechanism of accommodation in 1855. In conditions of far vision, the ciliary muscle is relaxed and the suspensory ligaments (Zinn's Zonular fibers) exercise a tension on the crystalline lens that induces a flattening of the lens capsule (see Figure 1.3, top). The eye is unaccommodated and the refractive power of the eye is adequate for far distances. In conditions of near vision, the contraction of the ciliary muscle shortens the ciliary ring, which progressively decreases the tension of the zonular fibers on the lens capsule. Due to the elasticity of the crystalline lens, there is an increase in its thickness and a decrease of

its equatorial diameter (Brown, 1973). The crystalline lens recovers a more spherical shape and the refractive power of the eye increases, focusing to near distances (Figure 1.3, bottom).

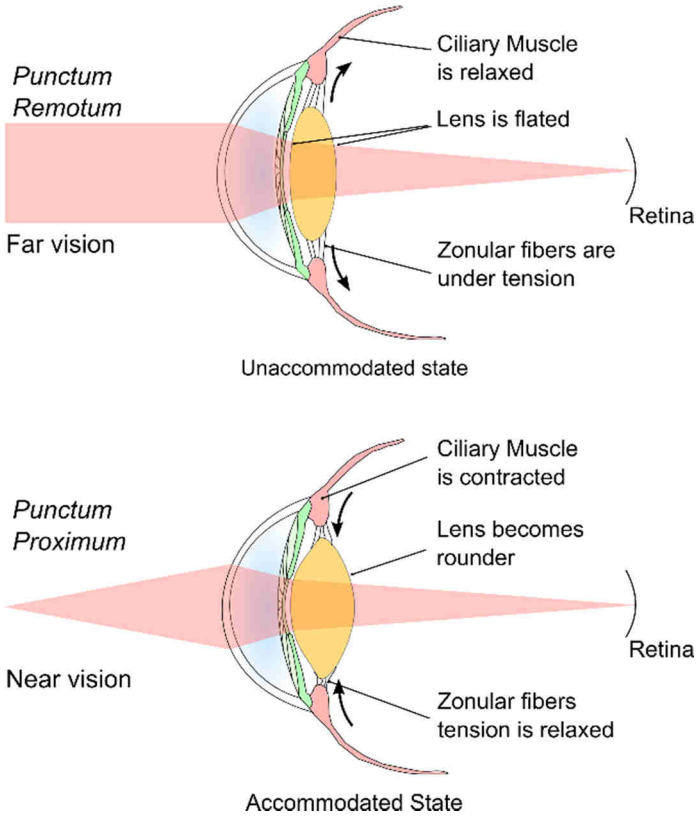

Figure 1.3: Helmholtz's theory of accommodation. Top: Unaccommodated state of the eye in far vision. Arrows indicate the force applied by the suspensory ligaments flattening the crystalline lens. Bottom: Accommodated state of the eye for near vision. The tension of the zonular fibers decreases and the lens becomes more round. Arrows indicate the direction of contraction of the ciliary muscle.

According to Helmholtz´s theory, a crystalline lens removed from the eye takes a natural anatomical aspect that corresponds to an accommodated eye. The mechanism of accommodation is continuously in action to maintain an image focused onto the retina where the subject fixes his attention.

Over the last centuries, Helmholtz's detractors have questioned the theory of accommodation many times. E.g., Marius Tscherning (Tscherning, 1909), one of Helmholtz's hardest opponents, held to the original contention that the lens was adjusted for distant vision instead of fully accommodated for near vision (Hartridge, 1925). Nonetheless, his theory of accommodation has been supported by Fincham in 1925 (Fincham, 1925) and later by many others who have repeated similar experiments with newer and more reliable instruments.

1.4 The accommodative response

The mechanism of accommodation brings about three main responses which occur when a person changes fixation between objects at different distances (Noorden & Campos, 1996). The two visual tasks that can happen in natural conditions are far-to-near or near-to-far accommodation, which respectively correspond to positive or negative changes in dioptric power of the eye. For a far-to-near accommodation task, the responses consist of convergence, accommodation and pupil constriction (miosis), collectively known as the near triad or near accommodative response. For a near-to-far task, divergence, disaccommodation and pupil dilation (midriasis) characterize the far triad response.

1.4.1 Convergence

Convergence is described as the motion of both eyes towards each other (Westheimer & Mitchell, 1956) (Westheimer & Mitchell, 1969) in order to change fixation to a closer object. Binocularly, it is caused mainly by retinal disparity (Stark, Kenyon, Krishnan, & Ciuffreda, 1980) but there are also accommodative cues (Alpern & Ellen, 1956), which are evident in monocular convergence. Divergence is the outwards motion of both eyes away from each other to fix them on a further object and it is also mainly induced by retinal disparity and secondarily by accommodative cues.

Tonic or dark vergence is the resting position of eyes when no stimulus is available to produce binocular fusion. It typically happens under very low light levels or in darkness and it is somehow dissociated from the resting accommodative state, or dark focus (Kotulak & Schor, 1986) (Leibowitz, Gish, & Sheehy, 1988) (Wolf, Bedell, & Pedersen, 1990) (Jiang, Gish, & Leibowitz, 1991). Dark vergence and dark focus are specific to each individual with considerable inter-subject variability and may have an anatomical genesis (Gilmartin & Hogan, 1985b).

Fusion vergence or reflex vergence corresponds to the position of both eyes providing binocular fusion to a single stimulus. It allows 3-D vision and distance information. Panum's fusional area corresponds to the range of eye positions where a point will appear binocularly fused and single. Out of this area, the point does not appear single and it leads to retinal disparity.

There is a certain amount of confusion in the literature between the terms "vergence" and "convergence", which many authors use as synonyms. Strictly speaking, vergence is the symmetric movement of eyes regardless of direction and therefore encompasses both convergence and divergence. However, in this thesis we will use "vergence" as in Geometrical Optics to refer to the reciprocal of the distance to the object. Therefore, to avoid confusion, when speaking about simultaneous eye movements we will use the term "convergence", with a negative sign in case of divergence.

As a final comment, the units of vergence/convergence in classical studies are “meter angle” but since they refer to reciprocal of a distance (from the eyes to the fixation point) in meters, we will simply use “diopters”.

1.4.2 Accommodation

Accommodation is a change in the dioptric power of the eye (Ciuffreda, 1991), due to the change in shape of the crystalline lens to focus objects at variable distances on the retina. Accommodation is usually measured in diopters (D) and it is equal to the reciprocal of the fixation distance (i.e., the distance to the anti-image of the retina) in meters. The primary stimulus to accommodation is the blurred retinal image (Phillips & Stark, 1977) also called monocular blur, which leads to the automatic adjustment response in order to maintain a sharp retinal image. This phenomenon is known as reflex accommodation and occurs unconsciously. Retinal disparity (convergence or divergence) plays also a significant role in activating accommodation (Fincham & Walton, 1957). Changes of target size or luminance, the longitudinal chromatic aberration, and the presence of high spatial frequencies are also secondary accommodation cues. These factors can act together or individually.

The amplitude of accommodation characterizes the ability of the eye to focus a target at different vergences. It is age dependent (Duane, 1912): In babies or young children, the amplitude of accommodation is more than 15 D (Sterner, Gellerstedt, & Sjöström, 2004), and decreases with aging (Applegate, Donnelly III, Marsack, & Koenig, 2007). The losses of elasticity, avoiding changes of the shape of the crystalline lens, is the main responsible for the accommodation amplitude decrease. Consequently, objects at near distances cannot be focused onto the retina and appear blurred. This loss of vision caused by aging is called the presbyopia.

In absence of stimulus, i.e., in total darkness, accommodation takes a resting state called dark focus of accommodation or resting state of accommodation (Tousey, Koomen, & Scolnik, 1953) (Leibowitz & Owens, 1975a) (Leibowitz & Owens, 1978). It is produced by the equilibrium of the ciliary muscular tone (McBrien & Millodot, 1987). This anatomical state of accommodation apparently leads to the phenomenon of night myopia under scotopic conditions (Levene, 1965) after an adaptation time (Miller, 1978).

Interaction of accommodation and convergence

To maintain good vision over time under natural binocular viewing conditions, both convergence and accommodation operate continuously, affecting each other through two major interactions, the cross-linked couples Accommodation-Convergence (AC) and Convergence-Accommodation (CA) (Judge, 1996). The couple CA corresponds to the amount of accommodation stimulated by convergence, while the interaction AC represents the convergence produced by an accommodative stimulus. The two cross-linked couples drive the accommodative

system efficiently by means of retinal disparity and monocular blur information (Figure 1.4) (Schor, 1999).

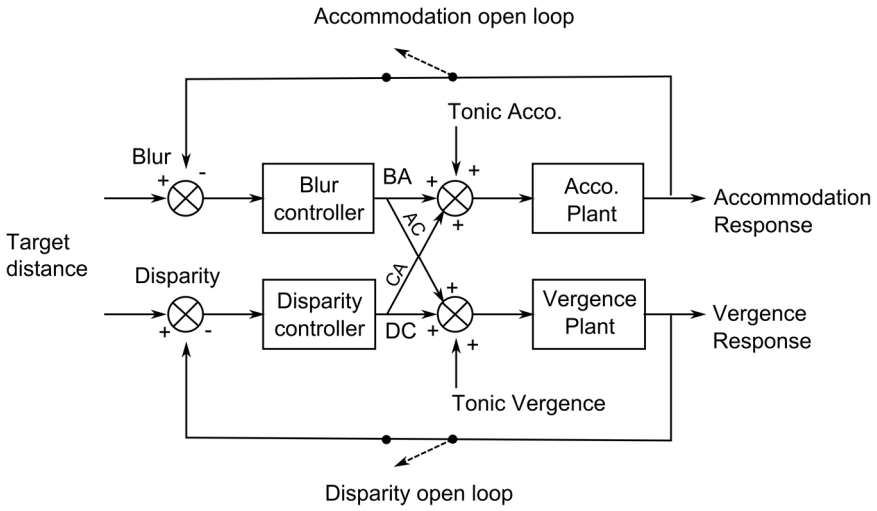

Figure 1.4: Accommodation-Convergence and Convergence-Accommodation dual interaction based on Hung and Semmlow (Hung & Semmlow, 1980) and Schor (Schor, 1992). AC: accommodation convergence; CA: convergence accommodation; BA: blur accommodation; DC: disparity convergence.

1.4.3 Pupillary response

Pupillary response is the change in size of the pupil. It spans roughly from 2 mm to 8 mm in diameter and it has a variety of causes such as accommodation, luminance, drugs, alcohol, sexual stimulation, emotional commotion, attention, REM sleep, etc., leading to two main responses: pupil constriction (miosis) and pupil dilation (mydriasis). In normal viewing conditions, the "accommodation reflex" induces a change in pupil size. It has similarities to the "light reflex" that occurs with a change in retinal luminance. In a brightly lit environment, the sphincter muscles constrict the pupil. On the contrary, the dilator muscles adjust the size of the pupil to low light level. The magnitude of pupil response is stronger and occurs faster with a change in luminance than for a change of fixation but the reaction to an accommodative cue approximately maintains pupil size over time as long as the near fixation distance is maintained (Noorden & Campos, 1996). Anisocoria is the difference in pupil size between eyes. Pupil size differences of several hundredths of millimeter are frequent and considered physiologically normal. Above one half-millimeter, anisocoria can be considered pathological.

1.5 Aberrations of the eye

Visual acuity depends on the optical quality of the eye. Regardless of neurological processes, two main groups of optical imperfections exist. They are the monochromatic/geometrical and chromatic aberrations.

1.5.1 Monochromatic aberrations

Monochromatic aberrations arise from the geometry, irregularities and misalignments of optical systems. In the human eye, the cornea and crystalline lens are the main sources of monochromatic aberrations and they affect retinal image quality. Rays of light entering to the pupil are biased by these imperfections and the Point Spread Function (PSF) quantifies retinal blur. Figure 1.5 shows a spherical wavefront for a perfect eye and a wavefront distorted by the ocular aberrations, which blur the point image projected onto the retina.

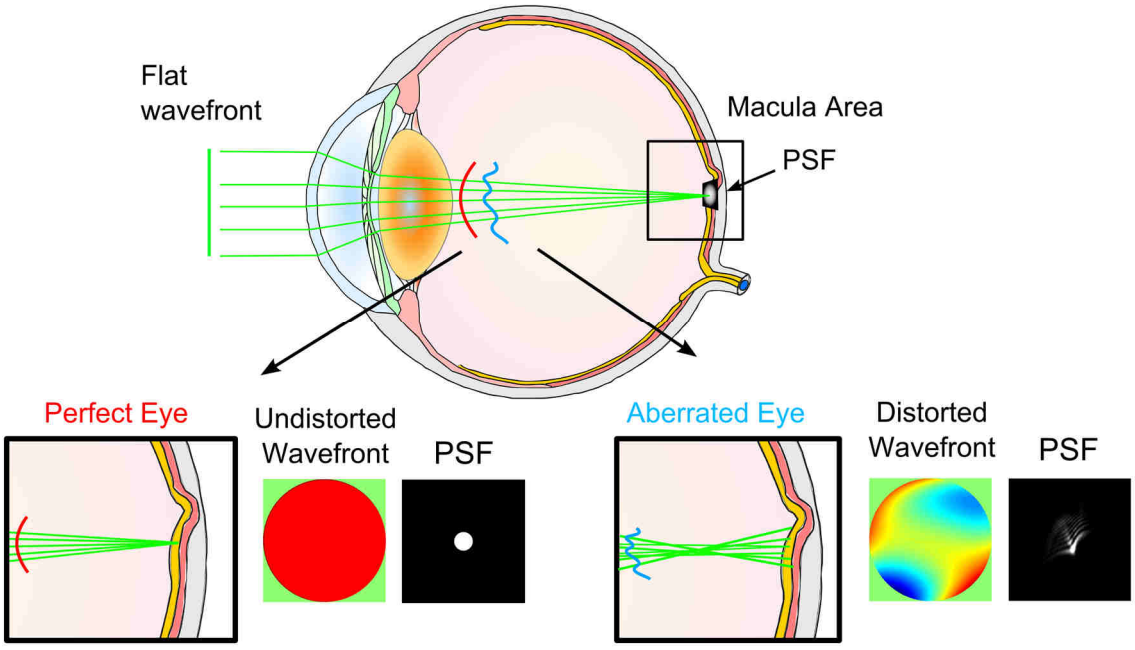

Figure 1.5: Monochromatic aberrations of the human eye. Bottom-left: In a perfect eye free of aberrations the wavefront is purely spherical and the Point Spread Function PSF is diffraction limited. Bottom-right: In a normal aberrated eye aberrations deteriorate the PSF and degrade image quality.

Monochromatic aberrations of the human eye are measured in object space as the difference between a reference plane wavefront in paraxial approximation and the real wavefront which is nearly always distorted (Charman, 1991) at the pupil plane. In a perfect eye, free of aberrations, the optical elements (cornea and lens) of the eye produce a pure spherical wavefront and they project the image in a single spot onto the retina in a diffraction-limited regime. On the contrary, the aberrations of normal eyes distort the wavefront. The amount of monochromatic aberrations increase with pupil size, which proportionally reduces image quality with respect to small pupils (Roorda, 2011). In addition, the neural visual system is adapted to the eye's aberrations (Artal et al., 2004) and neuronal compensation limits to some extent the effect of monochromatic blur.

Monochromatic aberrations are typically grouped into low-order and high-order aberrations. The low-order aberrations, corresponds to 2nd order and includes defocus and astigmatisms. These aberrations are the most prominent ones in the human eye, specially defocus but, on the other hand, are routinely corrected with ophthalmic or surgical methods.

The high-order aberrations are lower in magnitude and, accordingly, have a smaller impact on the optical quality of the eye, except in pathological cases such as keratoconus. Nonetheless, in scotopic luminance level, pupil dilation results in an increase of high-order aberrations, which in turn decrease optical quality. The Root Mean Square of Low- and High-Order Aberrations (RMS L-OA or H-OA) are indicators of the amount aberrations in both groups and does not appear to change systematically with accommodation (Radhakrishnan & Charman, 2007). The aberrations of cornea and internal optics have been shown to partially compensate one another. This is the case for spherical aberration, astigmatism and coma (Artal, Guirao, Berrio, & Williams, 2001). For clinical devices, low-order aberrations are typically converted into the sphere/cylinder/axis notation and given as an objective indicator of the subject's refraction (see section 1.6). Ocular aberrations are typically described mathematically as a set of orthonormal functions called Zernike polynomials (Zernike, 1934).

Zernike Polynomials

Historically, there have been different normalization and ordering schemes for Zernike polynomials, but nowadays the OSA standard (Thibos, Applegate, Schwiegerling, Webb, & Members, 2000), later ratified by ANSI standard (ANSI Z80.28, 2004), is customary in Vision Sciences. It allows a single index notation for simplicity but proper definition of Zernike polynomials involves two indexes: Radial order, n, is the degree of the radial polynomial; and azimuthal order, m, is the angular frequency. By definition, m can take values between –n and +n, with the same parity as n. Thus, any wavefront can be expressed as a linear combination of an infinite number of Zernike polynomials ${Z_n}^m$, describing each one a monochromatic aberration.

$$W(\rho,\theta) = \sum_{n=0}^{\infty} \sum_{m=-n}^{n} {C_n}^m {Z_n}^m(\rho,\theta) \qquad (1.1)$$

where ${C_n}^m$ are the expansion coefficients. It is important to bear in mind that while wavefront aberrations are defined over the eye's pupil, Zernike polynomials are defined over a unit circle, i.e., using a normalized radial unit instead of mm. This latter fact has advantages from a mathematical point of view and the relationship between normalized radial coordinates, ρ, and radial coordinates in mm, r, is simple enough: $\rho = \frac{r}{r_{pup}}$, where r_{pup} is the pupil radius in mm. However, it also means that Zernike coefficient values alone can lead to misconceptions about

the amount of aberrations in the eye, unless escorted by the pupil radius to put them in context. The Zernike polynomial series is defined as:

$$Z_n^m(\rho,\theta) = \begin{cases} N_n^m R_n^{|m|}(\rho)\cos m\theta\,, & m \geq 0 \\ -N_n^m R_n^{|m|}(\rho)\sin m\theta\,, & m < 0 \end{cases} \tag{1.2}$$

where $R_n^{|m|}(\rho)$ is the radial component:

$$R_n^{|m|}(\rho) = \sum_{s=0}^{(n-|m|)/2} \frac{(-1)^s (n-s)!}{s!\,[0.5(n+|m|)-s]!\,[0.5(n-|m|)-s]!}\rho^{n-2s} \tag{1.3}$$

and $N_n^{|m|}$ is the normalization factor:

$$N_n^m = \sqrt{\frac{2(n+1)}{1+\delta_{mo}}} \tag{1.4}$$

Figure 1.6 represents the first Zernike terms up to 5th order in a pyramid scheme.

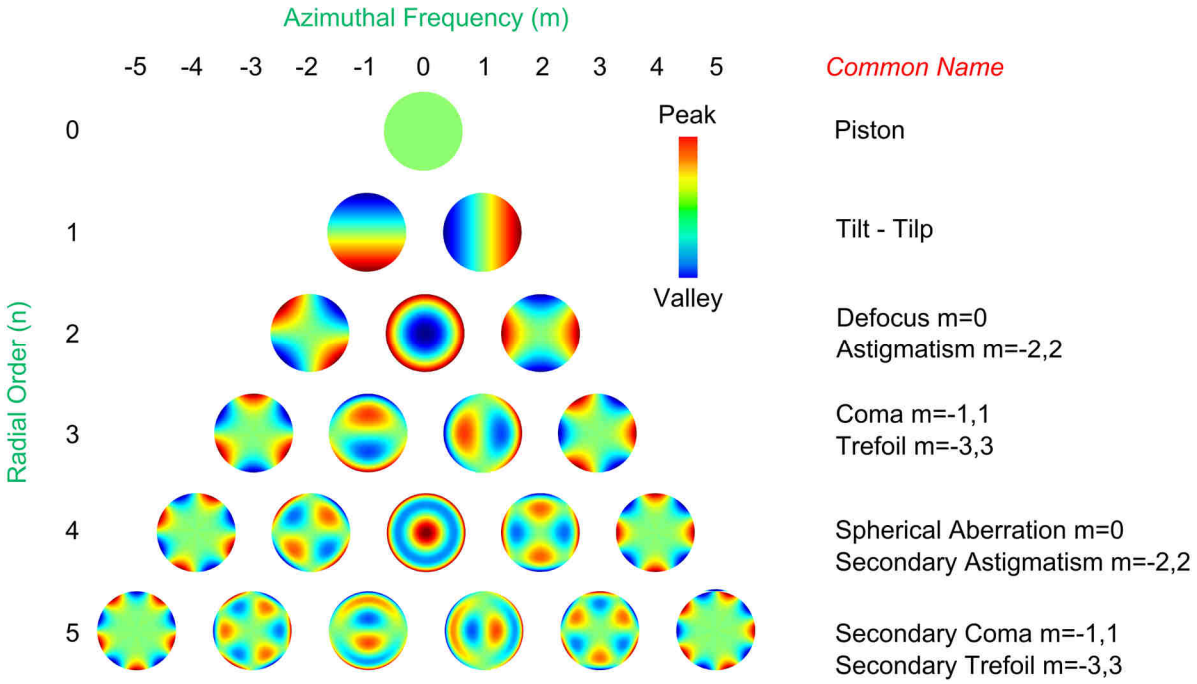

Figure 1.6: Zernike polynomial pyramid up to 5th order with their common name.

Figure 1.7 shows the corresponding PSF for each Zernike polynomial up to 5th order.

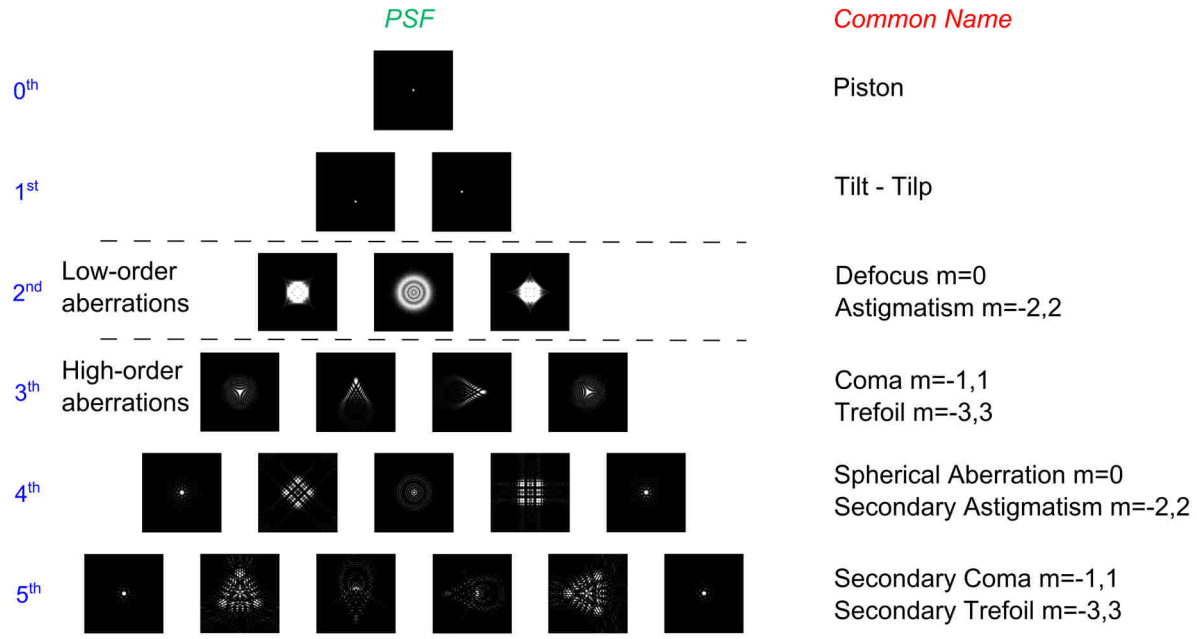

Figure 1.7: PSF for each monochromatic aberration up to 5th order. Dotted lines separate aberration groups: irrelevant (0th and 1st order), low-order (2nd) and high-order (3rd order or higher).

1.5.2 Chromatic aberrations

The dispersion properties of ocular media resemble those of water, which plays a major role in their composition. The refractive indexes increase for shorter wavelengths and decrease for longer wavelengths. This means that refraction is wavelength dependent and this fact is the origin of chromatic aberrations. Typically, two different types of chromatic aberration are distinguished: Longitudinal Chromatic Aberration (LCA), which is the change in power with wavelength; and Transverse Chromatic Aberration (TCA), that can be understood as a wavelength-dependent prismatic effect. Both have a significant presence in the human eye and contribute to limit the actual retinal image quality.

Longitudinal Chromatic Aberration

The wavelength dependence of the refractive index of the ocular media produces a change in the refractive power of the eye with wavelength. For a natural white spectrum, the human eye is not able to focus all wavelengths in one single spot onto the retina. Figure 1.8 illustrates this behavior for three wavelengths (short, mid, and long wavelengths in the visible spectrum) and the combined situation for a white spectrum. This phenomenon is known as Longitudinal (or axial) Chromatic Aberration.

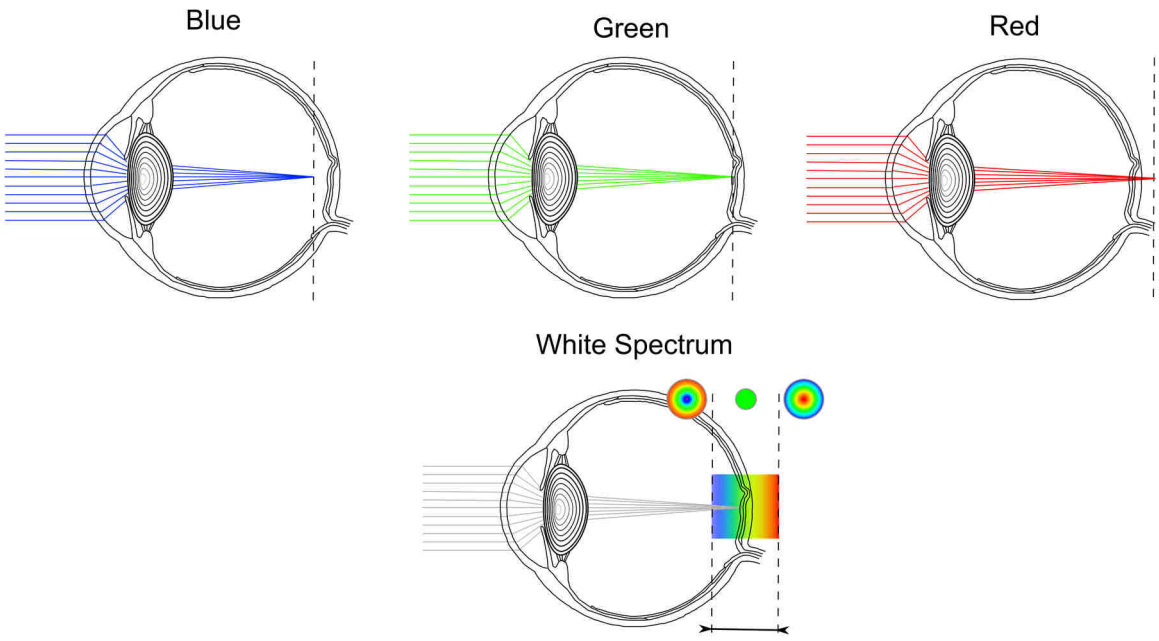

Figure 1.8: Longitudinal Chromatic Aberration (LCA) of the human eye. Short wavelengths (blue) focus in front of the retina whereas long wavelengths (red) focus behind. The white spectrum produces images of different wavelengths at different distances in front of or behind the retina. LCA was exaggerated for clarity.

For a normal eye emmetropic for green, blue light focuses at a shorter distance in front of the retina whereas red light focuses behind it. For a white spectrum, LCA causes a spread of the focus along the axis, which degrades retinal image quality (Figure 1.8). In terms of ocular refraction, the refractive power of the eye for short wavelengths is higher and leads to a myopic shift. On the contrary, the refractive power for long wavelengths is lower, inducing a hyperopic shift.

In Visual Optics, the terminology refers also to chromatic difference of focus or chromatic difference of refraction. It has been intensively studied in the whole visible spectrum (Bedford & Wyszecki, 1947) (Fincham, 1951) (Charman & Tucker, 1978) (Gilmartin & Hogan, 1985a) (Thibos, Ye, Zhang, & Bradley, 1992) (Rynders, Navarro, & Losada, 1998) (Marcos, Burns, Moreno-Barriusop, & Navarro, 1999) (Seidemann & Schaeffel, 2002) (Fonslow et al., 2008) and near infrared wavelengths (Llorente, Diaz-Santana, Lara-Saucedo, & Marcos, 2003) (Fernández, Unterhuber, et al., 2005) (Atchison & Smith, 2005) (Fernández & Artal, 2008) (Vinas, Dorronsoro, Cortes, Pascual, & Marcos, 2015). Hartmann-Shack wavefront sensors (Llorente et al., 2003) (Fernández, Unterhuber, et al., 2005) (Vinas et al., 2015), double-pass systems (Charman & Jennings, 1976) (López-Gil & Artal, 1997) (Vinas et al., 2015), refractometers (Marcos et al., 1999) (Seidemann & Schaeffel, 2002), optometers (Charman & Tucker, 1978) (Kruger & Pola, 1986) (Howarth, Zhang, Bradley, Still, & Thibos, 1988) (Kergoat & Lovasik, 1990) (Kruger, Nowbotsing, Aggarwala, & Mathews, 1995) and reflectometry (Vinas et al., 2015) have been employed to study LCA (Manzanera, Canovas, Prieto, & Artal, 2008).

Thibos et al (Thibos et al., 1992) obtained an equation for the chromatic difference of focus in the human eye based on Emsley's eye model (Emsley, 1948) (LeGrand, 1967). The chromatic shift, G_x, with respect to a reference wavelength (in microns) is given by:

$$G_x = p - \frac{q}{(\lambda - c)} \tag{1.5}$$

where p=1.68524, q=0.63346, c=0.21410 are given parameters obtained by fitting experimental LCA data and using 0.590 μm as reference wavelength. This equation has been extended to the infrared light (Atchison & Smith, 2005) where p, q, and c vary slightly: p=1.74638, q=0.63327, c=0.21836. Figure 1.9 compares both curves going into NIR.

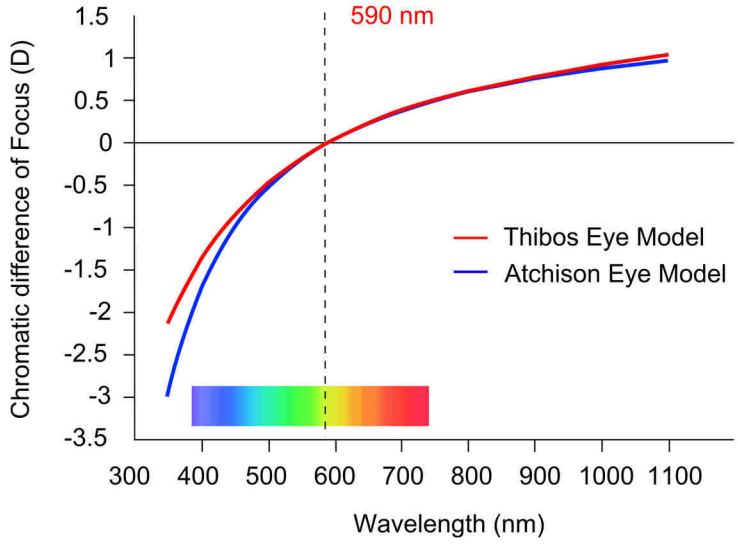

Figure 1.9: Chromatic difference of focus in diopters as a function of wavelength. Atchison and Thibos models are in blue and red respectively. Reference wavelength: 590 nm.

For an unaccommodated emmetropic eye the blue (400 nm) and red (700 nm) focus shift is about -1.6 D and +0.4 D in front and behind the retina respectively, producing around 2 D of total LCA between these two wavelengths. The visual effects of LCA are attenuated by the eye's spectral sensitivity (see Figure 1.10, red line). For wavelengths below 490 nm or above 640 nm sensitivity falls below 20 % and therefore, the blurring effects of LCA for these wavelengths on retinal images of white-light scenes will be significantly reduced in the perceived images. Additionally, under scotopic vision (Figure 1.10, orange line) the eye's spectral sensitivity shifts toward short-wavelengths with a peak centered on 507 nm. This phenomenon is known as Purkinje-shift (Purkinje, 1825) and occurs after a dark adaptation period (Wald, 1945).

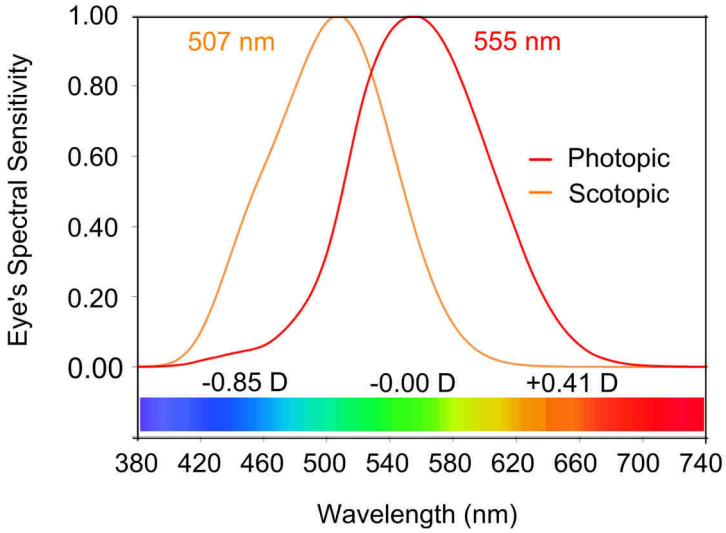

Figure 1.10: Normalized eye's spectral sensitivity in photopic (red) and scotopic (orange) conditions as a function of wavelength. The eye's spectral sensitivity peak is centered at 555-nm and 507-nm under photopic and scotopic luminance levels respectively.

LCA with accommodation

Studies on accommodation (Charman & Tucker, 1978) as a function of stimulus wavelength have measured the change in refractive power of the human eye. LCA has been demonstrated to be fairly constant across eyes (Ware, 1982), invariant across the field up to 40º (Rynders et al., 1998) (Jaeken, Lundström, & Artal, 2011) and relatively independent of age (Ware, 1982) (Howarth et al., 1988). Although LCA presented some variability across subjects (Aggarwala, Nowbotsing, & Kruger, 1995) (Llorente et al., 2003), little difference was measured between near and far steady accommodation states (Cooper & Pease, 1988). Manipulation of LCA or TCA did not influence the steady state error (Bobier, Campbell, & Hinch, 1992).

Furthermore, it has been suggested that LCA provides a directional accommodation cue (Kruger et al., 1995) (Aggarwala, Nowbotsing, et al., 1995) (Lee, Stark, Cohen, & Kruger, 1999) driving accommodation to both moving and stationary objects (Lee et al., 1999). It has been found that the accommodation errors induced by LCA in white and green light were relatively similar (Charman & Tucker, 1978) and maintained low by accommodation fluctuations (Alpern, 1958) (Charman & Heron, 1988). Other studies have shown that changes in focus of the eye are less efficient for narrow monochromatic light than for broadband sources (Aggarwala, Kruger, Mathews, & Kruger, 1995) (Kotulak, Morse, & Billock, 1995), and monochromatic aberrations have been suggested to reduce the effect of LCA when pupils were large (McLellan, Marcos, Prieto, & Burns, 2002). Furthermore, several studies (Rucker & Kruger, 2004a) (Rucker & Kruger, 2006) (Graef & Schaeffel, 2012) have reported over-accommodation at short wavelengths below 430 nm. All these factors influence the accommodation response of the eye and seem to have an impact on visual acuity.

Transverse Chromatic Aberration

The Transverse Chromatic Aberration (TCA) is the lateral shift of the image with wavelength, when rays of light go into the eye with an angle as seen on Figure 1.11.

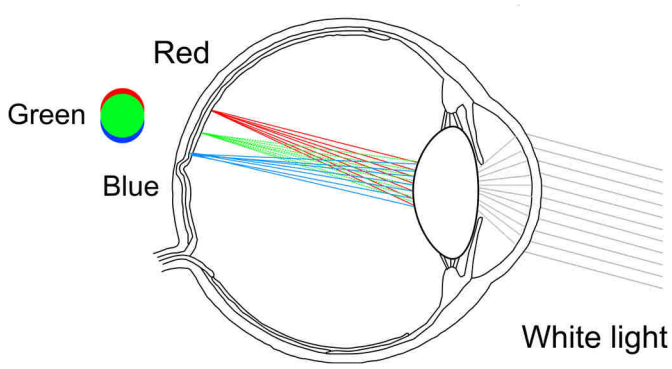

Figure 1.11: Transverse Chromatic Aberration of the human eye.

TCA does not depend on the focal distance, as LCA does, but it is proportional to the entrance pupil aperture. The rays of light of a white source are refracted at different angles as a function of wavelength. For eccentric objects, it corresponds to a change in size of the image as a function of wavelength.

1.6 Objective Refraction

Objective refraction intends to determine the refractive state of the eye without feedback from the patient, based only on instrumental techniques such as auto-refractors (McBrien & Millodot, 1985), laser optometers (Hennessy & Leibowitz, 1972), photorefractors (Choi et al., 2000) (Salmon, West, Gasser, & Kenmore, 2003), aberrometers (Liang, Grimm, Goelz, & Bille, 1994), double-pass systems (Santamaría, Artal, & Bescós, 1987) (Aldaba, Vilaseca, Díaz-Doutón, Arjona, & Pujol, 2012), retinoscopy (Schaeffel, Farkas, & Howland, 1987) or keratometry. In the case of aberrometers, these instruments measure the eye's monochromatic aberrations as a Zernike coefficient expansion (see section 1.5.1). Low-order aberrations, C_2^0 (defocus), C_2^{-2} (45º/135º astigmatism), and C_2^2 (90º/180º astigmatism), can be converted into a refractive power vector of the form [J_{45}, M, J_{180}] (Salmon et al., 2003). J_{45} and J_{180} represent the power of a Jackson cross-cylinder and M is the spherical lens power also known as second-order Spherical Equivalent, SE_2. Eq. (1.6) gives the spherical prescription in terms of ocular refraction in diopters:

$$SE_2\,[D] = -\frac{4\sqrt{3}\cdot {C_2}^0}{{r^2}_{pup}} \tag{1.6}$$

where r_{pup} is pupil radius in mm, and the Zernike coefficient is expressed in microns.

In order to improve accuracy of the second-order spherical equivalent SE_2, a factor Ms is sometimes added, which corresponds to a small amount of positive dioptric power associated to spherical aberration (Thibos, Bradley, & Applegate, 2004):

$$Ms\ [D] = +\frac{12\sqrt{5}\cdot {C_4}^0}{{r^2}_{pup}} \tag{1.7}$$

By combining Eqs. (1.6) and (1.7), the fourth-order Spherical Equivalent SE_4 can be obtained:

$$SE_4\ [D] = \frac{-4\sqrt{3}\cdot {C_2}^0}{{r^2}_{pup}} + \frac{12\sqrt{5}\cdot {C_4}^0}{{r^2}_{pup}} \tag{1.8}$$

This procedure can be extended to include higher orders Zernike terms with m = 0. Eq. (1.6) and/or (1.8) will be used to quantify objective refraction, considering only second-order or including the fourth-order terms.

1.7 The Hartmann-Shack principle

In 1900 Johannes Hartmann (Hartmann, 1900) developed a method based on Scheiner's disc principle to perform metrology of optical systems such as telescopes and other optical instruments (Thibos, 2000). The experiment consisted of an opaque plate with a number of holes (Hartmann mask), located in the exit path of an optical system. Each hole selects a ray and the local slope of the wavefront determines their tilt, and therefore the aberrations of the system can be calculated by determining the slopes of the bundle of rays.

One disadvantage of the Hartmann method is that each hole must be small enough to produce a spot on a screen, reducing the amount of available light. Trying to overcome this drawback, in 1971 Shack and Platt (Shack & Platt, 1971) (Platt & Shack, 2001) proposed using larger holes covered with lenses to produce individual spots while collecting more light. As was the case with the Hartmann screen, the displacement of each spot is proportional to the local slope of the wavefront over the corresponding lens aperture. The ensemble of spots produced by the lens array can be collected by means of an image detector and is known as the Hartmann-Shack pattern or image.

For a plane wavefront emanating from an optical system free of aberrations, each spot is on the focal point, i.e., in the optical axis of its respective micro-lens (red spots in Figure 1.12). For an aberrated wavefront, the local slope of the wavefront shifts each spot (blue spots).

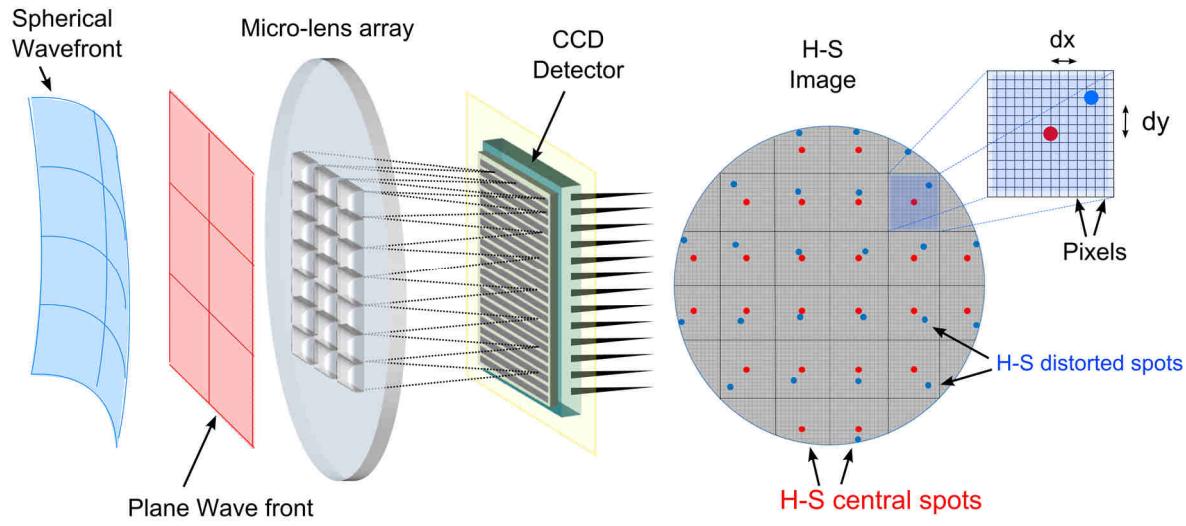

Figure 1.12: Hartmann-Shack architecture. Red spots correspond to an undistorted or plane wavefront, coincide with the focal points, and provide a reference for spot displacement in each micro-lens. Blue spots correspond to a distorted wavefront (pure defocus in this example). The shift of each spot is proportional to the average slope of the wavefront over the corresponding micro-lens.

The Hartmann-Shack principle is equivalent to the Hartmann test: by determining the spot positions, the local slope of the wavefront, i.e., its local first derivative is obtained and the optical aberrations are calculated by either zonal or modal integration (see section 1.7.3).

Nowadays, a very large assortment of micro-lens arrays is available providing a wide range of focal lengths and pitch, with different geometries and micro-lens shapes suitable for ophthalmological purposes. The typical value of focal length varies from some millimeters to several centimeters. Short focal lengths theoretically provide wider dynamical range but lower sensitivity, although both features also depend on the processing algorithm. Sub-millimeter micro-lens pitch values, even down to a hundred microns, are typical to sample the eye's pupil. Smaller pitch values provide better spatial resolution but limit the amount of light for each spot, so the actual value is typically a trade-off between these two characteristics. Rectangular micro-lens arrangements seem to be better fitted for modal wavefront reconstruction based on Zernike polynomials but hexagonal micro-lens arrays can be also found in the market. Finally, arrays of square and circular micro-lenses are also available, the latter producing better shaped spots at the cost of a small light loss.

1.7.1 Ocular aberrometry

Ocular aberrometry techniques have been based on Hartmann-Shack sensing (Liang et al., 1994) (MacRae & Fujieda, 1999) including the Hartmann-Shack Talbot effect (Sekine et al., 2006), Tscherning aberroscopy (Tscherning, 1894) (Mierdel, Kaemmerer, Mrochen, Krinke, &

Seiler, 2001), and laser ray-tracing (Navarro & Losada, 1997) (Navarro & Moreno-Barriuso, 1999) (Molebny, Panagopoulou, Molebny, Wakil, & Pallikaris, 2000) (Rozema, Van Dyck, & Tassignon, 2005). Other techniques have made use of optometers (Cornsweet & Crane, 1970) (Cornsweet & Crane, 1973) (J. Cooper, Ciuffreda, & Kruger, 1982) (Heron, Winn, Pugh, & Eadie, 1989) (Okuyama, Tokoro, & Fujieda, 1993), auto-refractors (Suryakumar, Meyers, Irving, & Bobier, 2007a) (Suryakumar, Meyers, Irving, & Bobier, 2007b) or dynamic skiascopy (MacRae & Fujieda, 1999). The first known attempt to study ocular aberrations beyond low order was made by Tscherning in 1894 (Tscherning, 1894) (Mrochen, Kaemmerer, Mierdel, Krinke, & Seiler, 2000). Tscherning used a mask with holes to project a spot pattern onto the retina. Instead of the regular grid that should occur, ocular aberrations produce a distorted pattern, which the subject was asked to draw. Conceptually, this idea is similar to Hartmann's, which it preceded.

In the 90's the Hartmann-Shack wavefront sensor was implemented for the first time in the human eye (Liang et al., 1994) (Liang & Williams, 1997) and has become the standard for ocular aberration measurement and in other areas such as astronomy. Many research laboratories used this technology, either their own making or from one of several companies marketing off-the-shelf easy-to-use plug-and-play H-S instruments. Also, most commercially available ocular aberrometers are based on the Hartmann-Shack principle. The main difference with aberrometry in other fields is the fact that the eye's image plane, the retina, is not accessible. Therefore, ocular aberrometry is based in double pass configuration. In the case of the H-S sensor, measurements are performed in the second pass, i.e., using retinal reflection as a pseudo-point source.

Since the first implementation of the H-S aberrometer (Liang et al., 1994) (Liang, Williams, & Miller, 1997), it has been intensively used to study the eye's wavefront aberrations (Salmon, Thibos, & Bradley, 1998) (Porter, Guirao, Cox, & Williams, 2001) (Thibos, Hong, Bradley, & Cheng, 2002) (Cagigal et al., 2002), their dynamics (Hofer, Artal, Singer, Aragón, & Williams, 2001) (Mira-Agudelo, Lundstrom, & Artal, 2009) and the effect of accommodation on ocular optics (Ninomiya et al., 2002) (Cheng et al., 2004) (Plainis, Ginis, & Pallikaris, 2005).

Implementation

As illustrated in Figure 1.13, a collimated beam goes into the eye through a beam splitter. Infrared light (IR) is typically used, although this entails some post-processing to compensate the eye's LCA from IR to visible, it allows an important increase in intensity since the safety constraints are much less restrictive. Additionally, it is more comfortable for the subject, who is not required to suffer the very bright visible sources typical of early H-S systems. The incident beam transmitted through the ocular media is focused onto the retina and its reflection acts as a pseudo-point source. The wavefront emanating of it travels backwards through the eye and is affected by ocular aberrations. An optical system, typically an afocal telescope, conjugates the pupil plane of the eye with the H-S micro-lens plane to sample the ocular wavefront.

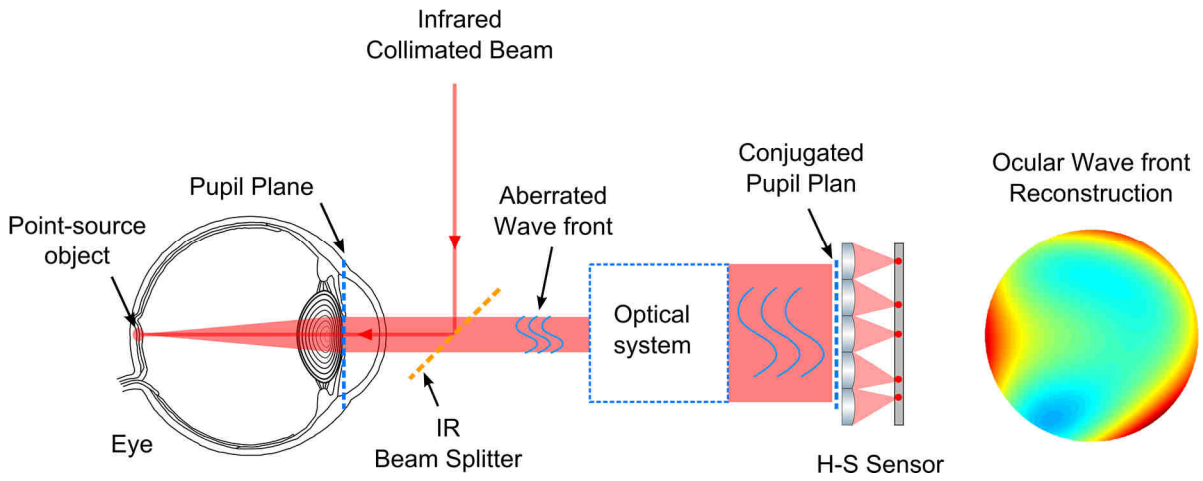

Figure 1.13: Double-pass Hartmann-Shack implementation for ocular wavefront measurement.

For an aberration-free ideal eye, the wavefront is flat at the pupil plane and the lenslet array produces a regular mosaic of spots on the lenses focal points. On the contrary, in a real eye, ocular imperfections disturb the wavefront and the H-S image consists of a distorted mosaic of spots.

Most of the current aberrometer have been designed and implemented monocular, since only a limited number of binocular aberrometers have been reported (Kobayashi et al., 2008) (Hampson, Chin, & Mallen, 2007) (Fernández et al., 2009) (Sabesan, Zheleznyak, & Yoon, 2012). Some of these binocular HSWS are, in fact, a component in their respective binocular Adaptive Optics vision simulators (Fernández et al., 2009) (Sabesan et al., 2012), with strict requirements for the subject' viewing conditions, that are not natural. To the best of our knowledge, only two instruments, working in an open field of view have been presented so far (Hampson et al., 2007) (Kobayashi et al., 2008) with stimuli in a direct line of sight. However, one of them consists of two separate H-S sensors, one for each eye (Kobayashi et al., 2008), while the other apparently has a fixed target and does not allow the subject to fixate to different vergences (Chin, Hampson, & Mallen, 2008). Furthermore, all previous systems had the main drawback of using infrared wavelengths shorter than 850-nm still visible for the subjects, which means the illumination beam must be switched off during visual testing or it produces a faint red spot superimposed on the stimulus.

1.7.2 Geometrical characteristics

Horizontal and vertical spot displacements $\Delta(x, y)$ are proportional to the local wavefront slope and depend on the micro-lens focal length. Figure 1.14 illustrates spot displacement for a single micro-lens as a function of local wavefront slope and lens focal length.

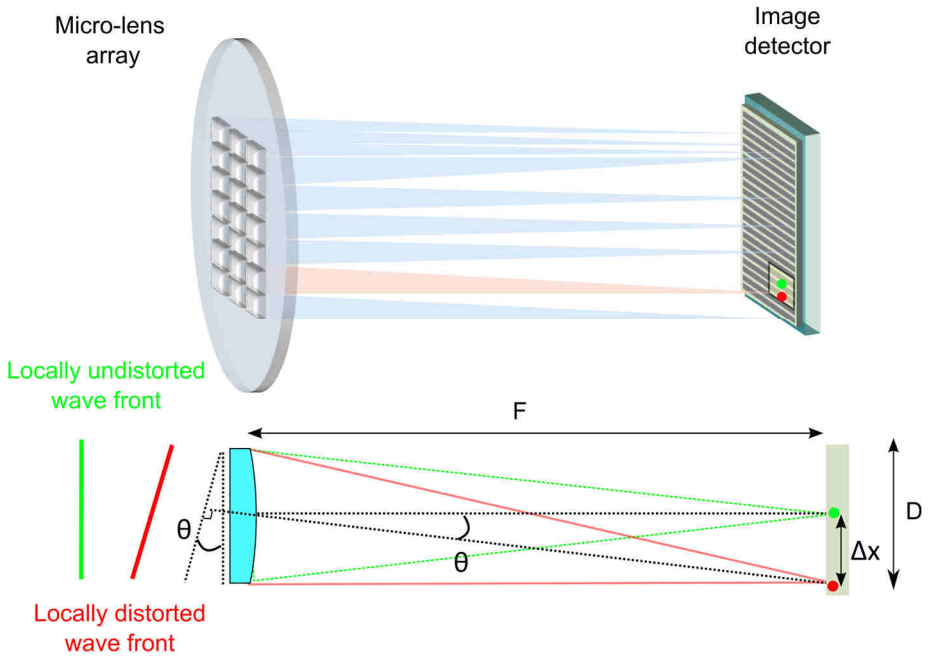

Figure 1.14: Geometry of the H-S principle. A locally tilted wavefront (red) shifts the spot from the micro-lens focal point (green) by an amount, Δx, proportional to the tilt angle, θ, and the lens focal length, F.

Eqs. (1.9) gives the geometrical relationship between the local gradient of wavefront W and the spot displacement on the CCD screen in x and y directions:

$$\frac{\Delta x}{F} = \tan(\theta x) = \frac{\partial W(x,y)}{\partial x}$$
$$\frac{\Delta y}{F} = \tan(\theta y) = \frac{\partial W(x,y)}{\partial y} \tag{1.9}$$

Where Δx and Δy are the horizontal and vertical displacements respectively, F is the focal length of the micro-lenses, θx and θy represent the horizontal and vertical wavefront tilt angles, and $\frac{\partial W(x,y)}{\partial x}$ and $\frac{\partial W(x,y)}{\partial y}$ are the wavefront function partial derivatives.

Since the micro-lenses in an H-S sensor are typically small and the wavefront is densely sampled, it is sometimes assumed that the spot displacements are proportional to the wavefront derivative at the micro-lens centers. This assumption can lead to small errors in wavefront reconstruction, especially in highly aberrated cases. Instead, we will consider that the spot position is related to the average wavefront slope over the lens, where A is the area of a lenslet:

$$\frac{\Delta x}{F} = \tan(\theta_x) = \langle \frac{\partial W(x,y)}{\partial x} \rangle = \frac{1}{A} \iint_A \frac{\partial W(x,y)}{\partial x} \partial x \partial y$$
$$\frac{\Delta y}{F} = \tan(\theta_y) = \langle \frac{\partial W(x,y)}{\partial y} \rangle = \frac{1}{A} \iint_A \frac{\partial W(x,y)}{\partial y} \partial x \partial y \tag{1.10}$$

Dynamic range and sensitivity considerations

Sensitivity is described as the lowest value of an aberrated wavefront that the sensor can measure. It is related to measurement noise. Accuracy is defined as the capability to measure with precision the value of a known aberrated wavefront. It is related to measurement bias. The dynamic range is the measurement range where the sensor shows good accuracy. Typically, the higher the dynamic range, the worse the sensitivity. In clinical devices, an appropriate sensitivity does not need to be better than $\lambda/10$ (0.05 μm) for ocular refraction measurements (typically for defocus) but can be frequently lower for high-order aberrations (Neal, Copland, & Neal, 2002) with a dynamic range of more than ten diopters for refraction and more than 1 μm for higher order aberrations.

The dynamic range and sensitivity are given by the maximum and minimum tilt angle θmax and θmin respectively (see Figure 1.14). These angles define the highest and lowest wavefront deviation that the sensor can detect. Eq. (1.11) gives the theoretical "slope/angle" dynamic range and sensitivity in radians in small angle approximation $\tan\theta \sim \theta$:

$$\theta\, max = \frac{D/2}{F} = \frac{P \cdot n}{F}$$
$$\theta\, min = \frac{P}{F} \tag{1.11}$$

where D is the lenslet diameter, F is the focal length, n is the number of pixels from the center of the micro-lens to its border, and P is the pixel size.

On the one hand, to increase dynamic range, two possibilities arise from the geometry: to increase lenslet size or decrease focal length. On the other hand, assuming the smallest measurable spot displacement is one pixel, sensitivity can be increased by decreasing pixel size or increasing focal length. Thus, H-S sensors with long focal length are well fitted to detect small variations of the wavefront slope in a reduced dynamic range. Conversely, sensors with short focal length provide larger dynamic range but lower sensitivity and the pixelization can be the dominant factor in the overall accuracy (Neal et al., 2002). Additionally, both the dynamic range and the sensitivity can be increased, almost independently, with software algorithms (Prieto, Vargas-Martin, Goelz, & Artal, 2000).

1.7.3 Wavefront reconstruction

There are two typical approaches to perform the integral required to obtain the wavefront shape from the local derivative data provided by the HSWS: zonal and modal reconstruction. In zonal reconstruction, integration is performed locally, using neighboring lenslet data. Zonal methods have the advantage of preserving high spatial frequencies but has the important drawback of being sensitive to local noise and there is no way to tell which aberrations dominate.

In modal reconstruction, the wavefront shape is described in terms of a functional basis, typically the Zernike polynomials but other functions can be also used. As shown in Eq. (1.12), wavefront local derivatives, can be expressed as a linear combination of Zernike derivatives. Since the wavefront derivatives are experimentally computed from spot displacement and the Zernike derivatives are analytically known, the differential equations in Eq. (1.12) become a system of algebraic equations whose solutions are the Zernike coefficients that express the wavefront. Modal reconstruction appears to be more efficient than zonal estimation, especially when only a fixed number of modes are of interest (Southwell, 1980). This method is less sensitive to noise and allows a smooth representation of the wavefront although sharp phase changes can fail to be registered. Currently, it is the most popular reconstruction method in ocular aberrometry.

$$\frac{\partial W(x,y)}{\partial x} = \sum_{k=1}^{m} c_k \frac{\partial z_k(x,y)}{\partial x}, \qquad \frac{\partial W(x,y)}{\partial y} = \sum_{k=1}^{m} c_k \frac{\partial z_k(x,y)}{\partial y} \tag{1.12}$$

1.8 Adaptive optics

Adaptive Optics (AO) is a technology for fast, dynamic correction of the aberrations of an optical system to improve image quality. Its basic hardware components are a wavefront sensor that measures the system aberrations and an active optical element that can manipulate the wavefront in order to compensate these aberrations. Additionally, a software package for rapid sensor signal processing, active element control, and communication between these elements is required.

Adaptive optics systems have been developed first for military purposes and astronomical observations. Figure 1.15 depicts an AO system based on a spatial light modulator, SLM, combined with a HSWS. In the 90's Liang et al. proposed the first adaptive optics system for the human eye (Liang et al., 1997) taking advantage of the recent improvements in wavefront sensing technology (Liang et al., 1994). Since then a large variety of AO instruments have been developed; based on deformable mirrors (Liang et al., 1997) (Fernández, Iglesias, & Artal, 2001) (Hofer, Chen, et al., 2001) (Diaz-Santana, Torti, Munro, Gasson, & Dainty, 2003) (Fernández & Artal, 2005) (Hampson & Mallen, 2011) and spatial light modulators (Prieto, Fernández, Manzanera, & Artal, 2004) (Fernández, Prieto, & Artal, 2009) (Cánovas, Prieto, Manzanera, Mira, & Artal, 2010).

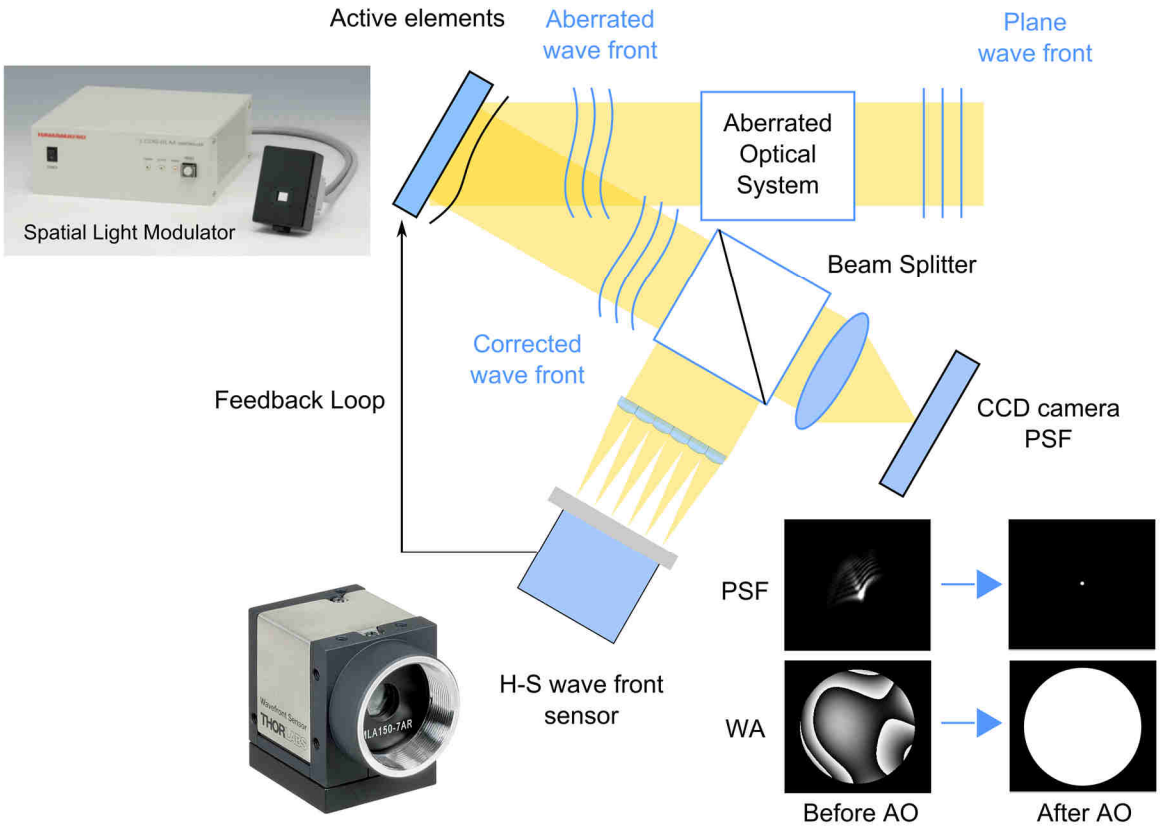

Figure 1.15: Schematic diagram of an Adaptive Optics system. The main parts are the wavefront modulator, the wavefront sensor and the intercommunicating feedback loop.

An active element such as a deformable mirror (DM) or a liquid crystal SLM is connected to a wavefront sensor (typically a Hartmann-Shack sensor) through an intercommunicating feedback loop in order to control the action of the active element on optical correction. Liquid Crystal Spatial Light Modulators are miniature liquid crystal devices in which the effective refractive index is locally controlled by applying voltage patterns that change the alignment of the liquid crystal molecules. DMs are based on continuous reflective surfaces that can be deformed by means of piezoelectric or magnetics actuators.

DMs feature high temporal response of several KHz, large strokes, large pitch and optical coating to achieve real-time accurate wavefront correction in a broad wavelength range. SLMs provide high resolution, large operating range allowing wrapped phase representations with no continuity constrains, low power consumption, and can be a low-cost solution (Prieto et al., 2004). The temporal response of the SLMs (Liquid Crystal on Silicon, LCoS), around 50 Hz, is significantly slower than deformable mirrors but is still well adapted for the human eye and studies of the dynamics of eye's wave aberrations (Hofer, Artal, et al., 2001). Additionally, for large aberrations diffraction effects can play an important role due to the pixelation of the LCOS screen at micrometer scale.

AO has been used to correct or compensate ocular aberrations to study the visual function of human eye (Artal et al., 2004) (Gambra, Sawides, Dorronsoro, & Marcos, 2009) (Tabernero, Schwarz, Fernández, & Artal, 2011) (Roorda, 2011), to carry out high-resolution retinal imaging (Liang et al., 1997) (Hofer, Chen, et al., 2001) (Hermann et al., 2004) (Poonja, Patel, Henry, & Roorda, 2005) (Fernández, Povazay, et al., 2005) and to manipulate and simulate aberration profiles for ophthalmic optics element testing (Piers, Fernandez, Manzanera, Norrby, & Artal, 2004) (Manzanera, Prieto, Ayala, Lindacher, & Artal, 2007) (Cánovas et al., 2010) (Schwarz, Prieto, Fernández, & Artal, 2011).

1.9 Night myopia

The human eye operates in a wide range of luminance with a lower limit below $10^{-4}/10^{-5}$ cd/m^2 for foveal vision. Three luminance ranges are usually distinguished (see Figure 1.16): Photopic, mesopic and scotopic, in decreasing luminance order.

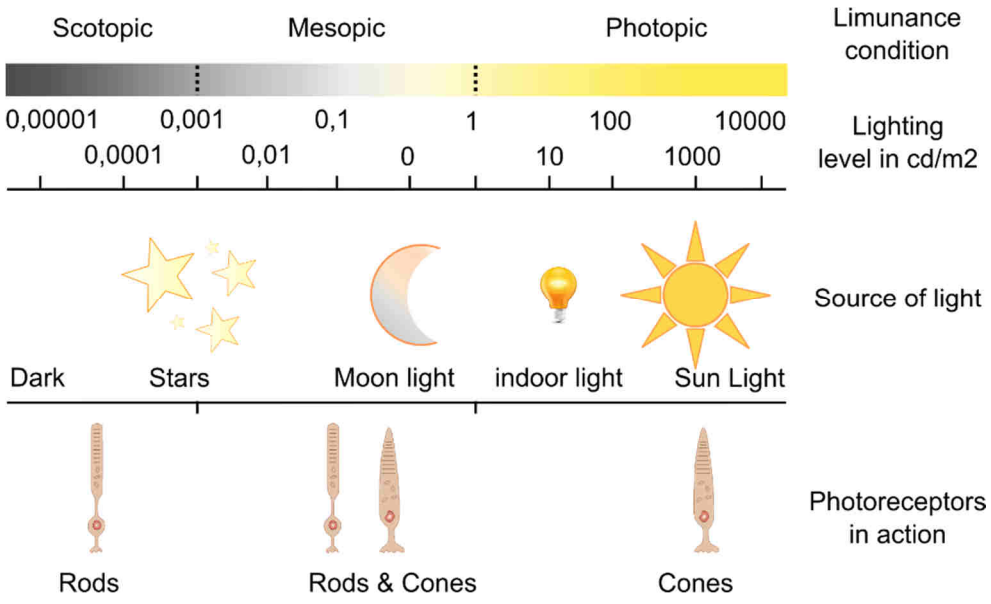

Figure 1.16: Luminance ranges. Figure based on (Stockman & Sharpe, 2006) modified by Schwarz (Christina Schwarz, 2013).

Photopic conditions represent the brighter luminance range, corresponding to normal daylight. Its lower limit is around 10 cd/m^2 although with some variability since there is no sharp transition into mesopic conditions. The cone photoreceptors, more densely concentrated at the fovea, are in action. They provide high foveal visual acuity. The cone mosaic has an overall sensitivity peak around 555 nm but in fact, three different types are usually present in the human retina: S-, M-, and L-cones, standing for short-, medium-, and long-wavelength-sensitive cones.

Scotopic conditions denote the range of low luminance below 10^{-3} cd/m^2 approximately, corresponding to starlight. Vision in this range mainly involves the rod photoreceptors, which

are several orders of magnitude more sensitive than cones. There is one type of rod in the human retina, with peak sensitivity around 507 nm. There are no rods in the central fovea and they are interspersed with cones in the peripheral retina, with peak density around 20º (Hofer, Carroll, Neitz, Neitz, & Williams, 2005). Contrary to cones, the rods provide poor visual acuity but they are more sensitive to motions.

The transition from cone to rod function defines an intermediate range of luminance called mesopic conditions. It is generally placed between 10^{-3} cd/m^2 and 1 cd/m^2 and it roughly corresponds to dim ambient light such as moonlight. These luminance ranges depend on each individual and the limits are not well established.

Several factors contribute to the decline of visual function in low light levels: the shift from cones to rods detection, the increase in aberrations with pupil dilation, the loss of visual acuity with decreasing luminance, etc., Additionally, many studies have reported a typical change in the refractive state of the eye towards myopia in most subjects at low luminance. This condition is known as night myopia (sometimes called nocturnal or twilight myopia) and its origin is still unclear (Hope & Rubin, 1984).

Since the first mention to the phenomenon of night myopia by Maskelyne in 1798 (Rayleigh, 1883) (Levene, 1965), many studies on the myopic shift under low light levels have been conducted to better understand the degradation in visual acuity with decreasing luminance. Over the years, a large range of values between -4 D and +1.5 D (night hyperopia) has been reported under monocular conditions (Otero & Dúran, 1941) (Wald & Griffin, 1947) (Leibowitz & Owens, 1975b) (Johnson, 1976) (Epstein, Ingelstam, Jansson, & Tengroth, 1981) (Arumi, Chauhan, & Charman, 1997). Under binocular viewing conditions, night myopia is less severe but still relevant (Ivanoff, 1955). The variability across subjects probably comes from the number of contributing factors and, to date has prevented a complete explanation of the phenomenon. Historically, a number of potential sources of night myopia have been proposed and studied.

Chromatic aberration (Wald & Griffin, 1947) (Bedford & Wyszecki, 1947) (Otero, Plaza, & Salaverri, 1949) (Levene, 1965) in combination with the Purkinje effect plays a moderate role in night myopia. Depending on the light source used for visual testing, it could induce a refractive change no bigger than 0.4 D (Wald & Griffin, 1947). The increase in spherical aberration as the pupil dilates at low luminance levels could also cause a myopic shift (Rayleigh, 1883) (Otero & Dúran, 1941) (Arnulf, Flamant, & Françon, 1948) (Koomen, Tousey, & Scolnik, 1949) (Koomen, Scolnik, & Tousey, 1951) (Ivanoff, 1955). Additionally, spherical aberration becomes relatively more negative as the eye accommodates. Also, the resting state of accommodation could play a role in the onset of night myopia as the visual stimuli becomes less visible (Owens & Leibowitz, 1980). Although dark vergence and dark accommodation seem to be fairly independent from each other (Kotulak & Schor, 1986), vergence and accommodation are cross-coupled (Fincham, 1962) (Wolf et al., 1990) (Jiang et al., 1991). Accommodative induced vergence and vergence induced

accommodation are only weakly correlated and vary widely across subjects. Both processes tend to an independent physiological resting state (Owens & Leibowitz, 1980) with individual differences in the threshold luminance level.

Dark focus, also known as tonic accommodation or resting state of accommodation, corresponds to the equilibrium state of the ciliary muscles tone (Gilmartin & Hogan, 1985b). It has been shown to be relatively stable over time (Miller, 1978) (Mershon & Amerson, 1980) and it is around 1 D on average (Leibowitz & Owens, 1975b) (McBrien & Millodot, 1987). It depends on the individual refractive state of the subject with a significant reduction in myopes. Recently, Artal et al. (Artal, Schwarz, Cánovas, & Mira-Agudelo, 2012) have demonstrated by using an adaptive optics based instrument that monocular night myopia is mainly caused by an accommodative error and spherical and chromatic aberrations play minor roles only.

1.10 Purpose and Outline of the Thesis

Technological advances allow high performance instrumentation for ophthalmology in the clinic. However, some optical limitations still exist and, for example, current instruments do not allow studying the eye's image quality under natural viewing conditions. In this thesis, we present a binocular infrared Hartmann-Shack wavefront sensor in an open-view configuration and several examples of its use to study accommodation responses in both eyes simultaneously in realistic vision conditions.

Objectives

The main objectives of this thesis are:

- Design, assembly, and calibration of a binocular Hartmann-Shack sensor using invisible IR light (1050 nm) that allows unobtrusive ocular wavefront measurements in an open-view field, combined with a real time binocular pupil tracker (25 Hz).

- Instrument testing and validation under experimental conditions in young subjects with normal vision: Simultaneous and continuous measurement of steady state of accommodation, convergence, pupil size, and aberrations for different target vergences.

- Study of the dynamics of accommodation responses: accommodation, pupil size, and convergence for a far-to-near visual task.

- Study of accommodation and refraction at low luminance under binocular and monocular viewing conditions.

- Study of accommodation in polychromatic light under binocular vision.

Outline

The thesis is divided into seven chapters. **Chapter 1** consists of an introduction and a general overview of the different topics studied in this work, including a review of the literature on the mechanism of accommodation of the human eye, the monochromatic and chromatic aberrations, the Hartmann-Shack principle, the ocular aberrometry and the night myopia phenomenon. **Chapter 2** describes the instrument and details the calibration procedures to determine the sensor's sensitivity, dynamic range for low- and high-order aberrations, and linearity. This chapter explains also the methods for pupil tracking, convergence estimation, eye safety limits and other software developments. **Chapter 3** includes the instrument validation consisting of the measurements of the accommodation response and monochromatic aberrations in a population of young subjects under steady states of accommodation. **Chapter 4** comprises the study of the dynamics of accommodation responses in real time under natural binocular and monocular vision. **Chapter 5** describes the experiment designed for measuring the accommodation and refraction at low luminance. **Chapter 6** contains the study of accommodation in polychromatic light under natural binocular vision. Finally, **chapter 7** lists the conclusions of this thesis.

Methods

2 Apparatus and calibration

This chapter presents a detailed description of the open-view Hartmann-Shack wavefront sensor including the different calibration procedures to assess the separating distance micro-lens/CCD, parallelism, sensor's sensitivity, and dynamic range. The eye safety section deals with the Maximum Permissible Exposure (MPE) calculation procedure for near infrared wavelength. Two sections discuss the customized software and infrared binocular pupil tracker, and its use for convergence estimation.

2.1 Open-view infrared instrument

We have developed an open-view binocular infrared Hartmann-Shack wavefront sensor using invisible illumination of 1050 nm. A large 45º tilted dichroic hot mirror (Edmund Optics, NT43-453, USA) transmits about 90 % of the visible spectrum 425-675 nm from the scene to the eye while reflecting over 95 % of the near infrared light 750-1125 nm coming from the eye towards the sensor, which is in a plane below the subject's line of sight. Thanks to the dichroic mirror, measurements can be performed while the subject can fixate to different targets with a natural feeling of the scene, an arrangement known as open-view field. Figure 2.1 shows a schematic drawing of the instrument with top views of a) the pupil-monitoring and b) the wavefront measurement paths.

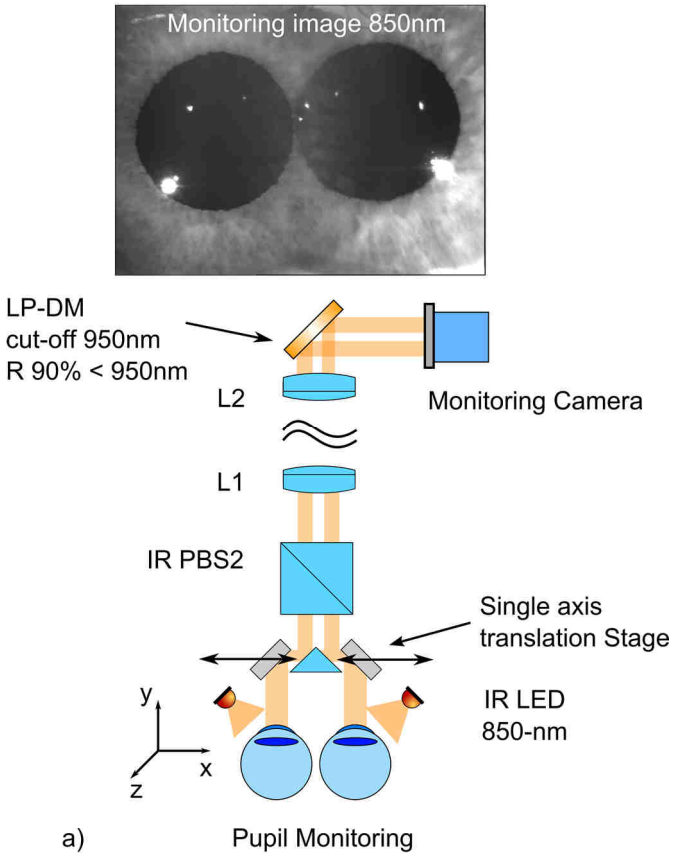

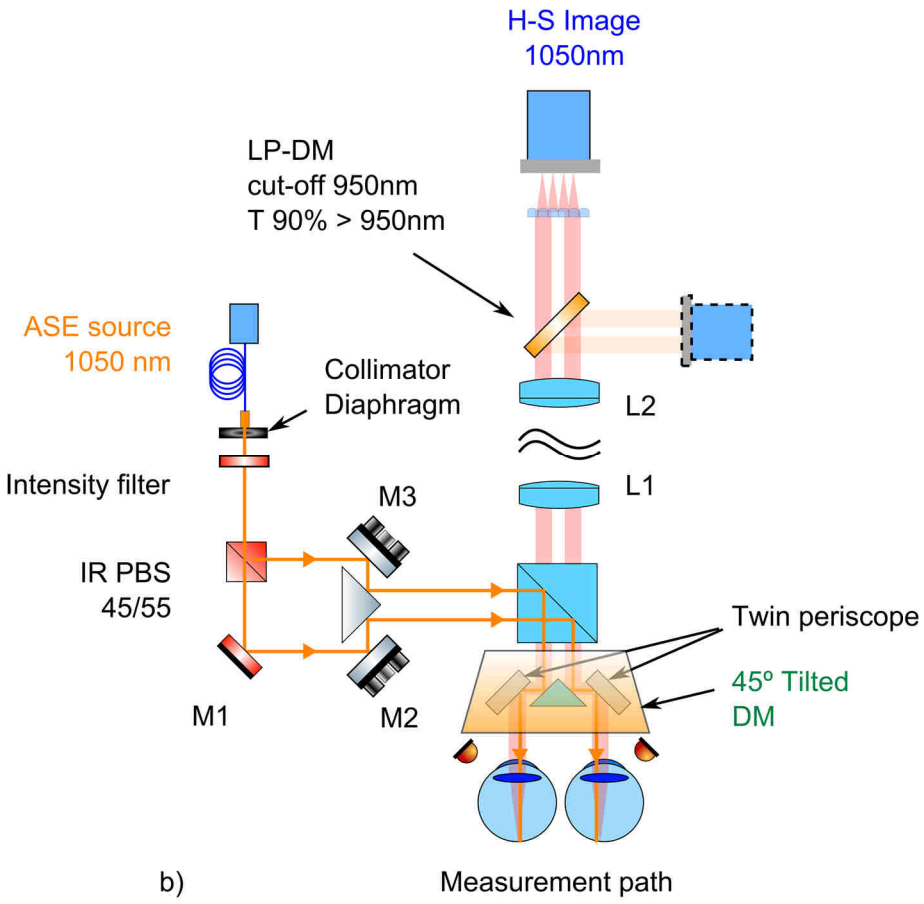

Figure 2.1: Schematic views of the instrument from above: a) Pupil-monitoring path; b) Measurement path.

Current aberrometers typically include light sources with wavelength around 800-850 nm, nominally infrared but still faintly visible for the power ranges involved. The use of a longer wavelength at a power level that is invisible, allows our instrument to measure unobtrusively both eyes' aberrations while the subject carries out any visual task under realistic conditions. As a counterpart, it has the drawback of shifting the defocus due to the longitudinal chromatic aberration with respect to the center of the visible spectrum, although this effect can be easily accounted for (see section 1.5.2). Our system uses a broadband Amplified Spontaneous Emission ASE source with peak emission at 1050 nm (Broadband ASE source, 1-μm band, Multiwave Photonics, Portugal) to illuminate both eyes simultaneously. The use of IR wavelengths up to 1070-nm have been showed to provide reliable results similar to shorter wavelengths commonly used in other ophthalmic instruments (Fernández & Artal, 2008). The intensity of each IR beams is about 30 μW at the pupil plane, several orders of magnitude below the safety limit standards (ANSI Z136.1, 2007). Section 2.7 describes the Maximum Permissible Exposure (MPE) for safe continuous measurement up to 10 s. A single diaphragm of 1-mm-diameter combined with a 45/55 (reflectance/transmission) IR Pellicle Beam Splitter, IR PBS, produces two 1-mm beams of similar intensity. Both of them are reflected on a second 8/92 beam splitter, IR PBS2, and

directed upwards by means of a twin periscope, with a couple of adjustable mirrors to separately control the position and direction of each beam into the eyes and also the position of the pupils on the sensor.

The large dichroic hot mirror, tilted 45° from horizontal, reflects the illumination beams toward the eyes and the retinal reflections toward the lower level where the H-S sensor is located, while the subject has an unimpeded open-view field of the world in front. Figure 2.2 shows the NIR dichroic mirror mounted on a 360º horizontal and vertical rotation stage with an accuracy of half degree.

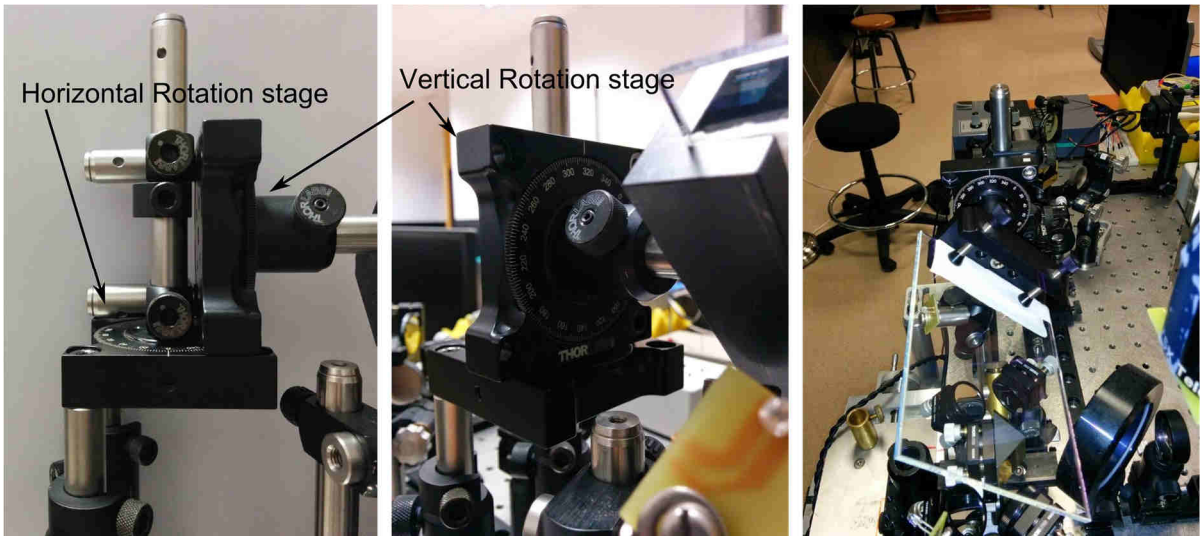

Figure 2.2: Dichroic mirror mount. It acts as an optical window transparent in the visible spectrum, allowing a large field of view.

The retinal reflections travel backwards through the twin periscopes, traverse the 8/92 beam splitter and go through a 0.5-magnification afocal telescope that conjugates the pupil plane onto the wavefront measurement plane, i.e., the micro-lens plane. The telescope is composed of two near IR achromatic doublets L1 and L2 designed for the range from 600 nm to 1150 nm. Additionally, the measurement light traverses a Long Pass-Dichroic Mirror (Thorlabs, DMLP950, USA), LP-DM, with of 950-nm cut-off required by the pupil monitoring system. This mirror reflects towards the monitoring camera 95% (420 – 900 nm) of light coming from the irises when illuminated by a couple of IR LEDs with emission centered at 850 nm, one for each eye, which are switched on for pupil monitoring tasks only, to align the subject and to ensure proper plane conjugation. Figure 2.3 shows the normalized spectra of the pupil monitoring light and the IR broadband ASE source.

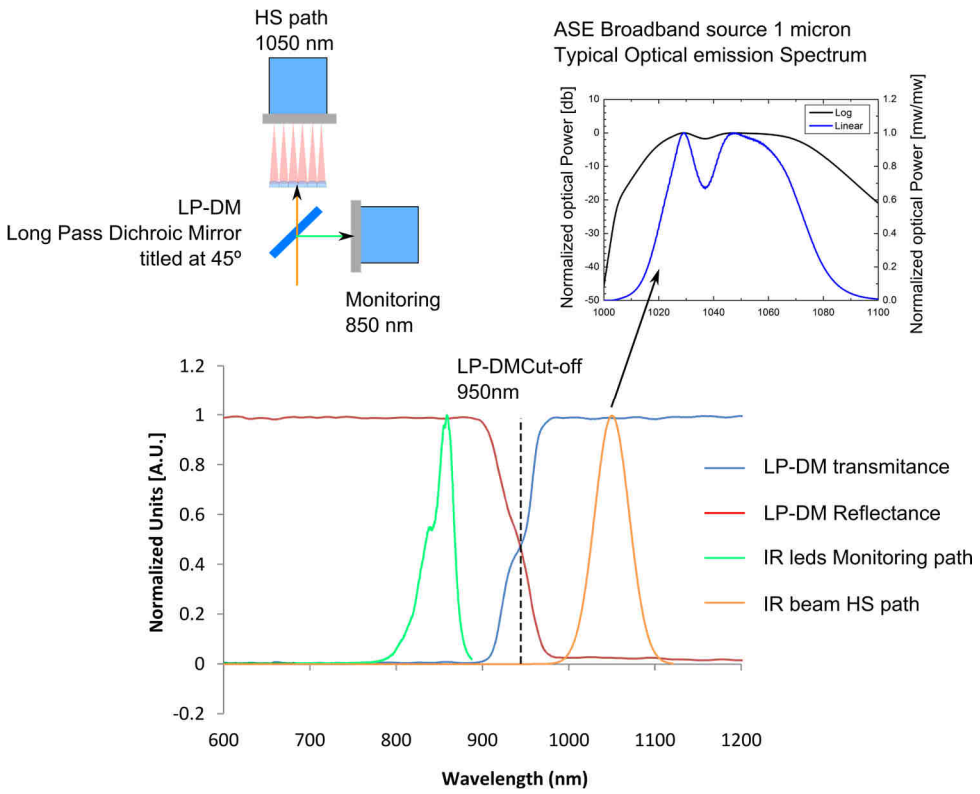

Figure 2.3: Top Left: Illustration of the long-pass dichroic mirror LP-DM tilted at 45º with 950-nm cut-off used to separate the H-S (1050-nm) and the pupil monitoring paths (850-nm). Top Right: emission spectrum of the ASE broadband source. Bottom: reflectance and transmittance properties of the LP-DM in red and blue respectively and both IR spectra (green and orange) in normalized units.

For calibration and alignment of the H-S sensor, another illumination arm was built parallel to the instrument. By means of a flip mirror located in the optical path, the system can be switched between measurement and calibration modes. The calibration arm consists of a simple optical rail, where several positions are marked between two pinholes, and a spatially filtered collimated 633-nm laser beam. Figure 2.4 shows general views of the instrument on the optical table.

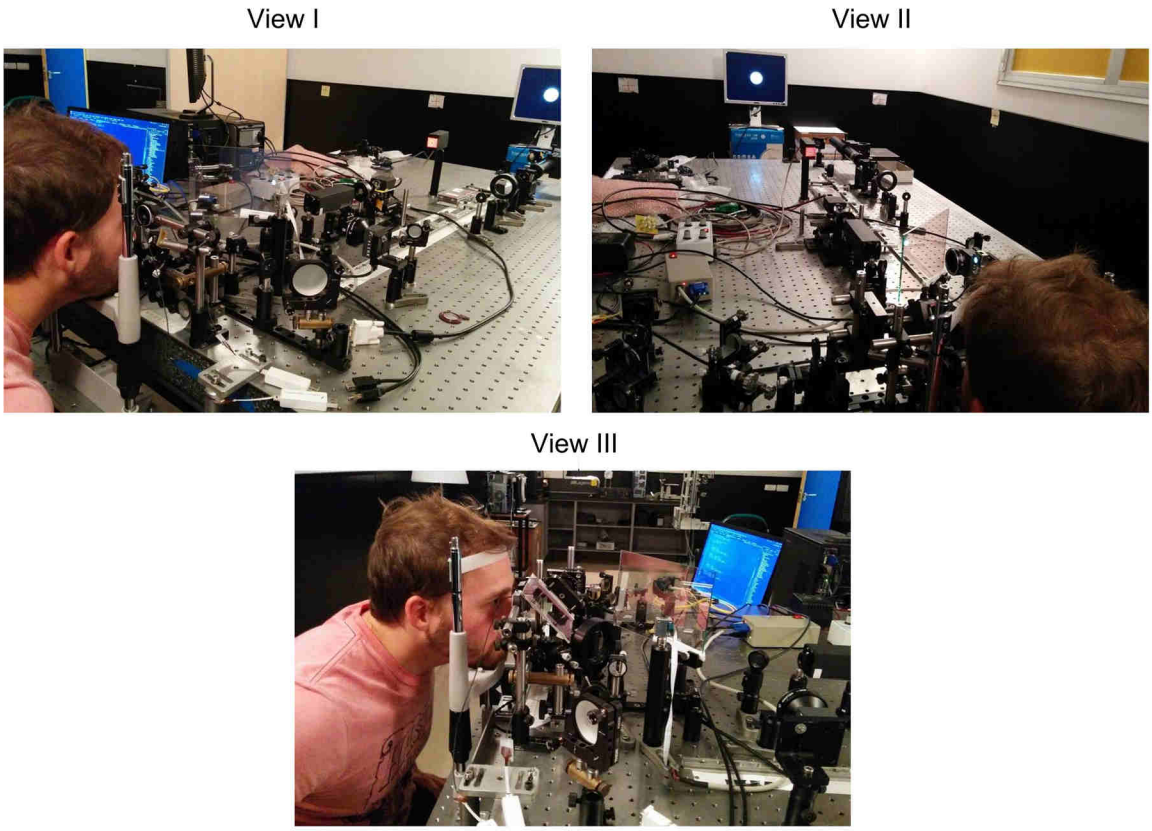

Figure 2.4: General views of the binocular H-S wavefront sensor.

As described in section 1.7.2, the range of local wavefront slopes that a sensor can detect is related to its geometrical characteristics (Campbell, 2009). Focal lengths around the centimeter and lenslet pitch of several tenths of millimeter are commonly used and they are well adapted for clinical devices.

A pure spherical wavefront was considered, since defocus is the most important ocular aberration, not only in magnitude but also from the point of variability, as it differs widely among subjects and changes with accommodation. For pupil radii values, r_{pup}, negligible values compared to the radius of curvature, R, a spherical wavefront resembles a parabola, $\phi(r) = r^2/2R$, where r is the radial coordinate, and can be expressed using Zernike polynomial $Z_2^{\,0} = \sqrt{3}\,(2\rho^2 - 1)$ with corresponding coefficient, $C_2^{\,0}$.

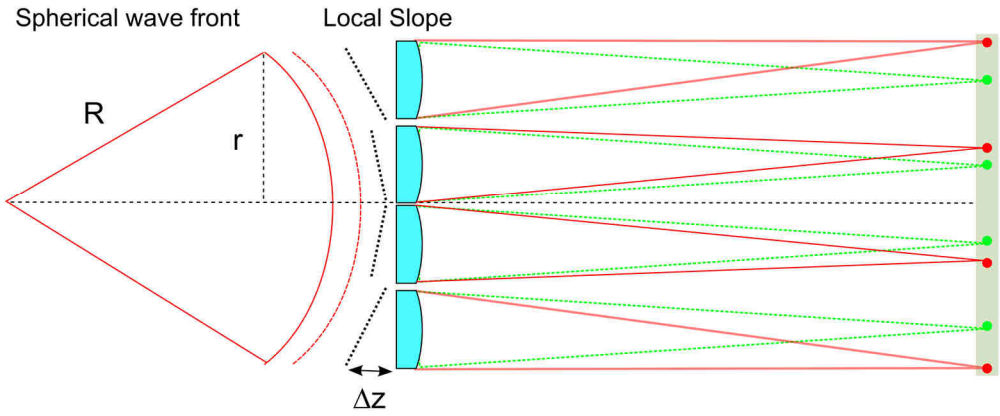

Figure 2.5: Spherical wavefront sampling. The maximum spot displacement, limiting the sensor dynamic range, occurs at the pupil edge.

In terms of curvature radius, the wavefront slope is $\frac{\partial\phi(r)}{\partial r} = \frac{r}{R}$. In terms of Zernike defocus, it is:

$$\frac{\partial\phi(r)}{\partial r} = \frac{\partial[\, {c_2}^0 \, {Z_2}^0(\rho,\theta)]}{\partial r} = {C_2}^0 \cdot 4\sqrt{3} \cdot \frac{r}{r_{pup}^2} \tag{2.1}$$

where $\rho = r/r_{pup}$ is the normalized radial coordinate used in Zernike polynomial definition. Either way, this wavefront slope produces a spot displacement $\Delta(r) = F \cdot \frac{d\phi(r)}{dr}$. Since $\frac{d\phi(r)}{dr}$ increases radially, the largest displacements occur at the pupil edge, i.e., approximately for $r = r_{pup}$, which corresponds to the furthest micro-lens sampling the pupil. If we constrain spot displacement to a maximum value, Δ_{max}, equal to half the micro-lens pitch, we can estimate the dynamic range of the H-S in terms of maximum Zernike defocus:

$${C_2}^0{}_{max} = \frac{\Delta_{max} \cdot r_{pup}}{4\sqrt{3} \cdot F} \tag{2.2}$$

and in terms of maximum measurable spherical equivalent (reciprocal of wavefront curvature radius),

$$SE_{max} = \frac{\Delta_{max}}{r_{pup} \cdot F} \tag{2.3}$$

This simple geometrical approach to estimate the theoretical dynamic range was applied for an arrangement combining a near infrared camera and a micro-lens array. Table 1 summarizes technical characteristics for the combination. The cameras are: 1) Hamamatsu, ref: C7500-51, and 2) IDS imaging, ref: lu-1242LE-NIR; and the micro-lens arrays is: Thorlabs, ref: MLA150-5C.

Micro-lens array	Pitch = 150µm F=5.2mm	
Fresnel Number	1.03	
Airy disk diameter [µm]	44.40 @ 1.050 26.77 @ 0.633	
CCD Detector	Hamamatsu Pixel size 8.6x8.3 µm	IDS imaging Pixel size 5.3X5.3 µm
θmin [milirad]	1.65x1.59 (~0.09º)	1.02 (~0.06º)
θmax [milirad]	14.42 (0.82º)	
Pupil diameter on sensor [mm]	4	
lenslets by pupil diameter	12	
Theoretical Sensitivity [D] @rpup 2-mm	0.82 (0.5 µm)	0.51 (0.3 µm)
Theoretical Dynamic range [D] @rpup 2-mm	±7.2 (4.16 µm)	

Table 1: HSWS specifications. Calculation were performed for a pupil of 4-mm diameter (rpup 2-mm) without optical magnification for one single lenslet at the pupil edge.

The used micro-lens array (MLA150-5C, Thorlabs Inc., Newton, NJ, USA) has a 5.2-mm nominal focal length and 150 µm lens pitch. With this arrangement, the pupil of the eye is effectively sampled with a spatial resolution of 300 µm. Despite delivering a worse theoretical sensitivity than the IDS camera, the main advantages of Hamamatsu C7500-21 camera (Hamamatsu Photonics KK, Hamamatsu City, Japan) are its better sensibility in near-infrared above 1 µm compared to conventional NIR cameras, and its large chip area (½ inch size) providing 768X576 resolution and 8.3X8.6 µm pixel size, well suited for binocular measurements. The acquisition frame rate allows image recording up to 25 Hz through a BNC output connected using a BNC-USB adapter. Each micro-lens corresponds to 18 X 18 pixels on the detector. The camera is mounted on a micrometer stage to adjust the distance between the CCD and the lenslet array in order to produce the sharpest spot image when illuminated with a collimated beam (see Figure 2.6). The whole arrangement is mounted on an aluminum board for alignment and potential calibration.

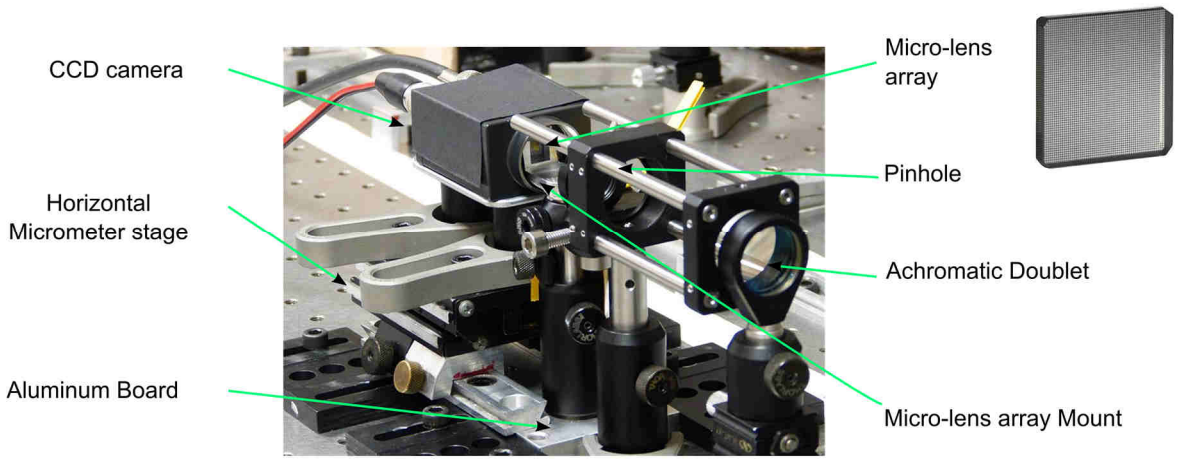

Figure 2.6: Detail of the binocular Hartmann-Shack sensor. It is composed of a CCD camera combined with a micro-lens array mounted on a micrometer stage. The achromatic doublet is the rear part of the relay telescope and is not mounted on the aluminum board

2.2 Micro-lens calibration

The micrometer horizontal stage displaces the NIR CCD camera with respect to the lenslet array to find the position where focal spots appear sharpest on the detector. Using an adjustable mechanical mount, the lenslet array can be coupled to the CCD with good parallelism. Spot displacement and local wavefront derivative are related through the micro-lens-CCD distance. Therefore, potential tilts affect wavefront estimation, and proper alignment all along the CCD chip is required, at least within mechanical tolerances (Neal et al., 2002). The geometrical focus of micro-lenses with low Fresnel Number (short focal lengths) is slightly shorter than the nominal focus due to diffraction effects. Thus, after implementation the detector plane is generally not at the geometrical focus of the micro-lens array (Ruffieux, Scharf, Herzig, Völkel, & Weible, 2006). In other words, the distance between both elements, where the sharpest spots are produced, does not correspond to the nominal focal length and an accurate calibration of the separating distance is needed to avoid measurement offset. It is important to note that using a distance between elements other than the micro-lens focal length does not alter the H-S functioning but scales spot displacements and, therefore, the aberrations estimates.

To experimentally determinate the distance between CCD and micro-lens array, a calibration arm, located in parallel to the instrument, allows introducing known power lenses at known distances from the sensor in the path of a collimated laser beam. This technique is a simple and easy-to-use method for calibration with high repeatability. The procedure is illustrated in Figure 2.7, where a plano-convex lens is displaced along an optical rail in the calibration path.

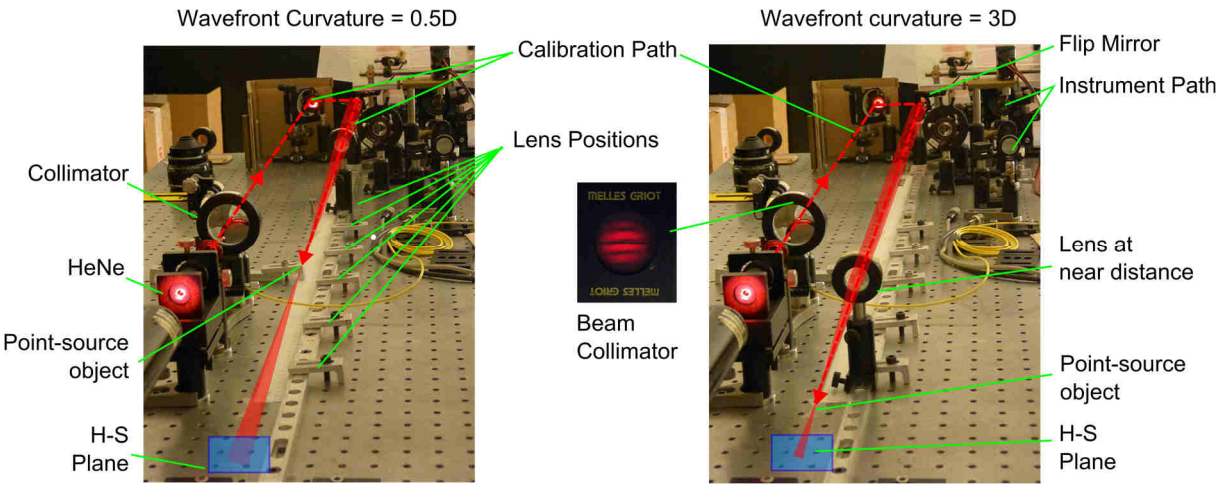

Figure 2.7: General view of the calibration path. The laser beam is in red and the H-S plane in blue.

Despite the use of the instrument at a NIR wavelength and due to the complexity of performing optical alignment and collimation at an invisible light, a red HeNe laser (633 nm) was used. A spatial filter and a lens of 200 mm focal length collimated the HeNe laser beam. It is important to note that since the outcome of the calibration procedure is the actual distance between lenslet array and CCD, and not the micro-lens focal length, chromatic aberration has no effect on the calibration procedure.

The system linearity was checked by displacing a 10-D convergent lens along the calibration arm. This had the effect of producing a pseudo point-source object at controlled distances from the micro-lens array and, consequently, known amounts of defocus in the micro-lens plane. Figure 2.8 shows a schematic of the set-up for calibration of the lenslet array/CCD distance. A reference image of the collimated beam was initially recorded to find the reference spot position for each micro-lens on the CCD. Then, the H-S patterns were processed to calculate the amount of defocus for each lens position.

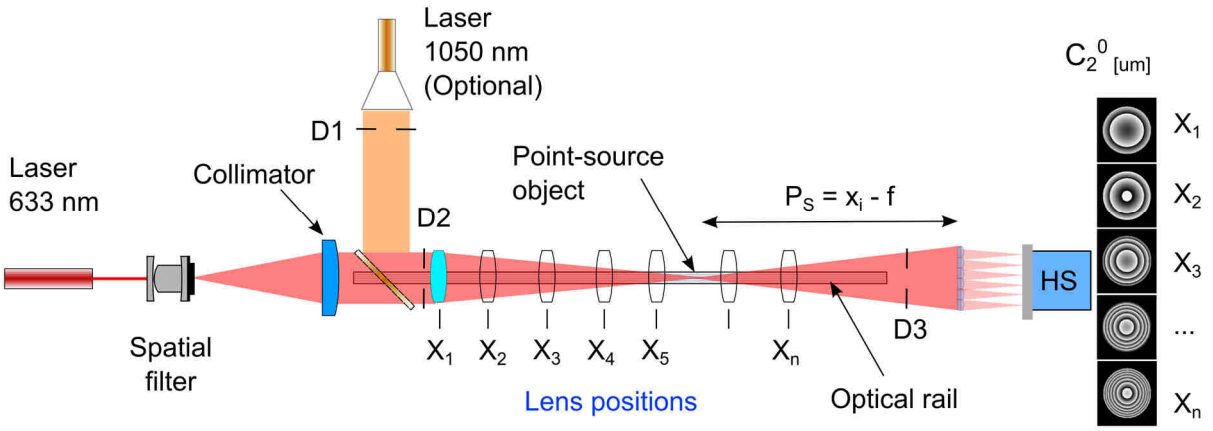

Figure 2.8: Schematic view illustrating the calibration procedure of the separating distance between the lenslet array and the CCD. X_1-X_n represent arbitrary but know lens positions in front of the sensor.

Three H-S videos of ten frames were recorded and processed to obtain the Zernike defocus coefficient for each lens position. Thirteen positions were selected from 950 mm to 220 mm in front of the detector with an accuracy of ±2 mm. The point-source object is formed at a distance $Ps = X_i - f$ in front of the lenslet array, where f is the focal length of the calibration lens and X_i is its position (X_1 to X_n) from the micro-lens plane. The estimation of the defocus coefficient C_2^0 provided by H-S sensor gives the radius of curvature of the wavefront:

$$R = -\frac{{r_{pup}}^2}{\left(4\sqrt{3}\cdot C_2^0\right)} \tag{2.4}$$

where r_{pup} is the pupil radius of measurement in millimeters.

In a perfect case, the radius of curvature R obtained through H-S measurements coincides with the point-source object distance P, but this is rarely the case. A linear fit between these two distances gives a direct interpretation of the data. The first term is the slope and it should be ideally 1. The slope indicates a scaling of the defocus estimation by the H-S sensor because of the use of the nominal focal length rather than the real separating distance between micro-lens and CCD. The second term of the fit is an offset of the measure that can come from lens positioning errors, or focal length, or chromatic aberration. In this independent term, these factors do not affect the calibration procedure. The Table 2 summarizes the H-S data obtained for the nominal focal length of 5.20 mm and the calibrated distance of 5.04 mm at 633 nm.

Measured Point-source Object distance [mm]	H-S Data @633nm C_2^0 [µm] F=5.20 mm	Calculated Point-source Object distance [mm] Ps F=5.20 mm	Calibrated H-S Data @633nm C_2^0 [µm] F=5.04 mm	Calculated Point-source Object distance [mm] F=5.04 mm
850	-0.164	874	-0.1713	843
735	-0.191	752	-0.198	728
69	-0.204	700	-0.213	677
610	-0.229	623	-0.239	604
565	-0.248	577	-0.257	562
485	-0.291	499	-0.299	483
440	-0.319	450	-0.330	435
335	-0.420	339	-0.44	328
290	-0.486	293	-0.500	284
250	-0.567	252	-0.593	243
210	-0.684	208	-0.713	202
165	-0.876	162	-0.916	158
135	-1.08	130	-1.1305	128

Table 2: Calibration data of the separating distance between micro-lens and CCD detector. Data are shown for the nominal focal length of 5.20 mm and the calibration length of 5.04 mm.

For the nominal focal length, the slope is not equal to 1 because the actual distance between the micro-lens array and the CCD that produces the sharpest spot image is slightly shorter (Li & Wolf, 1981) (Ruffieux et al., 2006). The calibrated distance is 5.04 mm, obtained by dividing the nominal focal length by the fitting slope (see Figure 2.9). This value must be used instead of the focal length in the Zernike calculation algorithm. When the procedure is repeated taking into account the calibrated distance, the slope of the data is equal to 1. Figure 2.9 plots the calculated distances for the nominal focal length (5.20 mm) and the calibrated distance (5.04 mm) as a function of lens position. The nearly perfect linear fit confirms the good linearity of the system, at least in the corresponding working range.

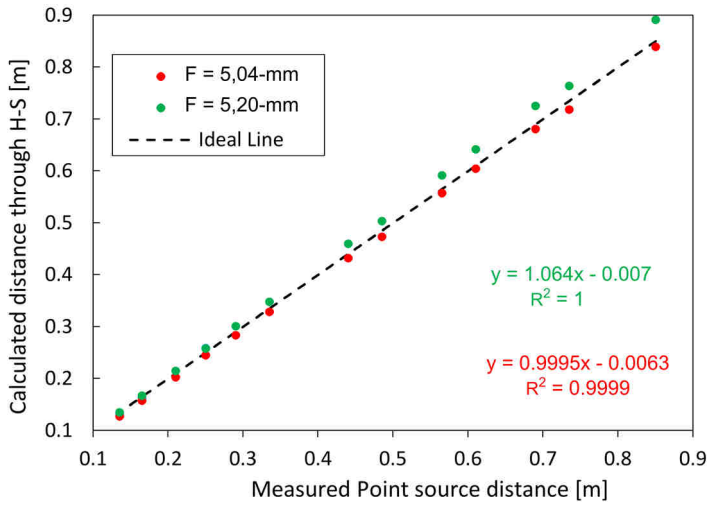

Figure 2.9: Linearity of the sensor and calibration of the micro-lens-CCD distance. The black dashed line is the ideal 1:1 relationship.

In order to achieve an accurate horizontal and vertical alignment of the micro-lens array and the detector, the back reflection on each surface is carefully lined up with the centered pinhole D2. Figure 2.10 exhibits a schematic draw of the lenslet array misalignment (left) and parallelism (right).

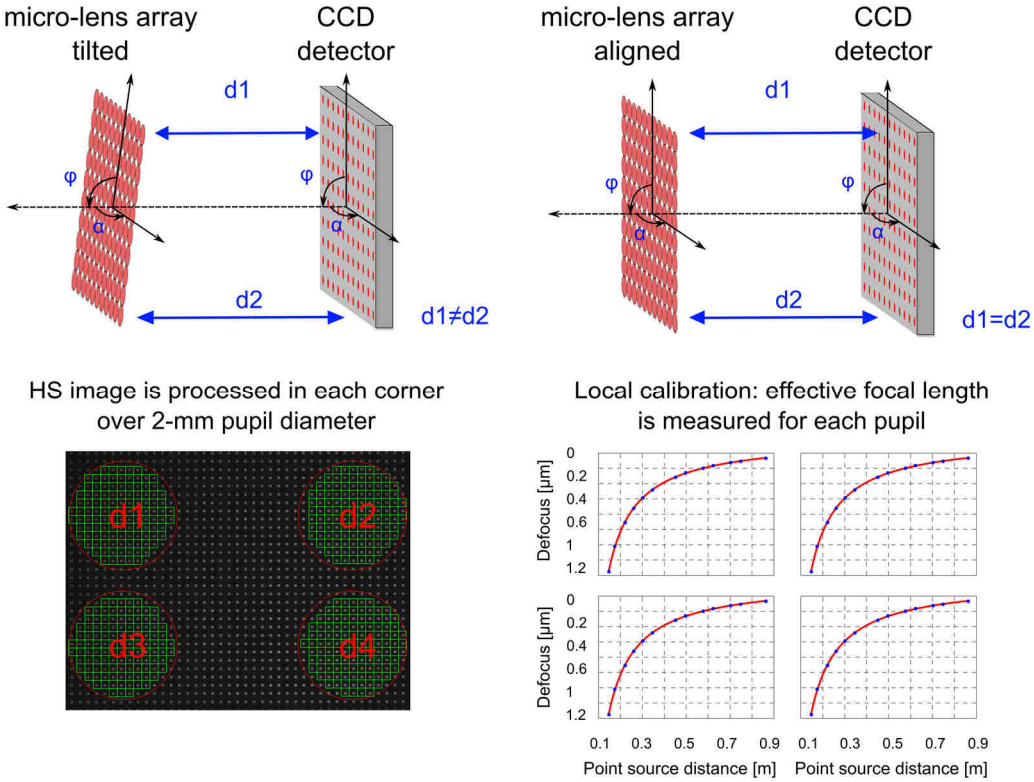

Figure 2.10: Local calibration of the distance between lenslet array and CCD for parallelism assessment. Top: Different calibration results in contralateral pupils reveal lenslet array tip and/or tilt. Bottom-Left: H-S pattern with four 2-mm diameter-processing pupils at the corners. Bottom-right: defocus fitting.

Since the expanding beam from the collimated lens fills the entire H-S area, a further test of the alignment between the lenslet array and the CCD consists of repeating the calibration procedure for four pupils, each one close to each corner of the H-S pattern. The differences between local estimates of the separating distance, which should be identical, d1=d2=d3=d4, can be taken as an indicator of lenslet-CCD alignment. Figure 2.11 shows the calculated pseudo point-source object distances obtained from the defocus coefficients for each corner. The separating distance is of 5.05 ± 0.01 mm on average.

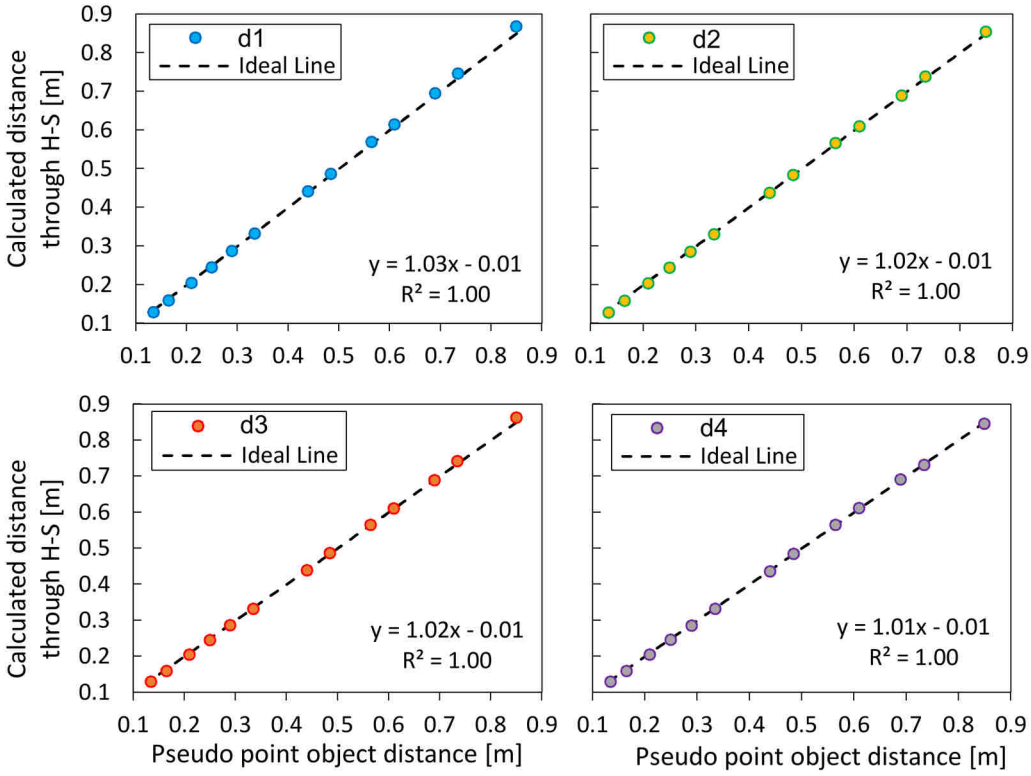

Figure 2.11: Linearity of the local distance as a function of pseudo-point object distance for a pupil of 2-mm diameter in each corner d1, d2, d3 and d4.

The effective distance can be evaluated all along the H-S pattern over a pupil of 2-mm diameter to highlight optical imperfections.

Figure 2.12 is a visual representation of the local separating distance as a function of the pupil coordinates. Therefore, the separating distance between the micro-lens array and the CCD appears to be homogeneous in the whole area of the sensor with low variations of ± 0.05 mm around 5 mm of separating distance on average.

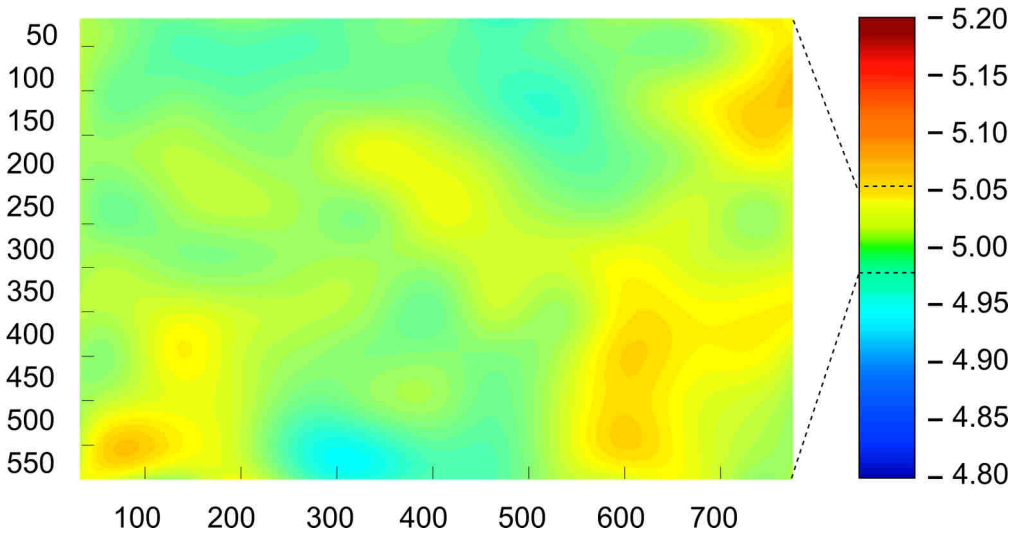

Figure 2.12: Map of the separating distance CCD-micro-lens array, obtained by interpolation of the data.

2.3 Sensor sensitivity and accuracy

In order to test the sensor sensitivity, a 0.5 D lens was moved in 10 cm steps in front of the sensor in order to induce small changes of defocus, $C_2{}^0$. Figure 2.13 illustrates the procedure. Measurements were taken for seven lens positions. The H-S images were processed for different pupil radii ranging from 0.75 mm to 2 mm to test the dependence of sensitivity on pupil size (see Table 3).

Point source distance [m]	Radius=0.75mm		Radius=1mm		Radius=1.25mm		Radius=1.5mm		Radius=2mm	
	Theoretical $C_2{}^0$	Measured $C_2{}^0$	Theo.	Meas.	Theo.	Meas.	Theo.	Meas.	Theo.	Meas.
1.905	0.042	0.039	0.076	0.081	0.119	0.120	0.171	0.176	0.303	0.305
1.855	0.043	0.036	0.078	0.075	0.121	0.119	0.175	0.175	0.311	0.312
1.805	0.044	0.046	0.080	0.085	0.125	0.128	0.180	0.183	0.319	0.323
1.715	0.047	0.040	0.084	0.083	0.131	0.130	0.189	0.187	0.336	0.333
1.605	0.050	0.042	0.090	0.091	0.140	0.139	0.202	0.201	0.359	0.359
1.505	0.054	0.049	0.096	0.097	0.150	0.149	0.215	0.215	0.383	0.382
1.395	0.058	0.055	0.10	0.105	0.162	0.164	0.233	0.236	0.414	0.416

Table 3: Sensor accuracy as a function of pupil size. Theoretical and measured defocus coefficients $C_2{}^0$ in microns are shown for each processing pupil and point-source object position.

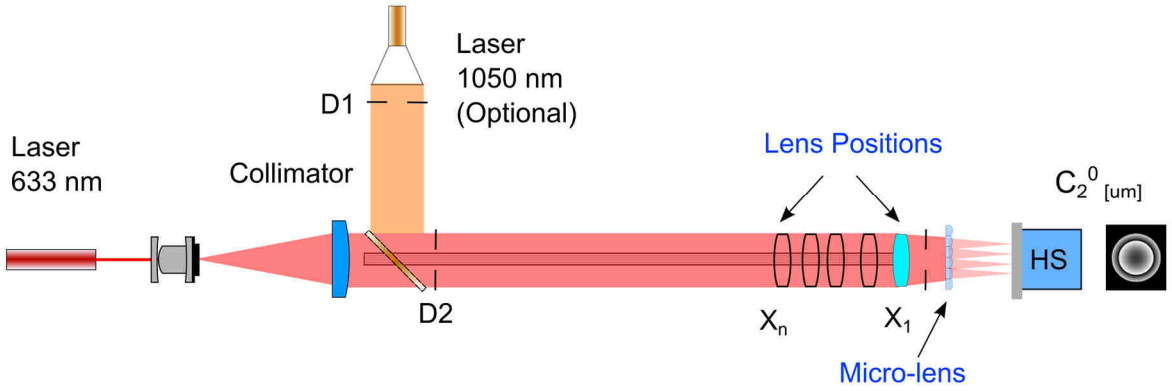

Figure 2.13 Schematic view illustrating the sensor sensitivity test. A 0.5-D lens was displaced in front of the sensor in order to produce defocus, C_2^0, changes as small as 0.02-μm.

Figure 2.14 compares the theoretical and measured values of the defocus coefficient, C_2^0, for seven lens positions (left), and the differences relative to the initial lens position (right).

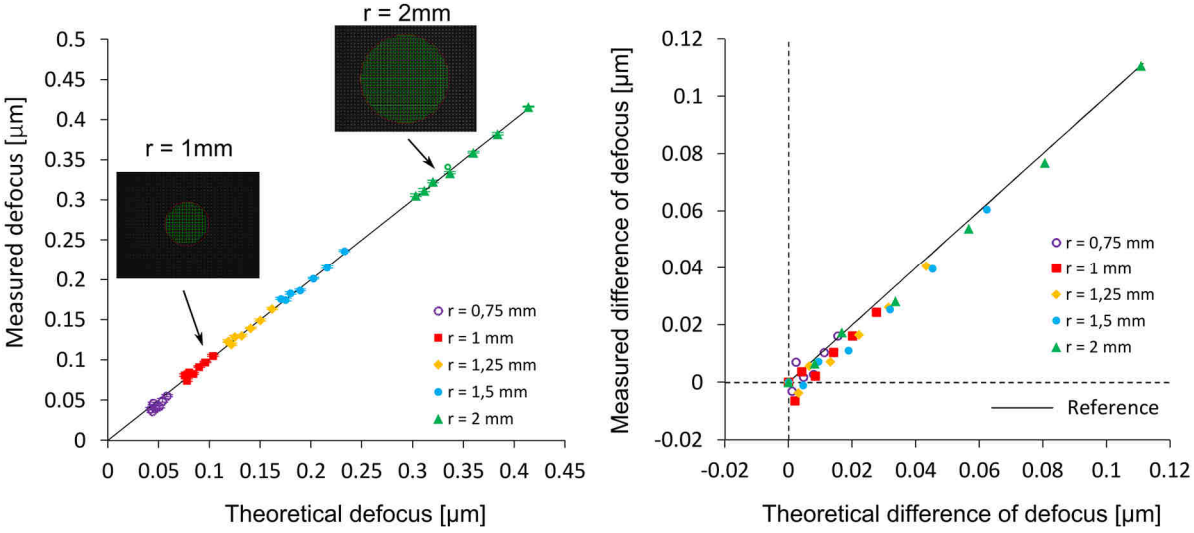

Figure 2.14: Sensor accuracy test. Left: Theoretically induced vs. experimentally measured Zernike defocus, C_2^0, for seven lens positions and five processing pupil radii. Error bars (almost eclipsed by the symbols) represent standard deviation across 10 measurements. Right: difference of defocus with respect to the first (closest) lens position. In both plots, each color represents results for a different processing pupil size and the black line is the ideal 1:1 relationship.

The sensor shows good defocus sensitivity (Figure 2.14, left), even when small pupils are used. In order to stress this point, the right panel of Figure 2.14 shows the differences of defocus with respect to the first lens position, demonstrating the capacity of the sensor to accurately measure changes in defocus until 0.02 μm (Neal et al., 2002). As an example, for a pupil radius of 1-mm, the sensor detects 0.01 μm of defocus changes. Student's t-tests applied to experimental defocus values for different lens positions produced p-values < 0.05 for pupil radii bigger than 1 mm. Conversely, for smaller pupil sizes, no statistical significance was found, which we take as

an indicator that the sensor was not sensitive to changes in defocus lower than 0.02 μm. For this reason, H-S processing with pupils lower than 1-mm of diameter was avoided in our experiments.

2.4 Instrument alignment

The instrument employed a 0.5-magnification afocal telescope composed of two NIR achromatic doublets, L1 and L2, of 300 mm and 150 mm focal length. Since both pupils were combined into the H-S through the same optical path, a misalignment of the optical elements could lead to local measurement errors.

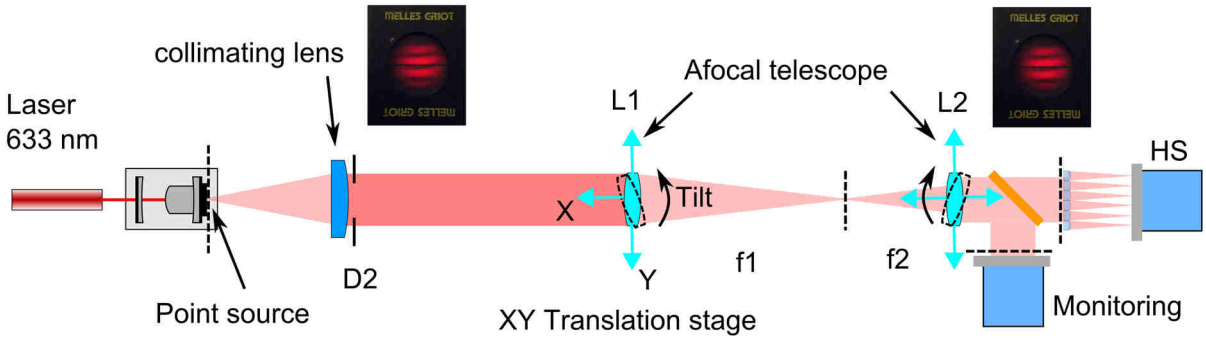

Figure 2.15: Schematic drawing of the instrument lenses alignment procedure.

Alignment consisted of several steps and was carried out by use of the collimated beam in the alignment/calibration arm and a pinhole, D2, located in a plane conjugated to the eye's pupil. Lenses were mounted on a XY micrometer translation stages for precise horizontal (x-axis) and lateral (y-axis) positioning, attached to an optical rail for a first rough alignment. Lens L1 was first positioned in order to produce an image at infinity of the eye's pupil plane. The afocal telescope alignment was carried out by the horizontally moving lens L2 (first on the optical rail and then with the micrometer) and the use of a shear plate. Centering was performed by laterally moving both lenses (y-axis). Tilt was corrected by slight rotations of the lenses until reflections of the beam on the front and back surfaces of each lens came back to the centered pinhole D2. Tip was not corrected, assuming a good parallelism of the mounts in vertical direction (z-axis). The monitoring camera was moved to produce a sharp image of D2, which means the camera is focused at the pupil plane. Then, the H-S sensor measurement plane (i.e., the lenslet array plane) was optically conjugated to infinity.

2.5 Dynamic range and linearity

The dynamic range of the instrument and the linearity of low- and high-order aberrations (up to 4^{th} order) were determined by two methods. Defocus and astigmatism were tested by use of trial lenses. Then, high-order aberrations ranges were determined by means of an Adaptive

Optics system. 2nd order aberrations were also tested with the AO system to validate both methods. These calibration procedures were carried out with the 633 nm HeNe laser.

Low-order aberrations

Pure spherical and cylindrical trial lenses (optical instrument CO, LTD China), were inserted in the input plane of the instrument and conjugated with the H-S sensor as shown in Figure 2.16.

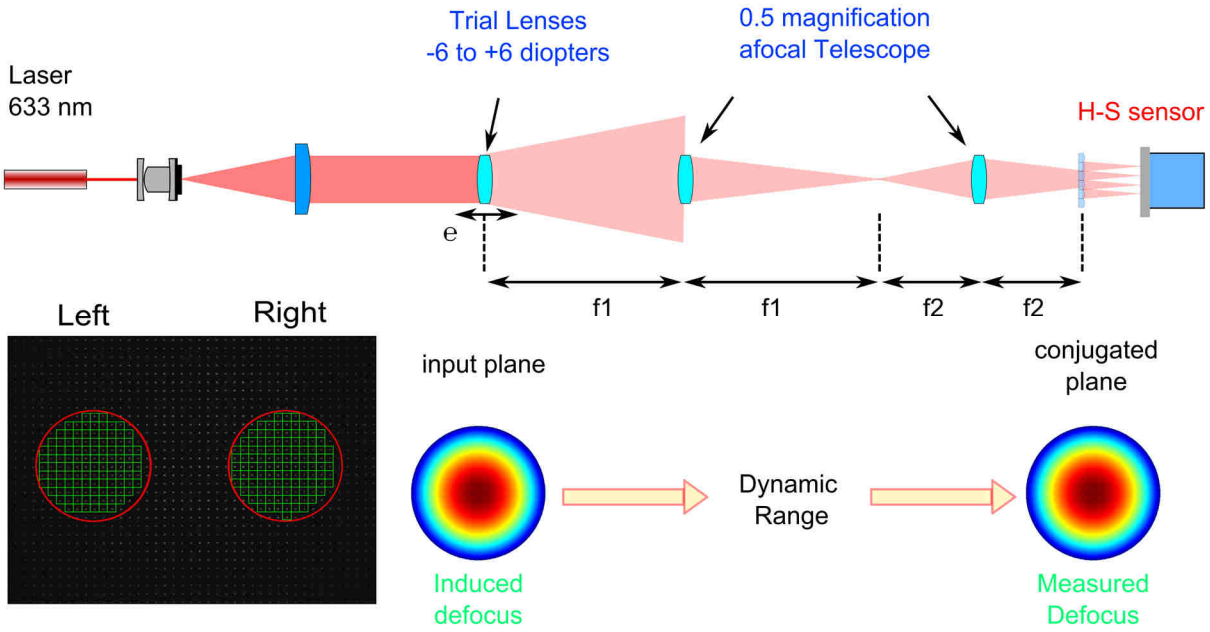

Figure 2.16. Optical set-up for testing defocus and astigmatism linearity by use of trial lenses.

Trial lenses of pure defocus from -6 D to +6 D in 0.25 D steps were tested. This range covers most of the typical ammetropies in normal subjects and the typical amount of accommodation in young adults for our experiments. Three twenty-frames video sequences were processed and averaged for each tested lens. Figure 2.17 (top panel) shows measured vs. nominal defocus in diopters. The behavior is visibly linear for a wide range but discrepancies become apparent around ±4 D. A 5% and/or 0.25-D error criterion yielded a dynamical range between -3.5 D to +3.5 D for both channels. Inside this range, defocus linearity was tested, as illustrated in the central panel, with a regression linear fit (black line). For both channels, the fitting was very close to linear (R^2 =0.999 in both cases), with slopes very close to one. Furthermore, the bottom panel in Figure 2.17 shows the RMS of high-order aberrations, RMS H-OA, and the residual spherical aberration, C_4^0, in microns. The low values obtained demonstrate that the sensor does not report erroneous high order artifacts when dealing with pure defocus inside the dynamical range.

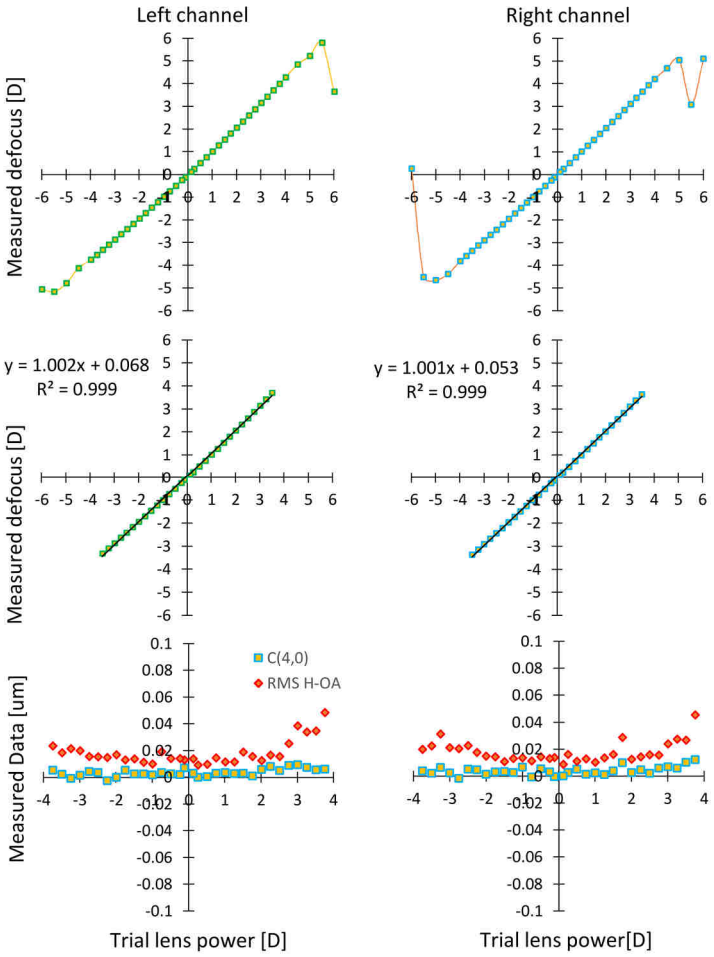

Figure 2.17: Dynamic range and linearity of defocus Zernike coefficient, C_2^0. Top: Measured defocus vs. trial lens power. Center: Linear fit (black line) inside the dynamical range. Bottom: residual spherical aberration and RMS of high-order aberrations.

Astigmatism dynamic range and linearity were analyzed by measuring positive and negative cylindrical trial lenses horizontally and vertically oriented (see Figure 2.18).

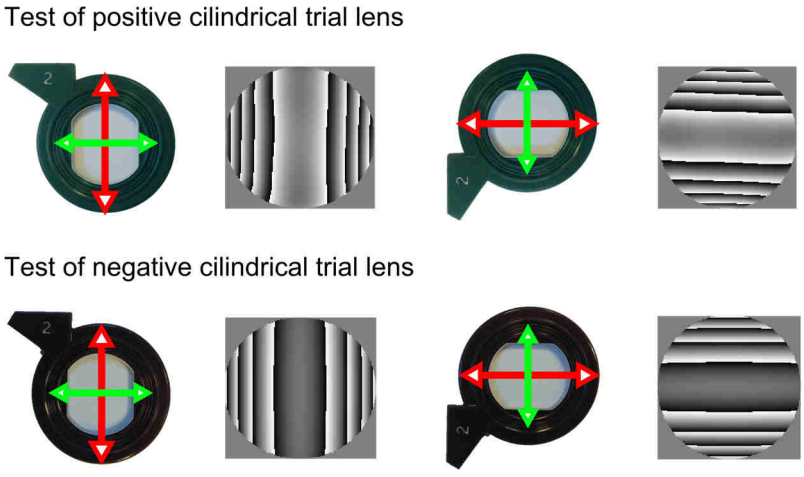

Figure 2.18: Test of positive and negative cylindrical trial lens in different orientations.

Top panel in Figure 2.19 shows measurement results for all the combinations. Since we use a "minus cylinder notation" to express sphero-cylindrical errors, measured astigmatism is always negative and sign to the results have been changed for positive lenses for the sake of clarity

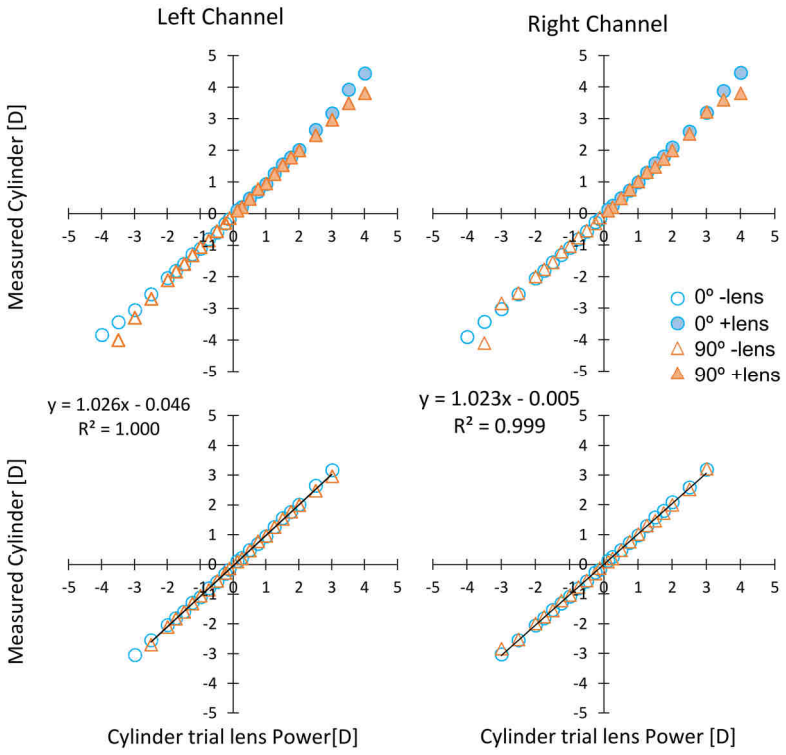

Figure 2.19: Dynamic range and linearity of cylinder power. Top: Measured cylinder vs. cylindrical trial lens power. Bottom: Linear fit (black line) inside the dynamical range.

The same error criterion was used to determine a dynamical range between -3 D to +3 D for both channels. Bottom panel in Figure 2.19 illustrates the fitting was very close to linear (R^2 >=0.999 in both channels).

High-order aberrations

Wavefront modulation by AO is an excellent tool for instrument calibration. It allows precise and individual control of each monochromatic aberration term (low- and high-order aberrations) for testing the dynamic range of our apparatus. The set-up employed a Liquid Crystal-on-Silicon Spatial Light Modulator (LCoS-SLM, Hamamatsu X14068, Japan). Figure 2.20 illustrates the optical set-up. Linear polarizers P1 and P2 selected the polarization axis for wavefront modulation. An intensity filter regulated the H-S spot intensity. A couple of mirrors, M1 and M2, redirected a collimated beam onto the LCoS screen at a low incident angle (<10º) for best modulation results.

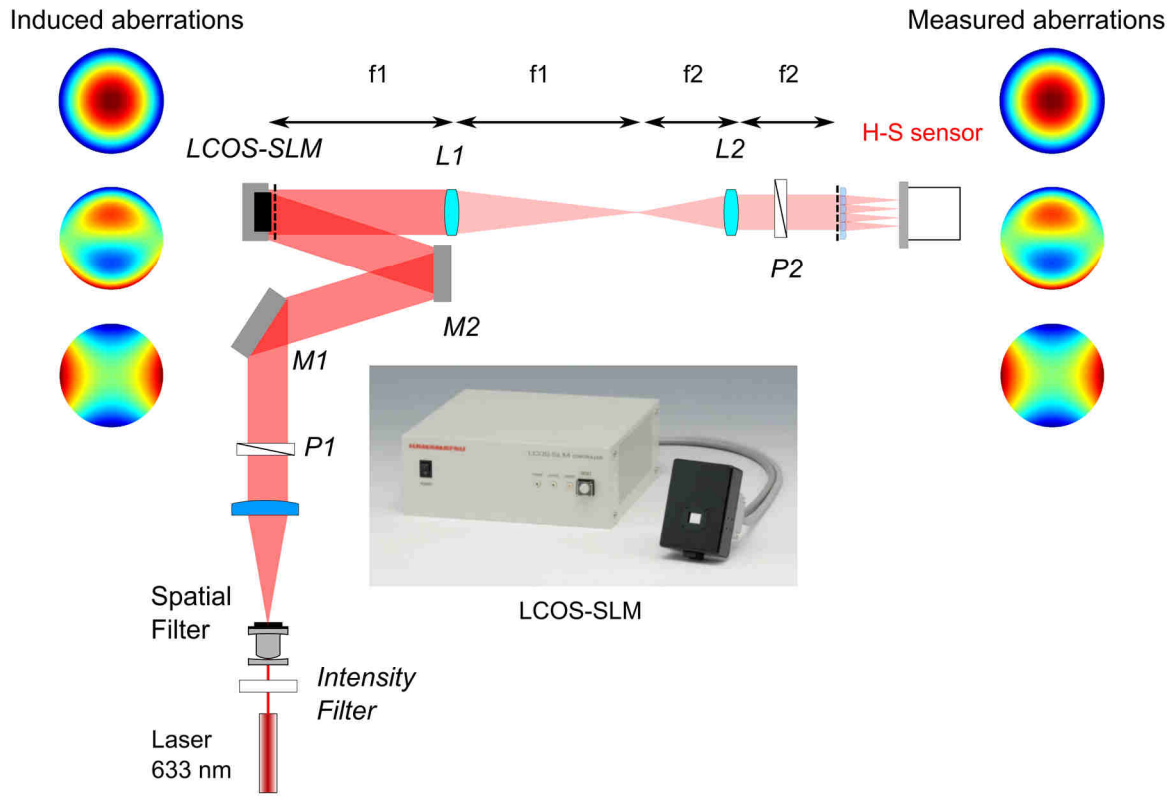

Figure 2.20: Schematic of the Adaptive Optics set-up to test the instrument operating range. The LCoS-SLM modulates a collimated beam introducing known amounts of individual monochromatic aberrations. Polarizers P1 and P2 control the polarization axis. Mirrors M1 and M2 redirect the incoming beam at a low incident angle, $<10^{o}$.

The operator selected the coefficient of Zernike to test and its value. The software automatically generated 2-π wrapped phase maps on two local areas of the LCoS, one for each measurement channel (one for each eye, see Figure 2.21, left). H-S images were processed over two pupils of 4-mm diameter (red circles in Figure 2.21, right) and aberrations were calculated. The instrument dynamic range was defined individually for each aberration up to 4^{th} order with a 5 % criterion error as described previously. Linearity was tested with a regression linear fit and similarity between channels was compared.

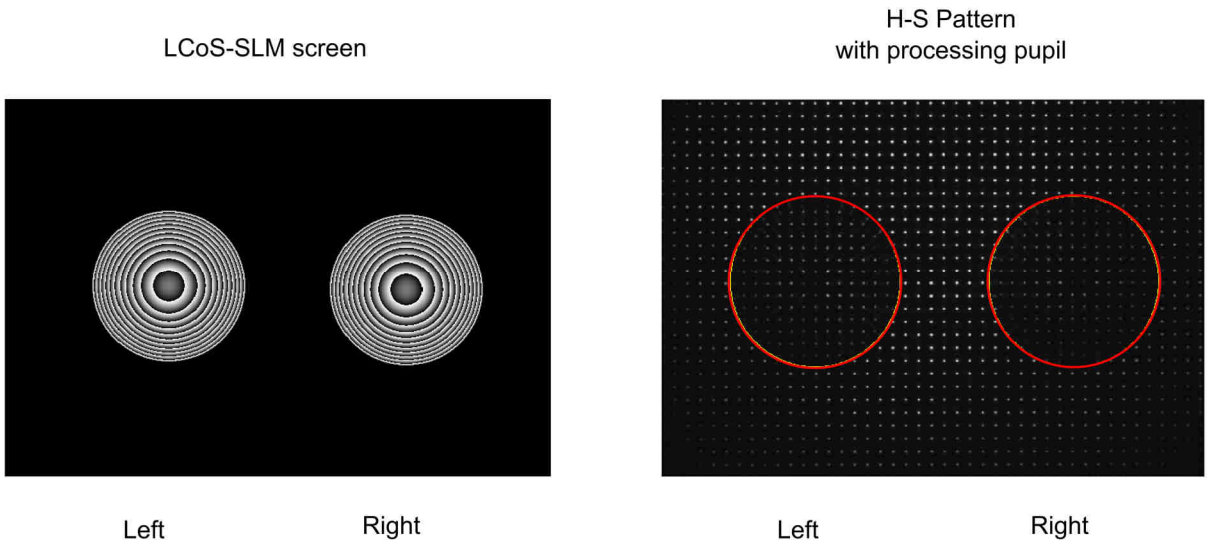

Figure 2.21: 2-π wrapped phase map of binocular defocus (left) and corresponding H-S pattern (right).

Figure 2.22 to Figure 2.25 show the linearity of the instrument for individual Zernike aberrations from 2nd to 4th order. Table 4 summarizes the dynamic range of the instrument for each studied Zernike mode.

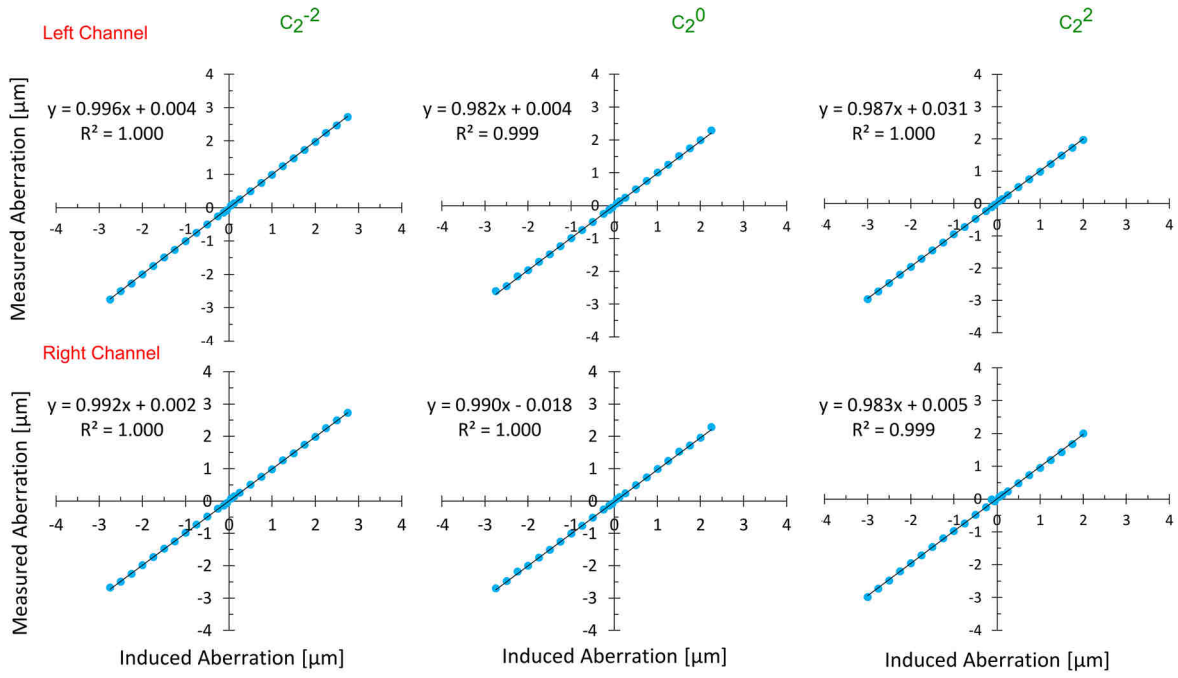

Figure 2.22: Instrument linearity for 2nd order aberrations. Top: Left channel, Bottom: Right channel. Black line represents regression linear fit to experimental data (blue circles).

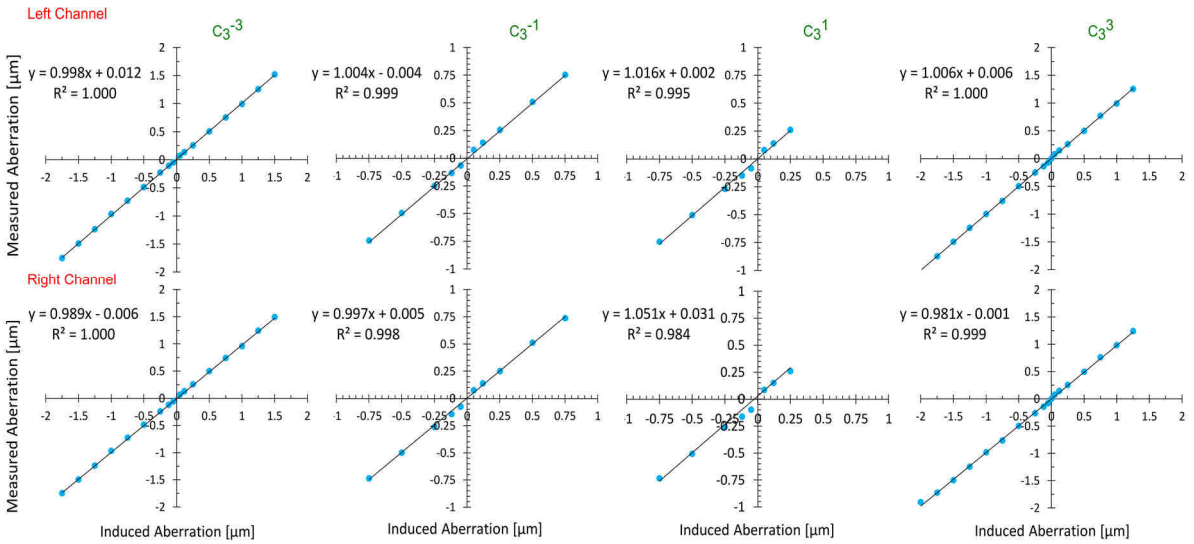

Figure 2.23: Instrument linearity for 3$^{\text{th}}$ order aberrations. Top: Left channel, Bottom: Right channel. Black line represents the regression linear fit to experimental data (blue circles).

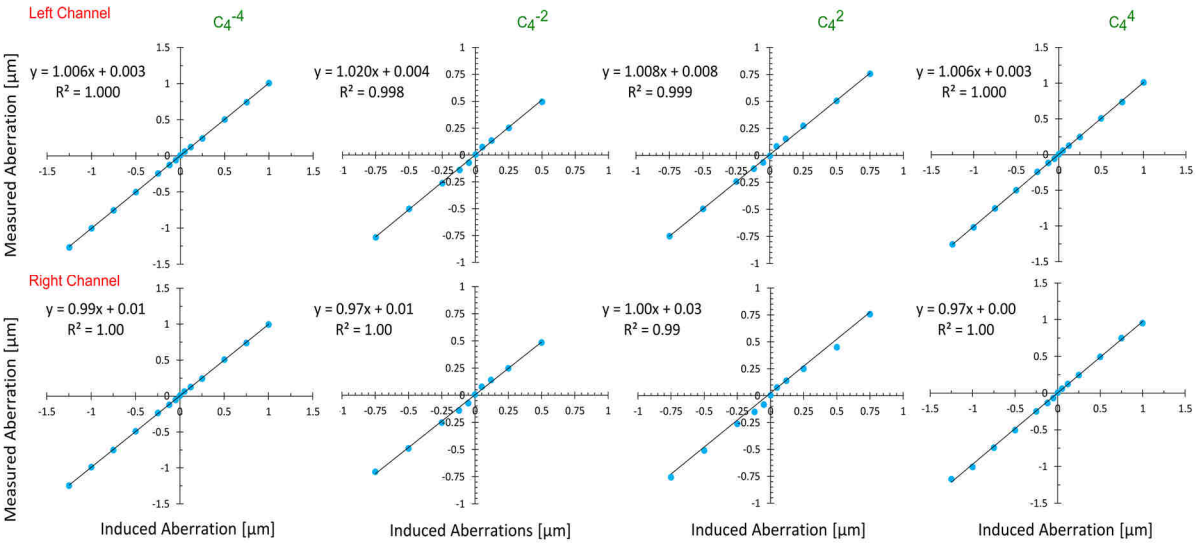

Figure 2.24: Instrument linearity for 4$^{\text{th}}$ order aberrations. Top: Left channel, Bottom: Right channel. Black line represents the regression linear fit to experimental data (blue circles).

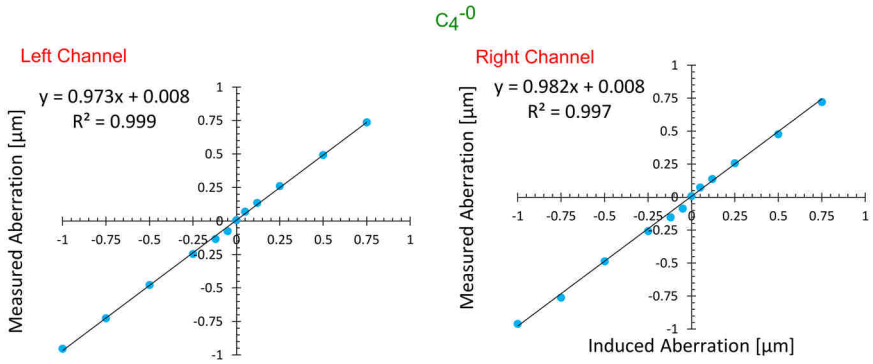

Figure 2.25: Instrument linearity for spherical aberration.

For each order, the fitting was very close to linear ($R^2 > 0.98$ in all cases), with slope close to 1. The dynamical range, defined by the 5 % criterion error, showed very similar results in both channels. The sensor provided reliable measurements of low- and high-order aberrations up to 4th order. By separating the sensor area in two independent zones, one for each eye, our instrument has shown a similar dynamic range and linearity for both channels, well suitable for a binocular use.

Zernike order	m=-4	-3	-2	-1	0	1	2	3	4
2nd			±2.75 µm		+2.25 µm - 2.75µm		+2.00 µm - 2.75µm		
3td		+1.50 µm - 1.75µm		±0.75µm		+0.25 µm - 0.75µm		+1.25 µm - 2.00µm	
4th	+1.00µm -1.25µm		+0.50 µm - 0.75µm		+0.75 µm - 1µm		±0.75 µm		+1.00 µm - 1.25µm

Table 4: Instrument dynamic range for each Zernike mode up to 4th order. Values are given for a pupil of 4mm of diameter.

2.6 Calibration with an artificial eye

Figure 2.26 gives an overview of the experimental set-up used to measure an artificial eye, coupled to trial lenses to simulate ammetropia, and placed in the pupil plane. Measurements were taken through the dichroic mirror and using 1050-nm illumination, i.e., with the instrument in operating conditions. The artificial eye was composed of a 50-mm lens, an 8-mm iris and a screen mounted on an adjustable stage to simulate an emmetropic eye. Known amounts of defocus were produced by adding trial lenses. Two crossed linear polarizers were used to suppress reflections on the lenses. However, this arrangement reduces significantly the intensity of the output wavefront. For an artificial eye, intensity of the infrared illumination is not a restriction and increasing the beam power improves H-S spot intensity. On the contrary, in the human eye there are safety limits (see section 2.7) in order to prevent retinal damage. Therefore, the crossed-polarizers technique to avoid corneal reflections was not used in real eyes.

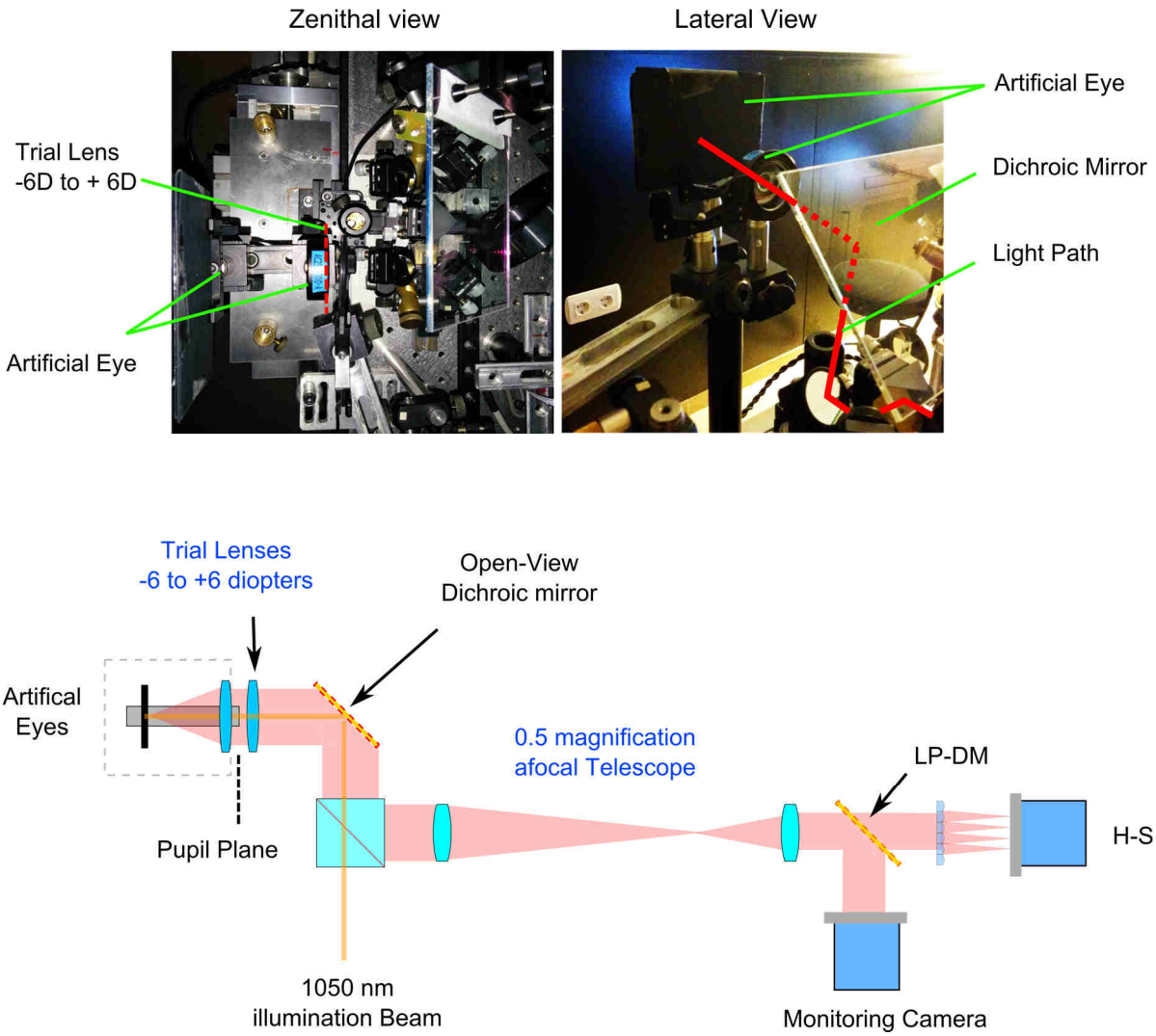

Figure 2.26: Top: Zenithal (left) and lateral view (right) of the experimental set-up. The infrared measurement light-path is shown in red in the right panel. Bottom: Lateral schematic view of the set-up.

Figure 2.27 shows pupil monitoring and H-S images of the artificial eye.

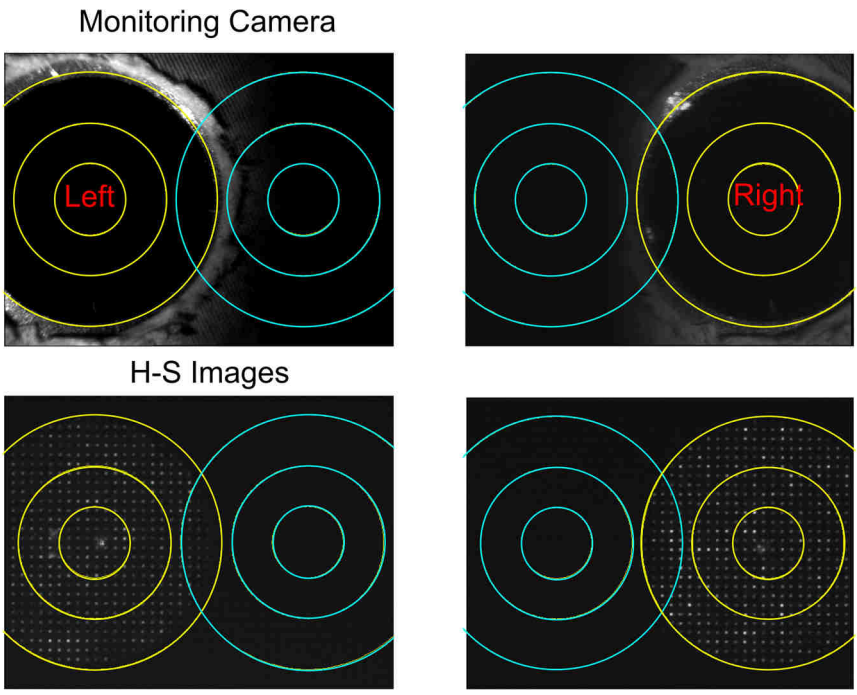

Figure 2.27: Pupil monitoring and H-S images when the artificial eye is measured through either the left or the right channel.

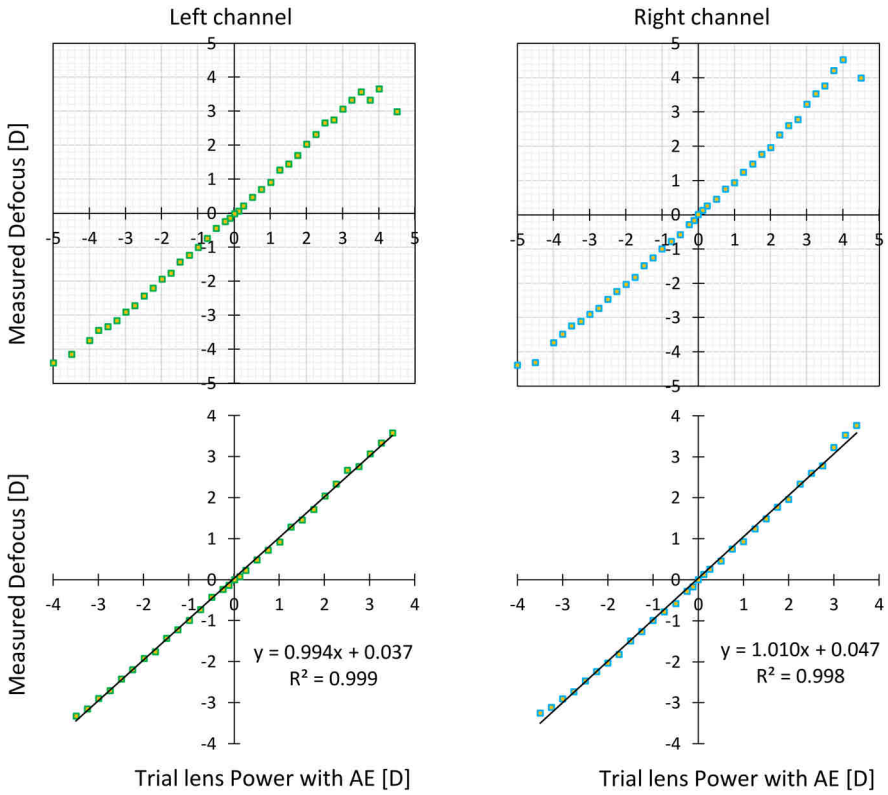

Figure 2.28: Defocus Zernike coefficient of an artificial eye and a set of trial lenses measured at 1050nm through the whole instrument in open-view configuration. Top: Measured defocus vs. trial lens power. Bottom: Linear fits inside the dynamic range.

Trial lenses ranging from -6 D to +6 D in 0.25 steps were measured and results can be seen in Figure 2.28. In both channels, the instrument showed similar behavior for 1050 nm and open-view conditions than for 633 nm. Discrepancies were observed for defocus values around 4 D and higher, and the linear range was found around ±3.5 D with a 5% error criterion.

H-S operating range and LCA

To determine the ocular refraction at the center of the visible spectrum, the chromatic defocus has to be corrected. This is a problem widespread among current aberrometers, which tend to employ infrared light. The chromatic difference from the infrared (1050nm) to 590 nm, which is typical reference visible wavelength (Thibos et al., 1992) is 1.2 D. Thus, for an emmetropic eye, LCA shifts the H-S spots outwards with wavelength as illustrated on the Figure 2.29.

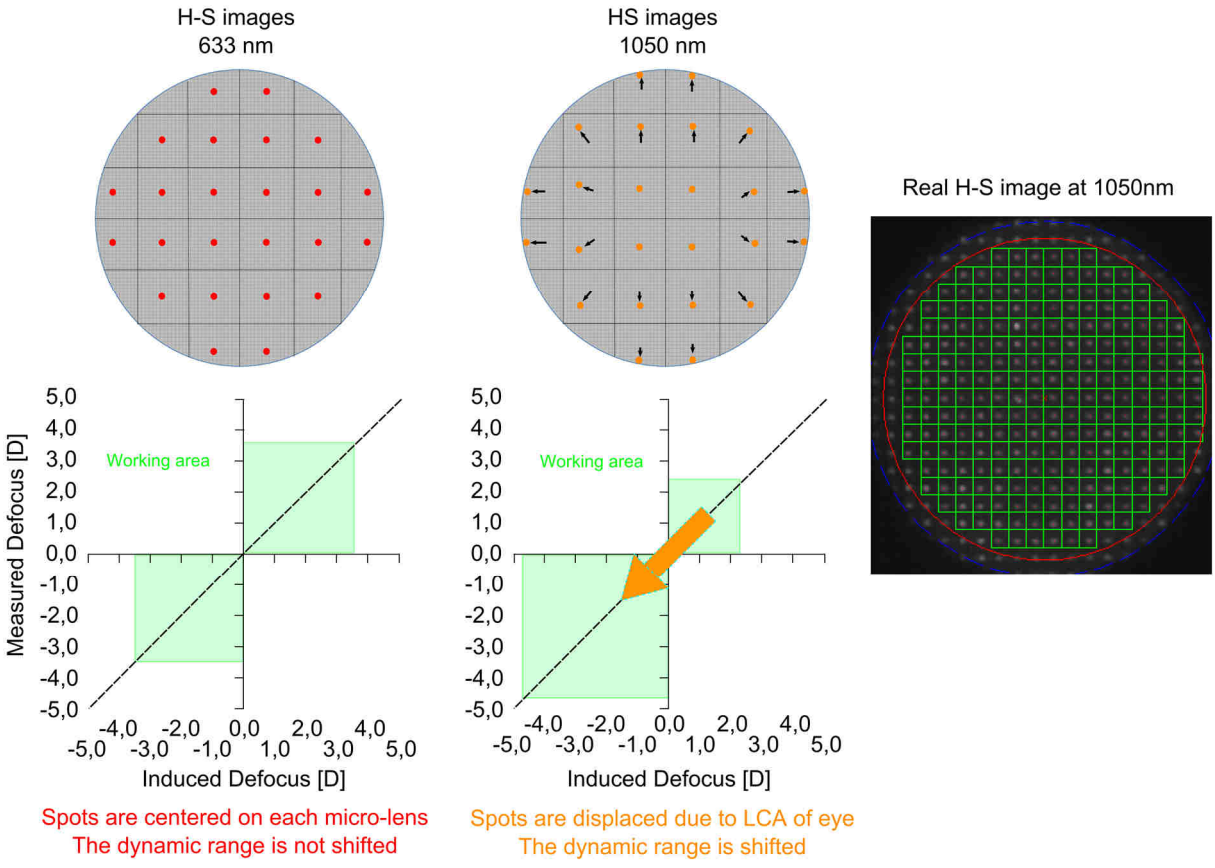

Figure 2.29: Effect of the LCA of the human eye on H-S images.

This chromatic shift reduces the dynamic range of the instrument for hyperopic eyes while extending it for myopic eyes whose wavefronts compress the spot mosaic, as is the case when the subjects are accommodating. Since nearsightedness is the most common refractive error, the increase of the dynamic range for myopic and accommodated eyes can be considered an indirect advantage of the use of infrared wavelength for refraction measurement.

2.7 Eye safety limits

The cornea mainly absorbs ultraviolet wavelengths below to 400 nm and the far infrared above 3000 nm. The crystalline lens absorbs ultraviolet light between 300 nm and 400 nm. From 400 nm to 1400 nm, the so-called retinal hazard region, the retina is much more susceptible to be damaged because of the transparency of the ocular media (Boettner & Wolter, 1962). The retinal pigment epithelium absorbs the visible radiation that can lead to non-reversible thermal damages of the retina by heat effect. For near infrared light up to 1400 nm the photoreceptors are not enough sensitive to radiation and no sensation results in the eye when exposed to these wavelengths, resulting in a much greater hazard for lasers operating in the near infrared. Figure 2.30 illustrates the wavelength absorption of the human eye.

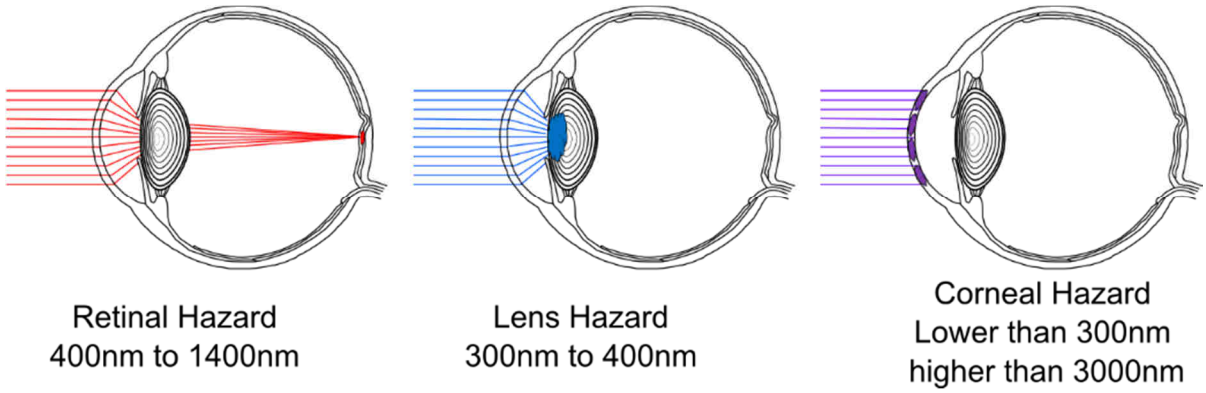

Figure 2.30: Wavelength absorption of the Human eye. The retinal hazard region is in red, the cataract hazard is in blue and the corneal hazard in purple.

The standard for safety of laser products, EN 60825-1 standard (EN 60825, 2007) defines the maximum admissible power of a laser beam (or power safety limit), which can penetrate into the eye as a function of exposure time and wavelength in order to avoid corneal and retinal damage.

The Maximum Permissible Exposure at the cornea, MPE, is the highest power or energy density that can be considered harmless for normal subjects. It defines the limit between safe use of a laser source and risk of eye thermal injuries. It depends on wavelength, exposure time, biological tissues involved and the angular dimension subtend by the apparent source: extended or point source. In ocular aberrometry, usually the illumination is a point source; the use of a collimated beam produces a tiny spot onto the retina where the whole energy is concentrated in a small area (Delori, Webb, & Sliney, 2007). Figure 2.31 shows the typical illumination beam in ocular aberrometry.

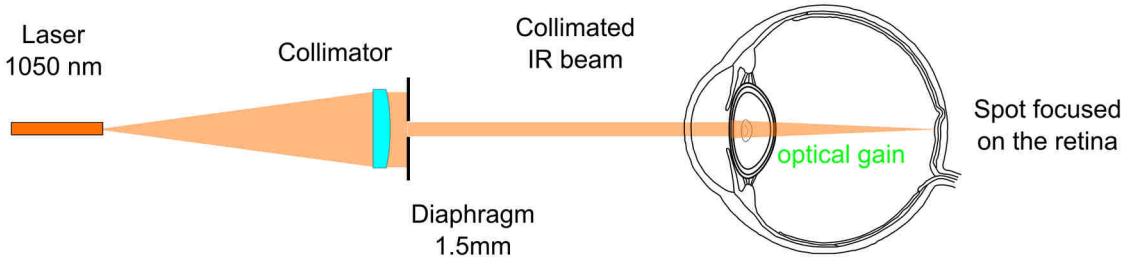

Figure 2.31: Illumination beam in ocular aberrometry. The apparent source is seen as a tiny spot and the intensity onto the retina is maximum.

In experimental conditions, for a collimated beam of laser radiation in the NIR range (700 – 1050 nm or 1050 – 1400 nm), the MPE and the maximum power at the cornea, P_{eye}, for exposure times up to 10 s, are shown below:

$700 < \lambda < 1050$		$1050 < \lambda < 1400$	
$MPE = 18 \cdot t^{0.75} \cdot C_4 \cdot C_6 \ \ [j.m^{-2}]$		$MPE = 90 \cdot t^{0.75} \cdot C_6 \cdot C_7 \ \ [j.m^{-2}]$	
$C_4 = 1$	$C_6 = 1$	$C_6 = 1$	$C_7 = 1$
$P_{eye} = MPE \cdot \left(\pi \cdot \left(\frac{D}{2}\right)^2\right) \cdot \frac{1}{t} \ \ [W]$			
$P_{eye} = 0.0019\ W$		$P_{eye} = 0.0019\ W$	

where C_4, C_6, C_7 are corrective factors, λ is the wavelength, D is the pupil diameter (for wavelengths between 400 to 1400 nm, 7-mm diameter pupil is considered) and t is the exposure time. Multiplying the MPE by the pupil area gives the maximum power of the laser before the MPE is exceeded which we can convert to an irradiance by dividing by the duration time. For a 10 seconds exposure time, MPE is 505 $j.m^{-2}$ and the maximum power of the laser tolerated P_{eye} is 0.0019 W for a point source. Experimentally, the infrared beam power was set to 30 μW for a beam diameter of 1-mm approximately, which is several order of magnitude lower (63 times) than the tolerated power at the cornea for an exposure time of 10 seconds (1.9 mW).

2.8 Software for experimental control

The software package is an evolution of the H-S processing tool developed over the last two decades at the Laboratory of Optics of the University of Murcia, LO.UM. Figure 2.32 and Figure 2.33 show the graphic interface. The package consists of a binocular wavefront analyzer (Figure 2.32) and a stimulus controller (Figure 2.33), both of them developed in Matlab (Mathworks, USA).

The binocular wavefront analyzer software records and processes H-S video sequences at a 25 Hz frame rate. It employs a binocular pupil tracker (described in detail in section 2.9), and algorithms for spot detection and computation of Zernike modes. It is combined with a blink removal algorithm for subject's comfort.

The operator selects the size of the measurement pupil and the number of Zernike coefficients to calculate. After processing the H-S frames, the wavefront analyzer provides monochromatic aberrations, refraction (Sphere, cylinder and axis), and pupil size in both eyes together with an estimate of vergence calculated from interpupillary distance.

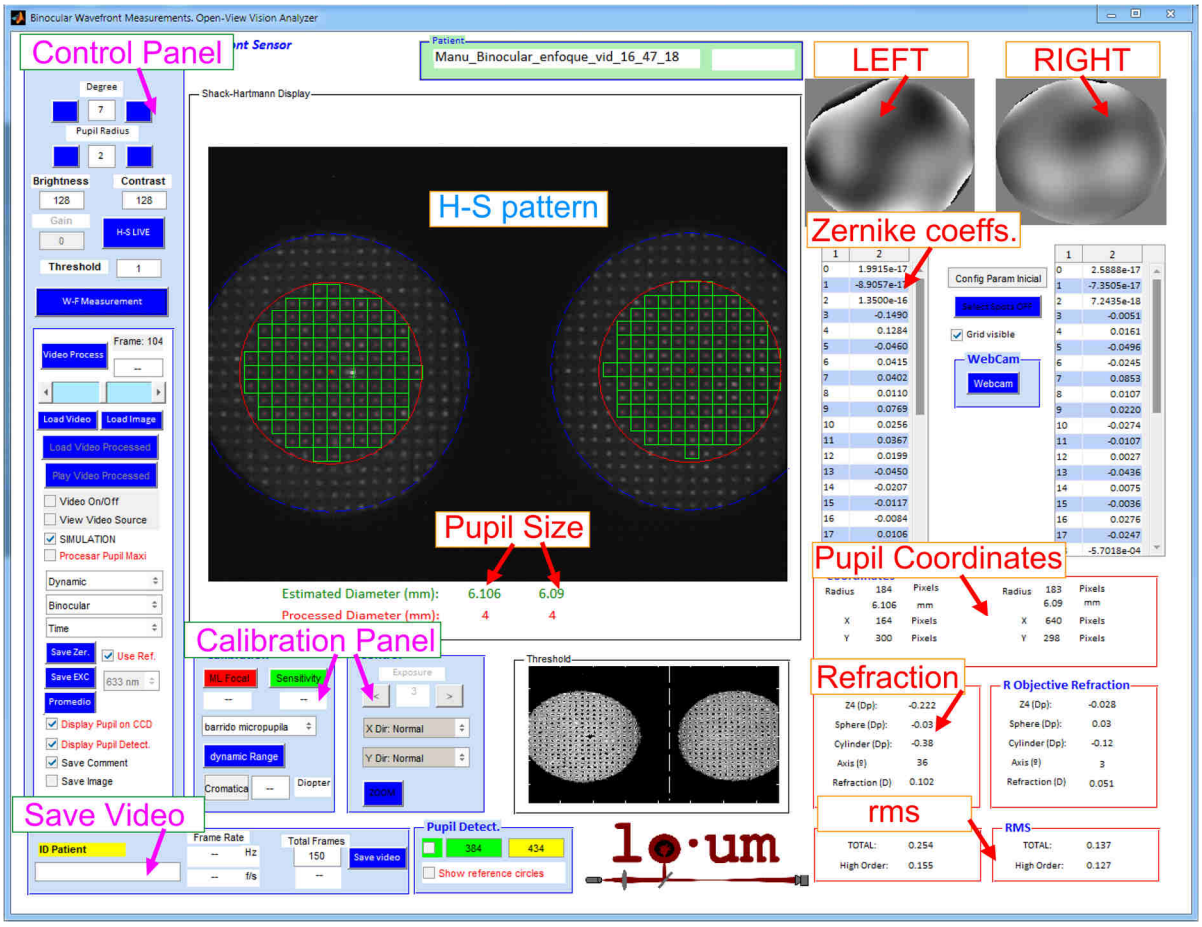

Figure 2.32: Graphic interface of the binocular wavefront analyzer module for data acquisition and off-line H-S processing.

An independent software module controls the stimuli (target shape, position, presentation time, color pattern, luminance and angular size) for visual tasks and can also independently record H-S videos for later processing. A TripleHead2Go external multi-display adapter (Matrox Graphics, Canada) was used to connect two monitors for dual stimulus display to the computer, as an extension of the desktop.

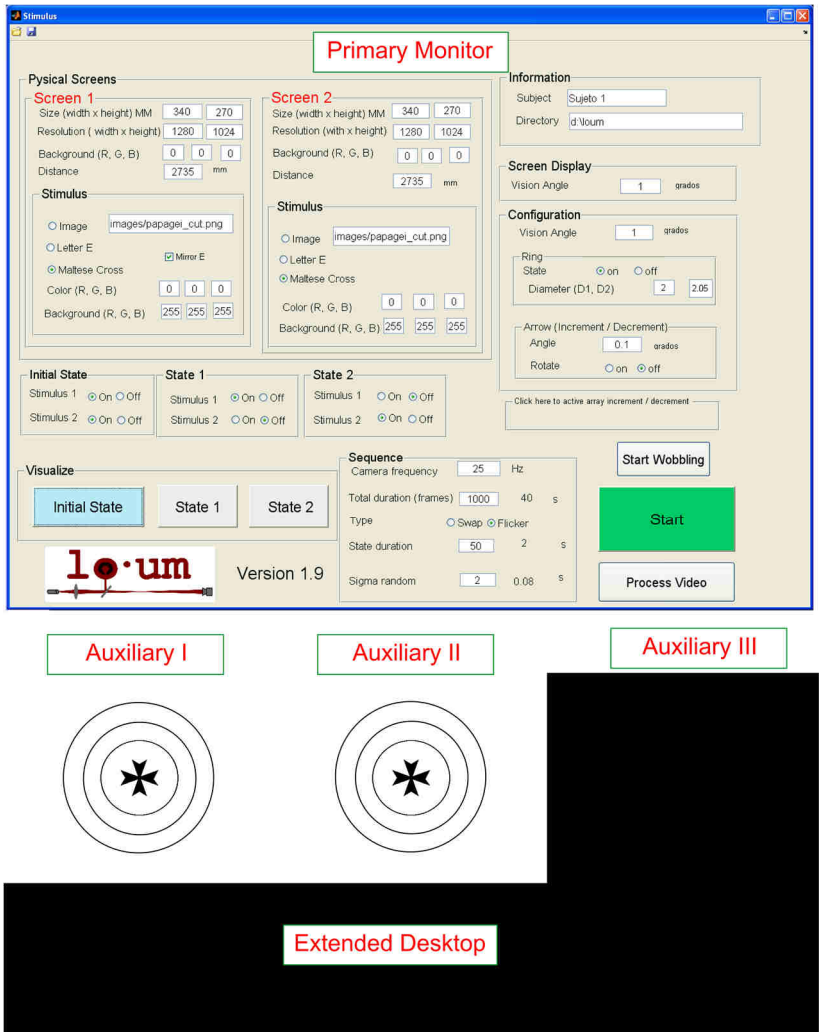

Figure 2.33: Graphic interface of the Stimulus Controller for stimuli display. As an example, Maltese crosses with circular rings are simultaneously shown in both monitors (developed by A. Gambin).

Through the external multi-display adapter, a wide variety of monitors can be connected, depending on experimental requirements. The monitors that we have used and reported in this PhD are a 19-inch LCD DELL 1908FP flat monitor (DELL INC, USA) and an OLED micro-display (SVGA, eMagin, Bellevue, WA, USA). The DELL monitor was used for far stimuli (around 3 m from the subject) and the OLED display for near stimuli (around 30 cm from the subject). Since both monitors have different characteristics (pixel size, resolution, pitch, etc.), conversion parameters maintain the angular size coherent between displays. DELL monitor resolution is 1280X1024 pixels with 26 µm pixel pitch. The OLED has 852X600 pixels with 15 µm pixel pitch and can be used in full color or monochrome mode.

Figure 2.34 shows the OLED and LCD monitor spectra. The normalized OLED white spectrum (top) shows a peak at 505 nm and the spectra for each channel (center) is broad and asymmetric, especially for the G channel, which shows a dual peak structure. The LCD monitor

shows three narrow peaks centered on 480, 546 and 612 nm (Figure 2.34, bottom). The white spectrum presents a normalized narrow white spectrum centered on 546 nm. The chromatic difference of focus of the human eye between 505 and 546 nm, the maximum sensitivity for OLED and LCD respectively, is +0.27 D.

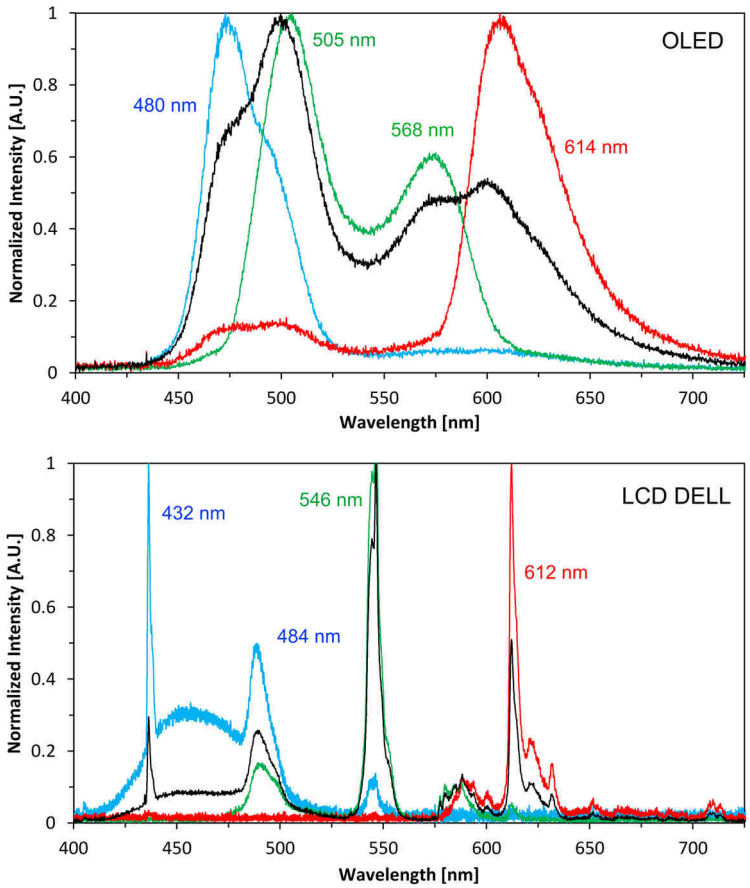

Figure 2.34: Spectrum of the OLED micro-display in polychromatic and monochromatic modes (top) (data collected by C. Schwarz) and RGB spectrum of the LCD Monitor (bottom).

2.9 Binocular Pupil Tracker

One of the main new features in the H-S analyzer software is a module for real-time evaluation of the both pupils' position and size, from the background light on the H-S images. This information is not only useful for future processing but also allows real-time wavefront measurement with the pupil images "floating" on the CCD area. On the one hand, this reduces the requirements for fixing the subject's head. On the other hand, and more importantly, it enables the subject to change fixation across the field of view instead of been restricted to a specific axis. At 1050 nm, part of the beam energy is scattered inside the eye. The backscattered light fills the entire pupil area making the pupil border easy to detect. The algorithm implemented in Matlab uses an automatic threshold function to quantify the background noise and the pupil signal. Once the pupil-to-noise ratio is determined, the algorithm scans the H-S

pattern in order to locate both pupils. Then Matlab's regionprops function analyzes the pupil border more accurately in two separated areas (one for each pupil) of the H-S pattern. This function allows finding objects such as spots of micro-lenses in the detected pupil. Finally, a robust fitting algorithm determines both pupils' diameter and geometric center. This information is then used by the aberration-calculation module to process the spots inside digital pupils of chosen size, centered on the subject's actual pupils.

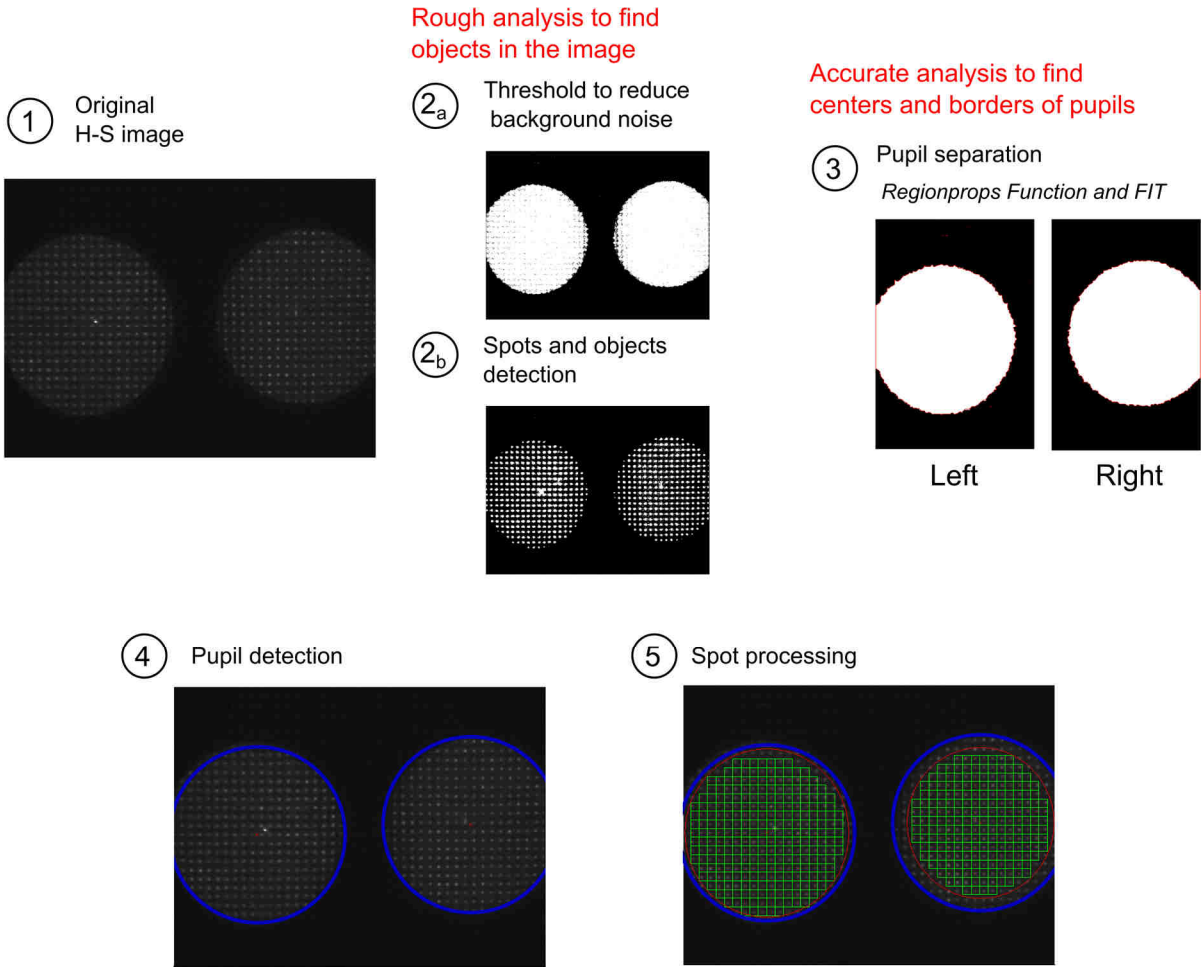

Figure 2.35: Overview of the H-S image analysis, involving binocular pupil tracking and H-S spot processing. The software package processes the H-S image to determine both pupils' diameter and geometric center. The latter parameter in used as a reference point for aberration calculation over measurement pupils of customized size centered on the subject's actual pupils.

2.9.1 Ocular convergence estimation

A change of line of sight between two fixation points at different distances produces rotation of the eyes in opposite direction. Since the pupil is several millimeters in front of the center of rotation of the eye, convergence (or divergence) produces a change in the interpupillary distance, IPD, as represented in Figure 2.36, and thus a pupil displacement on the H-S images proportional to the rotation angle, α.

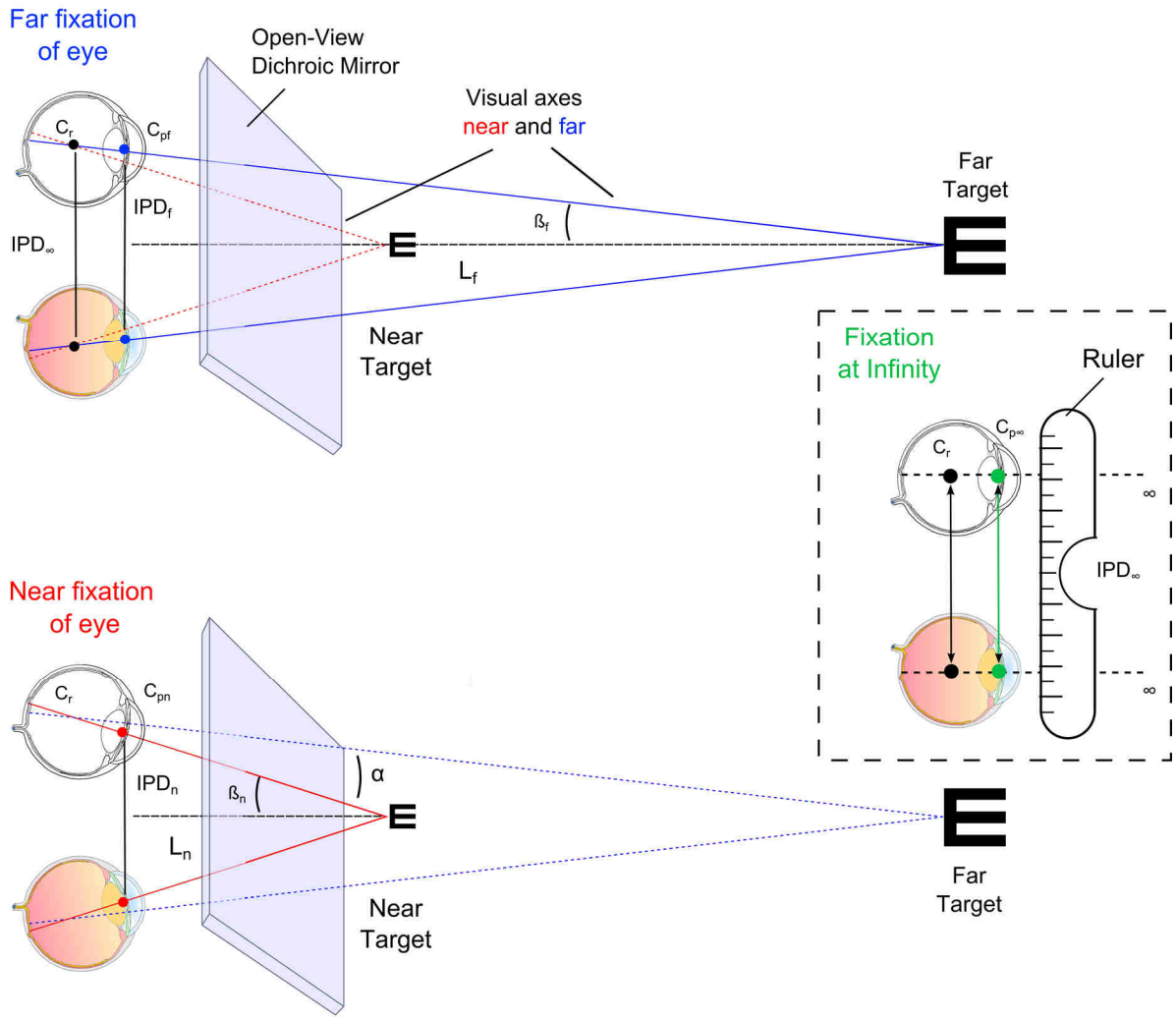

Figure 2.36: Schematics of convergence through the open-view dichroic mirror. L_f and L_n are the distances of fixation to the far and near fixation targets, respectively, IPD_f and IPD_n are the interpupillary distances, β_f and β_n are the vergence angles, and α is the convergence angle between far and near. C_{pn} and C_{pf} represent the center of the pupil and C_r is the center of rotation of the eye, the latter estimated from the interpupillary distance at infinity, IPD_∞ measured with an ophthalmic ruler (see right-hand side inset).

Vergence to a point in front of the subject is the reciprocal of the distance from the eyes to said point. We will use this term when referring to the distance to actual stimuli but it can also be used for fixation points (i.e., where the lines of sight cross each other), whether they coincide with the target or not. Convergence (i.e., the eyes' simultaneous rotation to change of fixation between targets at different distances) could be quantified by the rotation angle, α, but it is more usually expressed in terms of the change in vergence between the initial and final fixation points. As mentioned in the introduction, we will consider convergence as a rotation of both eye toward each other. The units of convergence are typically referred to as 'meter angle' (Pascal, 1955) but, since they are in fact m^{-1}, we will speak about convergence diopters for the sake of clarity when comparing accommodation (changing in focus), vergence (distance to the

object) and convergence (axial change of binocular fixation). As schematized in Figure 2.37 (top), a simple trigonometric relationship can be used to calculate convergence in diopters from the rotation angle, α, and the interpupillary distance:

$$\Delta V\ [D] = \frac{\tan \alpha}{IPD_{\infty}\ /2} \tag{2.5}$$

However, it is important to note that the dual periscope arrangement, used to fit both pupils into a single sensor, prevent absolute measurement of IPD. Instead, we can only obtain relative changes of interpupillary distance, ΔIPD. This parameter, nevertheless, can be used to estimate convergence following a less direct route. As shown in Figure 2.37, the rotation angle, α, can be obtained from ΔIPD using the distance from the center of rotation of the eye, C_r to the apparent center of the pupil, C_{pn} or C_{pf}:

$$\tan \alpha = \frac{d_{Cpf\ Cpn}}{d_{Cr\ Cpf}} = \frac{\Delta IPD/2}{d_{Cr\ Cpf}} \tag{2.6}$$

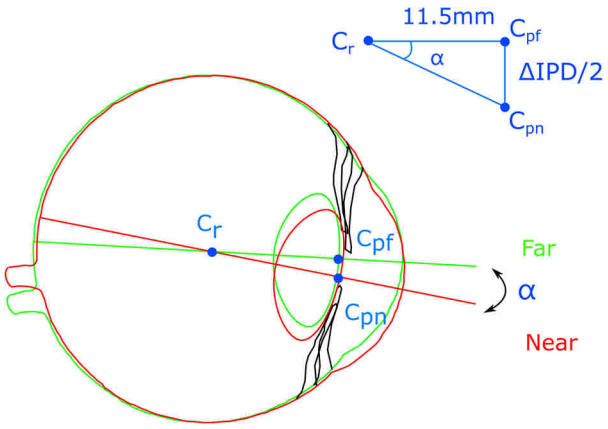

Figure 2.37: Illustration of the shift of the pupil's center due to a change of line of sight from far-to-near. α is the rotation angle between far and near vergences, C_{pf} and C_{pn} are the corresponding pupil's center positions and $dc_{pn}c_{pf}$ is the shift in the pupil's center, which we to take as equal to $\Delta IPD/2$, assuming symmetric pupil displacements.

The position of the center of rotation of the eye, C_r, varies slightly depending on the schematic eye model. From literature, the distance from the cornea to the center of rotation of eye, C_r, is 15 mm (Fry & Hill, 1962) and the distance from the cornea to the anterior face of the lens is 3.5 mm (Thibos et al., 1992) (Atchison & Smith, 2000). Thus, we take the distance from the pupil's center, C_p, to center of rotation, C_r, to be approximately 11.5 mm. By combining Eq.(2.5) and Eq.(2.6) and using 11.5 mm as the distance between center of rotation and center of the pupil, $d_{Cr\ Cpf}$, we can obtain estimates of convergence in diopters as:

$$\Delta V\ [D] = \frac{\Delta IPD}{1.15\ \cdot 10^{-2} \cdot IPD_{\infty}} \tag{2.7}$$

To estimate the relevance of errors in determining interpupillary distance, which is coarsely performed with an ophthalmic ruler, we have calculated the outcome of ±5-mm errors around a typical value of 65 mm. Table 5 and Figure 2.38 show the results. For several target vergences, the change in interpupillary distance, ΔIPD, was isolated from Eq. (2.7) IPD_∞ = 65 mm, and then used to estimate convergence from infinity for IPD_∞ = 60 mm and IPD_∞ = 70 mm using the same equation.

Target Positions, L[m]	Rotation angle β[º] IPD = 65 mm	dC_rC_{pf} [mm]	ΔV IPD = 60 mm	ΔV IPD = 65 mm	ΔV IPD = 70 mm
P1: 3 m	0.621	0.124	0.361	0.333	0.310
P2: 2.5 m	0.744	0.149	0.433	0.400	0.371
P3: 2 m	0.930	0.186	0.542	0.500	0.464
P4: 1.5 m	1.241	0.249	0.722	0.667	0.619
P5: 1 m	1.861	0.373	1.083	1.000	0.929
P6: 0.8 m	2.326	0.467	1.354	1.250	1.161
P7: 0.6 m	3.100	0.623	1.806	1.667	1.548
P8: 0.5 m	3.719	0.747	2.167	2.000	1.857
P9: 0.4 m	4.645	0.934	2.708	2.500	2.321
P10: 0.3 m	6.183	1.246	3.611	3.333	3.095
P11: 0.2 m	9.230	1.868	5.417	5.000	4.643

Table 5: For different target positions, rotation angle from infinity for IPD_∞ = 65 mm, corresponding pupil center displacement (for $d_{Cr\,Cpf}$ = 11.5 mm) and convergence estimates from these latter values using three different values of IPD_∞: 60, 65 (original value), and 70 mm.

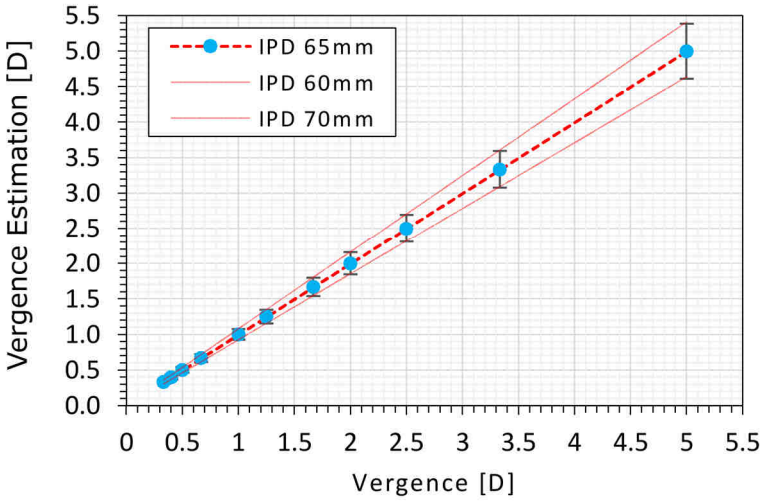

Figure 2.38: Vergence estimate confidence intervals for a ±5-mm confidence interval in IPD_∞ measurement (thin lines and error bars) around IPD_∞ 65mm (thick dotted line and symbols).

As shown in Table 5 and Figure 2.38, errors in IPD_{∞} measurement have low effect for far objects (low vergence values) but, since they are proportional to ΔIPD, they increase as the object becomes closer to the subject. However, a measurement error as big as ±5 mm would represent a misestimating around ±0.3 D for 3.33 D stimulus vergence (object at 30 cm), which is the highest vergence used in this work.

3 Instrument validation

As a first validation of the complete instrument, we performed measurements of defocus (accommodation), high-order aberrations, pupil size and interpupillary distance (convergence) in a small group of normal subjects accommodating to a stimulus placed at different vergences. The target was aligned axially with the dominant eye and was viewed under natural binocular vision.

3.1 Protocol

Measurements were performed in five normal subjects aged of 29 ± 5.9 years. One of the participants (subject Ml) wore a refractive correction (spectacles) of -1.5 D. Table 6 gives the ocular data obtained under binocular vision for a far stimulus (vergence of 0.33 D) through H-S measurements for a 4-mm-diameter pupil. Mean sphere was -0.04 ± 0.19 D and -0.22 ± 0.17 D, and mean cylinder was -0.51 ± 0.21 D and -0.39 ± 0.07 D, for DE and NDE respectively. The real (as opposed to apparent on the H-S images) interpupillary distance was measured using an ophthalmic ruler with an accuracy of ± 2 mm when the subjects were looking at infinity.

Subject	Age (Y)	Real IPD [mm]	Eye	Sphere [D] x Cylinder [D]	axis [º]
MA	28	60	OS	-0.05 x -0.33	8.6º
			OD *	-0.23 x -0.24	17.2º
ML	22	60	OS	-0.39 x -0.41	38.8º
			OD *	0.18 x -0.56	28.3º
JM	25	65	OS *	0.02 x -0.48	38.7º
			OD	-0.33 x -0.31	34.4º
AP	32	64	OS *	0.08 x -0.82	31.8º
			OD	-0.03 x -0.48	25.4º
AM	38	64	OS	-0.32 x -0.40	4.5º
			OD *	-0.23 x -0.45	6.7º

Table 6: Age, IPD, and objective refraction for the subjects in this study.

The stimulus consisted of a black Maltese cross over a white background, displayed on an OLED micro-display (eMagin, USA) at near distances or on an LCD monitor for far vergence. The luminance level was 20 ± 5 cd/m^2 for the OLED and for the LCD. The target was aligned with the line of sight of the dominant eye (asterisk on the Table 6) and the size of the stimulus was changed with position in order to maintain an angular size of 0.5º. Measurements were performed at 13 positions from 0.25 m to 2.75 m (see target vergence on Figure 3.1).

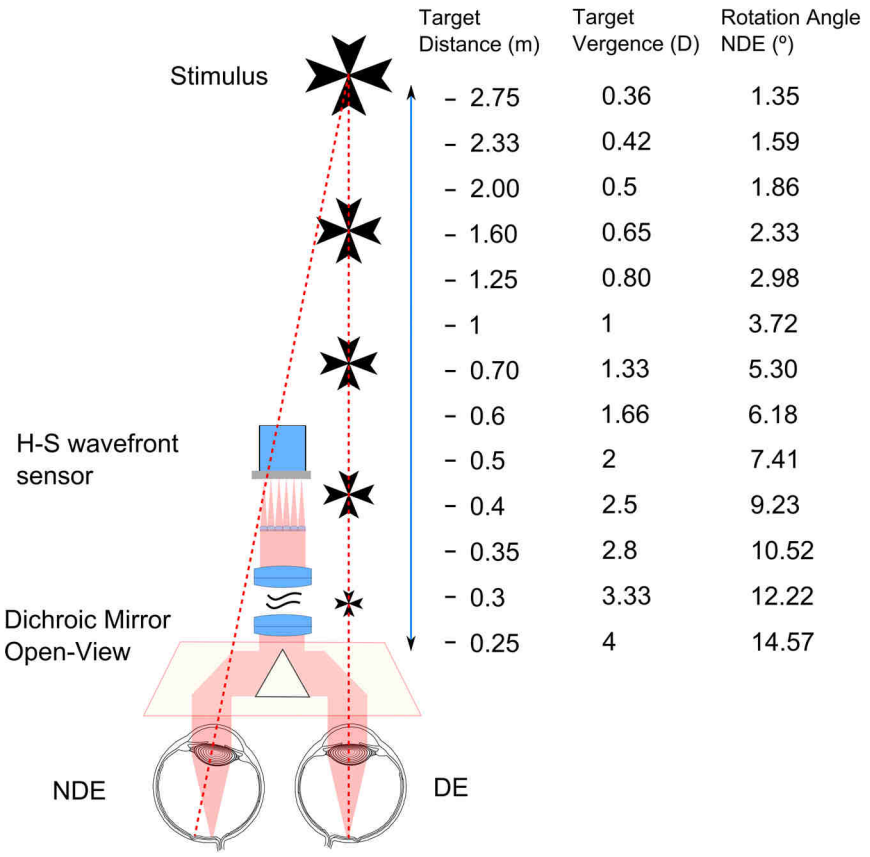

Figure 3.1: Schematic draw of the experimental set-up. Rotation angle corresponds to a standard value IPD = 65 mm. OLED display was used for distances ranged between 0.25 m and 1.60 m. LCD display was used for the rest of positions (far targets).

Data analysis

Three video sequences of 20 frames were recorded for each target vergence. Accommodation was analyzed by means of the spherical equivalent obtained from the defocus Zernike coefficient (C_2^0) (see section 1.6). The apparent interpupillary distance was measured on the sensor to analyze convergence. Binocularly, the non-dominant eye rotated nasally to realize the complete convergence since the dominant eye was aligned with the target, as illustrated on Figure 3.1. The position and size of the pupils were tested on each frame of the video sequence by use of a parallel algorithm in order to find and discard inconsistent data that could alter the estimate of convergence, accommodation and pupil size.

3.2 Experimental outcomes

Figure 3.2 plots the data obtained in the dominant eye (except for IPD) as a function of stimulus vergence under steady accommodation. H-S images were processed at a pupil of 4.5 mm of diameter for subjects Ma, Ml and Am. Subjects Jm and Ap had smaller natural pupils when accommodating to a near object and, therefore, a 4-mm pupil was used instead. This change is

not relevant because its impact in refraction should be small and only individual analysis was performed for other aberrations.

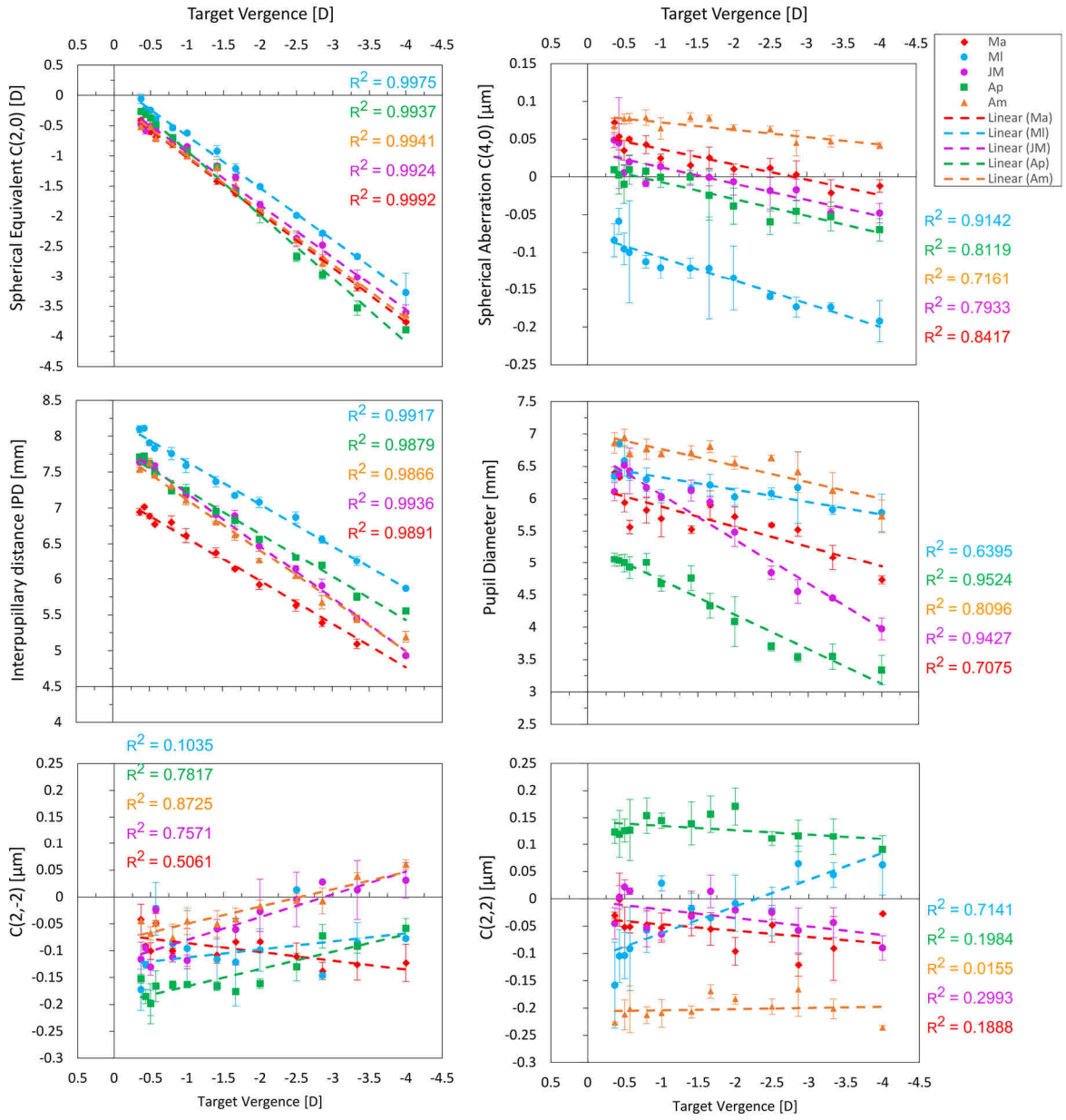

Figure 3.2: Data for steady accommodation: Spherical equivalent, SE_2 (top left), spherical aberration, $C_4^{\,0}$ (top right), astigmatisms, C_2^{-2} and $C_2^{\,2}$ (bottom left and right respectively), and pupil diameter (center right) of the dominant eye, and interpupillary distance, IPD (center left), for a range of stimulus vergence in five normal subjects. Each color corresponds to an individual. Error bars are standard deviation across repetitions. Dotted lines are regression lines with their respective R^2 value.

Accommodation and pupil size

Spherical equivalent (Figure 3.2, top left) shows a linear behavior from far to near following the stimulus position for all subjects, although there is a high inter-subject variability.

For low dioptric demand, accommodation is performed accurately. At near distances the spherical equivalent values do not coincide with the stimulus vergence indicating that subjects tend to underaccommodate (Schaeffel, Wilhelm, & Zrenner, 1993) (Charman, 1999) (He, Burns, & Marcos, 2000) (Plainis et al., 2005) (Seidemann & Schaeffel, 2003) (Kasthurirangan, Vilupuru, & Glasser, 2003) except for one subject. Accommodation of subject Ml (Blue data) follows also a linear tendency somewhat far from the rest of the participants. This could be explained by the fact that this subject was wearing glasses with a slightly under-correction, becoming slightly hyperopic. Excluding this subject, accommodation coincides on average with the stimulus vergence at about |0.8| D (Toates, 1972) (Plainis et al., 2005). A lag of accommodation of -0.36 ± 0.23 D was found for a target at 25 cm (i.e., 4 D).

The pupil size (center right panel) exhibited a linear decrease with increasing accommodation and high inter-subject variability. Pupil size ranged between 7 and 5 mm approximately for far and between 6 and 3.5 mm for near. The pupil constriction (miosis) was 1.44 ± 0.60 mm on average at 4 D.

Spherical aberration and astigmatisms

Figure 3.2 shows the changes of spherical aberration (top right panel) and astigmatism (bottom, right and left panel) with accommodation. A systematic negative shift of spherical aberration with accommodation was observed, a trend consistent with previous results (Atchison, Collins, Wildsoet, Christensen, & Waterworth, 1995) (He et al., 2000) (Ninomiya et al., 2002) (Cheng et al., 2004) (Plainis et al., 2005) (Li, Choi, Kim, Yu, & Joo, 2011). Although slightly less pronounces than that found in large population studies (Cheng et al., 2004), the decrease in spherical aberration between far (0.33 D) and near (4 D) accommodative states was statistically significant (p-value < 0.05).

Concerning Zernike coefficients, C_2^{-2} and $C_2{}^2$, a slight positive trend with accommodation was observed but the variation was relatively small and it was not statistically significant (p-value = 0.94 and 0.53 for C_2^{-2} and $C_2{}^2$ respectively). In two subjects, MA and JM, astigmatisms coefficients exhibited a linear decrease with accommodation.

Interpupillary distance: convergence

The apparent interpupillary distance IPD, measured on the sensor in millimeters, showed a linear decrease with stimulus vergence for each subject (Figure 3.2, center left). Using as a reference the vergence for the furthest stimulus position considered, the relative changes of convergence were calculated from the interpupillary values obtained between each target position (see section 2.9.1). Figure 3.3 plots the relative changes of convergence as a function of the accommodation for each individual (left) and the mean values of convergence (blue dotted line) and accommodation (red dotted line) on average as a function of the target vergence (right).

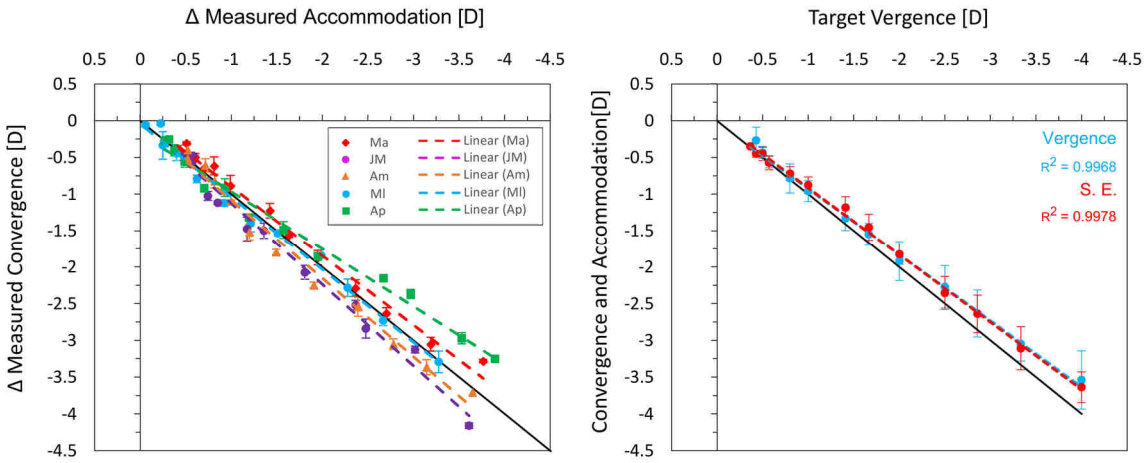

Figure 3.3: Left: Convergence as a function of accommodation, both parameters relative to the furthest stimulus position. Each color corresponds to an individual subject. Right: mean accommodation (red) and mean convergence (blue) as a function of target vergence. Error bars represent standard deviation across subjects.

Figure 3.3, left, shows good linear trend between accommodation and convergence. However, the slope varies among subjects and it is not always close to 1: while subject AP presented an apparent under-convergence, subject JM seemed to over-converge. This behavior could be an artifact: As described in section 2.9.1, an erroneous measurement (some millimeters) of the real interpupillary distance IPD_{∞} could induce a slight convergence offset, increasing linearly with the stimulus vergence (see Figure 2.38). Or it could be real: e.g., the so-called Panum's fusional area, allows fusion without perfect convergence. Despite the variability among subjects, Figure 3.3, right, shows that the mean values of convergence (blue symbols and line) and accommodation (red symbols and line) where similar to one another and showed consistent similar linear trends. These results can be taken as a validation of the use of the binocular pupil tracker to estimate convergence from an offset version of interpupillary distance on H-S images. Table 7 summarizes the coefficient of determination R^2 between convergence and accommodation for each individual subject and for mean values.

	Convergence [mm]	Accommodation [D]
R^2 [MA]	0.989	0.999
R^2 [ML]	0.991	0.997
R^2 [JM]	0.994	0.992
R^2 [AP]	0.988	0.993
R^2 [AM]	0.986	0.994
R^2 Average	0.996	0.997

Table 7: Coefficient of determination, R^2, between convergence and accommodation for each Individual subject and for mean values.

Aberrations with rotation of eye (NDE vs. DE)

Figure 3.4 plots the spherical equivalent and spherical aberration in the dominant eye (left panel) and the non-dominant eye (right panel), as a function of target vergence. Since the target was always aligned with the DE, the NDE accomplished the total convergence for each stimulus vergence and the corresponding rotation angle ranged between 1.35º for far (0.36 D) and 14.57º for near (4 D). This rotation produced a misalignment of the NDE with the H-S instrument that could affect wavefront measurements. Data from each eye was compared with one another in order to determine the experimental limit for the rotation angle and, hence, for vergence. SE (Figure 3.4, top) exhibited a linear decrease in both eyes. However, for target vergences of -3.5 D and closer, increasing discrepancies can be observed between the SE measured in the DE (Figure 3.4, top, left) and in the NDE (Figure 3.4, top, right). This vergence value involved a rotation of the NDE around 12.5º, which we take as an upper limit for individual eye rotation. When convergence is balanced between both eyes, i.e., the stimuli is aligned with the H-S axis, this limit stands for rotation of eye 6º, well below the limit value. The spherical aberrations (Figure 3.4, bottom) showed a similar negative shift in both eyes on average with no apparent effect of rotation of NDE, maybe due to low value.

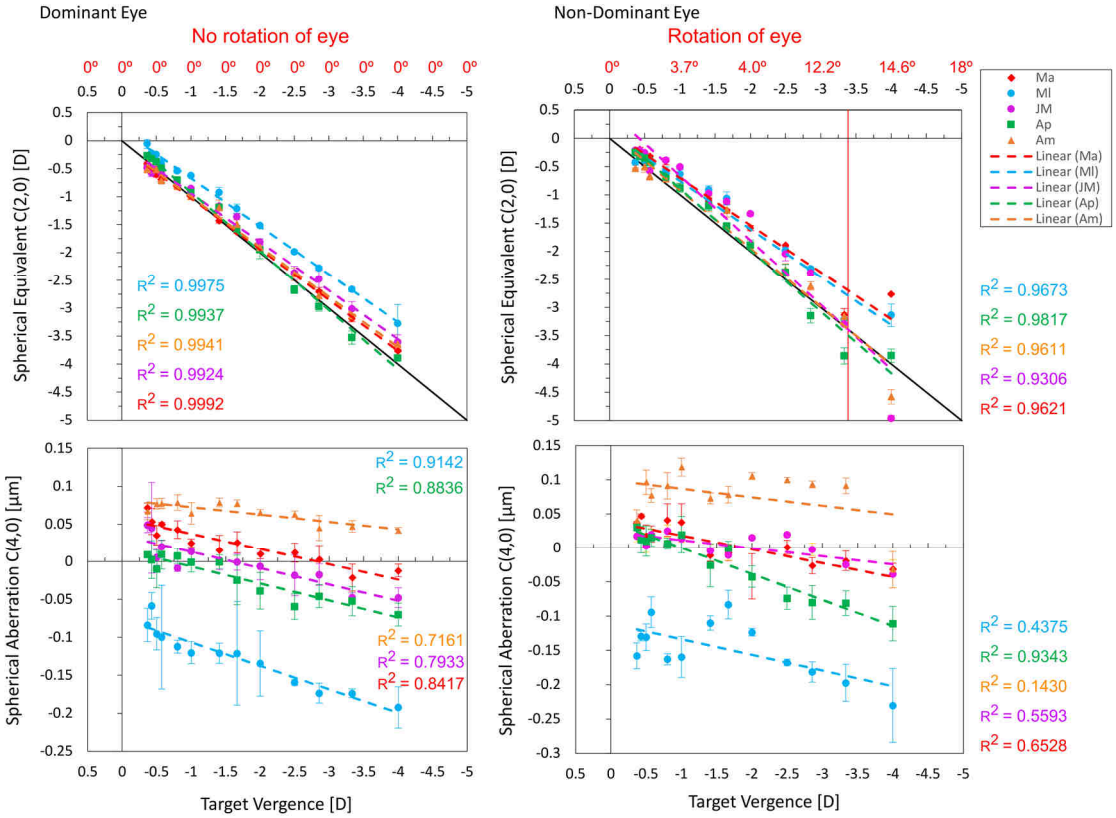

Figure 3.4: Spherical equivalent (top) and spherical aberration (bottom) as a function of target vergence in the DE (left panel) and the NDE (right panel). Error bars show the standard deviation across subjects. The corresponding angle of rotation for each eye is in red above the vergence values.

Figure 3.5 plots vertical and horizontal coma, $C_3^{\ 1}$ and C_3^{-1}, astigmatism, $C_2^{\ -2}$ and RMS of high-order aberrations as a function of target vergence. No clear general trend was observed for coma or astigmatism but they presented high inter-subject variability in both eyes. Some subjects have shown an increase with accommodation (Cheng et al., 2004) (Plainis et al., 2005) while others found a steady behavior. The RMS of High-Order aberrations RMS H-OA exhibited a positive trend with accommodation in both eyes, in agreement with literature (Cheng et al., 2004).

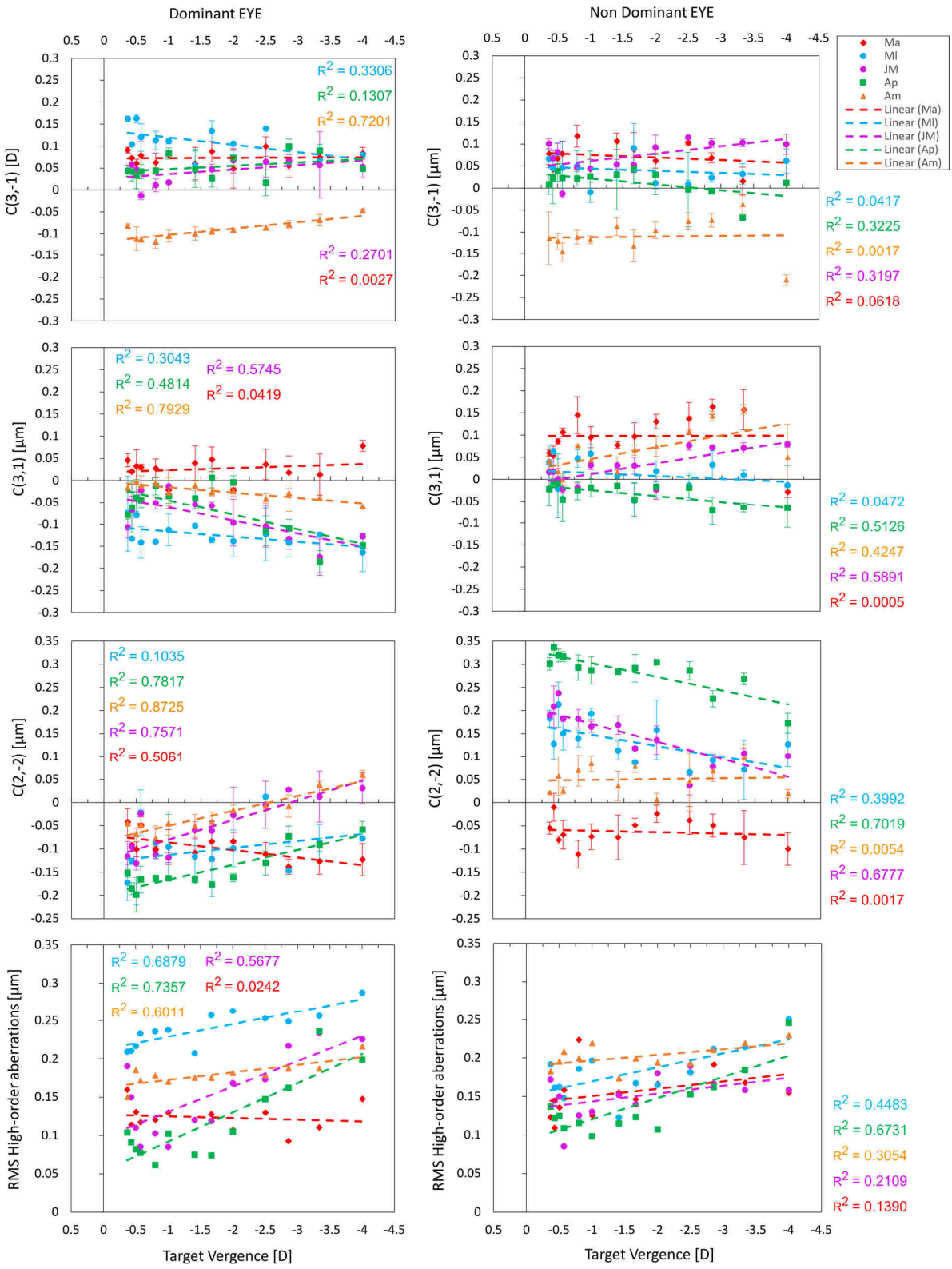

Figure 3.5: Examples of individual aberrations and high-order RMS as a function of target vergence in the dominant eye (left) and the non-dominant eye (right). Each color corresponds to a different individual. The error bars show the standard deviation across subjects.

3.3 Interpretation

In this experiment, we tested the binocular H-S wavefront sensor in open-view configuration. Refraction, pupil size, convergence and monochromatic aberrations were measured under steady-state of accommodation in five normal subjects for a range of stimulus vergences. The ability of a single sensor to perform accurate binocular measurement of accommodation combined with a binocular pupil tracker and in open-view configuration has been validated.

Accommodation (in terms of ocular refraction quantified by SE) showed a linear behavior from far to near following the target vergence (He et al., 2000) (Seidemann & Schaeffel, 2003) (Plainis et al., 2005). At low dioptric demand, accommodation was performed accurately, but at a near distances the SE did not reach vergence and subjects showed a lag of accommodation of -0.36 D on average for 4 D demand, in agreement with literature (Schaeffel et al., 1993) (Charman, 1999) (He et al., 2000) (Hazel, Cox, & Strang, 2003) (Kasthurirangan et al., 2003). Accommodation was on average in agreement with the stimulus vergence below |0.8| D. Pupil size decreased linearly with accommodation and presented high inter-subject variability (Plainis et al., 2005).

A systematic negative shift of spherical aberration with accommodation was observed in each individual subject (Drexler, Baumgartner, Findl, Hitzenberger, & Fercher, 1997) (Roorda & Glasser, 2004) (Plainis et al., 2005). Although the amount of spherical aberration varied across subjects, a similar linear decrease was observed in both eyes for each subject. Astigmatism Zernike coefficients exhibited a positive trend with accommodation although the changes were relatively small. Monochromatic aberrations showed trends in agreement with literature.

Interpupillary distance, IPD, showed a decreasing linear behavior from far to near as a function of target vergence. Relative changes in convergence estimated from IPD were similar to relative changes in accommodation on average over the studied range of stimulus vergence, although some subjects presented over and under convergence. The standard deviation of accommodation and convergence were of the same order of magnitude on average. The use of the IPD to estimate convergence is a reliable technique that allows a more simplistic optical design and can be a good alternative to other techniques such as Purkinje image recording. However, the reliability of convergence measurements depends on the initial IPD measurements with an ophthalmological ruler.

For a stimulus aligned with the DE, accommodation in the NDE (misaligned with the H-S instrument) coincides with accommodation in the DE for rotation angles below 12.5º. When both eyes contribute to convergence, this angle corresponds to an object located at 14.7 cm on the axis midway between the two pupils. Therefore, the instrument can be used for stimulus vergences below 6D.

The viability of the open-view sensor to perform accurate binocular measurements of accommodation, convergence, pupil size, and monochromatic aberrations, makes the instrument

a promising tool for studying binocular and monocular vision function and dynamics response when visual tasks are performed in realistic viewing conditions.

Experiments

4 Dynamics of accommodation responses

The dynamics of accommodation responses involved in a near accommodation task, known as the near triad, have been usually investigated separately and few instruments have been developed for the measurement of at least two of the responses (Cornsweet & Crane, 1970) (Cornsweet & Crane, 1973) (Heron et al., 1989) (Okuyama et al., 1993) (Suryakumar, 2005) (Suryakumar et al., 2007a). More recently, mechanism of accommodation has been studied under natural viewing conditions (Kobayashi et al., 2008).

The purpose of this experiment is to analyze the dynamics of accommodation responses between two accommodative states from far-to-near under natural viewing conditions.

4.1 Experimental procedure

Measurements were performed in 8 healthy young subjects (mean age of 27.8 ± 2.4 years). The dominant eye (DE), determined by Miles test (Miles, 1929), was the right eye (OD) for five subjects and the left eye (OS) for the other three. Refraction was determined through H-S measurements. The refractive state was of -0.48 ± 0.25 D for far fixation (2.75 m) under binocular vision. The mean cylinder was of -0.41 D ± 0.22 D. The IPD for each subject was measured with an ophthalmic ruler. Table 8 shows the individual data.

Subject	Real IPD [mm]	Age (Y)	Eye	SE [D]	Sphere [D] x Cylinder [D]	Axis [º]
I	60	27	OS	-0.39	-0.22 x -0.34	162.7
			OD *	-0.46	-0.32 x -0.28	31.3
II	63	26	OS	-0.26	0.08 x -0.67	159.5
			OD *	-0.38	0.01 x -0.75	12.5
III	60	32	OS	-0.69	-0.56 x -0.26	141.3
			OD *	-0.53	-0.42 x -0.23	148.7
IV	64	28	OS	-0.22	-0.04 x -0.36	180.0
			OD *	-0.21	-0.01 x -0.39	7.9
V	66	30	OS	-0.72	-0.53 x -0.37	23.6
			OD *	-1.0	-0.82 x -0.36	171.3
VI	64	28	OS *	-0.23	-0.10 x -0.24	164.4
			OD	-0.39	-0.23 x -0.33	6.1
VII	63	28	OS *	-0.43	-0.05 x -0.75	116.7
			OD	-0.29	-0.06 x -0.48	14.6
VIII	65	24	OS *	-0.62	-0.57 x -0.29	139.2
			OD	-0.60	-0.51 x -0.18	168.3

Table 8: Data of the subjects in this study.

To induce the accommodative process, two stimuli generators were placed at 2.75 m and 30 cm in front of the subject's eyes, aligned with a point midway between the subject's two

pupils, and visible in open-view field through the dichroic hot mirror. Rotation angle of eyes was about 6º, well below the experimental limit. Figure 4.1 illustrates the experimental set-up. The far stimuli generator was a flat LCD monitor (Dell, USA) and the near one was an OLED micro-display (eMagin, USA). Figure 2.34 in section 2.8 depicted the normalized spectrum of both displays. In both cases, the stimuli consisted of a black Snellen E letter (1.3º apparent size) displayed on a white background circle. The white spectrum of OLED and LCD monitors was centered on 505 nm and 546 nm, respectively. This wavelength shift is suspected to produce a chromatic difference of focus of 0.27 D due to ocular LCA. The light level was adjusted in both devices to be 15 cd/m^2. Linear polarizers were used to provide high contrast of the target on both displays. Both targets were simultaneously displayed through the measurement sequence.

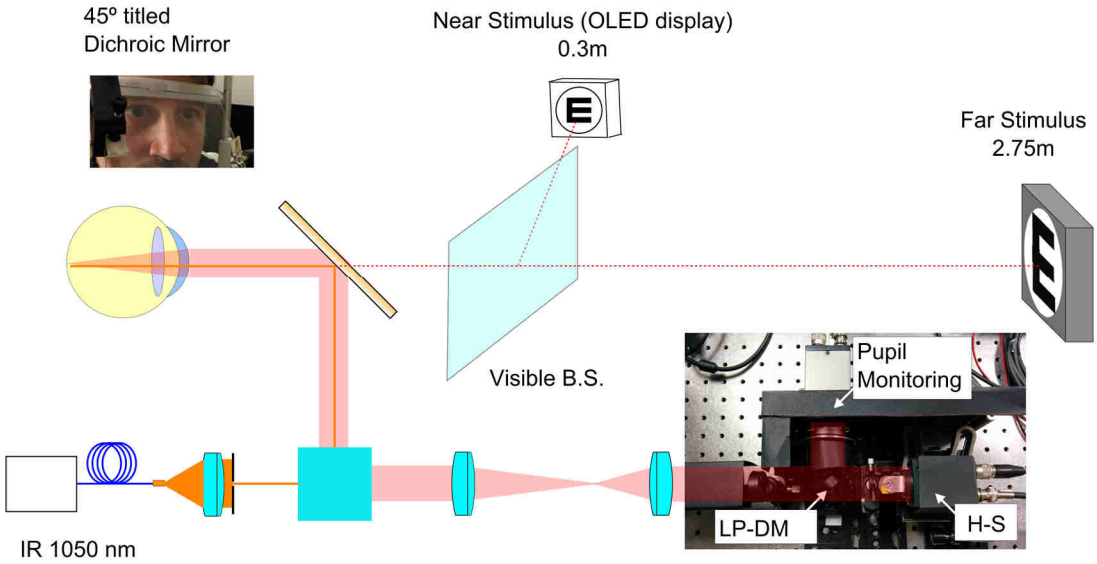

Figure 4.1: Lateral view of the instrument illustrating the two-level configuration. The far (Dell Monitor, 2.75 m) and near (OLED micro-display, 30 cm) visual targets are located in the line of sight of the subjects, aligned with a point midway between the two pupils' eyes. A visible-range beam splitter separate the far and near line of sight by transmission and lateral reflection respectively.

The near stimulus was observed by reflection on the 45º-tilted vertical beam splitter BS (45 R/55 T in the visible spectrum) located at 20 cm in the line of sight in front of the dichroic mirror. The subjects were instructed to perform voluntary far-to-near accommodation a couple of seconds after a sound signal announcing the beginning of the recording sequence. Measurements were performed under binocular conditions and for monocular vision with the dominant eye (DE) and with the non-dominant eye (NDE). Three ten-second sequences for each condition were recorded at 25 Hz. For monocular testing, a blocker was placed 15 cm in front of the dichroic mirror to hide the targets from the fellow eye while allowing measurement in both eyes. Subjects were not trained before the experiments given that the field of view was realistic and no complex task was required. Accommodation was natural and voluntary.

Data analysis

The grid of micro-lenses centered on each pupil was processed at a selected diameter. Series of wavefront aberrations were estimated for each eye off-line. The accommodation response was quantified by means of the second-order spherical equivalent SE_2 (see section 1.6). The H-S images were processed for a pupil of 4-mm diameter.

In order to quantify the temporal dynamics of accommodation two methods were used. First, in order to obtain results readily comparable with previous studies, accommodation time was analyzed by means of an exponential function (Beers & Van Der Heijde, 1994) (Yamada & Ukai, 1997) (Kasthurirangan et al., 2003) (Bharadwaj & Schor, 2006):

$$y = y_0 - a * (1 - e^{-(t/\tau)}) \tag{4.1}$$

where y is the accommodation state in diopters as a function of time, t, y_0 is the initial value of accommodation, a is the amplitude of the accommodative response, and τ is the time constant, which corresponds to the interval required to produce 63 % of the accommodative response. Figure 4.2 shows examples of exponential fitting of the accommodation responses for three subjects in binocular and monocular conditions from far-to-near. The use of this functional form allowed a first order approximation of the accommodation trace. For binocular conditions, the exponential fitting was generally good. On the contrary, monocular accommodation did not always resemble an exponential form in several cases, and fitting was poorer.

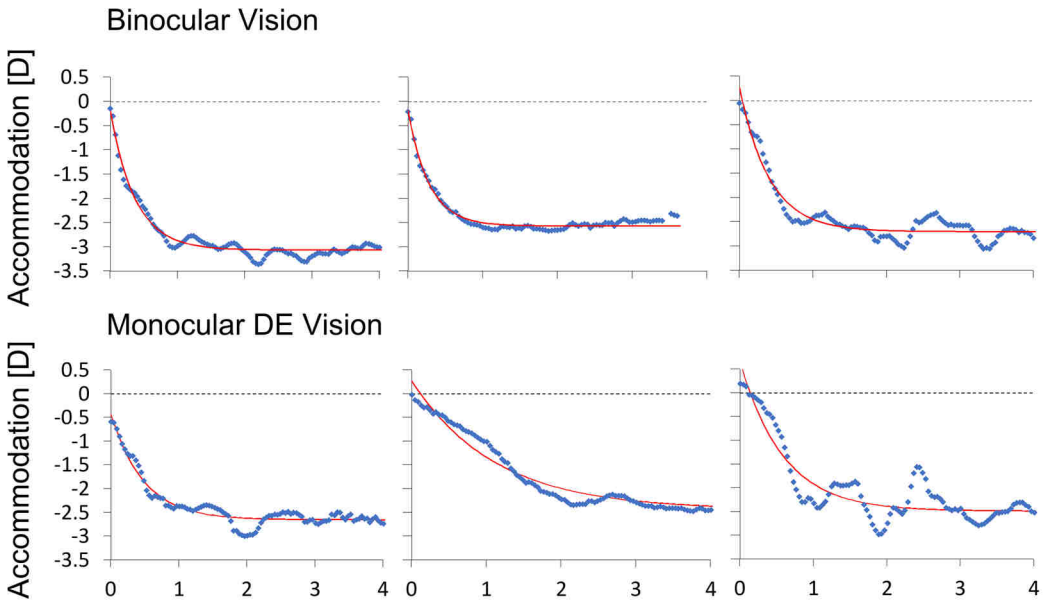

Figure 4.2: Examples of exponential fitting to the temporal responses of accommodation in three subjects in binocular (top row) and monocular vision (bottom row). Blue dots: experimental data; red line: fitting. The point corresponding to the onset of accommodation was manually determined.

Although the exponential fitting is convenient for studying accommodation dynamics, it does not correctly modeled convergence and pupil miosis. Therefore, in order to study the dynamics of the three mechanism, we computed the transition time for each process as the interval between two thresholds: average steady state for far minus standard deviation, and average steady state for near plus standard deviation. Both steady state values were calculated by averaging at least 2-second intervals at the beginning or the end of the 10-s sequences. Figure 4.3 depicts an example for time determination with the threshold method.

Convergence induces a rotation of both eyes in nasal direction. Therefore, the interpupillary distance (IPD) decreases. Due to the adjustable double periscopic system used to fit both eyes inside a single sensor, the distance between pupils that we obtained was an arbitrarily offsetted version of IPD, which we will denote oIPD. Although it cannot be used in absolute terms, oIPD is used to study convergence dynamics. Moreover, since the periscopic system remains unaltered throughout the experiment for each subject, the relative change in oIPD, ΔoIPD, is equal to the change in IPD. From this value, an estimate of the change in convergence can be obtained which involves the distance from the pupil to the eye's center of rotation, R, and the actual IPD (see details in section 2.9.1).

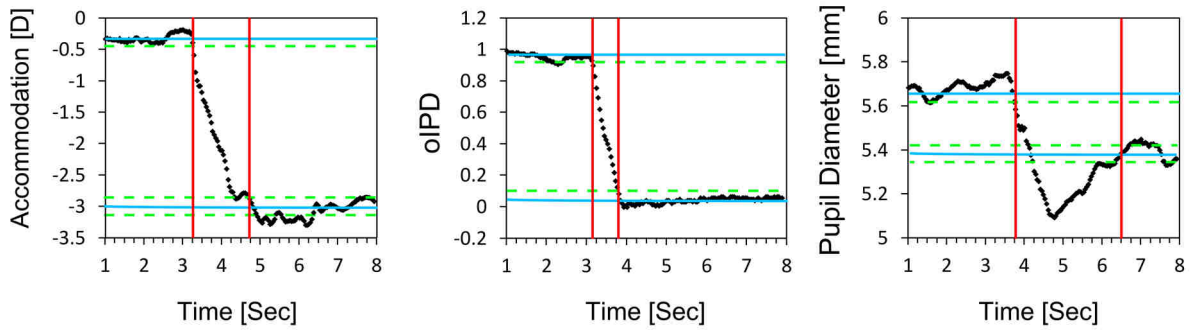

Figure 4.3: Example of threshold-based transition time evaluation used to quantify the temporal responses of each process of the near triad: accommodation (left), convergence from the relative interpupillary distance IPD (center) and pupil constriction (right). Black dots: experimental data; blue lines: steady state level for far and near; green dotted lines: threshold values corresponding to average ± standard deviation; and the red dashed lines demarcate time.

A standard value of 11.5 mm was used for R and an ophthalmic ruler was used to measure the actual IPD_{∞} for each subject when looking at the farthest distance binocularly.

4.2 Temporal dynamics of accommodation responses

As examples, Figure 4.4, Figure 4.5, and Figure 4.6 show the dynamics of near responses for three of the subjects under binocular (left), DE monocular (center) and NDE monocular (right) viewing conditions, all of them with right dominant eye OD. They are subjects I, II and IV on Table 8.

All three processes show a faster temporal response under binocular viewing conditions compared to the monocular cases. By use of the threshold method, convergence (estimated from interpupillary distance) is the fastest process, taking on average 0.80 ± 0.17 s, while accommodation takes 1.22 ± 0.28 s on average. As an example, for a threshold sets to 90 % of its initial value, accommodation time is 0.58 ± 0.25 s and convergence is 0.40 ± 0.14 s. An accommodative overshoot combined with a decrease of the accommodation slope (velocity) at the end of accommodation explain mainly this time difference when the threshold is changed.

Under monocular DE and NDE, both convergence and accommodation exhibit a similar temporal response. Accommodation takes 2.20 ± 0.67 s and 2.22 ± 0.58 s on average for DE and NDE respectively, while convergence takes 2.27 ± 0.80 s and 2.10 ± 0.69 s. The slopes of both responses decrease compared to the binocular case, which implies a velocity reduction of the accommodative process. The pupil constriction (miosis) shows the slowest temporal response with high inter-subject variability and greater fluctuations. The miosis amplitude is stronger under binocular vision about 0.80 ± 0.36 mm compared to monocular DE and monocular NDE vision: 0.61 ± 0.26 mm and 0.66 ± 0.40 mm respectively.

The use of an exponential function provides a time constant τ that it is not dependent of a given threshold, providing readily comparable to those in the literature. The time constant of accommodation was 0.28 ± 0.10 s, 0.55 ± 0.32 s and 0.52 ± 0.33 s under binocular, monocular DE, and monocular NDE vision respectively. These values are significantly lower than those estimated with the threshold method and comparable to those obtained in the literature with a similar type of analysis (Shirachi et al., 1978) (Yamada & Ukai, 1997) (Kasthurirangan et al., 2003). However, this method is not suitable to analyze convergence and pupil miosis given that they do not follow always an exponential curve.

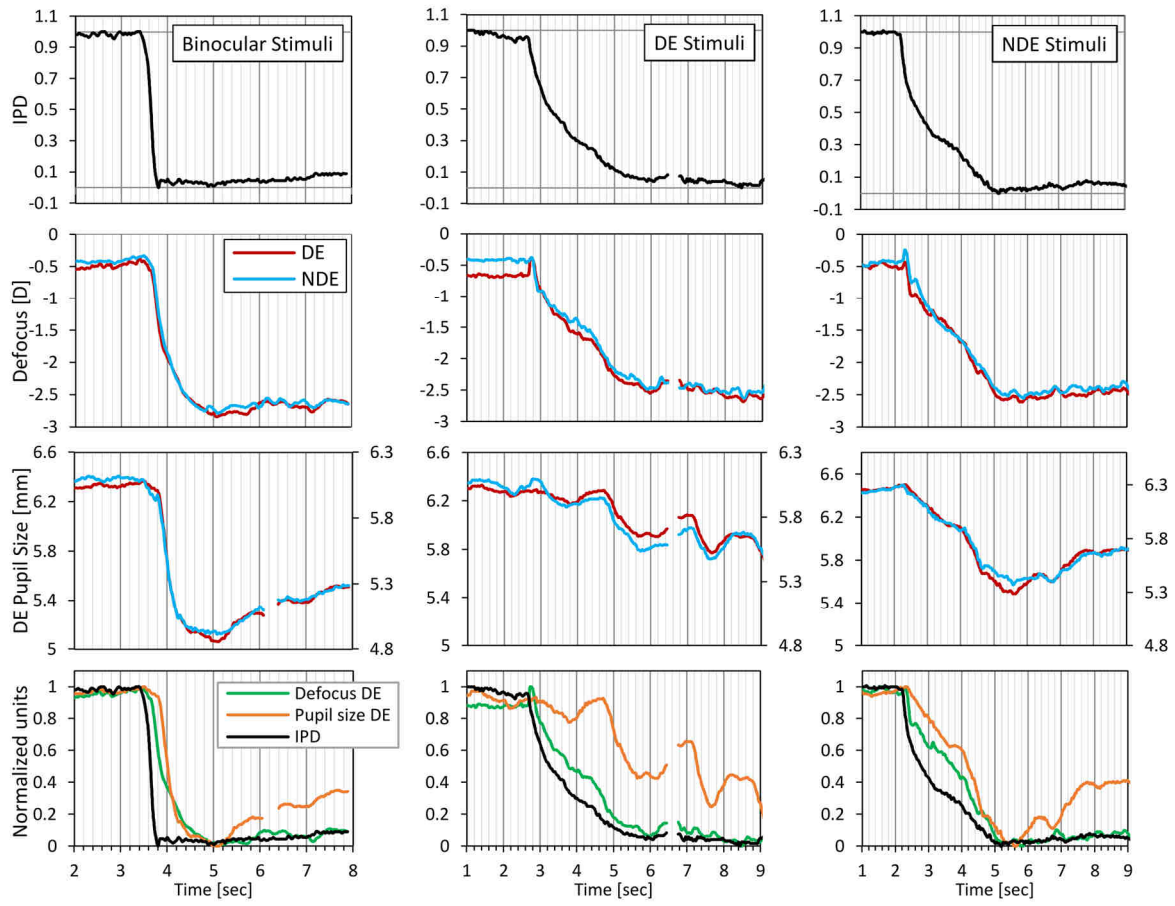

Figure 4.4: Responses of interpupillary distance, accommodation and pupil diameter as a function of time under binocular (left), monocular DE (center) and NDE (right) for subject I with right dominant eye. Top row: normalized relative interpupillary distance IPD. Center row up: Second-order spherical equivalent. Center row down: Pupil Diameter. Bottom row: Normalized comparison of the three responses.

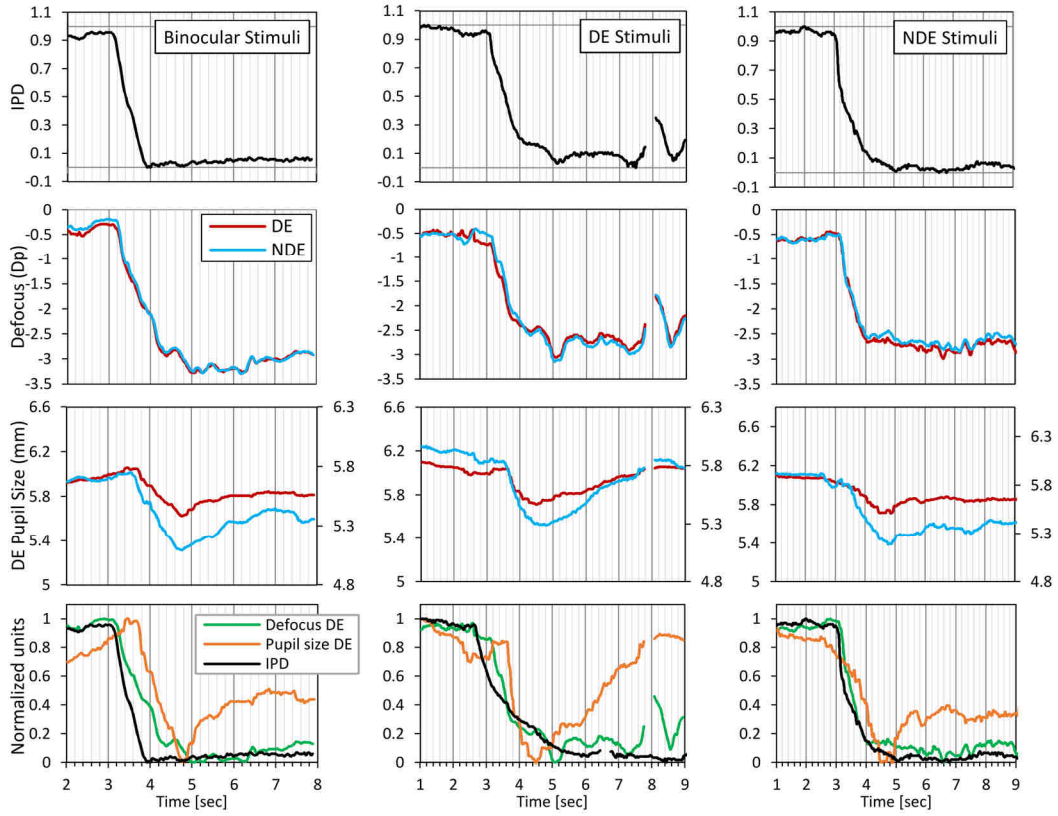

Figure 4.5: Id. Figure 4.4

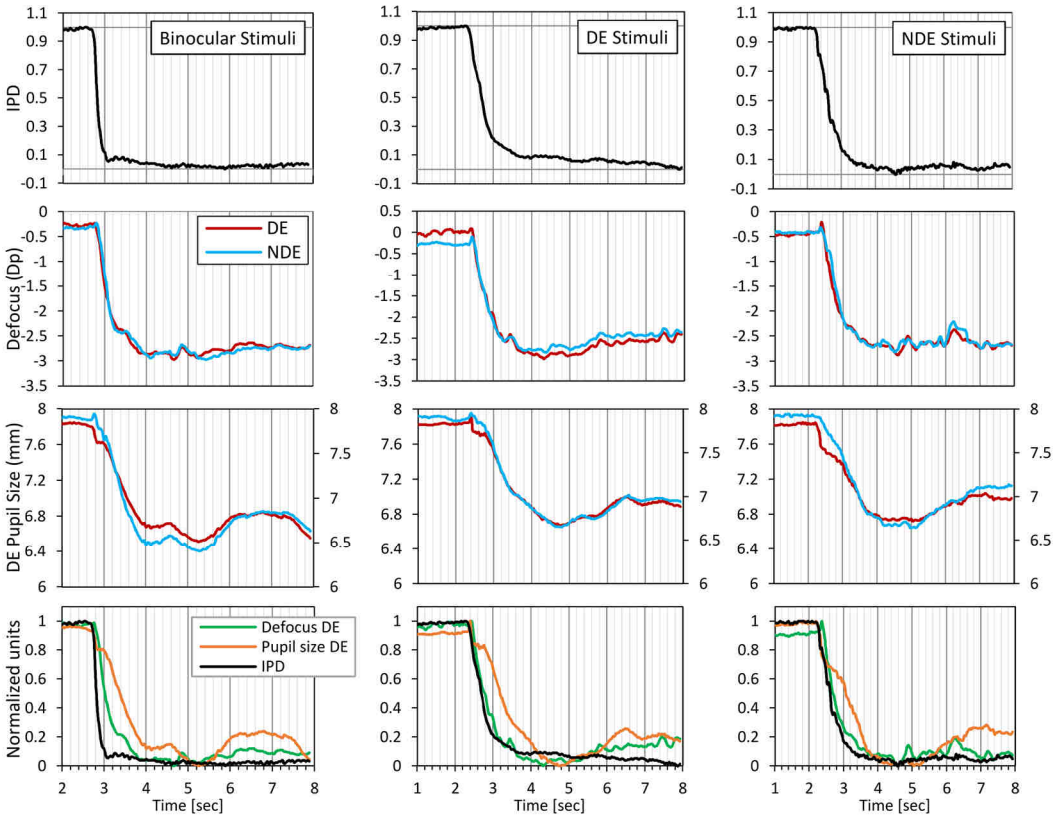

Figure 4.6: Id. Figure 4.4

Temporal dynamics of the accommodation response show strong similarity between eyes in monocular and binocular vision. In addition, accommodation shows greater fluctuations at a near steady state. Temporal dynamics of pupil constriction show also strong similarity between eyes in both viewing conditions, including for subjects with anisocoria. This behavior is observed for all participants involved in this study.

Figure 4.7 plots the average changes of accommodation, convergence and pupil size (vertical axis) as a function of the transition time for each process.

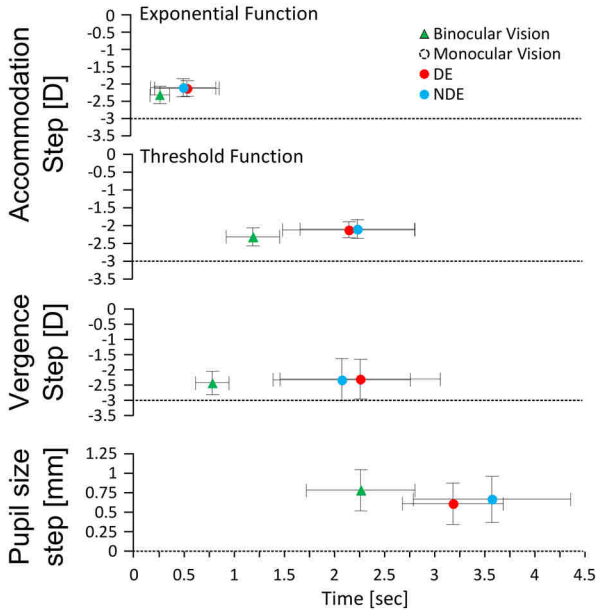

Figure 4.7: Average changes in accommodation (by means of an exponential fitting and a threshold method), convergence, and pupil constriction (bottom). Green, red, and blue symbols represent binocular and monocular DE and NDE viewing conditions respectively.

The accommodation step was 2.32 ± 0.30 D on average under binocular viewing, which corresponds to a lag of accommodation of about 0.65 D. Monocularly, the mean lag of accommodation was 0.86 D on average. These values are slightly larger than those typically found in the literature (Charman, 1999) (Seidemann & Schaeffel, 2003) (Kasthurirangan et al., 2003) of about 0.5 D for a 3D demand in binocular. Our results combined a lag for high demand and a lead for low levels that reduced the total step of accommodation. In addition, the use of low luminance targets as well as the use of a large letters as stimulus reduced the need to perform an accurate accommodation. Finally, there is a slight chromatic shift of 0.27 D of defocus with monitor spectra, decreasing the accommodation step.

4.3 Pupil motion and convergence

Figure 4.8, Figure 4.9, and Figure 4.10 show the measured defocus of both eyes together with the displacements of the pupil centers (three repetitions for the same subject) under

binocular (left), monocular DE (center) and monocular NDE (right) viewing conditions. DE and NDE results are in red and blue respectively. The origin for pupillary position was arbitrarily taken as the initial position of the DE. The apparent interpupillary distance, oIPD, is in black.

In binocular viewing condition (left panel), temporal dynamics of the two eyes present a strong similarity in their motion and appear to be synchronized, which is consistent with the expected behavior, involving symmetrical convergence. Both eyes follow an analogous trajectory in opposite directions towards each other, converging to the near stimulus (Figure 4.11 (a)). Binocular retinal disparity and blur accommodation cues cause fast and accurate convergence and accommodation. Both CA and AC processes are stimulated, which makes the accommodative reflex efficient.

In monocular viewing condition (central and right panels); only monocular blur in the stimulated eye is available to drive accommodation and the cross-linked couple AC induces convergence. When the accommodation process starts, the stimulated eye moves fast in the nasal direction in order to fixate on the near target, while the fellow eye shifts in the temporal direction opposite to the expected direction in a moment resembling a saccade. Temporal dynamics of the two eyes do not present similarity in their motion and asymmetric convergence is observed. It corresponds to the combination of a lateral saccades with accommodation-induced convergence. Nonetheless, both pupil motions are still triggered simultaneously. The saccadic-like movement occurs during a short time, maintaining the apparent interpupillary distance. Then, as the accommodation progresses, the fellow eye displacement is switched to nasal direction synchronized with accommodation, which as previously mentioned, is slower than for binocular vision. This peculiar behavior in both eyes is present for all the subjects participating in the study.

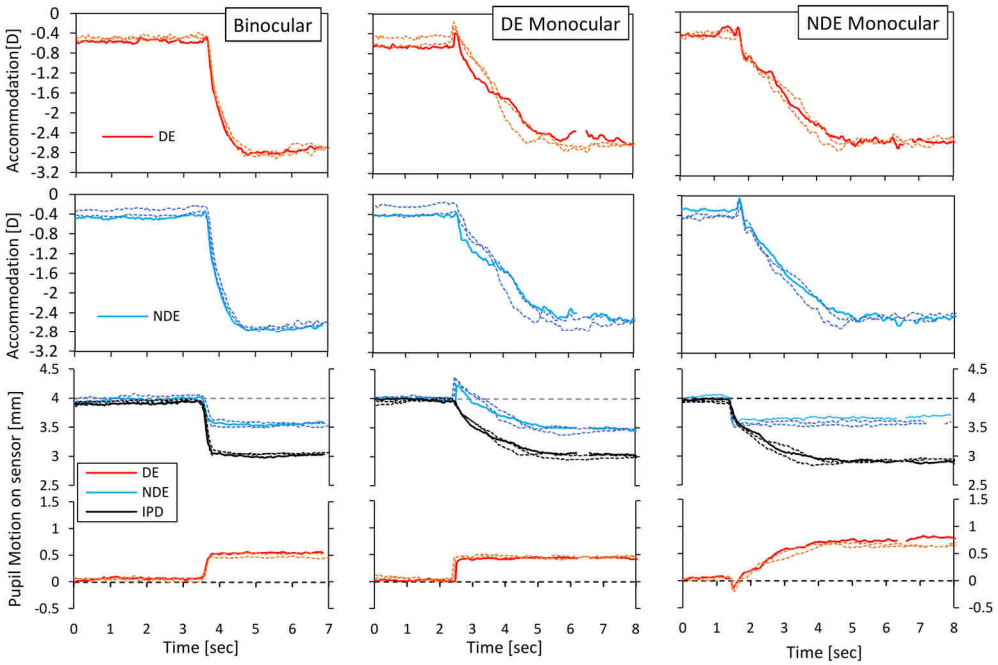

Figure 4.8: Subject I, DE (top row) and NDE (center row) accommodation results and pupil displacement (bottom row) when far-to-near accommodation is performed under binocular (left column), DE (center column) and NDE (right column) monocular fixation. Red and blue lines correspond to DE and NDE measurements respectively. In the bottom row, oIPD is in black. Dotted lighter lines show two additional repetitions in the same subjects in order to give an idea of repeatability.

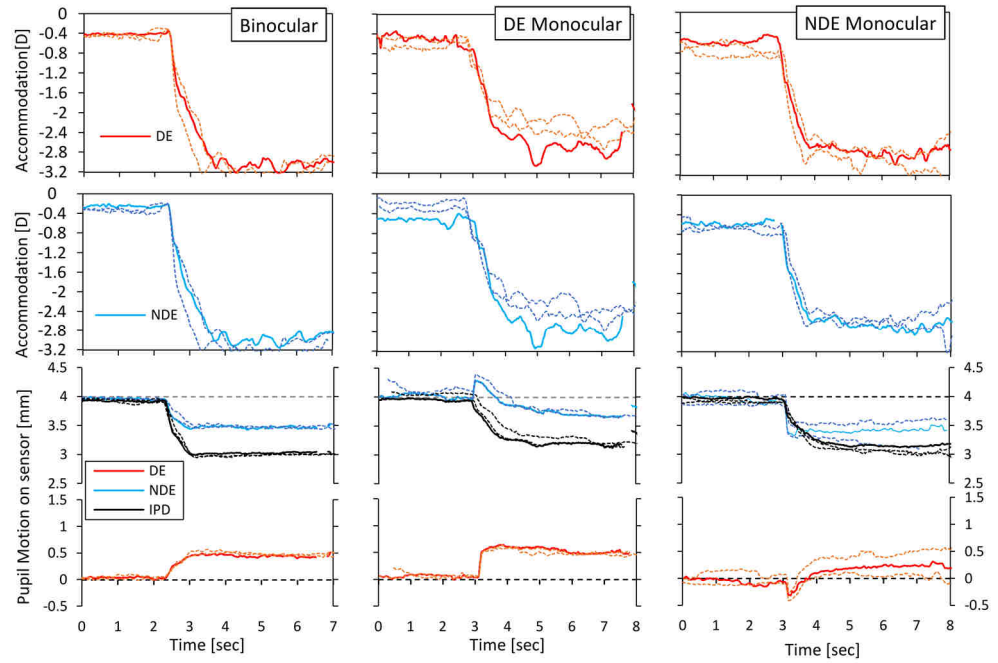

Figure 4.9: Id. Figure 4.8

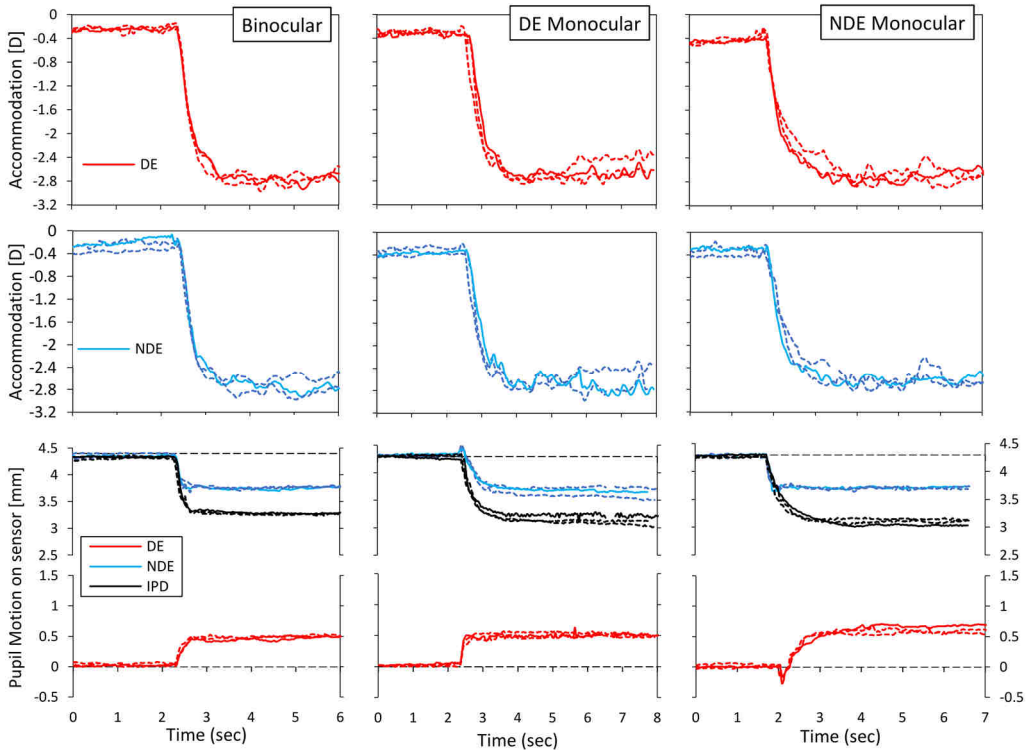

Figure 4.10: Id. Figure 4.8

Since disparity is absent when the subject switches between visual stimuli, a saccadic-like movement of both eyes is triggered at the onset of accommodation (Figure 4.11 (b). step 1). However, monocular blur induces accommodation, which in turn activates convergence through the link accommodation-convergence, AC (Figure 4.11 (b). step 2) in the absence of disparity.

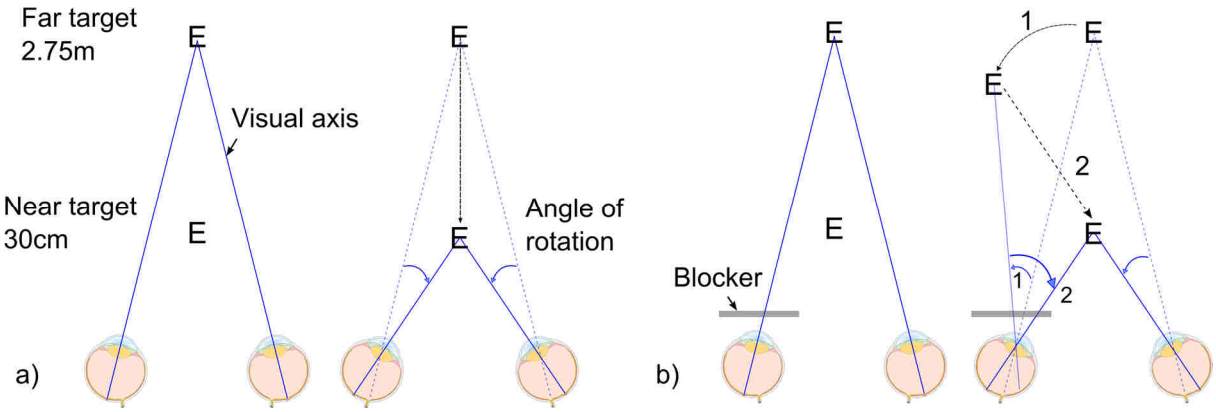

Figure 4.11: Schematic representation of the movement of the two eyes for far-to-near accommodation under binocular (a) and monocular vision (b). Binocular convergence involves simultaneous nasal rotation of both eyes. Conversely, monocular convergence is a two-step process: fast-synchronized rotation of both eyes in a saccadic-like movement (1) followed by a slow nasal rotation of the blocked eye synchronized with accommodation (2).

Figure 4.10 (Pupil motion) shows that both eyes do not always reach the position that corresponds to the fixation target as it happens under binocular conditions. Across repetitions and subjects, there is a tendency to underconvergence. Convergence step was 2.50 ± 0.37 D on average.

Figure 4.12 shows the normalized behavior of accommodation in both eyes and convergence (oIPD) for the five subjects with DE = OD. Under binocular vision, convergence is faster than accommodation (left panels). Retinal disparity is the primary signal to accommodation and seems to be predominant with accommodation following. Under monocular conditions, convergence is almost synchronized to accommodation in the absence of retinal disparity cues.

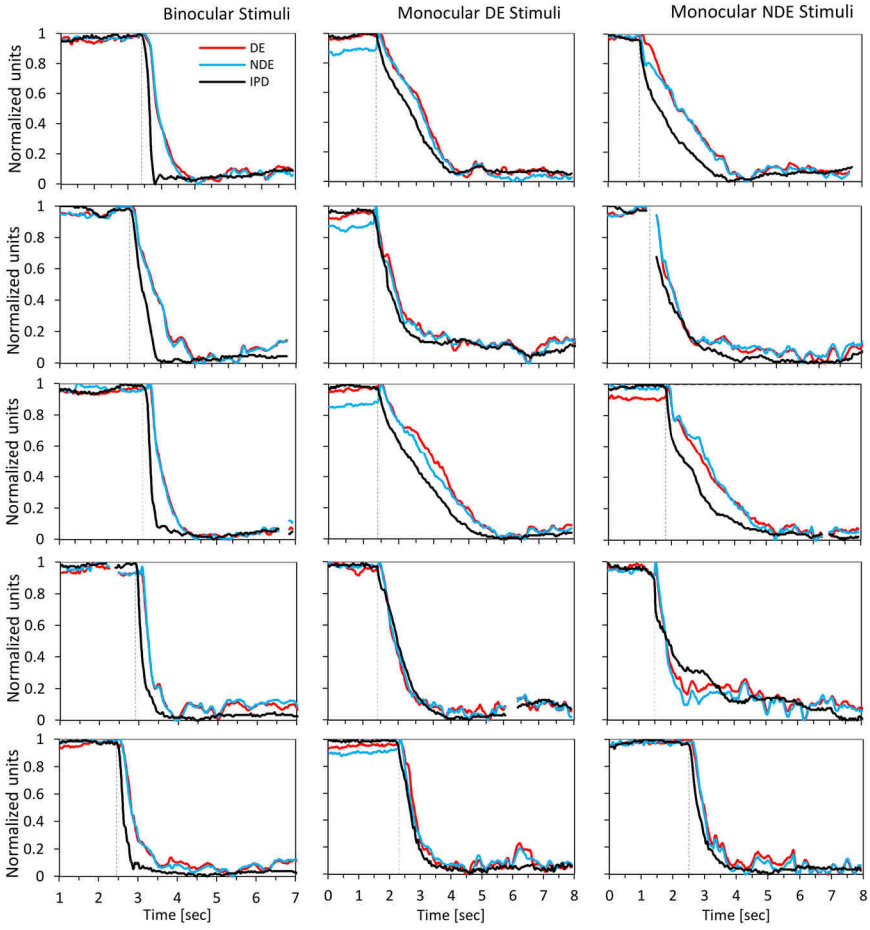

Figure 4.12: Behavior of convergence and accommodation of five subjects with right dominant eye, under binocular (left) and monocular DE (center) and NDE (right) vision. Normalized DE and NDE accommodation is in red and blue respective and normalized oIPD in black.

4.4 Discussion

In binocular vision, the three reflexes (accommodation, convergence and pupil size) were faster than in monocular. The rotation of eyes was triggered simultaneously and eye motions in

nasal direction were synchronized. Convergence was very fast, around 0.80 ± 0.16 s (measured with the threshold method), and efficiently performed when binocular retinal disparity and blur accommodation drive the response together. Accommodation time constant was 0.28 ± 0.10 s (exponential fitting) and the total time was 1.22 ± 0.28 s (threshold method). The temporal dynamics of accommodation response has shown strong similarity between eyes and this for each subject. Pupil constriction response was the slowest process, about 2.26 ± 0.25 s. Accommodation amplitude was -2.36 ± 0.30 D for 3 D demand. The corresponding lag of accommodation was 0.64 D, which was slightly more than obtained in previous studies. This can be explained in part by a chromatic shift between the two monitors used for the visual task. The convergence amplitude was 2.50 ± 0.37 D and the miosis amplitude was 0.80 ± 0.26 mm.

In monocular vision, accommodation, convergence and pupil size responses were slower and presented higher inter-subject variability compared to binocular cases. Convergence showed a complex behavior. At the onset of accommodation, a shift in temporal direction of the fellow eye was observed, interpreted as an initial saccadic-like movement. Then, the fellow eye motion was corrected in nasal direction to complete convergence synchronized with changes of accommodation. The motion of the eye receiving the stimulus was fast and similar to the binocular case. Thus, a dissociation of eye motions was observed when only monocular blur drove accommodation. In this condition, accommodation and the cross-link accommodation-convergence were the dominant processes of the mechanism of accommodation. Accommodation time constant was 0.55 ± 0.32 s and 0.51 ± 0.33 s (exponential fitting) for DE and NDE vision respectively and total duration was 2.20 ± 0.67 s and 2.22 ± 0.58 s (threshold method). Pupil constriction took 3.18 ± 0.50 s and 3.57 ± 0.80 s for DE and NDE vision respectively. The lag of accommodation was increased to 0.86 D and the miosis amplitude was decreased to 0.60 ± 0.24 mm. Temporal dynamics of accommodation response and pupil size have shown also strong similarity between eyes including for subjects with anisocoria in monocular.

To further study the interaction between accommodation and convergence, we repeated measurements in one subject with accommodation paralyzed (with Tropicamide 1 %) in one or both eyes, under binocular and monocular vision. 15-s videos were recorded with the change of stimulus triggered 5 s into them. Figure 4.13 and Figure 4.14 shows results for binocular and monocular conditions respectively.

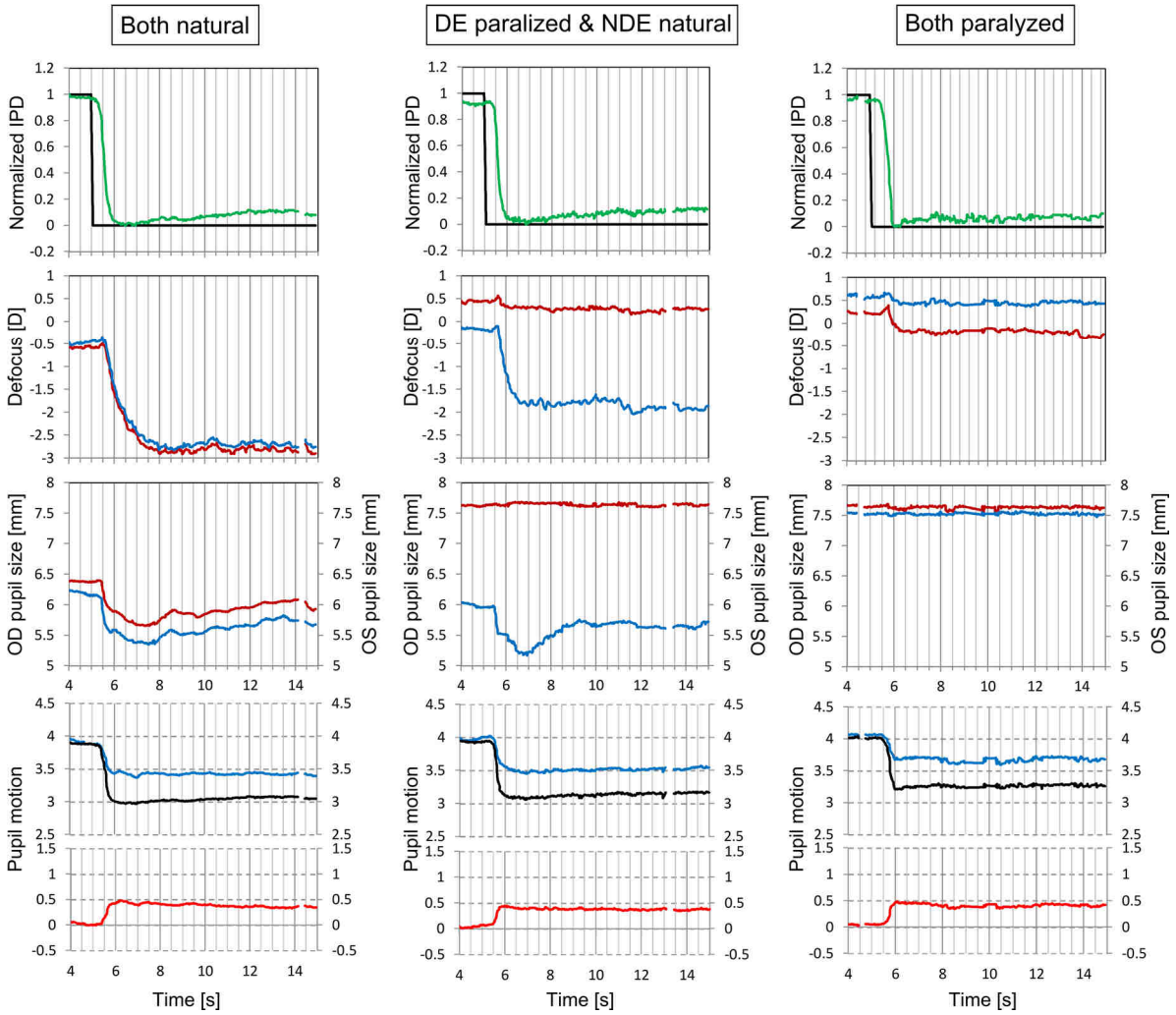

Figure 4.13: Dynamic response of the accommodative response under binocular vision with no cyclopegic drops (left column), DE paralyzed / NDE unparalyzed (central column), and both eyes paralyzed (right column). Rows, top to bottom: Normalized interpupillary distance (green) and stimulus switching (black); DE (red) and NDE (blue) accommodation; DE (red) and NDE (blue) pupil size; DE (red) and NDE (blue) pupil position, and apparent interpupillary distance (black).

For comparison purposes, the dynamic response of the accommodative response with both eyes unparalyzed is shown in the left column in both figures, closely resembling the results in section 4.2 for all the processes involved.

Convergence (green line in top row and black in bottom row) is carried out fast regardless of Tropicamide instillation in one or both eyes, revealing the important role of retinal disparity even for differently blurred images.

When the DE is paralyzed the refractive error shifts slightly towards positive values (+0.5, see mid-top row, central panel), which means this eye is mildly hyperopic. Although the NDE is not paralyzed, a slight reduction of accommodation can be observed for far and, more noticeably, for near. This fact could be interpreted as an increase on the lag of accommodation

when monocular blur information is provided only by one eye, or could be due to the fact that this is the non-dominant eye. When both eyes are paralyzed the refractive error for the NDE also shifts towards a hyperopic state (see mid-top, right panel).

The pupil size (mid-bottom row) exhibits around 0.2-mm anisocoria under binocular natural vision. When monocularly instilled with Tropicamide, the DE pupil becomes fully dilated to 7.6 mm but NDE miosis is induced normally and does not seem to be affected by the fellow eye condition. When both eyes are instilled with Tropicamide, both pupils are fully dilated to very similar values (7.6 and 7.5 mm for DE and NDE respectively).

Figure 4.14 shows the dynamic response of accommodative response for different cases of paralyzed accommodation under monocular vision.

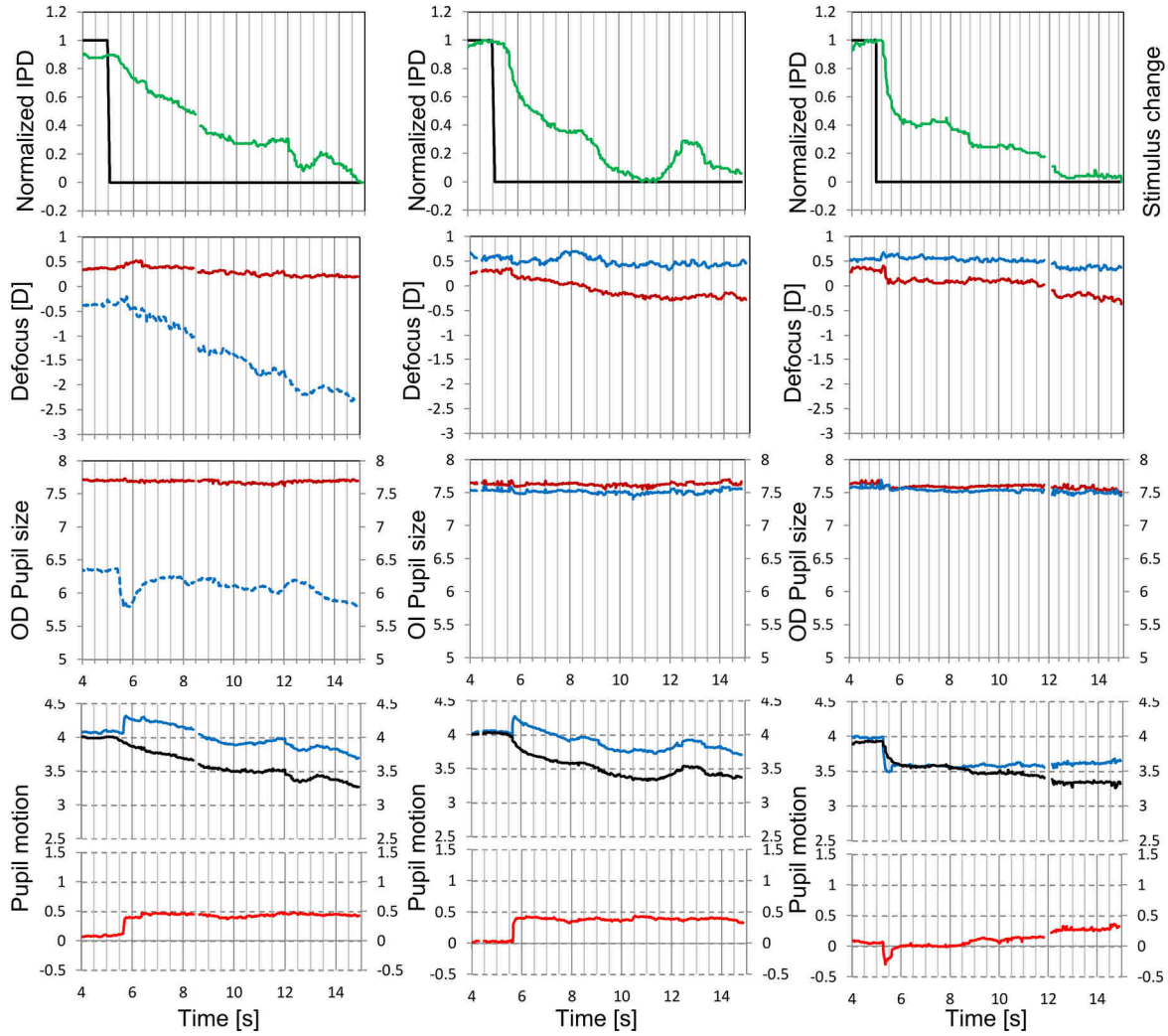

Figure 4.14: Dynamic response of the accommodative response under monocular vision. Columns, left to right: DE vision, DE paralyzed; DE vision, both eyes paralyzed; NDE vision, both eyes paralyzed. Rows, top to bottom: Normalized interpupillary distance (green) and stimulus switching (black); DE (red) and NDE (blue) accommodation; DE (red) and NDE (blue) pupil size; DE (red) and NDE (blue) pupil position and apparent interpupillary distance (black).

Although the accommodation of the eye receiving the visual stimulus (DE) was paralyzed, the fellow eye (NDE) is still accommodated despite receiving no visual stimulus. It is interesting to note that even in the absence of monocular blur and binocular disparity cues, convergence and accommodation were still triggered at the same time and, although, inefficient and very slow (about 8-10 seconds to accommodate), remained fairly synchronized. When both eyes were instilled with Tropicamide, accommodation was paralyzed but convergence still took place slowly. This behavior reveals a more complex process, possibly due to the knowledge by the subject of the approximate position of the near target due to previous observations.

Concerning eyes movements, the behavior was similar to that previously reported: A temporal shift of the fellow eye matching the fast nasal shift of the eye seeing the stimulus in a saccadic-like movement; followed by a slower (in this case, much slower) convergence movement of the fellow eye while the stimulated eye remains basically fixed.

5 Accommodation and refraction at low luminance

Night myopia, the myopic shift occurring at low luminance, has been studied during decades. Despite the significant amount of literature on the topic, it has to be pointed out that most of the experiments have been performed in monocular where convergence information and binocular summation were absent and only scarce data has been obtained under natural binocular vision (Wald & Griffin, 1947) (Leibowitz & Owens, 1975b) (Kotulak, Morse, & Rabin, 1995).

The purpose of this work was to investigate the possible mitigating effect of binocular vision on night myopia and its accommodative genesis. To this end, accommodation, convergence, aberrations and natural pupil size were measured under low light levels and in absolute darkness.

5.1 Experimental procedure

The visual target consisted of a high-contrast black E letter on a white circular background, displayed on a flat LCD monitor (DELL, USA) located 2.75 m in front of the subject. A linear polarizer sheet was used to increase the contrast of the monitor. The E letter subtended 1.3º from top to bottom and the white circular ring was 2.5º wide. The use of a large letter allowed subjects to see the target even at very low light levels.

A series of neutral density filter (NDF) sheets, with equal transmission in the visible spectrum from 400 to 700 nm, were placed at 20 cm in the line of sight of both eyes, covering a large field-of-view in order to decrease the target luminance. Figure 5.1 illustrates the set-up.

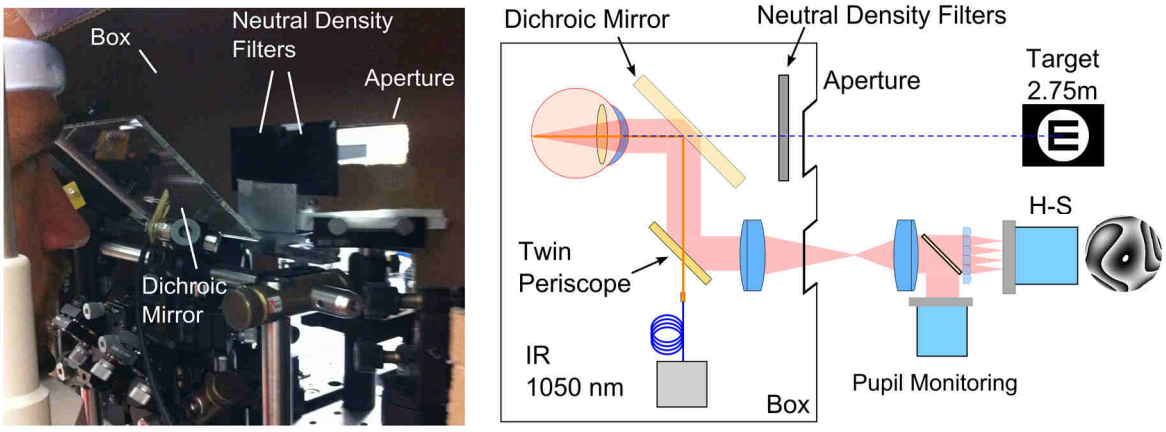

Figure 5.1: Apparatus. Left panel: picture of the elements inside the box, including the chin rest for the subject, the dichroic hot mirror to direct the IR measurement light towards the HS sensor while allowing direct view of the stimulus, and the neutral density filter holder for calibrated stimulus dimming to scotopic levels. Right panel: schematic side view of the experimental set-up. The HS sensor is located in a lower level and does not interfere in the subject's line of sight

For monocular conditions, the non-dominant eye's view of the stimulus was blocked between the dichroic mirror and the visual stimulus, thus, permitting binocular wavefront and convergence measurements. To avoid residual light affects at the low luminance conditions, the system was encased in a box with a black hood attached for covering the subject's head. The light coming from the stimuli came into the box through a rectangular aperture smaller than the NDFs.

Luminance was measured with a luminance meter (LC-100, Konica Minolta, Japan) when a white background was displayed on the monitor. The luminance level used in the experiment ranged from 183 cd/m^2 (photopic) to 0.0032 cd/m^2 (scotopic) in the darkest case. The white stimulus spectrum is the combination of the relatively narrow spectra of the monitor's RGB channels (Figure 5.2).

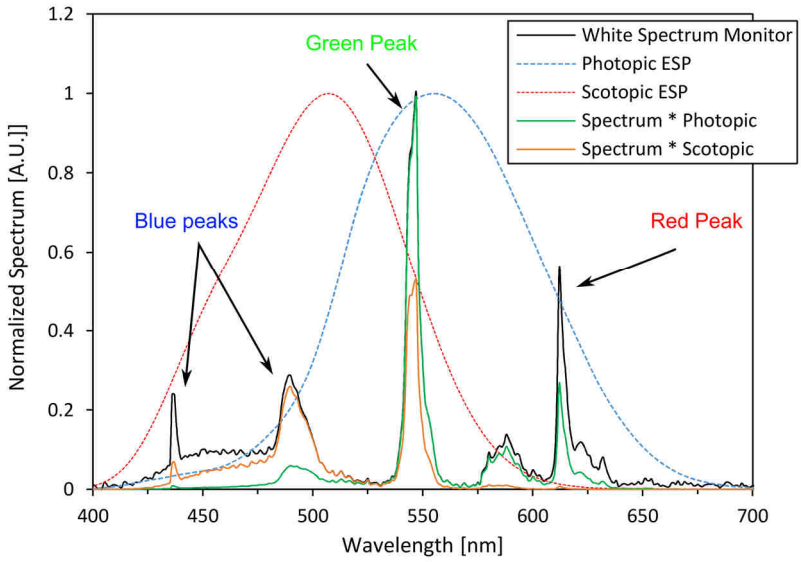

Figure 5.2: Normalized spectrum of the white stimulus (black line) combined with the Eye's Spectral Sensitivity for photopic (dotted blue line) and scotopic luminance (dotted red line). Orange and green lines are the resulting spectra.

Subjects

Measurements were carried out on 10 normal young nearly emmetropic subjects (Table 9). All of them were able to see the visual stimulus for the whole luminance range tested, both under monocular and binocular vision. The mean age was 28.4 ± 5.5 years. Mean spherical equivalent was -0.43 ± 0.27 D and ranged from -0.14 D to -0.82 D. Mean cylinder was -0.37 ± 0.2 D and ranged from -0.17 D to -0.77 D. All subjects presented natural pupil radii larger than 2.5 mm for all light levels except for the brightest one. The study adhered to the tenets of the Declaration of Helsinki.

Subjects	Real IPD [mm]	Age (Y)	Eye	SE [D]	Sphere [D] x Cylinder [D]	Axis [º]
Ma	60-61	27	OS	-0.46	-0.31 x -0.30	171.8
			OD *	-0.44	-0.31 x -0.26	31.6
Ap	64	29	OS *	-0.31	0.07 x -0.77	122.3
			OD	-0.30	0.01 x -0.60	21.3
Lu	60	32	OS	-0.48	-0.40 x -0.16	141.3
			OD *	-0.53	-0.41 x -0.24	151.5
Je	65	27	OS	-030	-0.03 x -0.65	32.3
			OD *	-0.40	-0.034 x -0.39	131.4
Ju	65	24	OS *	-0.59	-0.48 x -0.21	146.9
			OD	-0.49	-0.34 x -0.30	168
Ge	66	31	OS	-0.63	-0.37 x -0.52	28.8
			OD *	-0.82	-0.73 x -0.18	160.3
Da		22	OS	-0.81	-0.41 x -0.80	11
			OD *	-0.14	-0.20 x -0.66	163
Sm	61-62	42	OS *	-0.51	-0.24 x -0.44	118.2
			OD	-0.09	0.13 x -0.43	102.9
Lc	63-64	28	OS *	-0.04	0.16 x -0.40	5.8
			OD	-0.21	-0.02 x -0.38	5.0
Ml	60	22	OS	-0.58	-0.48 x -0.20	141.9
			OD *	-0.48	-0.40 x -0.17	14.3

Table 9: Ocular data obtained through H-S measurements when subjects fixated the target binocularly. The asterisk marks the dominant eye.

Spherical equivalent, pupil diameter, and apparent interpupillary distance were measured simultaneously under binocular and monocular (dominant eye) vision. Measurements were performed for seven light levels in decreasing order: 183, 100, 10, 1, 0.1, 0.01, and 0.0032 cd/m^2. This range of luminance spans from low photopic to high scotopic. The first three levels (photopic) were achieved by adjusting the monitor brightness without NDF. The lower light levels (mesopic and scotopic) were achieved by using NDFs with optical densities 1, 2, 3, and 3.5 (NE205/10/20/30B, Thorlabs GmbH, Germany) when the monitor brightness was set to 10 cd/m^2. In photopic conditions, room light was adjusted with a dimmer to be concordant with the target luminance. In mesopic and scotopic conditions room light was turned off. When changing between luminance levels, the subject was given at least 5 min to adapt. Since dark adaptation (Cohen et al., 2007) is slower than dark focus stabilization (McBrien & Millodot, 1987), a longer adaptation period of 30 min was provided for the dimmest condition. Three 5-second videos of binocular H-S images were recorded and results were averaged for each luminance condition. The whole experiment took around 60 to 90 minutes to complete. In a separate experiment, dark focus, i.e., the accommodative state in total darkness was measured in seven of the subjects. To compare results to those of the main experiment a similar procedure was repeated for a reduced number of luminance levels: 183, 1, and 0.0032 cd/m^2 was repeated. Finally, the monitor was switched off and measurements were taken in total darkness.

Data analysis

The accommodation response was quantified by means of the spherical equivalent SE (section 1.6) in both eyes, calculated first by means of equation (1.6), which only considers the defocus Zernike coefficient, C_2^0, and then by using equation (1.8), that includes the contribution of spherical aberration, C_4^0 (Thibos et al., 2004). In this work, a standard value of 2.5 mm was selected for the pupil radius. However, two subjects had natural pupils at the highest luminance level that were smaller than this value and we were forced to use a radius of 2 mm for them at that luminance only. This reduction, however is not expected to have a noticeable impact on the corresponding SE estimates.

The pupil tracker algorithm processed each frame of the measurement sequence in order to determine the size of both pupils and their position on the H-S plane that we denote oIPD. However, it is important to note that the twin periscope was adjusted at the beginning of the experiment for each subject and, consequently, the change in oIPD exactly mirrors the change in IPD and can be used to estimate relative convergence, ΔV (Chirre, Prieto, & Artal, 2015) (see section 2.9.1). The interpupillary distance, IPD, measured with an ophthalmic ruler, was 63 ± 2.2 mm on average.

5.2 Accommodation response

Figure 5.3 depicts the spherical equivalent, SE_2, as a function of decreasing luminance.

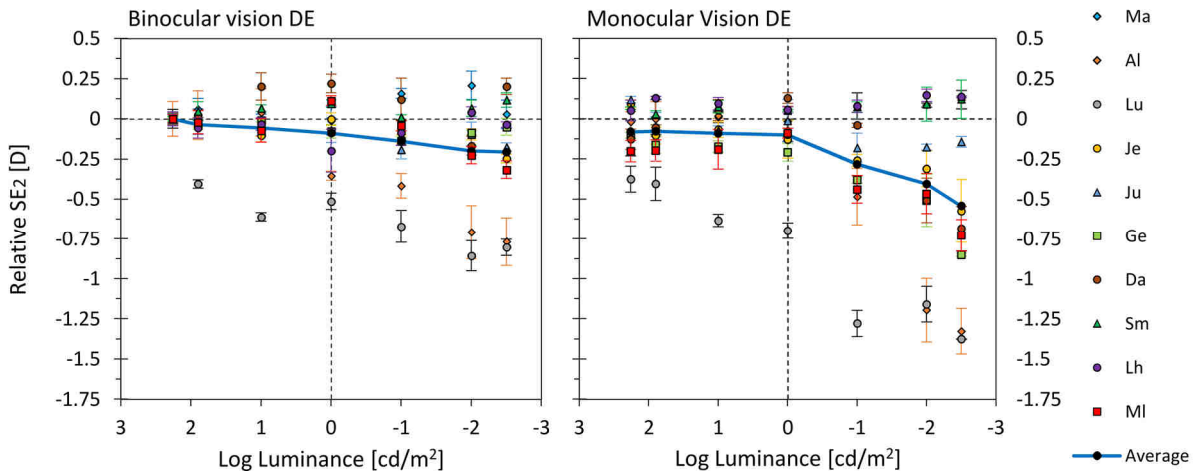

Figure 5.3: Relative spherical equivalent, SE_2, as a function of Log luminance under binocular (left) and monocular dominant-eye vision (right). Blue lines represent average values and symbols correspond to individual subjects. The error bars represent the standard deviation across three measurements for each subject at each luminance.

The average myopic shift under monocular vision was -0.54 ± 0.57 D from the highest to the lowest luminance considered (see Figure 5.3, right). A large variability was observed, with

some subjects showing a progressive increase in accommodation resulting in night myopia, while the refraction of others remained stable or even showed a slight increase. Individual changes in SE ranged from +0.16 D to -1.37 D. This variability is similar to that found in previous studies (Leibowitz & Owens, 1975b) (Owens & Leibowitz, 1976a) (Epstein, 1983) (Artal et al., 2012).

Binocularity reduced the magnitude of the phenomenon (Figure 5.3, left) to -0.21 ± 0.34 D on average, and for every subject individually. Individual changes in SE ranged between +0.20 D and -0.85 D. The behavior of binocular and monocular night myopia was always individually consistent, that is, the subjects with large monocular myopic shifts also had the largest values of binocular night myopia and the subjects showing night hyperopia, although slight, did so for both monocular and binocular vision.

The variability across repetitions for each subject and luminance condition was relatively low, both in monocular and binocular conditions. There was a tendency towards increased variability at dim light levels but the intra-subject standard deviation was always below 0.5 D. These results indicate that monocular night myopia is fairly repetitive for different luminance levels, as previously reported (Miller, 1978) (Mershon & Amerson, 1980), and the phenomenon is also stable for binocular conditions. Figure 5.4 plots the relative fourth-order spherical equivalent, SE_4, in order to illustrate the impact of spherical aberration on monocular and binocular night myopia.

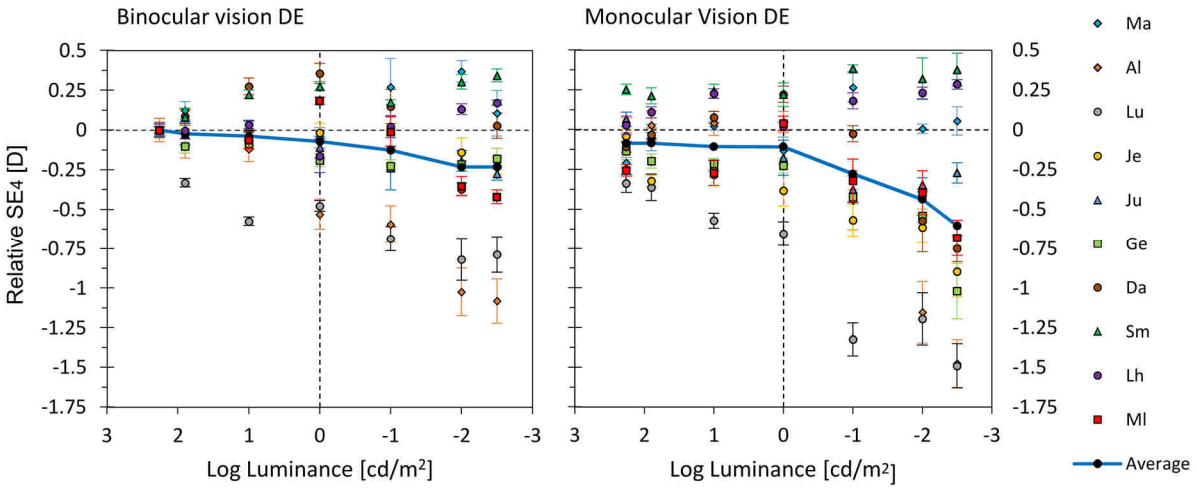

Figure 5.4: Relative fourth-order spherical equivalent including spherical aberration, SE_4, as a function of Log luminance under binocular (left) and monocular dominant-eye vision (right). Blue lines represent average values and symbols correspond to individual subjects. The error bars represent the standard deviation across three measurements for each subject at each luminance.

We found a similar behavior of SE_4 compared to SE_2 in both viewing conditions. The average decrease in SE_4 from the brightest to the dimmest case was -0.23 ± 0.44 D and -0.60 ± 0.65 D under binocular and monocular DE vision respectively, with values ranging between +0.35

D to -1.08 D binocularly and between +0.37 D to -1.50 D under monocular viewing. Including spherical aberration in the calculation of SE produces virtually the same mean values but slightly increases the standard deviation, as a result of the increased spread of values across subjects. The contribution of spherical aberration was small in all cases and, furthermore, always consistent with that of the defocus term: myopic for subjects with night myopia, hyperopic for subjects with night hyperopia, and very small for subjects without either. Due to the small size of the CCD and the fact that we are fitting both eyes in a single sensor, we were unable to measure spherical aberration in the large natural pupils occurring for dim light conditions. However, considering an r^4 behavior for C_4^0, extrapolation from 5 mm to the natural pupil size would result in a factor between 2 and 3 for the contribution of spherical aberration to the SE, still smaller than SE_2. These results suggest that spherical aberration play only a secondary role and its behavior seems related to accommodation, in agreement with previous studies (Artal et al., 2012).

The difference between monocular and binocular behavior can be more easily observed in Figure 5.5, left, where the average changes in SE2 are presented for both monocular (red line) and binocular (blue line) conditions together. Our results show that binocularity reduces night myopia on average and for each individual subject. A possible cause for this reduction could be the accommodative cue produced by fusional convergence: convergence accommodation could refine accommodation and reduces the mismatch between the accommodative state of the eye and the stimulus distance (Leibowitz et al., 1988). Since most studies in the literature were performed under monocular conditions, there has probably been a tendency to overestimate night myopia when compared to natural viewing conditions. Furthermore, the difference between monocular and binocular night myopia is consistent with the hypothesis of an accommodative genesis of the phenomenon, since retinal disparity can be expected to help focusing in binocular conditions.

5.3 Pupil diameter and convergence response

The central panel in Figure 5.5 shows the behavior of pupil size with luminance. As expected, natural pupil size increased with decreasing light level up to the point where the subjects reached their natural fully dilated state, around 0.1 cd/m^2. In addition, and as expected, the pupil for luminance values in the upper part of the range was slightly larger in monocular conditions than binocularly but the difference tended to disappear as the pupil approached its maximum size. Figure 5.5, right, shows the behavior of the interpupillary distance oIPD on average with decreasing luminance. For photopic to mid-mesopic levels, oIPD gradually increases as the luminance decreases. This behavior should not be due to an induced divergence, which is not to be expected, but to shifts in temporal direction of both pupil centers with pupil dilation.

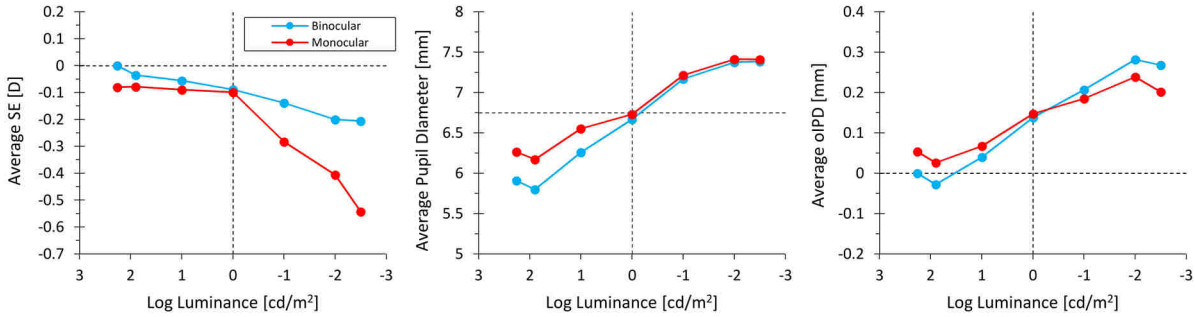

Figure 5.5: Average values across subjects of spherical equivalent SE_2 (left), pupil diameter (center) and offset interpupillary distance (right) as a function of Log luminance [cd/m^2]. Blue and red lines correspond to binocular and monocular conditions respectively.

Yang et al. (Yang, Thompson, & Burns, 2002) found shifts of the pupil center typically smaller than 0.3 mm, with a mean value of 0.133 mm temporal (Yang et al., 2002) from mesopic to scotopic conditions. However, important variations have been observed among studies and values up to 0.6 mm temporal have been reported (Walsh, 1988) (Wilson, Campbell, & Simonet, 1992) (Wyatt, 1995). On the contrary, for luminance levels lower than 0.1 cd/m^2, the pupils are almost fully dilated for most subjects and, consequently, the pupil centers should remain stable. Therefore, changes in oIPD in this range can be attributed to changes in convergence.

Figure 5.6 shows the differences in convergence, accommodation and pupil size between binocular and monocular conditions. For photopic conditions (down to 1 cd/m^2), accommodation and convergence apparently have different behaviors: While there was virtually no difference between monocular and binocular SE_2, there were changes in oIPD that suggested an unexpected apparent divergence. However, for these luminance values pupil size was larger, as expected, under monocular vision (positive difference) and the change in IPD can probably be attributed to a shift in the pupil centers. In fact, the larger the pupil size difference, the larger the observed change in oIPD, and therefore the apparent divergence somehow mimics the change in pupil size in this luminance range. Below 1 cd/m^2, there was little difference between monocular and binocular pupil size (black line). Consequently, the change in oIPD from binocular to monocular vision observed in mesopic and scotopic conditions should be mostly due to a change in convergence. In this range, estimated convergence and accommodation follow a similar tendency towards the subject tonic accommodation when one eye is blocked. In other words, the eye monocularly presented with a stimulus in low light levels tended to overaccommodate and also to overconverge. As a final comment on Figure 5.6, we would like to point out that, although the differences in this luminance range are very small, monocular pupils are still larger than their binocular counterparts are and, therefore, the change in convergence may be slightly overestimated, accounting for part of the gap between the red and blue lines.

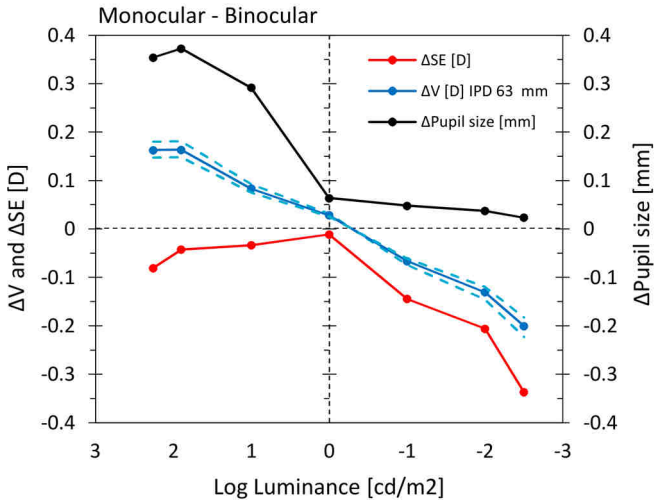

Figure 5.6: Changes in spherical equivalent (red) and convergence (blue), both of them in diopters (left-hand side axis), and pupil size (black) in mm (right-hand side axis), from binocular to monocular conditions, as a function of Log luminance of the stimulus. Dashed lines represent the confidence interval for the estimate of convergence corresponding to a ±5 mm tolerance for the value of IPD.

5.4 Dark focus and dark convergence

Figure 5.7 compares binocular and monocular night myopia (log luminance = –2.5) and dark focus in the dominant eye (left panel) and non-dominant eye (right panel). On average (bars), dark focus was myopic, with mean values -0.64 ± 0.59 D in the DE and -0.61 ± 0.66 D in the NDE. Monocular night myopia was on average -0.36 ± 0.43 D for DE and -0.42 ± 0.41 D for NDE, closer in both cases to dark focus than binocular night myopia (Mean values -0.15 ± 0.17 D for DE and -0.16 ± 0.21 D for NDE). Individually (symbols & colors), there was a large variability in focus shift across subjects but a good agreement between eyes for all the subjects. Five subjects showed myopic dark focus shifts and monocular and binocular night myopia, in descending order of magnitude in all cases; one subject exhibited a hyperopic dark focus shift and smaller amounts of monocular and binocular night hyperopia; and one last subject had virtually no dark focus shift and neither night myopia nor hyperopia, both monocular and binocularly. In all subjects, the results for these selected levels were in good agreement with earlier measurements.

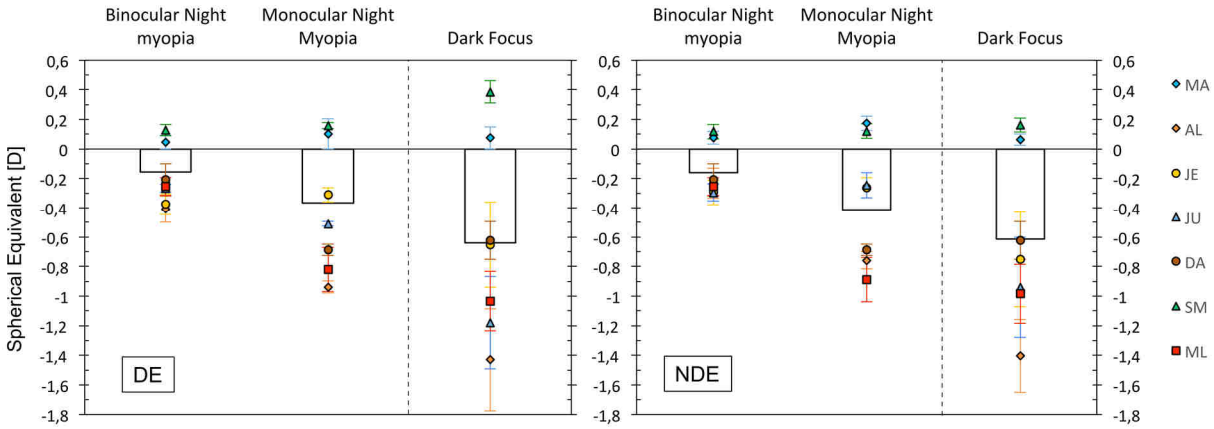

Figure 5.7: Spherical equivalent shift when viewing the stimulus in binocular and monocular vision for a -2.5 log luminance stimulus and in total darkness in the dominant eye DE (Left panel) and non-dominant eye NDE (right panel). All values are referred to the corresponding highest-luminance binocular case. Symbols and colors correspond to individual subjects and bars represent average values. The error bars represent the standard deviation across 3 measurements for each subject.

Figure 5.8 plots the dark focus as a function of binocular and monocular night myopia.

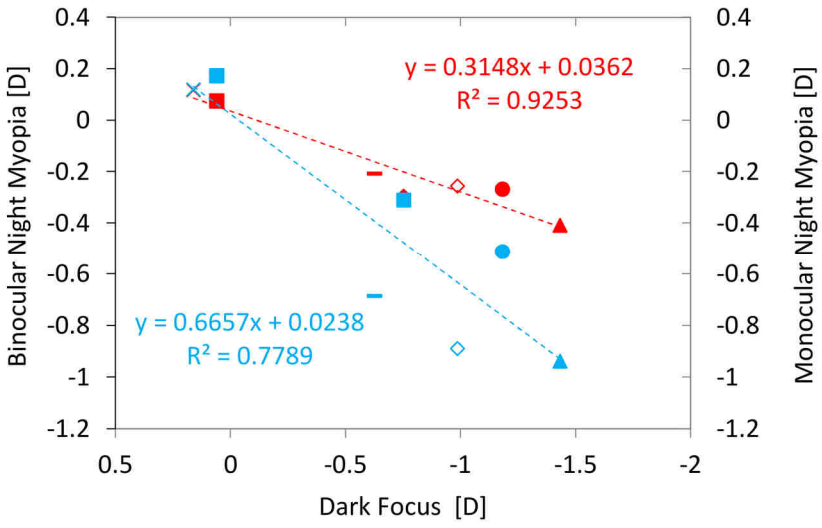

Figure 5.8: Dark focus vs. Binocular (red) and monocular night myopia (blue). Each Symbol corresponds to an individual subject. Dotted lines are linear fits.

We found a high correlation between dark focus vs. binocular (R^2=0.92) and monocular night myopia (R^2=0.77) respectively across subjects. The slope was 0.66 and 0.31 for monocular and binocular cases.

These results suggest that night myopia may be induced by dark focus, i.e., by the progressive shift of the accommodative state of the subject towards its default state in total darkness. As the luminance decreases, eyes presented with a stimulus in monocular conditions

tend to accommodate or disaccommodate towards their dark focus. For subjects with myopic dark focus, which in our study was the typical case, this tendency generates night myopia. On the contrary, subjects with hyperopic dark focus showed a small amount of night hyperopia. These results are in agreement with previous works (Leibowitz & Owens, 1975b) (Leibowitz & Owens, 1975a) (Leibowitz & Owens, 1978).

Figure 5.9, plots relative dark convergence vs. dark focus. Due to the shift in pupil centers with dilation at low luminance, the convergence estimates were probably biased. To circumvent this problem, the reference was taken at 1 cd/m^2, when pupils are close to their dilated state but, on the other hand, the shift of convergence towards its resting state can be expected to be small.

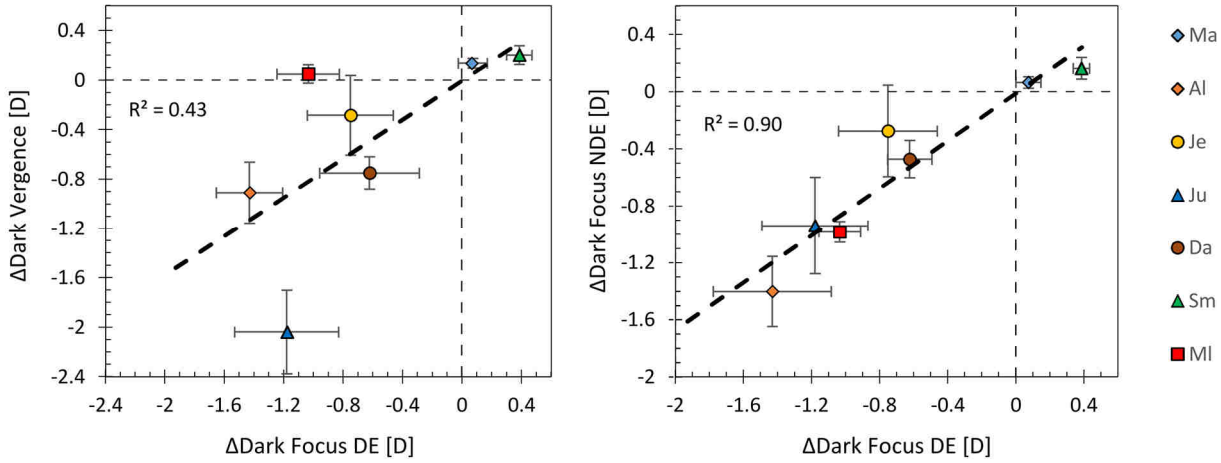

Figure 5.9: Left: DE dark focus vs. dark convergence. Right: DE vs. NDE dark focus. Each symbol corresponds to an individual subject. Error bars are standard deviation across measurements for each subjects. Dashed black lines are linear fits.

We found a moderate correlation (R^2=0.43) between dark convergence and dark accommodation with high inter-subject variability (Fincham, 1962) (Owens & Leibowitz, 1976b) (Kotulak & Schor, 1986) (Wolf et al., 1990) (Jiang et al., 1991). Figure 5.9, right, shows the correlation (R^2 = 0.90) between dark focus of dominant and the non-dominant eye. Both resting states of accommodation were found highly correlated and could suggest that exist a similarity in the tonic accommodation between eyes and thus in the amplitude of night myopia.

Considering all the subjects together, neither the difference between monocular and binocular night myopia, binocular night myopia and dark focus, or monocular night myopia and dark focus were statistically significant (p-values = 0.154, 0.056, and 0.084, respectively). However, we have shown that night myopia was dark-focus dependent. Discarding the subjects with hyperopic dark focus, these differences were all statistically significant (p-values = 0.031, 0.006, and 0.05).

5.5 Discussion

In order to investigate the possible sources of night myopia, we measured the changes in spherical equivalent and convergence as a function of stimulus luminance under natural binocular viewing conditions in a group of normal subjects, using an infrared open-view binocular wavefront sensor. Additionally, we performed measurements when the stimulus was viewed monocularly. The sensor also provided pupil size for both eyes simultaneously.

On average, the monocular accommodative error for decreasing luminance tended towards the average dark focus, producing night myopia. Under binocular vision, the average accommodative error was smaller for each luminance level, meaning that binocularity mitigated night myopia when convergence accommodation was available. High correlation was found between dark focus vs. binocular (R^2=0.92) and monocular (R^2=0.77) night myopia.

Individually, the same trend was observed although there was a wide range of behaviors, with some subjects showing large myopic changes in the accommodative state for low light levels and others remaining stable or even having a slight hyperopic shift. In each case, the subject´s dark focus seemed to be an indicator of the evolution of night myopia in both monocular and binocular conditions, and binocularity had a weakening effect. Possible causes of the binocular reduction were the convergence cue produced by retinal disparity and the binocular summation, which improved the detection threshold.

Spherical aberration apparently did not play a major role on night myopia. Although including the spherical aberration in the calculation of SE slightly increased the spread of the results across subjects, the contribution was always in the same direction as the defocus shift, and small compared to the total amount of night myopia in all subjects. Spherical aberration escorted the shift of the focus with an increasing impact in dim light when pupils were dilated and was not the consequence of the phenomenon of night myopia.

Convergence values obtained individually were biased by pupil size changes, which may be one reason for the moderate correlation, in agreement with literature, between dark converge and dark focus. However, comparing the difference between monocular and binocular convergence our results show on average an excess of accommodation at low light levels and an overconvergence. This result is in agreement with the idea that binocular mitigation of night myopia was due to a convergence cue improving the precision of the accommodative state although the interaction between night myopia and night convergence could be more complex. In the absence of stimulus, dark convergence was moderately correlated (R^2=0.43) with dark focus and we suspected that night myopia was mainly related to dark focus as previous studies have validated. Despite the dissociation between convergence and accommodation in total darkness, tonic accommodation was highly correlated between eyes (R^2=0.90), which could also explain the similarity of the phenomenon of night myopia in both eyes.

6 Accommodation in polychromatic light

In this chapter, the effect of color on the accommodative response was studied under natural binocular viewing conditions. Refraction, accommodation time and velocity, pupil size, convergence and dynamics of accommodation mechanism were analyzed as a function of stimulus wavelength.

6.1 Experimental procedure

Subjects

Measurements were performed in seven young subjects with normal vision, with ages ranging from 20 to 38 years old (mean age = 26.7 ± 5.9). The mean refractive state was measured when the subjects looked binocularly at a far target (0.5 D) with a stimulus back-illuminated in white light (centered at 549nm, FWHM = 44 nm). Average sphere was -0.35 ± 0.27 D (from -0.77 D to +0.05 D). Mean cylinder was -0.47 ± 0.31 D (from -0.19 D to -1.10 D). Table 10 shows ocular data in both eyes for each subject. The mean IPD, measured with an ophthalmic ruler, was 62 mm.

Subjects	Age (Y)	Eye	Sphere [D] x Axis[º]	Cylinder [D]	SA [µm]
I	28	OS	-0.37 x 169.7º	-0.40	0.075
		OD *	-0.64 x 17.2º	-0.22	0.179
II	28	OS	-0.68 x 137.9º	-0.32	-0.026
		OD *	-0.71 x 9.8º	-0.19	0.031
III	38	OS	-0.34 x 0.4º	-0.43	0.091
		OD *	-0.35 x 9.6º	-0.50	0.076
IV	24	OS *	-0.62 x 152.7º	-0.36	0.025
		OD	-0.45 x 174.3º	-0.36	0.053
V	28	OS *	-0.21 x 172.1º	-0.31	0.035
		OD	-0.26 x 1º	-0.47	0.061
VI	20	OS	-0.27 x 8.3º	-0.64	-0.024
		OD *	-0.25 x 16.2º	-0.63	-0.019
VII	21	OS	-0.46 x 138.7º	-0.31	0.095
		OD *	+0.06 x 19.2º	-1.10	0.034

Table 10: Ocular data for both eyes when subjects look at a 0.5D-vergence in white light under binocular vision.

The visual targets were composed of a black Maltese cross surrounded by five circular rings printed on a transparent film and coupled to a thin diffusing layer as illustrated on Figure 6.1. The Maltese cross subtended a visual angle of 1º. The printed film was back-illuminated by RGB (Right, Green, Blue) and White light (W) LEDs equally separated behind the diffusing layer to provide homogeneous back-illumination. The peaks of R, G, B, and W spectra were centered at 629 nm, 526 nm, 470 nm, and 546 nm respectively, Full width at half maximum (FWHM) was 14 nm, 30 nm, 22 nm, and 88 nm respectively. Figure 6.1 plots the theoretical chromatic difference of focus and RGB and W spectra together with the eye's spectral sensitivity.

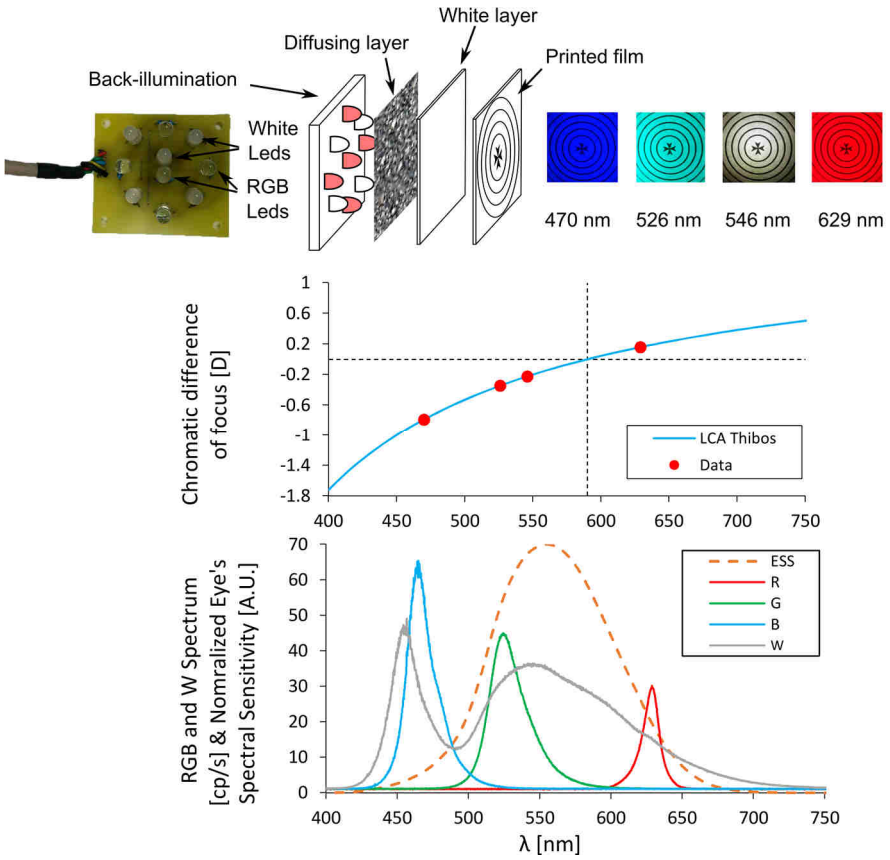

Figure 6.1: Top: Scheme of the RGBW target and picture of the illumination stage. The target consists of a diffusing layer and a transparent film where the black Maltese cross and rings are printed. Center: Ocular chromatic difference of focus for R, G, B, and W spectral peaks (symbols) and general trend with wavelength (line). Bottom: normalized spectrum of R, G, B, and W (red, green, blue and gray solid lines respectively) channels and eye's photopic spectral sensitivity (dashed yellow line).

The chromatic difference of focus of the human eye from IR (1050 nm) to W (546 nm) is 1.2 D (Fernández & Artal, 2008). The far and near stimuli were located at 2 m (0.5 D) and 30 cm (3.3 D) at a point midway between the two pupils, inducing an accommodative demand of 2.8 D. The operator controlled the stimulus luminance and color externally. Luminance for each color (R, G, B, and W respectively) was 12.5, 13.5, 8.4, and 45 cd/m^2 for far; and 14, 23, 6, and

27 cd/m^2 for near. These relatively low luminance values were selected to prevent excessive pupil constriction, especially in combination with accommodative miosis, in order to perform accurate H-S measurements.

The dynamics of accommodation, convergence, and pupil size responses were recorded in 10-seconds sequences at 25 Hz, 3 times per subject and color combination. Far and near steady states were averaged from 60 frames each. Pupil size was always larger than 5 mm for far and larger than 3.8 mm for near.

Several color combinations were considered for the stimuli from far-to-near: white-to-monochromatic (W→R, W→G, and W→B); same colors (R→R, G→G, B→B, and W→W) and extreme-to-extreme (R→B and B→R). Subjects performed voluntary far-to-near accommodation for each condition. Ambient light was dimmed during the measurements.

Data analysis

Fourth-order spherical equivalent, SE_4, was obtained from defocus, C_2^0, and spherical aberration, C_4^0, (see section 1.6) with LCA corrected from 1050-nm to 546-nm. The pupils were processed at the maximum available diameter. As miosis occurred when subjects performed the far-to-near task, the processing pupil was decreased following the changes in pupil size.

The accommodation response time was estimated by means of an exponential fit as described in section 4.1, providing a time constant, τ (Yamada & Ukai, 1997) (Kasthurirangan et al., 2003) (Suryakumar et al., 2007a) (Suryakumar et al., 2007b) (Hampson, Chin, & Mallen, 2010) (Chirre et al., 2015).

The SE_4 step, or accommodation step, was calculated as the difference between near and far steady states of accommodation, and the mean accommodation velocity, in diopters per second, was the refraction step divided by the time constant:

$$V_{acco} = \frac{0.63 * SE_{4\,step}}{\tau} \tag{4.2}$$

The coefficient 0.63 in this equation reflects the fact that an exponential process reaches 63 % of its final asymptotic state in τ seconds.

The instantaneous accommodation velocity $\mathrm{v}(t)$ was the derivative of the accommodation trace in time (no fitting) and the peak accommodation velocity was extracted:

$$\mathrm{v}(t) = \frac{d(SE_4)}{dt}$$
$$\mathrm{v}max(t) = max\left[\frac{d(S.E.)}{dt}\right] \tag{4.3}$$

6.2 Refraction steady states

Due to the wavelength dependence of the human eye, it is a well-known fact that the eye becomes myopic at short wavelengths and hyperopic at long wavelengths (see section 1.5.2 and Figure 6.1, on center). Therefore, changes in monocular blur should generate an accommodation cue to re-focus the image onto the retina as a function of stimulus wavelength. Figure 6.2 shows the mean refraction (SE_4) for far and near steady states of accommodation (left) and the refraction step (right).

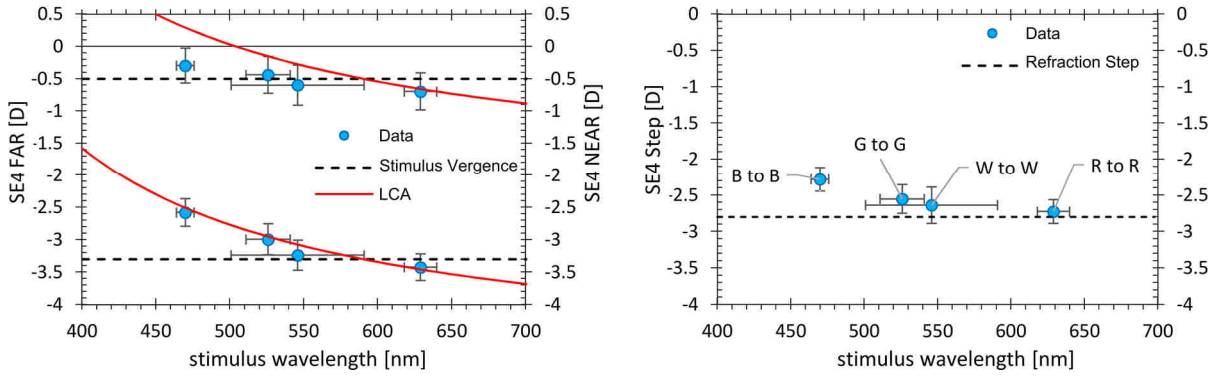

Figure 6.2: Mean refraction for far and near steady states of accommodation (left) and mean refraction step (right) as a function of wavelength same-color stimuli (cases R→R, G→G, B→B, and W→W). Blue circles are experimental data for steady states of accommodation. Vertical and horizontal error bars are standard deviation of refraction across subjects and FWHM of stimulus spectrum, respectively. Red curves represent the theoretical induced accommodation for both steady states in order to compensate the longitudinal chromatic aberration (stimulus vergence - theoretical chromatic difference of focus).

Far refraction was -0.69 ± 0.29 D, -0.44 ± 0.28 D and -0.29 ± 0.27 D for RGB, and -0.60 ± 0.31 D for W. Near refraction was -3.43 ± 0.20 D, -2.99 ± 0.24 D, and -2.58 ± 0.21 D for RGB and -3.24 ± 0.23 D for W. The experimental data followed a similar behavior than the theoretical accommodation (red curves) as a function of stimulus wavelength for both accommodative states, although some discrepancies were observed for short wavelengths and at far. The theoretical chromatic difference of focus from short-to-long wavelength (470 nm to 629 nm) was -0.97 D. Experimentally, we found a chromatic difference of -0.40 ± 0.06 D and -0.84 ± 0.05 D for far and near accommodation respectively. The mean refraction step (Figure 6.2, right) was -2.72 ± 0.16 D, -2.55 ± 0.19 D, and -2.28 ± 0.16 D for RGB and -2.64 ± 0.25 D for W for a theoretical step of -2.8 D. These results showed that accommodation did not compensate totally the effect of LCA at short wavelengths for far.

Figure 6.3 plots mean refraction under steady states accommodation (left) and mean refraction step (right) for extreme-to-extreme accommodation tasks (far-to-near combinations

R→B and B→R). At far stimulus vergence, refraction was -0.78 ± 0.33 D and -0.33 ± 0.28 D for R and B respectively and for near it was -2.87 ± 0.24 D and -3.37 ± 0.20 D.

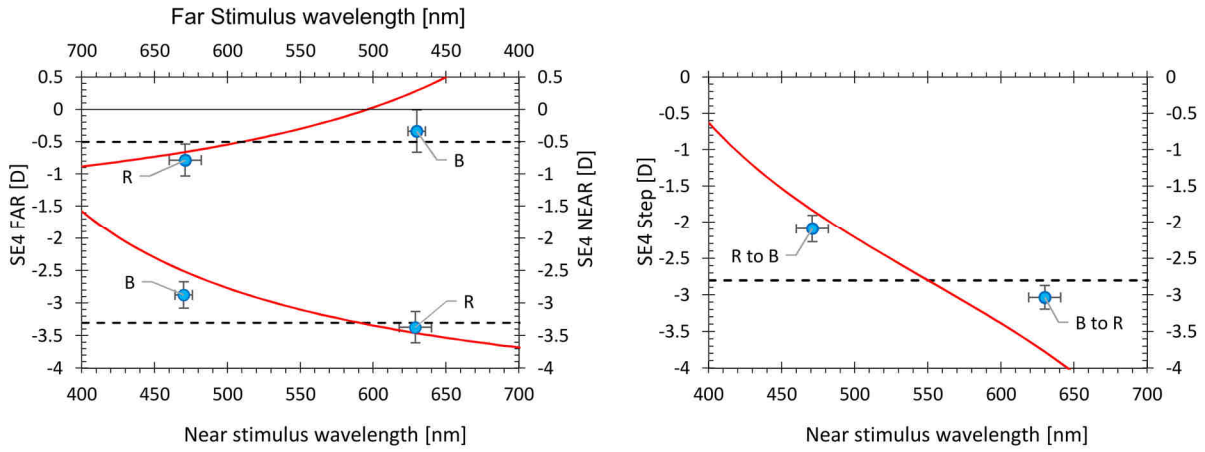

Figure 6.3: Mean refraction (SE_4) for far and near steady states of accommodation (left) and mean refraction step (right) as a function of stimulus wavelength for extreme-to-extreme accommodation (Combinations R→B and B→R). Symbols correspond to experimental data and curves to theoretical predictions based on ocular LCA.

Refraction step was -2.09 ± 0.19 D and -3.03 ± 0.16 D for red-to-blue (R→B) and blue-to-red (B→R) respectively. The chromatic difference of focus between blue and red was -0.44 ± 0.12 D for far and -0.50 ± 0.08 D for near. Experimental data followed a similar to predicted behavior but accommodation only partially counterbalanced the effect of LCA.

Figure 6.4 plots results for white-to-color accommodation tasks (Combinations W→R, W→G, W→B, W→W). For far accommodation in white light, refraction took values around -0.56 D with SD around 0.03 D, very close to the stimulus vergence (-0.5 D). Near refraction was -3.48 ± 0.21 D, -3.09 ± 0.20 D and -2.84 ± 0.13 D for RGB. For comparison, we have included in Figure 6.4 data points corresponding to the combination W→W, already presented in Figure 6.2. Experimental data followed the predicted trend, as accommodation counterbalanced the effect of LCA. The chromatic difference of focus was -0.64 ± 0.17 D for near accommodation, and the refraction step was -2.91 ± 0.22 D, -2.57 ± 0.19 D, and –2.26 ± 0.22 D for W→R, W→G, and W→B, respectively.

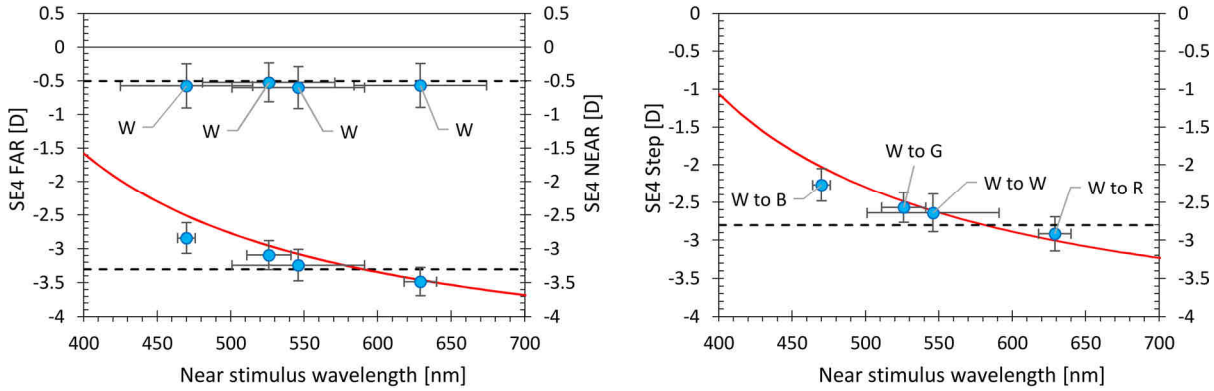

Figure 6.4: Mean refraction (SE_4) for far and near steady states of accommodation (left) and mean refraction step (right) as a function of stimulus wavelength for white-to-color accommodation tasks, (Combinations were W→R, W→G, W→B, and W→W).

6.3 Chromatic difference of focus

Figure 6.5 plots the experimental chromatic difference of focus with reference to the white light case. Red curves represents the chromatic difference of focus determined by Thibos et al (Thibos et al., 1992), which corresponds to the changes of accommodation as a function of wavelength mentioned in section 1.5.2. Purple curves correspond to the shifted version of Thibos' curve that best matches our experimental data. The computed shift of focus was obtained by fitting the experimental data to Eq. 1.5, leaving only p (vertical origin) as a free parameter and using Thibos' values for q and c (633.27 and 218.358 in nm).

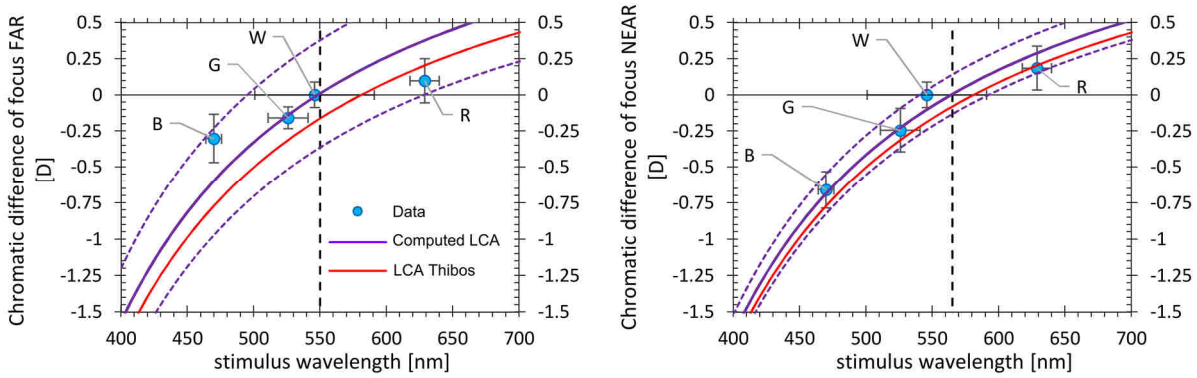

Figure 6.5: Computed chromatic difference of focus for far (left) and near (right) steady states of accommodation as a function of stimulus wavelength. Blue circles represent the experimental data. Vertical and horizontal error bars are standard deviation across subjects and stimulus spectral FWHM, respectively. Red curves correspond to the modelled chromatic difference of focus with respect to 590-nm (Thibos et al., 1992). Purple curves are shifted versions of the red lines, with a shift that best fits the experimental data. Dashed curves are the 95% confidence intervals.

For near accommodation (right panel), the computed CDF from experimental data agrees well with the expected theoretical CDF. Thibos' curve, once shifted, is included in the standard deviation of the experimental data. For far accommodation, the experimental data for blue and red wavelengths do not agree to the expected CDF. Furthermore, the increase on the standard deviation in the extreme parts of visible spectrum (R, B) means increased variability across subjects compared to the central part of the visible spectrum (G, W).

Figure 6.6 plots the chromatic difference of focus for red and blue stimuli in extreme-to-extreme tasks (R→B and B→R).

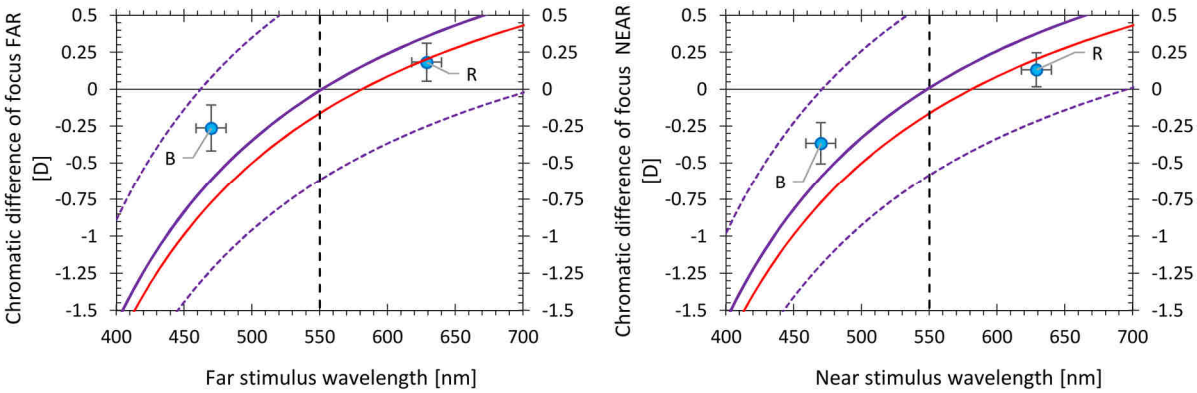

Figure 6.6: Computed chromatic difference of focus for far (left) and near (right) steady states of accommodation as a function of stimulus wavelength.

For these colors, accommodation did not fully compensate the effect of LCA neither for far nor for near.

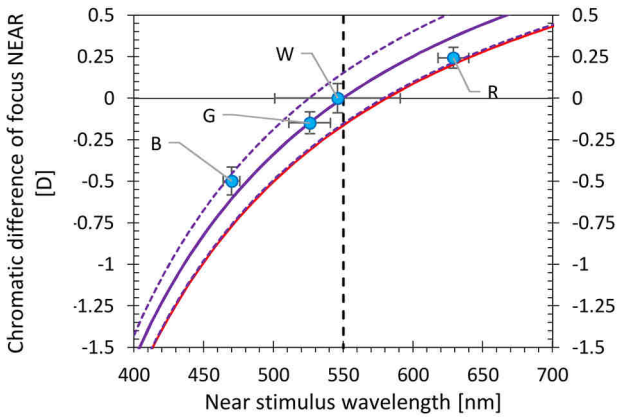

Figure 6.7: Computed chromatic difference of focus for near steady state as a function of stimulus wavelength after accommodation from a white far stimulus.

Figure 6.7 plots CDF for the near stimuli as a function of wavelength, after a white-to-color task. As expected, accommodation showed an experimental behavior similar to the theoretical curve and compensated quite well the LCA of human eye.

6.4 Mean accommodation time and velocity

Figure 6.8 plots the mean accommodation time (left panel) and the mean accommodation velocity (right panel). For same-color tasks (top panel), mean accommodation time ranged between 0.26 ± 0.06 s (R→R), 0.25 ± 0.039 s (G→G), 0.23 ± 0.03 s (B→B), and 0.27 ± 0.051 s (W→W). Mean accommodation velocity was 6.68 ± 1.01 D/s, 6.62 ± 1.04 D/s, 6.28 ± 0.65 D/s, and 6.23 ± 1.27 D/s for R→R, G→G, B→B, and W→W respectively. For extreme-to-extreme cases (central panel), mean accommodation time was 0.25 ± 0.07 s and 0.36 ± 0.07 s, and mean accommodation velocity was 5.57± 1.06 D/s and 5.45 ± 0.9 D/s for R→B and B→R respectively. Finally, for white-to-color tasks, mean accommodation time was 0.29 ± 0.07 D/s, 0.24 ± 0.04 D/s, and 0.23 ± 0.05 D/s, and 0.27 ± 0.05 D/s, and mean accommodation velocity was 6.66 ± 1.61 D/s, 6.99 ± 1.03 D/s, 6.47 ± 0.85 D/s, and 6.23 ± 1.27 D/s for W→R, W→G, W→B and W→W respectively. Data on average show high intersubject variability, which makes interpretation somehow difficult. Nonetheless, if accommodation data are evaluated individually some tendency can be observe such as an increase of accommodation time with refraction step.

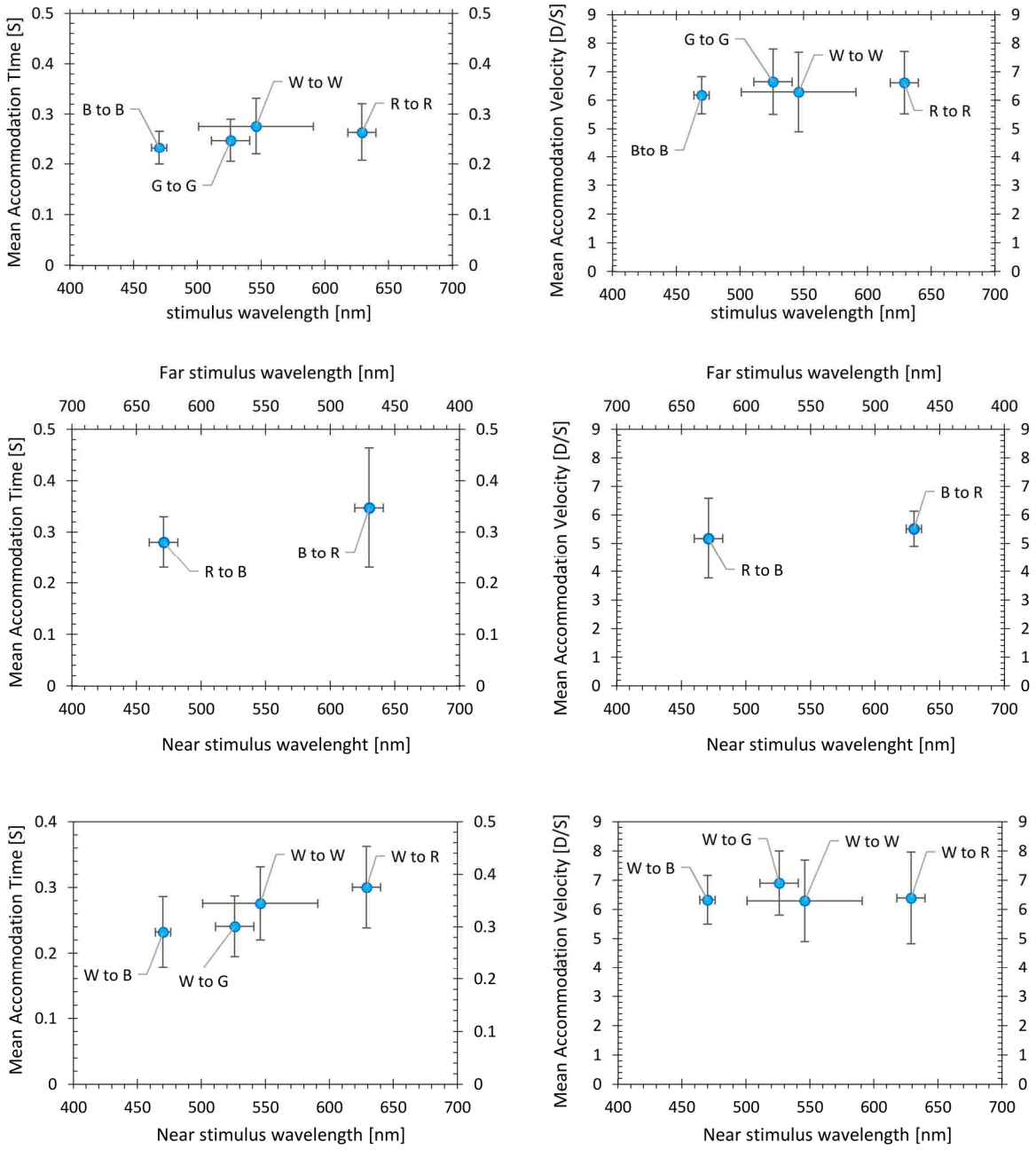

Figure 6.8: Mean accommodation time (left) and mean accommodation velocity (right) as a function of stimulus wavelength. Top row: Far and near stimuli of same color; central row: extreme-to-extreme accommodation; bottom row: white-to-color accommodation. Vertical and horizontal error bars are standard deviation across subjects and FWHM of the stimulus spectrum, respectively.

Table 11 summarizes the experimental data on average across subjects. Figure 6.9 plots mean accommodation time and velocity as a function of 63% refraction step for all color combination. A linear increase of the mean accommodation time with increasing refraction step can be seen (R^2=0.65). Conversely, the mean velocity of accommodation exhibits a large

variability with refractions step (see, Figure 6.9, right) and do not show a pattern or tendency (R^2=0.00) over the refraction step range.

Mean Value	Convergence step ± std [D]	Pupil miosis ± std [mm]	Refraction step ± std [D]	Time constant (τ) ± std [s]	Velocity (63% step) ± std [D/s]	Peak Velocity [D/s]
B→B	2.61±0.34	0.99±0.38	-2.28±0.16	0.23±0.03	6.28±0.65	7.63 ±2.05
G→G	2.54±0.32	0.93±0.26	-2.55±0.20	0.25±0.04	6.62±1.04	7.43±1.76
W→W	2.56±0.37	1.03±0.34	-2.64±0.25	0.27±0.05	6.23±1.27	7.35±1.92
R→R	2.56±0.38	0.93±0.38	-2.73±0.16	0.26±0.06	6.68±1.01	7.78±1.4
B→R	2.68±0.37	1.20±0.21	-3.03±0.16	0.36±0.07	5.45±0.9	6.68±0.80
R→B	2.63±0.30	0.91±0.28	-2.09±0.19	0.25±0.07	5.57±1.06	6.88±1.01
W→B	2.57±0.32	0.97±0.33	-2.27±0.22	0.23±0.05	6.47±0.85	7.80±1.25
W→G	2.54±0.33	1.02±0.33	-2.57±0.19	0.24±0.04	6.99±1.03	7.76±1.63
W→R	2.63±0.37	1.18±0.47	-2.91±0.22	0.29±0.07	6.66±1.61	8.25±1.65

Table 11: Experimental data obtained for each color combination. Errors are standard deviation across subjects.

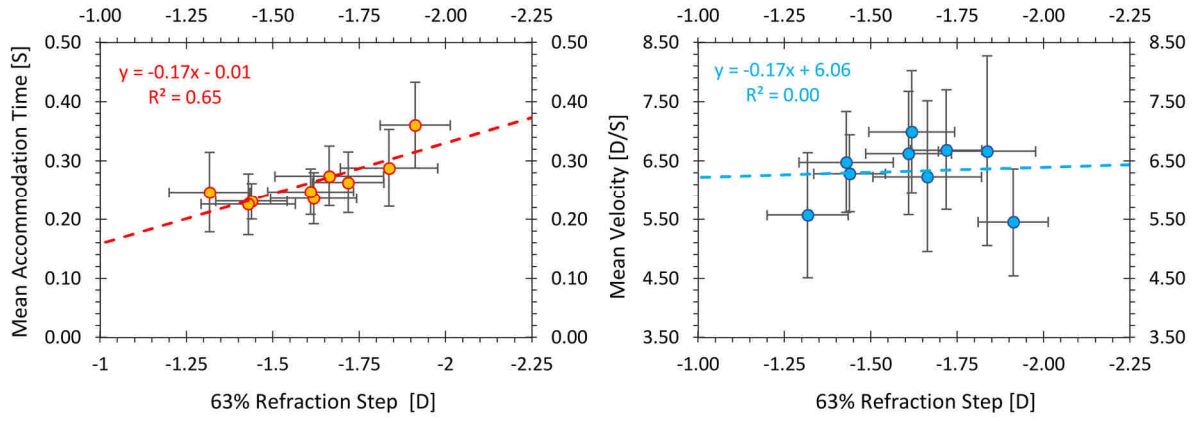

Figure 6.9: Mean accommodation time (left) and mean velocity (right) as a function of 63% refraction step (to be concordant with the time constant). Circles are experimental data and dotted lines are linear regression fit results. Horizontal and vertical error bars are standard deviation across subjects.

These results suggest a relation between accommodation time and stimulus wavelength, since accommodation is wavelength dependent. On the contrary, mean velocity of accommodation on average does not seem to be strongly influenced by stimulus wavelength.

Figure 6.10 shows the pupil constriction (miosis) and convergence step as a function of the total refraction step.

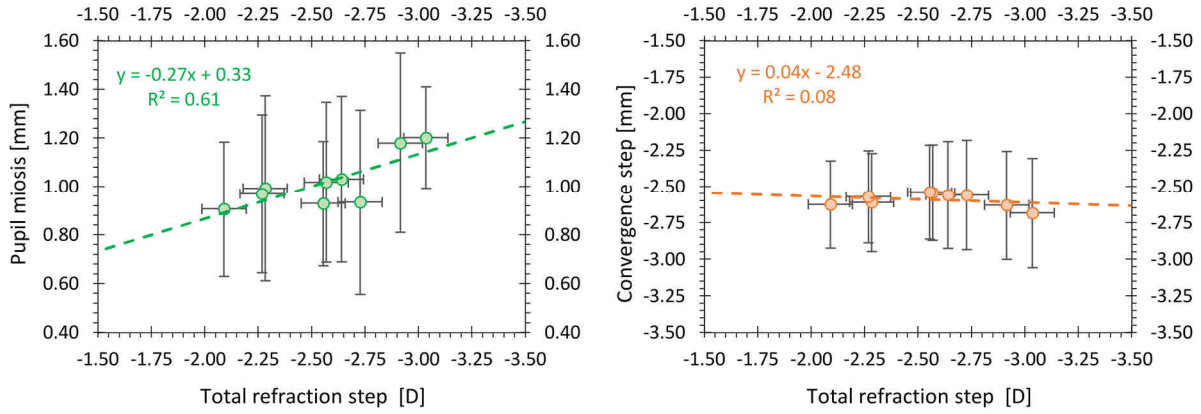

Figure 6.10: Mean pupil constriction (left) and mean convergence (right) as a function of total refraction step. Circles are experimental data and dotted lines are linear regression fit results. Horizontal and vertical error bars are the standard deviation across subjects.

The mean convergence step across subjects for same-color stimuli was -2.56 ± 0.38 D, -2.54 ± 0.32 D, -2.61 ± 0.34 D, and -2.56 ± 0.37 D for R, G, B, and W respectively (see Table 11), and was -2.68 ± 0.37 D and -2.63 ± 0.30 D for extreme-to-extreme stimuli. For comparison, the total refraction step was -3.03 ± 0.16 D and -2.09 ± 0.19 D for B→R and R→B respectively. Across subjects and color cases, mean convergence was -2.60 ± 0.05 D on average for a theoretical step of -2.80 D. A linear fit (R^2=0.08) shows a relatively unchanged convergence on average with refraction step.

Table 11, second column, and These results suggest a relation between accommodation time and stimulus wavelength, since accommodation is wavelength dependent. On the contrary, mean velocity of accommodation on average does not seem to be strongly influenced by stimulus wavelength.

Figure 6.10 left summarize data on pupil miosis. Values ranged between 0.91 and 1.20 with intersubject variability between ± 0.21 mm and ± 0.47 mm. The mean amplitude of miosis across subjects and same-colors conditions was 1.02 ± 0.11 mm. A linear increase in pupil constriction with increasing refraction step amplitude (R^2=0.61) can be seen.

Despite the fact that miosis amplitude increase and convergence remains unchanged on average with refraction step, absolute pupil size and convergence show high intersubject variability, making results difficult to interpret and individual analyze can help to better understand a general behavior or tendency with stimulus wavelength.

Paired T-tests were performed between subject mean values to determine the statistical significance of the changes in refraction (SE_4), accommodation time and velocity, and pupil miosis with stimuli color combination. Results for refraction and accommodation are shown in Table 12 through 14 respectively.

Spherical Equivalent SE4	Far and Near of same colors				Far : W and Near: RGB			Extreme-to-extreme	
	R→R	G→G	B→B	W→W	W→R	W→G	W→B	B→R	R→B
R→R	X	0.03	0.00	0.39	0.07	0.17	0.00	0.00	0.00
G→G		X	0.00	0.12	0.00	0.31	0.00	0.00	0.00
B→B			X	0.01	0.00	0.00	0.79	0.00	0.01
W→W				X	0.00	0.16	0.00	0.00	0.00
W→R					X	0.00	0.00	0.04	0.00
W→G						X	0.00	0.00	0.00
W→B							X	0.00	0.01
B→R								X	0.00
R→B									X

Table 12: Statistical analysis of the changes in mean refraction step as a function of stimuli color combination. Orange cells indicate statistically significance (p-value<0.05) and green cells correspond to p-values between 0.05 and 0.10.

Accommodation Time	Far and Near of same colors				Far : W and Near: RGB			Extreme-to-extreme	
	R→R	G→G	B→B	W→W	W→R	W→G	W→B	B→R	R→B
R→R	X	0.07	0.10	0.01	0.06	0.02	0.06	0.02	0.50
G→G		X	0.30	0.01	0.05	0.31	0.26	0.01	0.81
B→B			X	0.04	0.04	0.69	0.67	0.00	0.61
W→W				X	0.40	0.00	0.02	0.03	0.31
W→R					X	0.03	0.04	0.10	0.25
W→G						X	0.31	0.01	0.82
W→B							X	0.01	0.43
B→R								X	0.02
R→B									X

Table 13: Statistical analysis of the changes in mean accommodation time as a function of stimuli color combination. Orange cells indicate statistically significance (p-value<0.05) and green cells correspond to p-values between 0.05 and 0.10.

Accommodation Velocity	Far and Near of same colors				Far : W and Near: RGB			Extreme-to-extreme	
	R→R	G→G	B→B	W→W	W→R	W→G	W→B	B→R	R→B
R→R	X	0.082	0.38	0.16	0.96	0.12	0.53	0.09	0.19
G→G		X	0.49	0.06	0.92	0.15	0.74	0.09	0.24
B→B			X	0.92	0.53	0.13	0.49	0.07	0.19
W→W				X	0.34	0.01	0.60	0.44	0.66
W→R					X	0.41	0.73	0.23	0.38
W→G						X	0.09	0.01	0.04
W→B							X	0.04	0.07
B→R								X	0.66
R→B									X

Table 14: Statistical analysis of the changes in mean accommodation velocity as a function of stimuli color combination. Orange cells indicate statistically significance (p-value<0.05) and green cells correspond to p-values between 0.05 and 0.10.

The changes in refraction step with stimuli color combination were statistically significant in most cases (Table 12) as was the case for accommodation time (Table 13). This combined behavior was to be expected since both parameters are correlated. This result confirms the change in accommodation time with stimulus wavelength. On the contrary, accommodation velocity changes were typically non-significant (Table 14) expect in some cases for extreme-to-extreme color combinations.

6.5 Dynamics of accommodative response

Figure 6.11 plots the dynamic response of accommodation, convergence and pupil size for three subjects when far-to-near accommodation was performed for stimuli of same wavelength (B→B, G→G, W→W, and R→R, from top to bottom). As previously mentioned, to re-focus the image onto the retina an effort of accommodation or disaccommodation is required to compensate chromatic blur. This has the effect of shifting the accommodation curves (blue line) along the y-axis as a function of stimulus wavelength. In addition, an offset version of the interpupillary distance, oIDP, can be used to study the dynamics of the convergence response. As previously discussed, our system does not allow direct measurements of convergence for far and near steady state, and it estimates the change in convergence between two accommodation states only. Thus,

convergence response (black curves) was shifted vertically (y-axis) to match the theoretical stimulus vergence for far (-0.5 D).

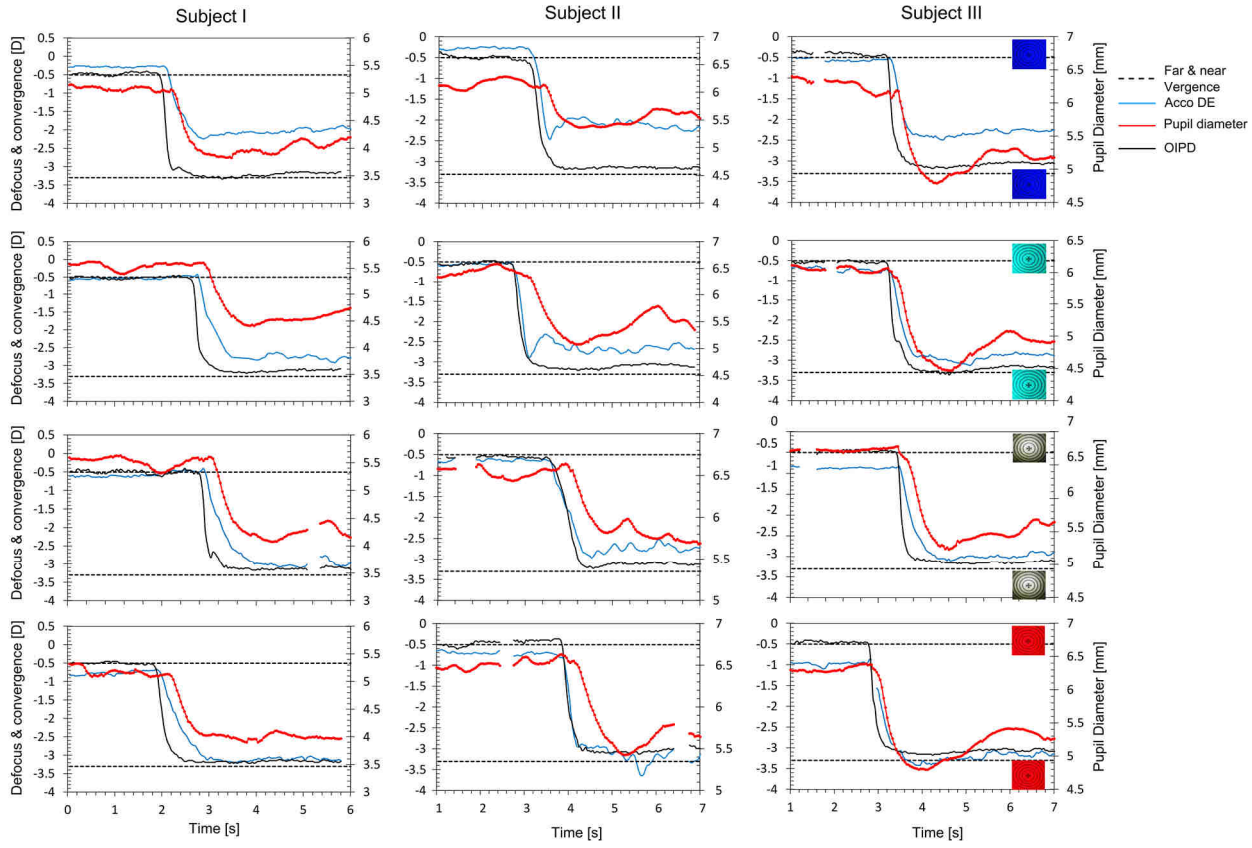

Figure 6.11: Dynamic of accommodative response in three subjects from left to right for far-to-near stimuli of same color. Top: blue stimuli. Center-up: green stimuli. Center-down: white stimuli. Bottom: red stimuli. Accommodation of the DE eye, convergence and pupil size response are in blue, black and red respectively. The dotted black lines show far (-0.5D) and near (-3.3D) stimulus vergence.

Figure 6.12 plots the dynamic response of accommodation, convergence and pupil size for three subjects when white-to-color accommodation was performed (W→B, W→G, W→W, and W→R from top to bottom).

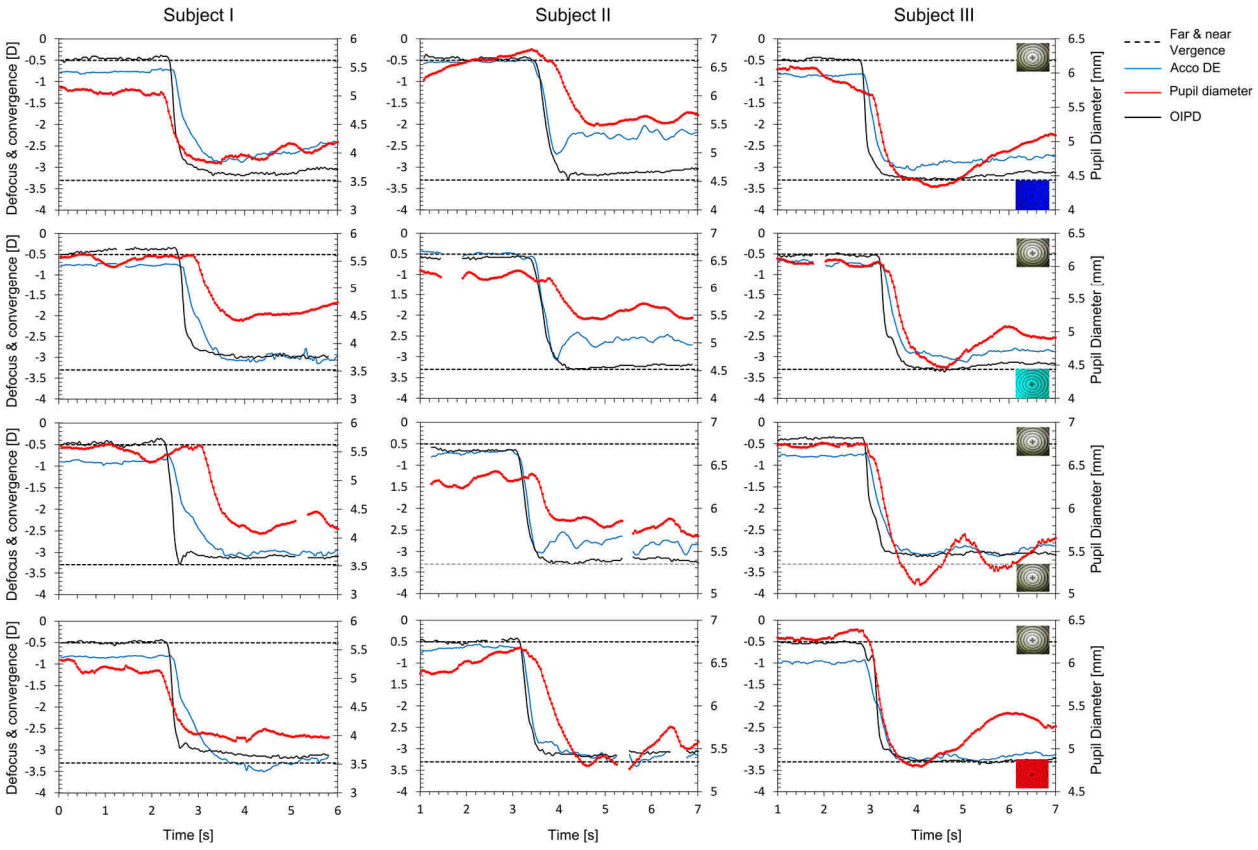

Figure 6.12: Dynamic response of near triad in three subjects from left to right and for white-to-color accommodation. Top: W→B. Center-up: W→G. Center-down: W→W (different repetition than for Figure 6.11). Bottom: W→R. DE accommodation, convergence and pupil size response are in blue, black and red respectively.

Figure 6.13 plots the dynamic response of accommodation, convergence and pupil size for same three subjects when extreme-to-extreme accommodation was performed (B→R and R→B).

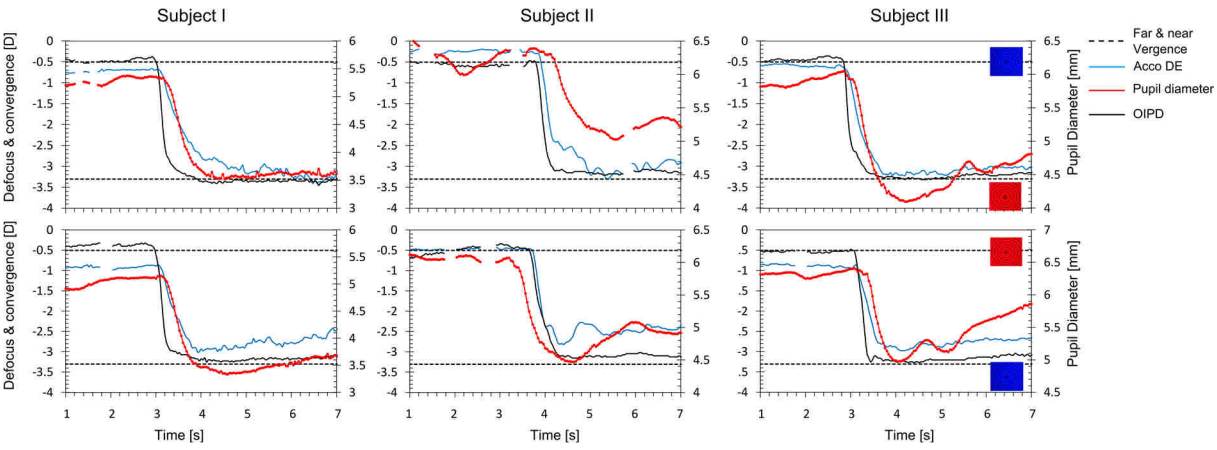

Figure 6.13: Dynamic response of near triad in three subjects from left to right and for white-to-color accommodation. Top: B→R. Bottom: R→B. DE accommodation, convergence and pupil size response are in blue, black and red respectively. Dotted black lines show far and near stimulus vergence.

6.6 Discussion

Changes in accommodation, pupil size, convergence, and temporal dynamic of the accommodative response were studied in seven subjects when voluntary far-to-near accommodation was performed under natural binocular viewing conditions for different combinations of colored stimuli in the visible spectrum from 470 nm to 629 nm.

Refraction estimated from the fourth-order spherical equivalent showed a consistent behavior of accommodation as a function of stimulus wavelength, in agreement with previous studies (Charman & Tucker, 1978) (Aggarwala, Nowbotsing, et al., 1995) (Aggarwala, Kruger, et al., 1995) (Seidemann & Schaeffel, 2002) (Rucker & Kruger, 2004b). For near stimuli, experimental SE_4 closely followed the theoretical predictions based on LCA, and accommodation compensated fairly well the chromatic blur. However, data for far accommodation presented some discrepancies for blue wavelength: The eye's accommodation did not accommodate as far as expected to compensate the chromatic blur. A statistical analysis showed that changes in refraction step with color combinations were statistically significant. The chromatic difference of focus from short to long wavelength (470 nm to 629 nm) was 0.50 ± 0.10 D (ranging between 0.33 D and 0.62 D) for far accommodation and was 0.74 ± 0.17 D (between 0.55 D and 0.98 D) for near. This behavior is consistent with previous studies in the deep blue (Kröger & Binder, 2000) (Seidemann & Schaeffel, 2002). It has been suggested that monochromatic aberrations could defend the eye from chromatic blur (McLellan et al., 2002) for large pupils, and this could be a potential reason for the discrepancies at far vergence when pupils were larger, and thus monochromatic aberrations greater. For long wavelengths, we found that experimental data resembled theoretical accommodation.

Accommodation time ranged between 0.23 ± 0.03 s and 0.36 ± 0.07 s, with a tendency to increase through the visible spectrum from short to long wavelength, concordant with the increase in the refraction step. A statistical analysis showed that changes of accommodation time with refraction step were statistically significant. Mean accommodation velocity varied widely across subjects and color combinations and ranged between 5.17 ± 1.06 D/s and 6.99 ± 1.03 D/s. No clear trend was found with refraction step through the visible spectrum and changes of mean velocity of accommodation were not statistically significant. The peak velocity of accommodation also varied widely across subjects and color combination ranged between 6.68 ± 0.80 D/s y 8.25±1.65 D/s.

A linear increase in pupil constriction with increasing refraction step was observed. Amplitude of miosis was 1.02 ± 0.11 mm on average across subjects and color combinations.

Convergence, estimated from the interpupillary distance, was of -2.59 ± 0.05 D on average for a -2.80 D demand. No statistical changes in convergence step were observed as a function of stimulus wavelength. Retinal disparity and monocular blur, somewhat seem to provide conflicting information to the visual system: The first helping to maintain convergence at the stimulus

vergence by binocular fusion; the latter driving accommodation changes to counterbalance the eye's longitudinal chromatic aberration and may explain why some discrepancies were observed at short wavelengths.

Conclusions

7 Conclusions

The aim of this thesis was to design, build, and calibrate a binocular Hartmann-Shack wavefront sensor operating in infrared to study accommodation response and monochromatic aberrations of the human eye in open-view configuration under realistic viewing conditions. The instrument included a real time binocular pupil tracker at 25 Hz for convergence and pupil size measurement. The instrument's capabilities were first tested and validated in a group of normal young subjects. The instrument was then applied in three experiments. 1) The study of the dynamics of accommodation response under natural binocular and monocular vision for a far-to-near visual task; 2) the study of the accommodation response and refraction at low luminance in relation with the phenomenon of night myopia; and 3) the evaluation of the effect of polychromatic light in the accommodation mechanism.

1. An infrared Hartmann-Shack (H-S) wavefront sensor was developed for measuring the accommodation response and monochromatic aberrations in both eyes simultaneously. The instrument allowed unobtrusive measurements at 1050 nm up to 25 Hz. A two levels-design provided an "open-view" configuration where the field of view was realistic.

2. The H-S instrument demonstrated good capacities, allowing simultaneous measurement of refraction, pupil size and monochromatic aberrations in both eyes as well as convergence from the interpupillary distance under steady states accommodation.

3. The instrument operating range was limited to a maximum rotation of eye about 12.5º for monocular convergence. If convergence is split evenly between eyes, this allows measurements of target vergence up to 7 D.

4. Temporal dynamics of the accommodation responses (accommodation, pupil miosis and convergence) have shown strong similarity between eyes in binocular and monocular vision, except for eye motion in monocular. All three processes have shown a faster temporal response in binocular.

5. In monocular vision, an initial fast saccadic-like eye movement in temporal direction of the fellow eye occurred at the onset of accommodation. Then, monocular blur provided a cue to accommodate and the cross-link accommodation-convergence triggered convergence of the fellow eye in nasal direction, synchronized with accommodation.

6. An increasing myopic shift of accommodation was observed on average with decreasing luminance and with high intersubject variability. Some subjects presented no changes or slight hyperopic shifts of accommodation.

7. The shift of accommodation at low luminance in binocular had the same tendency as in monocular vision for all subjects but with a reduced magnitude, probably caused by binocular summation.

8. The dark focus or tonic accommodation was highly correlated between eyes ($R^2 = 0.90$) and to the magnitude of defocus shift in both monocular (R^2=0.77) and binocular (R^2=0.92) vision. This is explained the similarity of night myopia phenomenon between eyes and it suggests that the shift of accommodation at low luminance has an accommodative genesis.

9. Dark convergence was moderately correlated ($R^2 = 0.43$) with dark focus suspecting a dissociation of vergence and accommodation in total darkness.

10. Refraction measured in the visible spectrum showed consistent changes of the accommodation process to counterbalance the effect of longitudinal chromatic aberration, although with some discrepancies at short wavelength.

11. A linear increase of accommodation time following an increase of the refraction step suggested a correlation with stimulus wavelength, while mean and peak velocity of accommodation were not influenced by wavelength.

12. No significant changes of convergence were observed with refraction step. Retinal disparity and monocular blur seem to provide conflicting information: the first helping to maintain convergence at the stimulus vergence, the latter driving accommodation changes to counterbalance the eye's longitudinal chromatic aberration.

References

Reference

Aggarwala, K. R., Kruger, E. S., Mathews, S., & Kruger, P. B. (1995). Spectral bandwidth and ocular accommodation. *Journal of the Optical Society of America. A, Optics, Image Science, and Vision*, *12*(3), 450–455.

Aggarwala, K. R., Nowbotsing, S., & Kruger, P. B. (1995). Accommodation to monochromatic and white-light targets. *Investigative Ophthalmology and Visual Science*, *36*(13), 2695–2705.

Aldaba, M., Vilaseca, M., Díaz-Doutón, F., Arjona, M., & Pujol, J. (2012). Measuring the accommodative response with a double-pass system: comparison with the Hartmann-Shack technique. *Vision Research*, *62*, 26–34. http://doi.org/10.1016/j.visres.2012.03.021

Alpern, M. (1958). Variability of accommodation during steady fixation at various levels of illuminance. *Journal of the Optical Society of America*, *48*(3), 193–197. http://doi.org/10.1364/JOSA.48.000193

Alpern, M., & Ellen, P. (1956). A quantitative analysis of the horizontal movements of the eyes in the experiment of Johannes Mueller. I. Method and results. *American Journal of Ophthalmology*, *42*, 289–296. http://doi.org/10.1016/0002-9394(56)90380-4

ANSI Z136.1. (2007). *ANSI Z136.1 American National Standard for Safe Use of Lasers*.

ANSI Z80.28. (2004). *Methods for reporting optical aberrations of eyes*.

Applegate, R. A., Donnelly III, W. J., Marsack, J. D., & Koenig, D. E. (2007). Three-dimensional relationship high-order root-mean-square between wavefront error, pupil diameter, and aging. *Journal of the Optical Society of America A*, *24*(3), 578–587.

Arnulf, A., Flamant, F., & Françon, M. (1948). Etude expérimentale de la myopie acquise par l'oeil en vision de nuit. *Rev. Opt. Théor. Instrum*, *27*, 741–745.

Artal, P., Chen, L., Fernández, E. J., Singer, B., Manzanera, S., & Williams, D. R. (2004). Neural compensation for the eye ' s optical aberrations. *Jounral of Vision*, *4*(4), 281–287. http://doi.org/10.1167/4.4.4

Artal, P., Guirao, A., Berrio, E., & Williams, D. R. (2001). Compensation of corneal aberrations by the internal optics in the human eye. *Journal of Vision*, *1*(1), 1–8. http://doi.org/10:1167/1.1.1

Artal, P., Schwarz, C., Cánovas, C., & Mira-Agudelo, A. (2012). Night myopia studied with an adaptive optics visual analyzer. *PloS One*, *7*(7), 1–6.

Arumi, P., Chauhan, K., & Charman, W. N. (1997). Accommodation and acuity under night-driving illumination levels. *Ophthalmic and Physiological Optics*, *17*(4), 291–299.

Atchison, D. A., & Charman, W. N. (2010). Thomas Young ' s contribution to visual optics : The Bakerian lecture " On the mechanism of the eye ." *Journal of Vision*, *10*(16), 1–16.

Atchison, D. A., Collins, M. J., Wildsoet, C. F., Christensen, J., & Waterworth, M. D. (1995). Measurement of monochromatic ocular aberrations of human eyes as a function of accommodation by the howland aberroscope technique. *Vision Research*, *35*(3), 313–323. http://doi.org/10.1016/0042-6989(94)00139-D

Atchison, D. A., & Smith, G. (2000). Optics of the human eye. *Butterworth-Heinemann*.

Atchison, D. A., & Smith, G. (2005). Chromatic dispersions of the ocular media of human eyes. *Journal of the Optical Society of America. A, Optics, Image Science, and Vision*, *22*(1), 29–37.

Bedford, R. E., & Wyszecki, G. (1947). Axial chromatic aberration of the human eye. *Journal of the Optical Society of America*, *47*(6), 564–565.

Beers, A. P. A., & Van Der Heijde, G. L. (1994). In vivo determination of the biomechanical properties of the component elements of the accommodation mechanism. *Vision Research*, *34*(21), 2897–2905.

Bharadwaj, S. R., & Schor, C. M. (2006). Dynamic control of ocular disaccommodation: first and second-order dynamics. *Vision Research*, *46*(6–7), 1019–1037.

Bobier, W. R., Campbell, M. C., & Hinch, M. (1992). The influence of chromatic aberration on the static accommodative response. *Vision Research*, *32*(5), 823–832.

Boettner, E. A., & Wolter, J. R. (1962). Transmission of the ocular media. *Investigative Ophthalmology & Visual Science*, *1*(6), 776–783.

Brown, N. (1973). The change in shape and internal form of the lens of the eye on accommodation. *Experimental Eye Research*, *15*(4), 441–459.

Cagigal, M. P., Canales, V. F., Castejón-Mochón, J. F., Prieto, P. M., López-Gil, N., & Artal, P. (2002). Statistical description of wave-front aberration in the human eye. *Optics Letters*, *27*(1), 37–39.

Campbell, C. E. (2009). The range of local wavefront curvatures measurable with Shack-Hartmann wavefront sensors. *Clinical and Experimental Optometry*, *92*(3), 187–193.

Cánovas, C., Prieto, P. M., Manzanera, S., Mira, A., & Artal, P. (2010). Hybrid adaptive-optics visual simulator. *Optics Letters*, *35*(2), 196–198.

Charman, W. N. (1991). Wavefront aberration of the eye: A review. *Optometry and Vision Science*, *68*(8), 574–583.

Charman, W. N. (1999). Near vision, lags of accommodation and myopia. *Ophthalmic & Physiological Optics : The Journal of the British College of Ophthalmic Opticians (Optometrists)*, *19*(2), 126–33.

Charman, W. N., & Heron, G. (1988). Fluctuations in accommodation : A review. *Ophthalmic & Physiological Optics*, *8*, 153–164.

Charman, W. N., & Jennings, J. A. M. (1976). Objective measurements of the longitudinal chromatic aberration of the human eye. *Vision Research*, *16*(9), 999–1005.

Charman, W. N., & Tucker, T. (1978). Accommodation and color. *Journal of the Optical Society of America*, *68*(4), 459–471.

Cheng, H., Barnett, J. K., Vilupuru, A. S., Marsack, J. D., Applegate, R. A., Kasthurirangan, S., & Roorda, A. (2004). A population study on changes in wave aberrations with accommodation. *Journal of Vision*, *4*, 272–280.

Chin, S. S., Hampson, K. M., & Mallen, E. A. H. (2008). Binocular correlation of ocular aberration

dynamics. *Optics Express*, *16*(19), 14731–14745.

Chirre, E., Prieto, P. M., & Artal, P. (2015). Dynamics of the near response under natural viewing conditions with an open-view sensor. *Biomedical Optics Express*, *6*(10), 4200–4211.

Choi, M., Weiss, S., Schaeffel, F., Seidemann, A., Howland, H. C., Wilhelm, B., & Wilhelm, H. (2000). Laboratory, clinical, and kindergarten test of a new eccentric infrared photorefractor (PowerRefractor). *Optometry and Vision Science : Official Publication of the American Academy of Optometry*, *77*(10), 537–48. Retrieved from http://www.ncbi.nlm.nih.gov/pubmed/11100892

Ciuffreda, K. J. (1991). Accommodation and its anomalies. *Vision and Visual Dysfunction*, *1*, 231–279.

Cohen, Y., Zadok, D., Barkana, Y., Shochat, Z., Ashkenazi, I., Avni, I., & Morad, Y. (2007). Relationship between night myopia and night-time motor vehicle accidents. *Acta Ophthalmologica Scandinavica*, *85*(4), 367–370.

Cooper, D. P., & Pease, P. L. (1988). Longitudinal chromatic aberration of the human eye and wavelength in focus. *American Journal of Optometry and Physiological Optics*, *65*(2), 99–107. Retrieved from http://www.ncbi.nlm.nih.gov/pubmed/3364521

Cooper, J., Ciuffreda, K. J., & Kruger, P. B. (1982). Stimulus and response AC/A ratios in intermittent exotropia of the divergence-excess type. *British Journal of Ophthalmology*, *66*(6), 398–404.

Cornsweet, T. N., & Crane, H. D. (1970). Servo-controlled infrared optometer. *Journal of the Optical Society of America*, *60*(4), 548–554.

Cornsweet, T. N., & Crane, H. D. (1973). Accurate two-dimensional eye tracker using first and fourth Purkinje images. *Journal of the Optical Society of America*, *63*(8), 921–928.

Delori, F. C., Webb, R. H., & Sliney, D. H. (2007). Maximum permissible exposures for ocular safety (ANSI 2000), with emphasis on ophthalmic devices. *Journal of the Optical Society of America A*, *24*(5), 1250–1265.

Diaz-Santana, L., Torti, C., Munro, I., Gasson, P., & Dainty, C. (2003). Benefit of higher closed-loop bandwidths in ocular adaptive optics. *Optics Express*, *11*(20), 2597–2605.

Drexler, W., Baumgartner, A., Findl, O., Hitzenberger, C. K., & Fercher, A. F. (1997). Biometric investigation of changes in the anterior eye segment during accommodation. *Vision Research*, *37*(19), 2789–2800.

Duane, A. (1912). Normal values of the accommodation at all ages. *Journal of the American Medical Association*, *LIX*(12), 1010–1013.

Emsley, H. H. (1948). *Visual Optics, 4th ed.* (4th ed., H).

EN 60825. (2007). *EN 60825 Safety of laser products. Equipment classification and requirements*.

Epstein, D. (1983). Accommodation as the primary cause of low-luminance myopia. Experimental evidence. *Acta Ophthalmologica*, *61*(3), 424–430.

Epstein, D., Ingelstam, E., Jansson, K., & Tengroth, B. (1981). Low-luminance myopia as measured with a laser optometer. *Acta Ophthalmologica*, *59*(6), 928–943.

Fernández, E. J., & Artal, P. (2005). Study on the effects of monochromatic aberrations in the accommodation response by using adaptive optics. *Journal of the Optical Society of America*, *22*(9), 1732–1738.

Fernández, E. J., & Artal, P. (2008). Ocular aberrations up to the infrared range: from 632.8 to 1070 nm. *Optics Express*, *16*(26), 21199–21208.

Fernández, E. J., Iglesias, I., & Artal, P. (2001). Closed-loop adaptive optics in the human eye. *Optics Letters*, *26*(10), 746–748. http://doi.org/10.1364/OL.26.000746

Fernández, E. J., Povazay, B., Hermann, B., Unterhuber, A., Sattmann, H., Prieto, P. M., … Drexler, W. (2005). Three-dimensional adaptive optics ultrahigh-resolution optical coherence tomography using a liquid crystal spatial light modulator. *Vision Research*, *45*(28), 3432–3444. http://doi.org/10.1016/j.visres.2005.08.028

Fernández, E. J., Prieto, P. M., & Artal, P. (2009). Binocular adaptive optics visual simulator. *Optics Letters*, *34*(17), 2628–2630.

Fernández, E. J., Unterhuber, A., Povazay, B., Hermann, B., Artal, P., & Drexler, W. (2005). Chromatic aberration correction of the human eye for retinal imaging in the near infrared. *Optics Express*, *14*(13), 6213–25.

Fincham, E. F. (1925). The changes in the form of the crystalline lens in accommodation. *Optical Society*, *XXVI*, 239–269.

Fincham, E. F. (1951). The accommodation reflex and its stimulus. *The British Journal of Ophthalmology*, *35*(7), 381–393.

Fincham, E. F. (1962). Accommodation and convergence in the absence of retinal images. *Vision Research*, *1*, 425–440.

Fincham, E. F., & Walton, J. (1957). The reciprocal actions of accommodation and convergence. *Journal of Physiology*, *I*(37), 488–508.

Fonslow, B. R., Stein, B. D., Webb, K. J., Xu, T., Choi, J., Kyu, S., & Iii, J. R. Y. (2008). Longitudinal chromatic aberrations of the human infant eye. *Journal of the Optical Society of America. A, Optics, Image Science, and Vision*, *25*(9), 2263–2270. http://doi.org/10.1038/nmeth.2250.Digestion

Fry, G. A., & Hill, W. W. (1962). The center of rotation of the eye. *American Journal of Optometry and Archives of American Academy of Optometry*, *39*, 581–595.

Gambra, E., Sawides, L., Dorronsoro, C., & Marcos, S. (2009). Accommodative lag and fluctuations when optical aberrations are manipulated. *Journal of Vision*, *9*(6), 1–15.

Gilmartin, B., & Hogan, R. E. (1985a). The magnitude of longitudinal chromatic aberration of the human eye between 458 and 633 nm. *Vision Research*, *25*(11), 1747–1753. http://doi.org/10.1016/0042-6989(85)90148-8

Gilmartin, B., & Hogan, R. E. (1985b). The relationship between tonic accommodation and ciliary muscle innervation. *Investigative Ophthalmology & Visual Science*, *26*(7), 1024–1028.

Graef, K., & Schaeffel, F. (2012). Control of accommodation by longitudinal chromatic aberration and

blue cones. *Journal of Vision*, *12*(1), 1–12. http://doi.org/10.1167/12.1.14

Hampson, K. M., Chin, S. S., & Mallen, E. A. H. (2007). Binocular Shack-Hartmann sensor for the human eye. *Journal of Modern Optics*, *55*(4–5), 703–716. http://doi.org/10.1080/09500340701469674

Hampson, K. M., Chin, S. S., & Mallen, E. A. H. (2010). Effect of temporal location of correction of monochromatic aberrations on the dynamic accommodation response. *Biomedical Optics Express*, *1*(3), 879–894.

Hampson, K. M., & Mallen, E. A. H. (2011). Binocular adaptive optics system with dynamic convergence control. In *AOIM* (pp. 120–121).

Hartmann, J. (1900). Bemerkungen über den Bau and die justierung von spektrographen. *Zeitschrift Für Instrumentenkunde*, *20*, 47–64.

Hartridge, H. (1925). Helmholtz's theory of accommodation. *The British Journal of Ophthalmology*, *9*(5), 521–523.

Hazel, C. A., Cox, M. J., & Strang, N. C. (2003). Wavefront aberration and its relationship to the accommodative stimulus-response function in myopic subjects. *Optometry and Vision Science*, *80*(2), 151–158.

He, J. C., Burns, S. A., & Marcos, S. (2000). Monochromatic aberrations in the accommodated human eye. *Vision Research*, *40*(1), 41–48.

Helmholtz, H. (1855). Ueber die accommodation des auges. *Albrecht von Graefes Archiv Für Ophthalmologie*, *2*(1), 1–74.

Hennessy, R. T., & Leibowitz, H. W. (1972). Laser optometer incorporating the Badal principle. *Behavior Research Methods & Instrumentation*, *4*(5), 237–239.

Hermann, B., Fernández, E. J., Unterhuber, A., Sattmann, H., Fercher, A. F., Drexler, W., … Artal, P. (2004). Adaptive-optics ultrahigh-resolution optical coherence tomography. *Optics Letters*, *29*, 2142–2144.

Heron, G., Winn, B., Pugh, J. R., & Eadie, A. S. (1989). Twin channel infrared optometer for recording binocular accommodation. *Optometry and Vision Science : Official Publication of the American Academy of Optometry*, *66*(2), 123–9.

Hofer, H., Artal, P., Singer, B., Aragón, J. L., & Williams, D. R. (2001). Dynamics of the eye's wave aberration. *Journal of the Optical Society of America A*, *18*(3), 497.

Hofer, H., Carroll, J., Neitz, J., Neitz, M., & Williams, D. R. (2005). Organization of the human trichromatic cone mosaic. *The Journal of Neuroscience : The Official Journal of the Society for Neuroscience*, *25*(42), 9669–9679.

Hofer, H., Chen, L., Yoon, G.-Y., Singer, B., Yamauchi, Y., & Williams, D. R. (2001). Improvement in retinal image quality with dynamic correction of the eye's aberrations. *Optics Express*, *8*(11), 631–643. http://doi.org/10.1364/OE.8.000631

Hope, G. M., & Rubin, M. L. (1984). Night myopia. *Survey of Ophthalmology*, *29*(2), 129–136.

Howarth, P. A., Zhang, X. X., Bradley, A., Still, D. L., & Thibos, L. N. (1988). Does the chromatic aberration of the eye vary with age? *Journal of the Optical Society of America A*, *5*(12), 2087. http://doi.org/10.1364/JOSAA.5.002087

Hung, G. K., & Semmlow, J. L. (1980). Static behavior of accommodation and vergence: computer simulation of an interactive dual-feedback system. *IEEE Transactions on Bio-Medical Engineering*, *27*(8), 439–447. http://doi.org/10.1109/TBME.1980.326752

Ivanoff, A. (1955). Night binocular convergence and night myopia. *Journal of the Optical Society of America A*, *45*(9), 769–770.

Jaeken, B., Lundström, L., & Artal, P. (2011). Peripheral aberrations in the human eye for different wavelengths: off-axis chromatic aberration. *Journal of the Optical Society of America A*, *28*(9), 1871–1879. http://doi.org/10.1364/JOSAA.28.001871

Jiang, B.-C., Gish, K. W., & Leibowitz, H. W. (1991). Effect of luminance on the relation between accommodation and convergence. *American Academy of Optometry*, *68*(3), 200–225.

Johnson, C. A. (1976). Effects of luminance and stimulus distance on accommodation and visual resolution. *Journal of the Optical Society of America*, *66*(2), 138–142.

Judge, J. (1996). How is binocularity maintained during convergence and divergence ? *Royal College of Ophthalmologists*, 172–176.

Kasthurirangan, S., Vilupuru, A. S., & Glasser, A. (2003). Amplitude dependent accommodative dynamics in humans. *Vision Research*, *43*(27), 2945–2956.

Kergoat, H., & Lovasik, J. V. (1990). Influence of target color and vergence of light on ocular accommodation during binocular fixation. *Current Eye Research*, *9*(10), 935–953.

Kobayashi, M., Nakazawa, N., Yamaguchi, T., Otaki, T., Hirohara, Y., & Mihashi, T. (2008). Binocular open-view Shack-Hartmann wavefront sensor with consecutive measurements of near triad and spherical aberration. *Applied Optics*, *47*(25), 4619–4626.

Koomen, M., Scolnik, R., & Tousey, R. (1951). A study of night myopia. *Journal of the Optical Society of America*, *41*(2), 80–90.

Koomen, M., Tousey, R., & Scolnik, R. (1949). The spherical aberration of the eye. *Journal of the Optical Society of America*, *39*(5), 370–376.

Kotulak, J. C., Morse, S. E., & Billock, V. A. (1995). Red-green opponent channel mediation of control of human ocular accommodation. *Jounral of Physiology*, *482*(1995), 697–703.

Kotulak, J. C., Morse, S. E., & Rabin, J. C. (1995). Optical compensation for night myopia based on dark focus and CA / C ratio. *Investigative Ophtalmology & Visual Science*, *36*(8), 1573–1580.

Kotulak, J. C., & Schor, C. M. (1986). The dissociability of accommodation from vergence in the dark. *Investigative Ophthalmology and Visual Science*, *27*(4), 544–551.

Kröger, R. H., & Binder, S. (2000). Use of paper selectively absorbing long wavelengths to reduce the impact of educational near work on human refractive development. *The British Journal of Ophthalmology*, *84*(8), 890–893. http://doi.org/10.1136/bjo.84.8.890

Kruger, P. B., Nowbotsing, S., Aggarwala, K. R., & Mathews, S. (1995). Small amounts of chromatic aberration influence dynamic accommodation. *Optometry and Vision Science : Official Publication of the American Academy of Optometry*, *72*(9), 656–666.

Kruger, P. B., & Pola, J. (1986). Stimuli for accommodation: blur, chromatic aberration and size. *Vision Research*, *26*(6), 957–971. http://doi.org/10.1016/0042-6989(86)90153-7

Lee, J. H., Stark, L. R., Cohen, S., & Kruger, P. B. (1999). Accommodation to static chromatic simulations of blurred retinal images. *Ophthalmic & Physiological Optics : The Journal of the British College of Ophthalmic Opticians (Optometrists)*, *19*(3), 223–235. Retrieved from http://www.ncbi.nlm.nih.gov/pubmed/10627841

LeGrand, Y. (1967). Form and Space Vision, Revised Edition. Translated by Millodot M, Heath GG. *Bloomington: Indiana University Press*, 58–60.

Leibowitz, H. W., Gish, K. W., & Sheehy, J. B. (1988). Role of vergence accommodation in correcting for night myopia. *American Journal of Optometry and Physiological Optics*, *65*(5), 383–386.

Leibowitz, H. W., & Owens, D. A. (1975a). Anomalous myopias and the intermediate dark focus of accommodation. *Science (New York, N.Y.)*, *189*(4203), 646–648.

Leibowitz, H. W., & Owens, D. A. (1975b). Night myopia and the intermediate dark focus of accommodation. *Journal of the Optical Society of America*, *65*(10), 1121–1128.

Leibowitz, H. W., & Owens, D. A. (1978). New evidence for the intermediate position of relaxed accommodation. *Documenta Ophthalmologica*, *46*(1), 133–147.

Levene, J. R. (1965). Nevil Maskelyne, F.R.S., and the discovery of night myopia. *Notes and Records of the Royal Society of London*, *20*(1), 100–108.

Li, Y. J., Choi, J. A., Kim, H., Yu, S. Y., & Joo, C. K. (2011). Changes in ocular wavefront aberrations and retinal image quality with objective accommodation. *Journal of Cataract and Refractive Surgery*, *37*(5), 835–841.

Li, Y., & Wolf, E. (1981). Focal shifts in diffracted converging spherical waves. *Optics Communications*, *39*(4), 211–215.

Liang, J., Grimm, B., Goelz, S., & Bille, J. F. (1994). Objective measurement of wave aberrations of the human eye with the use of a Hartmann-Shack wave-front sensor. *Journal of the Optical Society of America A*, *11*(7), 1949–1957.

Liang, J., & Williams, D. R. (1997). Aberrations and retinal image quality of the normal human eye. *Journal of the Optical Society of America A*, *14*(11), 2873–2883.

Liang, J., Williams, D. R., & Miller, D. T. (1997). Supernormal vision and high-resolution retinal imaging through adaptive optics. *Journal of the Optical Society of America A*, *14*(11), 2884–2892.

Llorente, L., Diaz-Santana, L., Lara-Saucedo, D., & Marcos, S. (2003). Aberrations of the human eye in visible and near infrared illumination. *Optometry and Vision Science*, *80*(1), 26–35. http://doi.org/10.1097/00006324-200301000-00005

López-Gil, N., & Artal, P. (1997). Comparison of double-pass estimates of the retinal-image quality obtained with green and near-infrared light. *Journal of the Optical Society of America. A, Optics,*

Image Science, and Vision, *14*(5), 961–971. http://doi.org/10.1364/JOSAA.14.000961

MacRae, S., & Fujieda, M. (1999). Slit skiascopic-guided ablation using the Nidek laser. *Journal of Refractive Surgery (Thorofare, N.J. : 1995)*, *16*(5), S576–S580. Retrieved from http://www.ncbi.nlm.nih.gov/pubmed/11019877

Manzanera, S., Canovas, C., Prieto, P. M., & Artal, P. (2008). A wavelength tunable wavefront sensor for the human eye. *Optics Express*, *16*(11), 7748–7755. Retrieved from http://www.ncbi.nlm.nih.gov/pubmed/18545485

Manzanera, S., Prieto, P. M., Ayala, D. B., Lindacher, J. M., & Artal, P. (2007). Liquid crystal Adaptive Optics Visual Simulator: Application to testing and design of ophthalmic optical elements. *Optics Express*, *15*, 16177–16188.

Marcos, S., Burns, S. a., Moreno-Barriusop, E., & Navarro, R. (1999). A new approach to the study of ocular chromatic aberrations. *Vision Research*, *39*, 4309–4323.

McBrien, N. A., & Millodot, M. (1985). Clinical evaluation of the Canon Autoref R-1. *American Journal of Optometry and Physiological Optics*, *62*(11), 786–792.

McBrien, N. A., & Millodot, M. (1987). The relationship between tonic accommodation and refractive error. *Investigative Ophthalmology & Visual Science*, *28*(6), 997–1004.

McLellan, J. S., Marcos, S., Prieto, P. M., & Burns, S. a. (2002). Imperfect optics may be the eye's defence against chromatic blur. *Nature*, *417*(6885), 174–176.

Mershon, D. H., & Amerson, T. L. (1980). Stability of measures of the dark focus of accommodation. *Investigative Ophtalmology & Visual Science*, *19*(2), 217–221.

Mierdel, P., Kaemmerer, M., Mrochen, M., Krinke, H. E., & Seiler, T. (2001). Ocular optical aberrometer for clinical use. *Journal of Biomedical Optics*, *6*(2), 200–204.

Miles, W. R. (1929). Ocular dominance demonstrated by unconscious sighting. *Journal of Experimental Psychology*, *12*(2), 113–126.

Miller, R. J. (1978). Temporal stability of the dark focus of accommodation. *American Journal of Optometry and Physiological Optics*, *55*(7), 447–450.

Mira-Agudelo, A., Lundstrom, L., & Artal, P. (2009). Temporal dynamics of ocular aberrations: monocular vs binocular vision. *Ophthalmic And Physiological Optics*, *29*(3), 256–263.

Molebny, V. V., Panagopoulou, S. I., Molebny, S. V., Wakil, Y. S., & Pallikaris, I. G. (2000). Principles of ray tracing aberrometry. *Journal of Refractive Surgery (Thorofare, N.J. : 1995)*, *16*(5), S572–S575.

Mrochen, M., Kaemmerer, M., Mierdel, P., Krinke, H. E., & Seiler, T. (2000). Principles of Tscherning aberrometry. *Journal of Refractive Surgery*, *16*(5), S570–S571.

Navarro, R., & Losada, M. A. (1997). Aberrations and relative efficiency of light pencils in the living human eye. *Optometry & Vision Science*, *74*(7), 540–547.

Navarro, R., & Moreno-Barriuso, E. (1999). Laser ray-tracing method for optical testing. *Optics Letters*, *24*(14), 951–953. http://doi.org/10.1364/OL.24.000951

Neal, D. R., Copland, J., & Neal, D. (2002). Shack-Hartmann wavefront sensor precision and accuracy. *Proceedings of SPIE*, *4779*, 148–160.

Ninomiya, S., Fujikado, T., Kuroda, T., Maeda, N., Tano, Y., Oshika, T., … Mihashi, T. (2002). Changes of ocular aberration with accommodation. *American Journal of Ophthalmology*, *134*(6), 924–926.

Noorden, G., & Campos, E. (1996). The near vision complex. In *Binocular vision and ocular motility* (pp. 85–100).

Okuyama, F., Tokoro, T., & Fujieda, M. (1993). Binocular infrared optometer for measuring accommodation in both eyes simultaneously in natural-viewing conditions. *Applied Optics*, *32*(22), 4147–4154.

Otero, J. M., & Dúran, A. (1941). Rendimiento fotométrico de sistemas ópticos a bajas luminosidades. *An. Fis. Quim.*, 337–349.

Otero, J. M., Plaza, L., & Salaverri, F. (1949). Absolute thresholds and night myopia. *Journal of the Optical Society of America*, *39*(2), 167.

Owens, D. A., & Leibowitz, H. W. (1976a). Night myopia: cause and a possible basis for amelioration. *American Journal of Optometry and Physiological Optics*, *53*(11), 709–717.

Owens, D. A., & Leibowitz, H. W. (1976b). Oculomotor adjustments in darkness and the specific distance tendency. *Perception & Psychophysics*, *20*(1), 2–9.

Owens, D. A., & Leibowitz, H. W. (1980). Accommodation, convergence, and distance perception in low illumination. *American Journal of Optometry and Physiological Optics*, *57*(9), 540–550.

Pascal, J. I. (1955). A physiological unit of convergence. *Archives of Ophthalmology*, *53*(4), 616–616. http://doi.org/10.1001/archopht.1955.00930010624029

Phillips, S., & Stark, L. (1977). Blur: a sufficient accommodative stimulus. *Documenta Ophthalmologica*, *43*(1), 65–89.

Piers, P. A., Fernandez, E. J., Manzanera, S., Norrby, S., & Artal, P. (2004). Adaptive optics simulation of intraocular lenses with modified spherical aberration. *Investigative Ophthalmology & Visual Science*, *45*(12), 4601–4610. http://doi.org/10.1167/iovs.04-0234

Plainis, S., Ginis, H. S., & Pallikaris, A. (2005). The effect of ocular aberrations on steady-state errors of accommodative response. *Journal of Vision*, *5*(7), 466–477.

Platt, B., & Shack, R. (2001). History and principles of Shack-Hartmann wavefront sensing. *Journal of Refractive Surgery*, *17*(5), S573-577.

Poonja, S., Patel, S., Henry, L., & Roorda, A. (2005). Dynamic visual stimulus presentation in an adaptive optics scanning laser ophthalmoscope. *Journal of Refractive Surgery*, *21*(5), S575–S580.

Porter, J., Guirao, A., Cox, I. G., & Williams, D. R. (2001). Monochromatic aberrations of the human eye in a large population. *Journal of the Optical Society of America*, *18*(8), 1793–1803.

Prieto, P. M., Fernández, E. J., Manzanera, S., & Artal, P. (2004). Adaptive optics with a programmable

phase modulator: applications in the human eye. *Optics Express*, *12*(17), 4059–4071.

Prieto, P. M., Vargas-Martin, F., Goelz, S., & Artal, P. (2000). Analysis of the performance of the Hartmann-Shack sensor in the human eye. *Journal of the Optical Society of America A.*, *17*(8), 1388–1398.

Purkinje, J. (1825). *Neue Beiträge zur Kenntniss des Sehens in Subjectiver Hinsicht*. (G. Reimer, Ed.). Berlin.

Radhakrishnan, H., & Charman, W. N. (2007). Age-Related changes in ocular aberrations with accommodation. *Journal of Vision*, *7*(11), 1–21.

Rayleigh, J. W. S. (1883). On the invisibility of small objects in a bad light. *Proc Camb Phil Soc*.

Roorda, A. (2011). Adaptive optics for studying visual function : A comprehensive review. *Journal of Vision*, *11*(6), 1–21. http://doi.org/10.1167/11.5.6.Introduction

Roorda, A., & Glasser, A. (2004). Wave aberrations of the isolated crystalline lens. *Journal of Vision*, *4*(4), 250–261.

Rozema, J. J., Van Dyck, D. E. M., & Tassignon, M. J. (2005). Clinical comparison of 6 aberrometers. Part 1: Technical specifications. *Journal of Cataract and Refractive Surgery*, *31*(6), 1114–1127. http://doi.org/10.1016/j.jcrs.2004.11.051

Rucker, F. J., & Kruger, P. B. (2004a). Accommodation responses to stimuli in cone contrast space. *Vision Research*, *44*(25), 2931–2944. http://doi.org/10.1016/j.visres.2004.07.005

Rucker, F. J., & Kruger, P. B. (2004b). The role of short-wavelength sensitive cones and chromatic aberration in the response to stationary and step accommodation stimuli. *Vision Research*, *44*, 197–208.

Rucker, F. J., & Kruger, P. B. (2006). Cone contributions to signals for accommodation and the relationship to refractive error. *Vision Research*, *46*(19), 3079–3089. http://doi.org/10.1016/j.visres.2006.04.009

Ruffieux, P., Scharf, T., Herzig, H. P., Völkel, R., & Weible, K. J. (2006). On the chromatic aberration of microlenses. *Optics Express*, *14*(11), 4687–4694.

Rynders, M. C., Navarro, R., & Losada, M. a. (1998). Objective measurement of the off-axis longitudinal chromatic aberration in the human eye. *Vision Research*, *38*(4), 513–522.

Sabesan, R., Zheleznyak, L., & Yoon, G. (2012). Binocular visual performance and summation after correcting higher order aberrations. *Biomedical Optics Express*, *3*(12), 3176–3189.

Salmon, T. O., Thibos, L. N., & Bradley, A. (1998). Comparison of the eye's wave-front aberration measured psychophysically and with the Shack–Hartmann wave-front sensor. *Journal of the Optical Society of America A*, *15*(9), 2457.

Salmon, T. O., West, R. W., Gasser, W., & Kenmore, T. (2003). Measurement of refractive errors in young myopes using the COAS Shack-Hartmann aberrometer. *Optometry and Vision Science*, *80*(1), 6–14.

Santamaría, J., Artal, P., & Bescós, J. (1987). Determination of the point-spread function of human

eyes using a hybrid optical–digital method. *Journal of the Optical Society of America A*, *4*(6), 1109–1114. http://doi.org/10.1364/JOSAA.4.001109

Schaeffel, F., Farkas, L., & Howland, H. C. (1987). Infrared photoretinoscope. *Applied Optics*, *26*(8), 1505–1509.

Schaeffel, F., Wilhelm, H., & Zrenner, E. (1993). Inter-Individual variability in the dynamics of natural accommodation in humans: Relation to age and refractive errors. *Journal of Physiology*, *32*(461), 301–320.

Schor, C. (1999). The influence of interactions between accommodation and convergence on the lag of accommodation. *Ophthalmic and Physiological Optics*, *19*(2), 134–150. http://doi.org/10.1046/j.1475-1313.1999.00409.x

Schor, C. M. (1992). A dynamic model of cross coupling between: Simulations of step and frequency responses. *Optometry & Vision Science*, *69*(4), 258–269.

Schwarz, C. (2013). *Influence of aberrations on Binocular Vision by means of Adaptive Optics Instruments*. Universidad de Murcia.

Schwarz, C., Prieto, P. M., Fernández, E. J., & Artal, P. (2011). Binocular adaptive optics vision analyzer with full control over the complex pupil functions. *Optics Letters*, *36*(24), 4779–4781. Retrieved from http://www.ncbi.nlm.nih.gov/pubmed/22179881

Seidemann, A., & Schaeffel, F. (2002). Effects of longitudinal chromatic aberration on accommodation and emmetropization. *Vision Research*, *42*(21), 2409–2417.

Seidemann, A., & Schaeffel, F. (2003). An evaluation of the lag of accommodation using photorefraction. *Vision Research*, *43*(4), 419–430.

Sekine, R., Shibuya, T., Ukai, K., Komatsu, S., Hattori, M., Mihashi, T., … Hirohara, Y. (2006). Measurement of wavefront aberration of human eye using talbot Image of two-Dimensional brating. *Optical Review*, *13*(4), 207–211.

Shack, R. V., & Platt, B. C. (1971). Production and use of a lenticular Hartmann screen. *Journal of the Optical Society of America*, *61*, 656–660.

Shirachi, D., Liu, J., Lee, M., Jang, J., Wong, J., & Stark, L. (1978). Accommodation dynamics I. Range nonlinearity. *American Journal of Optometry and Physiological Optics*, *55*(9), 631–641.

Southwell, W. H. (1980). Wave-front estimation from wave-front slope measurements. *Journal of the Optical Society of America*, *70*(8), 998–1006. http://doi.org/10.1364/JOSA.70.000998

Stark, L., Kenyon, R. V., Krishnan, V. V., & Ciuffreda, K. J. (1980). Disparity vergence: a proposed name for a dominant component of binocular vergence eye movements. *American Journal of Optometry and Physiological Optics*, *57*(9), 606–609.

Sterner, B., Gellerstedt, M., & Sjöström, A. (2004). The amplitude of accommodation in 6-10-year-old children - not as good as expected! *Ophthalmic & Physiological Optics : The Journal of the British College of Ophthalmic Opticians (Optometrists)*, *24*(3), 246–251.

Stockman, A., & Sharpe, L. T. (2006). Into the twilight zone: The complexities of mesopic vision and luminous efficiency. *Ophthalmic and Physiological Optics*, *26*(3), 225–239.

Suryakumar, R. (2005). *Study of the dynamic interactions between vergence and accommodation*.

Suryakumar, R., Meyers, J. P., Irving, E. L., & Bobier, W. R. (2007a). Application of video-based technology for the simultaneous measurement of accommodation and vergence. *Vision Research*, *47*(2), 260–8.

Suryakumar, R., Meyers, J. P., Irving, E. L., & Bobier, W. R. (2007b). Vergence accommodation and monocular closed loop blur accommodation have similar dynamic characteristics. *Vision Research*, *47*(3), 327–337.

Tabernero, J., Schwarz, C., Fernández, E. J., & Artal, P. (2011). Binocular visual simulation of a corneal inlay to increase depth of focus. *Investigative Ophthalmology & Visual Science*, *52*(8), 5273–5277. http://doi.org/10.1167/iovs.10-6436

Thibos, L. N. (2000). Principles of Hartmann-Shack aberrometry. *Journal of Refractive Surgery*, *16*(5), S563–S565. Retrieved from http://www.ncbi.nlm.nih.gov/pubmed/11019873

Thibos, L. N., Applegate, R. A., Schwiegerling, J. T., Webb, R., & Members, V. S. T. (2000). Standards for reporting the optical aberrations of eyes. In *Vision Science and its Applications, Proceedings* (Vol. 35, pp. 232–244). Santa Fe, New Mexico.

Thibos, L. N., Bradley, A., & Applegate, R. A. (2004). Accuracy and precision of objective refraction from wavefront aberrations. *Journal of Vision*, (4), 329–351.

Thibos, L. N., Hong, X., Bradley, A., & Cheng, X. (2002). Statistical variation of aberration structure and image quality in a normal population of healthy eyes. *Journal of the Optical Society of America A.*, *19*(12), 2329–2348.

Thibos, L. N., Ye, M., Zhang, X., & Bradley, A. (1992). The chromatic eye: a new reduced-eye model of ocular chromatic aberration in humans. *Applied Optics*, *31*(19), 3594–3600.

Toates, F. M. (1972). Accommodation function of the human eye. *Physiological Reviews*, *52*(4), 828–863.

Tousey, R., Koomen, M., & Scolnik, R. (1953). Accommodation and night myopia. *Journal of the Optical Society of America*, *43*(10), 926–927.

Tscherning, M. (1894). Die monochromatischen aberrationen des menschlichen auges. *Z. Psychol. Physiol. Sinne.*, *17*, 456–471.

Tscherning, M. (1909). *Hermann v. Helmholtz et la théorie de l'accommodation*. (O. D. et Fils, Ed.)*Octave Doin et Fils , Éditeurs*. Paris.

Vinas, M., Dorronsoro, C., Cortes, D., Pascual, D., & Marcos, S. (2015). Longitudinal chromatic aberration of the human eye in the visible and near infrared from wavefront sensing , double-pass and psychophysics. *Biomedical Optics Express*, *23*(4), 513–522. http://doi.org/10.1364/OE.23.00948

Wald, G. (1945). Human vision and the spectrum. *Science (New York, N.Y.)*, *101*(2635), 653–658.

Wald, G., & Griffin, D. R. (1947). The change in refractive power of the human eye in dim and bright light. *Journal of the Optical Society of America*, *37*(5), 321–336.

Walsh, G. (1988). The effect of mydriasis on the pupillary centration of the human eye. *Ophthalmic & Physiological Optics : The Journal of the British College of Ophthalmic Opticians (Optometrists)*, *8*(2), 178–182.

Ware, C. (1982). Human axial chromatic aberration found not to decline with age. *Graefe's Archive for Clinical and Experimental Ophthalmology*, *218*(1), 39–41. http://doi.org/10.1007/BF02134100

Westheimer, G., & Mitchell, A. M. (1956). Eye movement responses to convergence stimuli. *Archives of Ophthalmology*, *55*(6), 848–856.

Westheimer, G., & Mitchell, D. E. (1969). The sensory stimulus for disjunctive eye movements. *Vision Research*, *9*(7), 749–755.

Wilson, M. A., Campbell, M. C., & Simonet, P. (1992). Change of pupil centration with change of illumination and pupil size. *Optometry and Vision Science : Official Publication of the American Academy of Optometry*, *69*(2), 129–136.

Wolf, K. S., Bedell, H. E., & Pedersen, S. B. (1990). Relations between accommodation and vergence in darkness. *American Academy of Optometry*, *67*(2), 89–93.

Wyatt, H. J. (1995). The form of the human pupil. *Vision Research*, *35*(14), 2021–2036.

Yamada, T., & Ukai, K. (1997). Amount of defocus is not used as an error signal in the control system of accommodation dynamics. *Ophthalmic and Physiological Optics*, *17*(1), 55–60.

Yang, Y., Thompson, K., & Burns, S. A. (2002). Pupil location under mesopic, photopic, and pharmacologically dilated conditions. *Investigative Ophthalmology & Visual Science*, *43*(7), 2508–2512.

Zernike, V. F. (1934). Beugungstheorie des schneidenver-fahrens und seiner verbesserten form, der phasenkontrastmethode. *Physica*, *1*(7–12), 689–704.

Acknowledgments

Acknowledgment

First, I would like to express my love and thanks to my family. Particularly to my parents Béatrice and Dominique, my twin brother Alex and my partner María Inmaculada. They have always accepted my choices without no complaints and they unfailingly supported me during these last 4 years. They helped me to take the best decisions specially in the most difficult moments. They are my strength and for this reason, the success of this work is dedicated to them. Obviously, this includes my Spanish family José Antonio and Concepción. They offered me the best Murcian cooking in a beautiful and relaxing place in the heart of the Ricote valley. They contributed greatly to this success in this long way. Thank you to exist and to be part of my life.

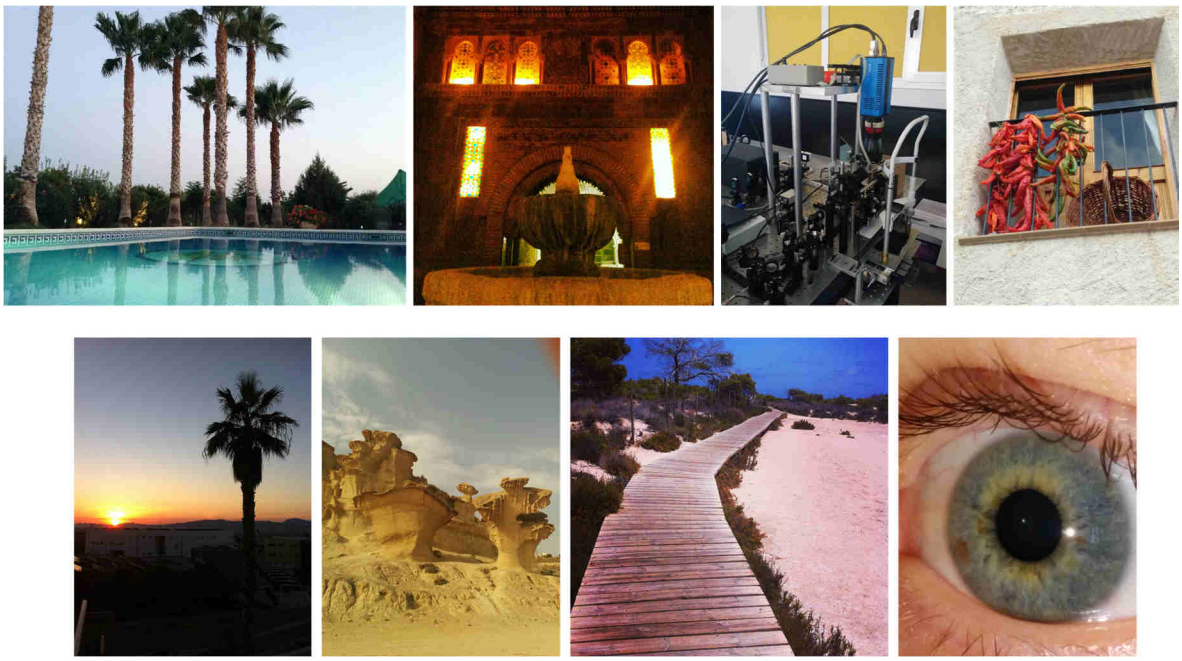

This work is not only the result of a single person, but it is the contribution of many people with expertise in different fields. They have dedicated time, effort, and support in the long term and for this reason I will never forgot.

I would like to express my deepest and sincere gratitude to my thesis advisor, Professor Pablo Artal director of the laboratory of optics and supervisor of this work. Prof. Artal stimulated my very large interest in optics, instrumentation and biomedical engineering in the field of ophthalmology. His laboratory provides a high-quality scientific environment and an excellent technological support, which permitted me to carry out my PhD serenely.

Obviously, I am very grateful to Pedro María Prieto Corrales, an excellent professor of physics and optics, and supervisor of this work. I appreciated greatly his human qualities, his time, honesty and the advice in visual and physiological optics. His decisive hard work for correcting the English grammar of the manuscript was undeniable.

I am particularly grateful to Professor Harilaos Ginis from University of Crete and my colleagues and friends Alexandros Pennos and Dimitrios Christaras. They have been part of my daily life during many years. I always enjoyed their friendship, generosity and Greek spirit that made my stay so pleasant.

I thank the Laboratory of Optics of the University of Murcia and the LO.UM members that have been involved at some point in my thesis. Special thanks goes to Carmen Martinez. His assistance and dedication with paperwork, and his generous personality make her a great colleague. Further, I am also grateful to Juan Tabernero for the professionalism and the scientific spirit. I really appreciated the advice about life and future in science. Thanks to Christina Schwarz my colleague during the first years of my PhD, for his significant help and the advice in adaptive optics and scientific analysis. Thanks to Adrían and Juan, informatics engineers, for the help in matlab and software issues. Thanks to my friend Jesús for our running outdoor sessions at the athletic stadium, that helped me to relax after long days in the lab. Finally, I would like to express my acknowledgment to the rest of members and ex-members of LO.UM Alejandro, Antonio, Astrid, Bart, Benjamin, Consuelo, Eloy, Encarna, Esther, Joshua, Juan Francisco, Juan Manuel, Daniel, Maelle, Martin, Mary and Silvestre.

Furthermore, I am grateful to the Spanish "Ministerio de Ciencia e Innovacion" for the financial support FPI predoctoral fellowship FIS-2010-14926 reference BES-2011-043899, the European Research Council Advanced Grant ERC-2013-AdG-339228 (SEECAT) and the Spanish SEIDI, grant FIS2013-41237-R.

Publications

Publications

Fernandez, E. J., Prieto, P. M., Chirre, E., & Artal, P. (2013). Performance of a 6-Pi liquid crystal on silicon (LCoS) spatial light modulator under white light illumination for visual applications. In *Optics InfoBase Conference Papers*.

Chirre, E., Prieto, P. M., & Artal, P. (2014). Binocular open-view instrument to measure aberrations and pupillary dynamics. *Optics Letters*, *39*(16), 4773–4775.

Chirre, E., Prieto, P. M., & Artal, P. (2015). Dynamics of the near response under natural viewing conditions with an open-view sensor. *Biomedical Optics Express*, *6*(10), 4200–4211.

Tabernero, J., Chirre, E., Hervella, L., Prieto, P. M., & Artal, P. (2016). The accommodative ciliary muscle function is preserved in older humans. *Scientific Reports*, 1–7.

Chirre, E. Prieto, P. M., & Artal, P. (2016). Night myopia is reduced in binocular vision. *Journal of vision, 16(8), 1–10.*